

# **Pulsed-DC Reactive Sputtered Aluminum Oxide For The Surface Passivation Of Crystalline Silicon Solar Cell**

Submitted in partial fulfilment of the requirements of the

Degree of

## **Doctor of Philosophy**

By

### **Meenakshi Bhaisare**

(Roll No. 07407005)

Under the guidance of

### **Prof. Anil Kottanthalayil**



Department Of Electrical Engineering

INDIAN INSTITUTE OF TECHNOLOGY BOMBAY

2019

*Dedicated to my Mother, Father  
and my beloved son Divyaan.*

## **Thesis Approval**

The Thesis entitled

### **Pulsed-DC reactive sputtered aluminum oxide for the surface passivation of crystalline silicon solar cell**

by

Meenakshi Bhaisare  
(Roll No.07407005)

is approved for the degree of  
Doctor of Philosophy

S Sundar Kumar Iyer  
Prof. S. Sundar Kumar Iyer

J Vasi  
Prof. J. Vasi

Anil Kottantharayil  
Prof. Anil Kottantharayil

K. Siby K. George  
Prof. Siby K. George

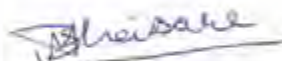
Date: October 23, 2019

Place: IIT Bombay, Mumbai

## **Declaration**

I declare that this written submission represents my ideas in my own words and where others' ideas or words have been included, I have adequately cited and referenced the original sources. I also declared that parts of chapter 3, chapter 4, chapter 5, chapter 6 and chapter 7 are either published in international journal/conferences or have been submitted for publication. The list of publication is attached at the end of this thesis.

I also declare that I have adhered to all principles of academic honesty and integrity and have not misrepresented or fabricated or falsified any idea/data/fact/source in my submission. I understand that any violation of the above will be cause for disciplinary action by the Institute and can also evoke penal action from the sources which have thus not been properly cited or from whom proper permission has not been taken when needed.



Meenakshi Bhaisare

Roll No. : 07407005

Date : 23/10/2019

Place : IIT Bombay, Mumbai

## Abstract

Advancements in renewable energy technologies for the electricity generation have led to less dependency on fossil fuels like petrol and coal. In particular, the solar photovoltaic (SPV) technology has become a fast-growing field today, among different renewable energy technologies with an impressive research and development in this field and cost reductions. The basic energy conversion device in SPV is the “solar cell” that uses photons from the sunlight as input source to generate charge carriers followed by transportation of these charge carriers into the external circuit. More efficient solar cell means more electricity generated per unit area of the conversion device. The particular focus on manufacturing of most efficient and low-cost solar cells brings in many challenges in the field of research and development.

The crystalline silicon (c-Si) solar cells have shown highest conversion efficiency of  $\eta = 26.7\%$  among different cell technologies, and also dominates most of the PV market due to high compatibility with the existing very large scale integration (VLSI) silicon technology and manufacturing. In a conventional c-Si solar cell, various factors need to be addressed to achieve high efficiency. Among these factors, the loss of light generated carrier due to recombination at the surface of silicon may be realized by the surface passivation layer.

The aluminum oxide ( $\text{AlO}_x$ ) film was widely investigated as passivation layer of p-type c-Si surface, because of its inherent property of high density of negative fixed oxide charges ( $Q_f$ ) in the film which are used to repel electrons from the p-type surface and hence could minimize the surface recombination losses, this mechanism is known as field-effect passivation. In this report, we present the reactive sputter (RS) deposited  $\text{AlO}_x$  film for passivation layer of p-type c-Si surface. To achieve the low-cost factor of surface passivated solar cell manufacturing, the high-quality film is obtained using RS technique with pulsed-DC power supply. Integration of RS technique in cell-line manufacturing for film deposition is a big challenge to the solar industries.

The work comprises of process development and optimization for deposition of high quality  $\text{AlO}_x$  film by RS technique, to be applied as surface passivation layer of p-type c-Si. The process development involves, characterization of the film using electrical, material and opto-electronic measurement techniques to assess the film quality and applicability as passivation

layer. The quality of the  $\text{AlO}_x$  film deposited by RS technique was not studied very well in terms of its interfacial properties. Also the biggest challenge using this technique was repeatability and uniformity of the film quality. In this work, we have used an industry standard RS system from Applied Material Inc. called Endura, which is already in use in semiconductor industries for metal deposition. We have used this system for  $\text{AlO}_x$  dielectric film deposition on c-Si substrate using  $\text{O}_2$  as reactive gas and Ar as sputter gas ambient. To achieve uniform and repeatable results using RS system for high quality film deposition, have led us to develop new recipes and further optimize them as per the requirement. A rigorous study on the material and interfacial property was carried out using sophisticated instruments. These studies are benchmarked to the  $\text{AlO}_x$  film deposited using different techniques like chemical vapor deposition (CVD) and atomic layer deposition (ALD), reported in the literature.

The optimized process condition for pulsed-DC RS  $\text{AlO}_x$  film deposition, with the application of optimized post-deposition annealing (PDA) condition on the film, results in reasonably good surface passivation with effective surface recombination velocity ( $S_{\text{eff}}$ ) of  $40 \text{ cm.s}^{-1}$  on p-type (FZ) c-Si wafer with  $7.8 \Omega.\text{cm}$  resistivity. The electrical measurements shows, this film carries high negative fixed oxide charges ( $Q_f$ ) of  $6 \times 10^{12} \text{ cm}^{-2}$  that supports field-effect passivation and low density of interface states ( $D_{it}$ ) of  $2.3 \times 10^{11} \text{ eV}^{-1}.\text{cm}^{-2}$  that supports chemical passivation. The technique has also shown high deposition rate of  $5 \text{ nm}.\text{min}^{-1}$  with optimized process condition, which is significantly higher as compared to typical thermal ALD processes investigated for solar cells applications. The film has shown thick interfacial layer (IL) of  $8.2 \text{ nm}$  at  $\text{AlO}_x/\text{c-Si}$  interface, for  $26 \text{ nm}$  film deposition, using high-resolution transmission electron microscope (TEM). The composition of the film and IL were assessed using elemental depth-profile through X-ray photoelectron spectroscope (XPS). Which shows the IL was found to be aluminum silicate. Using fourier transform infra-red spectrometer (FTIR) measurement, the presence of absorbance peak at  $1090 \text{ cm}^{-1}$  also confirms the formation of interfacial oxide in the film after annealing.

The electron energy loss spectroscopy (EELS) measurement was used to study the origin of  $Q_f$  in the RS  $\text{AlO}_x$  film and IL, which shows the presence of both tetrahedral ( $T$ ) and octahedral ( $O$ ) coordinated Al in as-deposited condition. However the concentration of  $T$  coordinated Al increases after annealing at optimized condition, hence supports the finding of

increase in negative  $Q_f$  after annealing. The  $T/O$  peak intensity ratio was studied for distribution of  $Q_f$ , which shows presence of high negative  $Q_f$  at IL/ c-Si interface and gradual decrease of these charges near IL/ $\text{AlO}_x$  interface. The presence of different intermediate oxidation states of Si  $2p$  at the IL of the film annealed in different conditions, was obtained using depth-resolved XPS measurements. This study of different intermediate oxidation states in the IL, was used to understand reason behind an improvement in  $D_{it}$  values after annealing of film.

The thermal stability of pulsed-DC RS  $\text{AlO}_x$  film against firing temperature as required by industrial screen-printed solar cell fabrication process was also studied in this work. The films were deposited using optimized process condition and subjected to optimized PDA condition for this study. The film was exposed to elevated temperature of 400-700 °C for 2 s using rapid thermal processing (RTP) in  $\text{N}_2$  ambient, which shows the surface passivation degrades for the firing temperature at 700 °C. This temperature is lower than the typical firing temperatures (~ 850 °C) used for manufacturing of industrial screen-printed solar cells. The film, however, may be used as passivation layer on advance passivated emitter and rear cell (PERC) structure with Ni/Cu contact where the firing temperature is in the range of 500 °C or less. The thermal stability of stack structure for  $\text{AlO}_x$  film capped with inductively coupled plasma (ICP)-CVD  $\text{SiN}_x:\text{H}$  was also studied, as many reports suggests an improvement in thermal stability for the stack structure against firing temperature. Through electrical characterization, we have observed net decrease in negative  $Q_f$  with marginal improvement in  $D_{it}$  for the stack structure. Also the surface passivation has shown relatively poor quality as compared to single layer  $\text{AlO}_x$  film. Hence additional film did not make any improvement in high temperature thermal stability for surface passivation of p-type c-Si, unlike the ALD and PECVD  $\text{AlO}_x$  films reported elsewhere.

In conclusion, the pulsed-DC RS deposited  $\text{AlO}_x$  film may be applied as the surface passivation layer in silicon solar cell structures for advanced structures such as PERC.

## Acknowledgements

I would like to express my sincere gratitude to my supervisor Prof. Anil Kottanthalayil for giving me an opportunity to work under his guidance in the field of crystalline silicon solar cell technologies. I am extremely grateful for his support, affection and constant encouragement throughout the journey. He has always helped me to stay motivated and focused on the assigned research work and bring out new ideas to work and try upon. The learning under his guidance has embarked upon me ‘the patience and positive perspective’ towards the research work. I cannot thank him enough for mentoring me to pursue my Ph.D.

My sincere gratitude to Prof. J. Vasi for supporting and encouraging me to pursue my research work. I would like to thank him for all the moral support required during this time. I would thank Prof. B. M. Arora, Prof. C. S. Solanki and again thank Prof. J. Vasi, for being in the review committee and suggesting me valuable inputs after time-to-time evaluation of the work.

I am grateful to the professors at Department of Electrical and Engineering, for their constructive inputs at various stages with special thanks to Prof. R. Pinto, Prof. U. Ganguly, and Prof. K L Narasimhan. I would like to thank Prof. B. J. Fernandes, Head of Department, for his support towards my Doctoral thesis. I would like to thank Ms. Madhumita, Mr. Santosh, Ms. Vaishali and Ms. Tanvi for their help in all the administrative matters.

I acknowledge the Ministry of New and Renewable Energy (MNRE) for fund support during the course of my Ph.D. degree through the National Centre for Photovoltaic Education and Research (NCPRE). I acknowledge the “IITB Nanofabrication Facility” (IITBNF), Department of Electrical Engineering, and NCPRE at IIT Bombay for providing the laboratory facility to carry out this thesis work. I wish many thanks to all the staff members for their friendly support throughout the work with special thanks to Mrs. Thankamani N., Sunil K., Pradeep N., Sandeep M., Rajendra S., Anjum A., Gayatri V., Sandeep K. and Guru B. A note of thanks to Dr. Diksha M. and Ms. Valli for their cooperation in the administrative work.

I acknowledge Sophisticated Analytical Instrument Facility (SAIF), IIT Bombay, for their assistance in carrying out HR-TEM measurements. I acknowledge The Industrial Research and Consultancy Centre (IRCC) Facility, IIT Bombay for assistance in carrying out AFM and XPS

measurements. I also thank Dr. D.S. Sutar, Ms. Anuradha and all the staff and students to carry out these measurements. I acknowledge Raja Ramanna Centre for Advance Technology (RRCAT), Indore, for carrying out the XRR measurements. I would like to thank Dr. M. Modi and staff to help me carry out the measurements. I acknowledge the International Centre for Materials Science, Jawaharlal Nehru Centre for Advanced Scientific Research (JNCASR), Bengaluru, for performing the EELS measurements. I would like to thank Dr. Dileep K. under the guidance of Dr. R. Datta, who performed the measurement and help me interpret the data for analysis.

I would like to thank my group members; Abhishek M., Kousik M., Sandeep S. S., Shaivalini S., Manini G., Mayur W., Amit G., and Senthil S., Gaudhaman J., Sanchar A., Kalaivani S., Sonali W., Manali K., Amruta J., Bandana S., for making the work environment more enjoyable and comfortable. I would like to express my love and gratitude to my friends from IIT Bombay; Sakshi, Nihit, Sreenivas, Kunal, Aashish, Preeti, Reeti, Pratima, Khadija and Moumita for all the personal favours and for making my stay at IIT Bombay as most memorable and unforgettable part of my life. A special thanks to my seniors cum mentors Sandhya C., Pawan S. and Harshil R. for all the help and support during the immature part of my research. I would also acknowledge and thanks my friends Shanti, Richa, Praveena, Rahul and Sandip (brother-in- law) for encouraging me during all this time.

I thank my dear parents Mrs. Sevan and Mr. Ramesh Bhaisare, my elder brothers Hemant and Ravi and my dear sister Reena for all their blessings, encouragement and support which is beyond the words. Special thanks to my brother Hemant for his guidance and showing me this path with all his support. I would like to thank my dear husband Himanshu Marmat who is being always encouraging, supporting and stood beside me during my research career. Last but not the least I would like to thank my beloved son Divyaan for being patience during this time and showering me with his love all the time. Special note of thanks to my parents for being patience and supporting me with my kid during this time. None of this would have been possible without their blessings and unconditional love.

With all my respect and love, I humbly dedicate this thesis to them.

Meenakshi Bhaisare

# List of Contents

<b>Abstract</b>	<b>ii</b>
<b>Acknowledgements</b>	<b>v</b>
<b>List of Figures</b>	<b>xi</b>
<b>List of Tables</b>	<b>xvii</b>
<b>List of Symbols</b>	<b>xviii</b>
<b>List of Acronyms</b>	<b>xxiii</b>
<b>Chapter 1. Introduction</b>	<b>1</b>
1.1    Recombination mechanisms in crystalline silicon	4
1.2    Solar cell performance parameters	8
1.3    Surface passivation of crystalline silicon	13
1.3.1    Chemical passivation	13
1.3.2    Field-effect passivation	13
1.4    Application of different materials as surface passivation layers	15
1.4.1    Silicon dioxide ( $\text{SiO}_2$ )	15
1.4.2    Amorphous silicon nitride ( $\text{a-SiN}_x$ )	16
1.4.3    Hydrogenated amorphous silicon ( $\text{a-Si:H}$ )	17
1.4.4    Aluminum oxide ( $\text{AlO}_x$ )	17
1.5    Thesis motivation	17
1.6    Thesis outline	18
<b>Chapter 2. Literature Review and Experimental Techniques</b>	<b>19</b>
2.1    Introduction	19
2.2    Theoretical understanding of $\text{AlO}_x/\text{c-Si}$ interface	20
2.3    Various techniques used to deposit $\text{AlO}_x$ film for passivation of c-Si surface	21
2.3.1    Atomic layer deposition	21
2.3.2    Plasma enhanced or assisted chemical vapor deposition	26

2.3.3	Reactive sputter deposition technique	29
2.4	Experimental techniques	31
2.4.1	Electrical characterization	31
2.4.2	Material characterization	37
(a)	Spectroscopic ellipsometer	37
(b)	X-ray reflectometer	38
(c)	Atomic force microscope	39
(d)	X-ray photoelectron spectroscope	40
(e)	Transmission electron microscope	41
(f)	Electron energy loss spectroscopy	42
(g)	Fourier transform infra-red spectroscope	43
(h)	Ultra violet-visible-near infrared spectroscope	44
2.4.3	Opto-electronic characterization	45
2.5	Summary	47
<b>Chapter 3</b>	<b>Pulsed-DC Reactive Sputter Deposited AlO<sub>x</sub> Film</b>	<b>49</b>
3.1	Introduction	49
3.2	Pulsed-DC reactive sputter deposition technique	50
(a)	Process power	52
(b)	Process time	52
(c)	Process pressure	52
(d)	Substrate temperature	52
(e)	Pulsed-DC power supply	53
3.3	Experimental details	53
3.4	Hysteresis behaviour	54
3.5	Material characterization	55
3.5.1	Film density and surface morphology	55
3.5.2	Film composition	59
3.5.3	Deposition rate and optical property	61
3.6	Electrical characterization	62
3.7	Summary	65

<b>Chapter 4</b>	<b>Optimization of Post-Deposition Annealing for the Improvement of Passivation</b>	<b>67</b>
4.1	Introduction	67
4.2	Experimental details	68
4.3	Electrical characterization	69
4.4	Surface passivation	73
4.5	Material characterization	76
4.5.1	Cross-sectional imaging by TEM	76
4.5.2	Elemental analysis by XPS	78
4.6	Summary	79
<b>Chapter 5</b>	<b>Origin and Distribution of Charges in AlO<sub>x</sub> film Deposited on c-Si by Pulsed-DC Reactive Sputtering</b>	<b>80</b>
5.1	Introduction	80
5.2	Experimental details	83
5.3	EELS measurements	84
5.4	Exploration of intermediate oxidation states using XPS	87
5.5	FTIR investigation of the films	94
5.6	Band-gap energy measurement using low-loss EELS spectra	95
5.7	Band-gap energy measurement using UV-Vis-NIR spectroscope	98
5.8	Conclusion	100
<b>Chapter 6</b>	<b>Impact of Deposition Process Conditions on the Quality of Interface between Pulsed-DC Reactive Sputtered AlO<sub>x</sub> and Silicon</b>	<b>102</b>
6.1	Introduction	102
6.2	Impact of process power density	103
6.2.1	Electrical characterization	105
6.2.2	Surface passivation	107
6.2.3	Physical characterization of the films	108
6.3	Impact of substrate temperature during deposition	111
6.4	Impact of process gas	113
6.5	Summary	116

<b>Chapter 7</b>	<b>Thermal Stability of Passivation for Pulsed-DC Reactive Sputtered AlO<sub>x</sub> Film</b>	<b>118</b>
7.1	Introduction	118
7.2	Experimental details	119
7.3	Thermal stability of single layer pulsed-DC RS AlO <sub>x</sub> film	121
7.4	Thermal stability of AlO <sub>x</sub> /SiN <sub>x</sub> :H stack structure	123
7.4.1	Electrical characterization	124
7.4.2	Surface passivation	127
7.5	Summary	130
<b>Chapter 8</b>	<b>Conclusions and Future Work</b>	<b>131</b>
8.1	Future direction	132
<b>References</b>		<b>135</b>
<b>List of Publications</b>		<b>151</b>

# List of Figures

Figure 1.1	Market shares of different photovoltaic technologies.	2
Figure 1.2	Recombination mechanisms in semiconductor material: (a) band-to-band, (b) Auger and (c) trap-assisted recombination.	4
Figure 1.3	(a) Typical p-n junction solar cell structure, (b) I-V characteristics of p-n junction solar cell.	8
Figure 1.4	Impact of surface recombination on p-n junction solar cell efficiency $\eta$ simulated using PC1D simulator, by (a) varying the $S_{\text{front}}$ , while keeping $S_{\text{rear}}$ constant (b) varying the $S_{\text{rear}}$ , while keeping $S_{\text{front}}$ constant.	12
Figure 1.5	Surface passivation mechanism for crystalline silicon viz. (a) chemical passivation and field-effect passivation further characterized as (b) by high-low doping and (c) passivation using dielectric layer with electrostatic charges, i.e., $Q_f$ .	14
Figure 1.6	The impact of chemical and field-effect passivation on the surface recombination velocity simulated using the equations for $S_{\text{eff}}$ and $S_{\text{eff,max}}$ , as shown in eq. (1.3) and (1.5), for different values of negative $Q_f$ and $N_{\text{it}}$ . The $n_s$ and $p_s$ were obtained using PC1D simulator. The values used for the defect carriers cross sections $\sigma_n = \sigma_p: 10^{-16} \text{ cm}^2$ .	15
Figure 2.1	Schematic diagram of typical (a) thermal ALD and (b) plasma assisted-ALD systems.	22
Figure 2.2	Reaction cycles for $\text{Al}_2\text{O}_3$ deposition using (a) thermal ALD and (b) plasma assisted-ALD system.	23
Figure 2.3	Schematic diagrams of typical (a) batch ALD reactor and (b) spatial ALD systems for solar industry applications.	25
Figure 2.4	Schematic diagram of typical PECVD system.	27
Figure 2.5	Schematic diagram of typical reactive sputter system using RF power supply.	29
Figure 2.6	MOS capacitor structure for electrical characterization of the dielectric film.	31
Figure 2.7	The high frequency C-V and G-V plot for the dielectric film measured on MOS capacitor at frequency, $f = 100 \text{ kHz}$ .	32

Figure 2.8	The J-V plot for the dielectric film measured on MOS capacitor.	36
Figure 2.9	The Weibull distribution plot of the $E_{BD}$ for 20 MOS capacitor devices tested on a wafer.	36
Figure 2.10	Typical schematic diagram and working principle of spectroscopic ellipsometer.	37
Figure 2.11	Typical schematic diagram and working principle of X-ray reflectometer.	38
Figure 2.12	Typical schematic diagram of atomic force microscope.	39
Figure 2.13	Typical schematic diagram and working principle of X-ray photoelectron spectrometer.	41
Figure 2.14	Typical schematic diagram and working principle of transmission electron microscope.	42
Figure 2.15	The typical schematic diagram of Fourier transform infra-red spectroscope.	43
Figure 2.16	The typical block diagram of UV-Vis-NIR spectroscope showing different units in system.	44
Figure 2.17	The typical schematic diagram of life-time measurement system.	46
Figure 3.1	(a) Schematic diagram of the reactive sputtering system and (b) waveform of pulsed-DC power supply with $V_p$ . Time $\tau_{ON}$ is target surface sputtering time and $\tau_{OFF}$ is the time when charges at the target surface get neutralized.	51
Figure 3.2	Hysteresis behaviour of cathode voltage as a function of oxygen ( $O_2$ ) flow rate for different PD conditions in pulsed-DC RS system. The arrows indicate the forward and reverse direction of variation of $O_2$ flow.	54
Figure 3.3	(a) Thickness and (b) RI of as-deposited and annealed $AlO_x$ film deposited at different PD.	56
Figure 3.4	Surface roughness and thickness of as-deposited $AlO_x$ film measured by XRR and extracted using Parratt formalism for different PD conditions.	57
Figure 3.5	The film density for $AlO_x$ obtained by XRR measurement using Parratt formulism for film deposited at different PD.	58

Figure 3.6	Contact mode AFM measurement of AlO <sub>x</sub> films deposited with Ar:O <sub>2</sub> flow ratio of (a) 2:5 and (b) 3:5, and PD of 0.69 W.cm <sup>-2</sup> .	59
Figure 3.7	(a) Al 2p spectra and (b) O 1s spectra of Al <sub>x</sub> O <sub>y</sub> films for different O <sub>2</sub> flow ratio measured using XPS.	60
Figure 3.8	Deposition rate and RI of AlO <sub>x</sub> film for different O <sub>2</sub> flow rate, keeping the Ar flow constant at 15 sccm and PD at 0.69 W.cm <sup>-2</sup> .	61
Figure 3.9	High frequency C-V characteristics curve of a typical MOS capacitor for AlO <sub>x</sub> film deposited at PD of 0.69 W.cm <sup>-2</sup> and Ar:O <sub>2</sub> flow of 2:5.	62
Figure 3.10	High frequency C-V plot of AlO <sub>x</sub> MOS capacitor with films deposited at PD of 0.69 W.cm <sup>-2</sup> and 1.3 W.cm <sup>-2</sup> . The inset shows the normalised C/C <sub>acc</sub> curve for both conditions to assess shift in V <sub>FB</sub> .	63
Figure 3.11	(a) Weibull distribution plot of E <sub>BD</sub> and (b) J-V plot for MOS capacitor device with AlO <sub>x</sub> film deposited using Ar:O <sub>2</sub> gas flow ratio of 2:5.	64
Figure 4.1	Figure 4.1 The C-V and G-V characteristics plot of MOS capacitors measured at f = 100 kHz for as-deposited AlO <sub>x</sub> film and after annealing in FGA {(a), (d)}, N <sub>2</sub> {(b), (e)} and N <sub>2</sub> + O <sub>2</sub> {(c), (f)} ambient at 420 °C, 470 °C and 520 °C for 20 min.	70
Figure 4.2	Extracted value of (a) negative Q <sub>f</sub> and (b) D <sub>it</sub> from MOS capacitors for as-deposited and annealed AlO <sub>x</sub> film in different PDA conditions.	71
Figure 4.3	Study of relation between S <sub>eff</sub> and τ <sub>bulk</sub> for different values of τ <sub>eff</sub> extracted using eq. (2.29).	73
Figure 4.4	(a) The τ <sub>eff</sub> measured and (b) corresponding calculated value of S <sub>eff</sub> on as-deposited AlO <sub>x</sub> film and after annealing in different PDA conditions.	74
Figure 4.5	Minimum value of S <sub>eff</sub> at Δn of 4×10 <sup>14</sup> cm <sup>-3</sup> for as-deposited AlO <sub>x</sub> film and after PDA of AlO <sub>x</sub> film in different conditions.	76
Figure 4.6	Cross-sectional TEM image of (a) as-deposited AlO <sub>x</sub> film deposited on c-Si and (b) AlO <sub>x</sub> film annealed in N <sub>2</sub> + O <sub>2</sub> gas at 520 °C for 20 min.	77
Figure 4.7	Atomic concentration of Al 2p, O 1s and Si 2p elemental depth-profiles of AlO <sub>x</sub> film deposited on c-Si for annealing in N <sub>2</sub> + O <sub>2</sub> ambient at 520 °C for 20 min.	78

Figure 5.1	(a) Tetrahedral ( <i>T</i> ) structure of Al <sup>3+</sup> coordinated with four O <sup>2-</sup> ions and (b) octahedral ( <i>O</i> ) structure of Al <sup>3+</sup> coordinated with six O <sup>2-</sup> ions.	81
Figure 5.2	(a,b,c) Cross-sectional TEM image of AlO <sub>x</sub> films with different scanning spots and (d,e,f) corresponding EELS spectrum. (a,d) as-deposited film, (b,e) film annealed in N <sub>2</sub> + O <sub>2</sub> ambient and (c,f) in FGA ambient at 520 °C.	85
Figure 5.3	The <i>T/O</i> peak intensity ratios at different sampling points in the AlO <sub>x</sub> and IL regions of the as-deposited film, and in IL region of the annealed AlO <sub>x</sub> film.	86
Figure 5.4	Depth-profile for Al 2p, O 1s and Si 2p elements in (a) as-deposited AlO <sub>x</sub> film and after annealing in (b) N <sub>2</sub> + O <sub>2</sub> and (c) FGA ambient at 520 °C for 20 min.	87
Figure 5.5	The Si 2p XPS spectra fitted for different intermediate oxidation states in the IL region of AlO <sub>x</sub> /c-Si for as-deposited and annealed AlO <sub>x</sub> film. The spectra is shown for only at one depth level (46_Dependent Level) for clarity.	89
Figure 5.6	The Si 2p <sub>3/2</sub> peak position of Si <sup>0</sup> (bulk) for core level Si 2p at different #_Depth Level for as-deposited AlO <sub>x</sub> film and after annealing in N <sub>2</sub> + O <sub>2</sub> and FGA ambients at 520 °C.	90
Figure 5.7	Different intermediate oxidation states in-terms of shift in binding energy (eV) with respect to Si 2p <sub>3/2</sub> peak at #_Depth Level in IL of (a) as-deposited AlO <sub>x</sub> film and AlO <sub>x</sub> film (b) annealed in N <sub>2</sub> + O <sub>2</sub> ambient and (c) FGA ambient at 520 °C.	92
Figure 5.8	The presence (%) and distribution of (a) Al-O rich aluminosilicate (ARA) and (b) Si-O rich aluminosilicate (SRA) sub-oxide states in different samples at #_Depth Level in the IL region.	93
Figure 5.9	Absorbance spectra for as-deposited and annealed AlO <sub>x</sub> film in N <sub>2</sub> + O <sub>2</sub> and FGA ambient at 520 °C, using FTIR measurement. “Stret.” stands for stretching mode.	94
Figure 5.10	The E <sub>BG</sub> measured using low-loss EELS spectra at the AlO <sub>x</sub> layer (a,b,c) and IL region (d,e,f) for: (a,d) as-deposited film, (b,e) film annealed in N <sub>2</sub> + O <sub>2</sub> and (c,f) FGA ambient at 520 °C.	97
Figure 5.11	Tauc plot of the absorbance spectra measured using UV-Vis-NIR	99

	spectroscope for (a) as-deposited $\text{AlO}_x$ film and (b) film annealed in $\text{N}_2 + \text{O}_2$ and (c) FGA ambient at 520 °C.	
Figure 6.1	(a) Film thickness for as-deposited and annealed films, (b) deposition rate assessed from $T_{\text{ox}}$ and deposition time (b) RI of film for as-deposited and annealed films in $\text{N}_2 + \text{O}_2$ ambient at 520 °C. The film deposited at different PD conditions.	104
Figure 6.2	(a,b) The C-V and (c,d) G-V characteristics of MOS capacitor with film deposited at different PD between 0.13-1.3 $\text{W.cm}^{-2}$ . Film are annealed in $\text{N}_2 + \text{O}_2$ ambient at 520 °C for 20 min.	105
Figure 6.3	Extracted values of (a) Negative $Q_f$ and (b) $D_{it}$ for $\text{AlO}_x$ deposited at different PD conditions. The film was annealed in $\text{N}_2 + \text{O}_2$ ambient at 520 °C for 20 min.	106
Figure 6.4	(a) Measured $\tau_{\text{eff}}$ and (b) corresponding $S_{\text{eff}}$ on as-deposited and annealed films deposited at $\text{PD} = 0.13 \text{ W.cm}^{-2}$ and $1.3 \text{ W.cm}^{-2}$ .	108
Figure 6.5	Cross-sectional TEM image of as-deposited $\text{AlO}_x$ film deposited at low PD of $0.13 \text{ W.cm}^{-2}$ .	109
Figure 6.6	Atomic concentration of Al 2p, O 1s and Si 2p elemental depth-profiles for (a) as-deposited and (b) annealed $\text{AlO}_x$ films deposited at low PD of $0.13 \text{ W.cm}^{-2}$ and (c) as-deposited and (d) annealed $\text{AlO}_x$ films deposited at high PD of $1.3 \text{ W.cm}^{-2}$ .	110
Figure 6.7	(a) Thickness and (b) RI measured by SE for film deposited with different PD conditions and substrate temperature of room temperature (RT), 100 °C, 200 °C and 320 °C. Open symbol: as-deposited film and close symbol: annealed film.	111
Figure 6.8	Extracted values of negative $Q_f$ (a,c) and $D_{it}$ (b,d) from C-V and G-V MOS characteristics plot for $\text{AlO}_x$ film deposited at different substrate temperature. Films deposited at $\text{PD} = 1.3 \text{ W.cm}^{-2}$ and annealed in $\text{N}_2 + \text{O}_2$ ambient at 520 °C for 20 min.	112
Figure 6.9	(a) Thickness and (b) RI values measured by using SE for different process gases used during film deposition.	114
Figure 6.10	Extracted values of (a) Negative $Q_f$ and (b) $D_{it}$ from C-V and G-V MOS characteristics plot for $\text{AlO}_x$ films deposited using different	115

	process gas viz.: Ar & O <sub>2</sub> and O <sub>2</sub> only and keeping process pressure = 3.5 mTorr.	
Figure 7.1	Sample preparation for $\tau_{\text{eff}}$ measurement of (a) single layer AlO <sub>x</sub> film and (b) stack structure of AlO <sub>x</sub> /SiN <sub>x</sub> :H layer for thermal stability study.	120
Figure 7.2	Thermal stability of AlO <sub>x</sub> film subjected to high temperature exposure in RTA in N <sub>2</sub> . The films were subjected to various PDA conditions. The S <sub>eff</sub> was measured at $\Delta n = 10^{15} \text{ cm}^{-3}$ .	122
Figure 7.3	(a) The C-V and (b) G-V characteristics plot for AlO <sub>x</sub> film (close symbol) and AlO <sub>x</sub> /SiN <sub>x</sub> :H stack structure (open symbol). Black color: as-deposited AlO <sub>x</sub> film and blue color: annealed AlO <sub>x</sub> film.	125
Figure 7.4	Extracted values of (a) negative Q <sub>f</sub> and (b) D <sub>it</sub> from C-V and G-V characteristics, respectively, for single layer AlO <sub>x</sub> film (black color) and AlO <sub>x</sub> /SiN <sub>x</sub> :H stack structure (blue color). The results are shown for as-deposited and annealed AlO <sub>x</sub> film.	126
Figure 7.5	(a) Measured $\tau_{\text{eff}}$ and (b) corresponding S <sub>eff</sub> value on p-type c-Si (FZ) wafer for single layer annealed AlO <sub>x</sub> film (close symbols) and stack structure AlO <sub>x</sub> /SiN <sub>x</sub> :H (open symbols) with the AlO <sub>x</sub> film annealed before SiN <sub>x</sub> :H deposition.	128
Figure 7.6	Thermal stability for single layer AlO <sub>x</sub> film (close symbol) and AlO <sub>x</sub> /SiN <sub>x</sub> :H stack structure (open symbol) at different firing temperatures in RTA process. The AlO <sub>x</sub> film was annealed in N <sub>2</sub> + O <sub>2</sub> ambient at 520 °C for 20 min for both the cases.	129
Figure 8.1	Typical p-type c-Si PERC solar cell with rear-surface passivated using AlO <sub>x</sub> film.	132
Figure 8.2	Process flow proposed for fabrication of PERC structure p-type c-Si solar cell using AlO <sub>x</sub> film as rear-surface passivation layer.	133

## List of Tables

Table 1.1 Best conversion efficiency reported for different PV technologies solar cells on laboratory scale.	3
Table 1.2 The p-n junction c-Si solar cell parameters input to PC1D simulator to study the impact of surface recombination velocity of the front and rear surface on solar cell $\eta$ .	11
Table 3.1 The extracted values of EOT, $\epsilon_{r-AlO_x}$ , $V_{FB}$ and $Q_f$ from high frequency C-V measurement for $AlO_x$ film deposited at different PD.	63
Table 3.2 Comparison of the $E_{BD}$ for $AlO_x$ film deposited using different methods from the published report.	65
Table 4.1 The value of $S_{eff}$ for $AlO_x$ film annealed in $N_2 + O_2$ ambient at 520 °C, with $\tau_{bulk}$ measured in IM solution and estimated using upper limit value by generalized parameterization at $\Delta n = 4 \times 10^{14} \text{ cm}^{-3}$ .	75
Table 5.1 The relative contribution of intermediate oxidation states for different samples.	93
Table 5.2 The peak position and respective chemical bonds associated with it, for as-deposited and annealed $AlO_x$ film in $N_2 + O_2$ and FGA ambient at 520 °C.	95
Table 5.3 Values of $AlO_x$ film $E_{BG}$ , measured using low-loss EELS spectra and UV-Vis-NIR spectroscope for as-deposited and annealed films in $N_2 + O_2$ and FGA ambient at 520 °C.	100

## List of Symbols

<b>Symbol</b>	<b>Description</b>	<b>Unit</b>
$\alpha$	Absorption coefficient	$\text{cm}^{-1}$
$\alpha_c$	Critical angle	degree
$\Delta\sigma$	Excess photoconductance	S
$\Delta n$	Excess minority carrier density	$\text{cm}^{-3}$
$\Delta n_s$	Excess electron concentration at the semiconductor surface	$\text{cm}^{-3}$
$\Delta V_{FB}$	Difference in flat-band voltage	V
$\Delta V_{MG}$	Difference in mid-gap voltage	V
$\epsilon$	Permittivity of the material	$\text{F. cm}^{-1}$
$\epsilon_r$	Relative permittivity of dielectric material	
$\epsilon_0$	Permittivity of free space, $8.854 \times 10^{-14}$	$\text{F. cm}^{-1}$
$\epsilon_{ox}$	Dielectric constant of the oxide film	
$\epsilon_{r-AlOx}$	Dielectric constant of aluminum oxide	
$\epsilon_{r-SiO2}$	Dielectric constant of silicon dioxide	
$\epsilon_s$	Relative permittivity of silicon	
$\eta$	Efficiency	%
$\lambda$	Wavelength	m
$\mu_n$	Electron mobility	$\text{cm}^2.(\text{V.s})^{-1}$
$\mu_p$	Hole mobility	$\text{cm}^2.(\text{V.s})^{-1}$
$\nu$	Frequency of vibration	Hz
$\sigma_n$	Electron capture cross-section area	$\text{cm}^2$
$\sigma_p$	Hole capture cross-section area	$\text{cm}^2$
$\tau$	Minority carrier life-time	s
$\tau_{Auger}$	Life-time due to Auger recombination	s
$\tau_{bulk}$	Life-time due to bulk recombination	s
$\tau_{eff}$	Effective minority carrier life-time	s
$\tau_n$	Electron life-time in p-type	s
$\tau_p$	Hole life-time in n-type	s
$\tau_{ON}$	Reactive sputter time	s
$\tau_{OFF}$	Pulse-reverse time to neutralize the target surface charges	s

$\tau_{BtB}$	Life-time due to band-to-band recombination	s
$\tau_s$	Life-time due to surface recombination	s
$\tau_{SRH}$	Life-time due to Shockley-Read-Hall recombination	s
$\phi_B$	Bulk potential	eV
$\phi_M$	Metal work-function	eV
$\phi_{MS}$	Work function difference between the metal gate and semiconductor	eV
$\phi_S$	Semiconductor work-function	eV
$\phi$	Work function depends on spectrometer and material	eV
$\chi$	Electron affinity for Semiconductor	V
$\omega$	Angular frequency	rad.s <sup>-1</sup>
$a(\lambda)$	Wavelength dependent molar absorption coefficient	L.mol <sup>-1</sup> .cm <sup>-1</sup>
$A$	Absorbance	
$A$	Cross-sectional area of device	cm <sup>2</sup>
$b$	Path length	cm
$B$	Band-to-band recombination coefficient	cm <sup>3</sup> .s <sup>-1</sup>
$c$	Concentration of chemical bonds	mol.L <sup>-1</sup>
$C_{acc}$	Accumulation capacitance	F. cm <sup>-2</sup>
$C_{MG}$	Capacitance at mid-gap voltage	F.cm <sup>-2</sup>
$C_{FB}$	Flat band capacitance	F.cm <sup>-2</sup>
$C_p$	Auger recombination coefficient for holes	cm <sup>6</sup> .s <sup>-1</sup>
$C_{min}$	Minimum value of capacitance	F.cm <sup>-2</sup>
$C_{max}$	Capacitance at voltage corresponding to $G_{max}$	F.cm <sup>-2</sup>
$C_{S,min}^{HF}$	Minimum value of semiconductor capacitance	F.cm <sup>-2</sup>
$C_{S,FB}$	Semiconductor flat band capacitance	F.cm <sup>-2</sup>
$C_{S,MG}$	Semiconductor capacitance at mid-gap voltage	F.cm <sup>-2</sup>
$D_{it}$	Energy density of interface state	cm <sup>-2</sup> .eV <sup>-1</sup>
$D_n$	Diffusion coefficient for electrons	cm <sup>2</sup> .s <sup>-1</sup>
$D_p$	Diffusion coefficient for holes	cm <sup>2</sup> .s <sup>-1</sup>
$E$	Photon energy	eV
$E_{BD}$	Effective breakdown field	V.cm <sup>-1</sup>
$E_{BG}$	Band-gap energy	eV

$E_C$	Conduction band energy	eV
$E_f$	Fermi level energy	eV
$E_v$	Valance band energy	eV
$E_T$	Trap-energy level	eV
$f$	Frequency	Hz
$G$	Generation rate	$\text{cm}^{-3}.\text{s}^{-1}$
$G_{\max}$	Peak conductance	$\text{S.cm}^{-2}$
$h$	Planck's constant, $6.62 \times 10^{-34}$	J.s
$I_0$	Reverse saturation current	A
$I_L$	Light-generated current	A
$I_m$	Current at maximum power point	A
$I_{\text{total}}$	Total diode current	A
$I_{sc}$	Short-circuit current	A
$I$	Intensity of light	$\text{W.m}^{-2}$
$I_0$	Intensity of light from the reference sample	$\text{W.m}^{-2}$
$J$	Current density	$\text{A.cm}^{-2}$
$J_0$	Reverse saturation current density	$\text{A.cm}^{-2}$
$J_{0b}$	Base saturation current density	$\text{A.cm}^{-2}$
$J_{0e}$	Emitter saturation current density	$\text{A.cm}^{-2}$
$J_G$	Gate leakage current density	$\text{A.cm}^{-2}$
$k$	Boltzmann constant, $1.38 \times 10^{-23}$	$\text{J.K}^{-1}$
$L_{\text{bulk}}$	Bulk diffusion length	cm
$L_D$	Debye length	cm
$L_{\text{eff}}$	Effective diffusion length	cm
$L_n$	Diffusion length of electrons	cm
$L_p$	Diffusion length of holes	cm
$n$	Ideality factor	
$n^+$	Highly doped phosphorous concentration	$\text{cm}^{-3}$
$n_0$	Electron density at thermal equilibrium	$\text{cm}^{-3}$
$N_A$	Acceptor impurity concentration	$\text{cm}^{-3}$
$N_C$	Effective density of states for electrons in conduction band	$\text{cm}^{-3}$
$N_D$	Donor impurity concentration	$\text{cm}^{-3}$

$n_i$	Intrinsic concentration	$\text{cm}^{-3}$
$N_{it}$	Interface state density	$\text{cm}^{-2}$
$n_s$	Electron densities at the surface	$\text{cm}^{-3}$
$N_V$	Effective density of states for holes in valance band	$\text{cm}^{-2}$
$p^+$	Highly doped boron concentration	$\text{cm}^{-3}$
$p_0$	Hole density at thermal equilibrium	$\text{cm}^{-3}$
$P_{in}$	Input to p-n junction solar cell	W
$p_s$	Hole densities at the surface	$\text{cm}^{-3}$
$q$	Charge on electron, $1.6 \times 10^{-19}$	C
$Q_f$	Fixed oxide charges	$\text{cm}^{-2}$
$R_{Auger}$	Auger recombination rate	$\text{cm}^{-3}.\text{s}^{-1}$
$r_e$	Classical electron radius, $2.81 \times 10^{-18}$	M
$R_{BtB}$	Band-to-band recombination rate	$\text{cm}^{-3}.\text{s}^{-1}$
$R_s$	Shockley-Read-Hall recombination rate at surface	$\text{cm}^{-2}.\text{s}^{-1}$
$S_{eff}$	Effective surface recombination velocity	$\text{cm}.\text{s}^{-1}$
$S_{eff,maz}$	Maximum value of effective surface recombination velocity	$\text{cm}.\text{s}^{-1}$
$S_{front}$	Surface recombination velocity at front surface of p-n junction	$\text{cm}.\text{s}^{-1}$
$S_r$	Surface recombination velocity	$\text{cm}.\text{s}^{-1}$
$S_{rear}$	Surface recombination velocity at rear surface of p-n junction	$\text{cm}.\text{s}^{-1}$
T	Absolute temperature	K
$T_{ox}$	Film thickness	nm
$v_{th}$	Thermal velocity of electrons	$\text{cm}.\text{s}^{-1}$
V	Applied voltage	V
$V_{BD}$	Breakdown voltage	V
$V_{FB}$	Flat-band voltage	V
$V_G$	Gate Voltage	V
$V_m$	Voltage at maximum power point	V
$V_{MG}$	Mid-gap voltage	V
$V_{MG,ideal}$	Ideal value of mid-gap voltage	V
$V_p$	Pulsed voltage	V

$V_{oc}$	Open-circuit voltage	V
W	Wafer thickness	cm
$W_{dep}$	Depletion width	cm
$X_{d,max}$	Maximum depletion length	cm
$X_{MG}$	Depletion width at mid-gap	cm

## List of Acronyms

<b>Acronym</b>	<b>Description</b>
AC	Alternate current
AFM	Atomic force microscope
ALD	Atomic layer deposition
ARA	Aluminum-oxygen rich aluminosilicate
ARC	Anti-reflection coating
As-dep	As-deposited
b-Si	Black silicon
BE	Binding energy
BSF	Back surface field
c-Si	Crystalline silicon
CPV	Concentrating photovoltaic
C-V	Capacitance versus voltage
CVD	Chemical vapor deposition
CZ	Czochralski
DC	Direct current
DI	De-ionized
DSC	Dye-sensitized solar cells
ECR	Electron cyclotron resonance
EELS	Electron energy loss spectroscopy
ELNES	Energy loss near edge spectra
EOT	Equivalent oxide thickness
FF	Fill factor
FGA	Forming gas ambient
FWHM	Full width at half maximum
FTIR	Fourier transform infra-red spectroscope
FZ	Float zone
G-L	Gaussian-Lorentzian
G-V	Conductance versus voltage
HF	Hydrofluoric

ICP-CVD	Inductive coupled plasma chemical vapour deposition
IL	Interfacial layer
IM	Iodine-Methanol
IPD	Inter-poly dielectrics
IR	Infra-red
I-V	Current versus voltage
J-V	Current density versus voltage
KE	Kinetic energy
LFC	Local-fired contact
LPCVD	Low pressure chemical vapour deposition
Multi-Si	Multicrystalline silicon
Mono-Si	Monocrystalline silicon
MPP	Maximum power point
MOS	Metal oxide semiconductor
MOCVD	Metal-organic chemical vapor deposition
<i>O</i>	Octahedral coordination
PA-ALD	Plasma-assisted atomic layer deposition
PC1D	One-dimensional numerical semiconductor simulation tool for personal computer
PD	Power density
PDA	Post-deposition annealing
PECVD	Plasma enhanced chemical vapour deposition
PERC	Passivated emitter and rear cell
PERL	Passivated emitter with rear locally diffused
PMA	Post-metallization annealing
PSG	Phosphor silicate glass
PV	Photovoltaic
PVD	Physical vapor deposition
pulsed-DC	Pulsed-direct current power supply
QSSPC	Quasi-steady-state photoconductance
RCA	Radio Corporation of America
RF	Radio frequency power supply

RI	Refractive index
RMS	Root mean square
RT	Room temperature
RTA	Rapid thermal annealing
RTP	Rapid thermal processing
RS	Reactive sputter
SCS	Semiconductor characterization system
SE	Spectroscopic ellipsometer
SPV	Solar photovoltaic
SRA	Silicon-oxygen rich aluminosilicate
SRH	Shockley-Read-Hall theory
<i>T</i>	Tetrahedral coordination
TEM	Transmission electron microscope
TMA	Tri-methylaluminum
UV	Ultra-violet
UV-Vis-NIR	Ultra violet-visible-near infrared spectroscope
VLSI	Very large scale integration
XRR	X-ray reflectometer
XPS	X-ray photoelectron spectroscope

# **Chapter 1. Introduction**

Advancements in renewable energy technologies for the electricity generation have led to less dependency on fossil fuels like petrol and coal. Fossil fuels could extinguish with time, whereas the renewable source of energy like wind, solar and hydro are abundantly available on earth. In particular the solar photovoltaic (SPV) technology has become a fast-growing field today among the renewable energy technologies with an impressive research and development in this field and cost reductions. The SPV technologies were easily scalable and have applications in small-scale to large-scale electricity generation. The basic energy conversion device in SPV is known as “solar cell,” which uses photons from the sunlight as the input source to generate charge carriers, followed by transportation of these charge carriers into external circuit. More efficient solar cell means more electricity generated per unit area of the conversion device. However this should be available at a reasonable cost for affordable electricity. This particular area of manufacturing high efficient solar cells brings in many challenges in the field of research and development.

The solar cells can be classified into different categories, based on their manufacturing technology. Figure 1.1 shows different solar cell technologies with the market share percentage contributed by these technologies namely: thin-films, crystalline silicon (c-Si) and other compound semiconductor technologies [1,2]. Organic PV technologies are negligible fraction of manufacturing today. Table 1.1 lists the best conversion efficiency ( $\eta$ ) for these technologies on the laboratory scale [3].

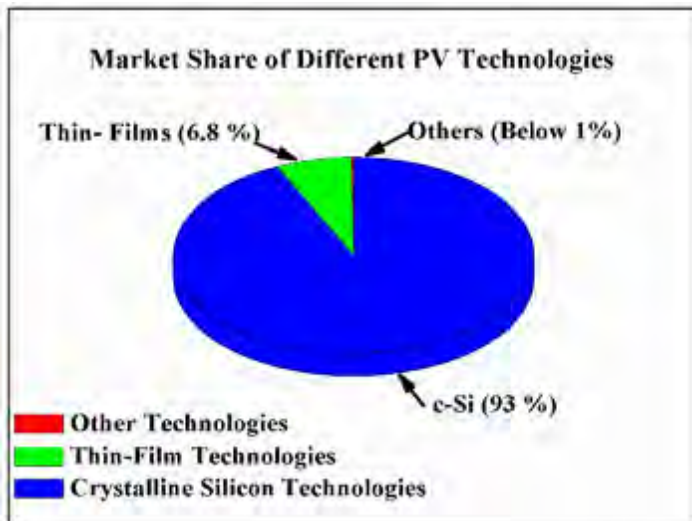


Figure 1.1 Market shares of different photovoltaic technologies [1,2].

The solar cell technologies can be classified into wafer based and thin-film technologies. The thin-film solar cells can be further classified into organic and inorganic type solar cells. The organic solar cells are made by using polymers or organic molecules, for electricity generation, and are also classified under the “emerging technology”. These are relatively low-cost technologies due to simple fabrication process steps and are lighter in weight due to the use of flexible substrates like plastic. The dye-sensitized solar cell (DSC) under this technology has shown best cell efficiency,  $\eta$  of  $11.9 \pm 0.4\%$ , whereas organic solar cells has shown  $\eta$  of  $11.2 \pm 0.3\%$  [2]. With this technology, the stability and proper encapsulation are the major concerns [4].

On the other hand thin-film (inorganic) and c-Si wafer based solar cell technologies have shown relatively good light conversion efficiency as compared to organic solar cells. For the CdTe and CIGS thin-films solar cells,  $\eta$  of  $21.0 \pm 0.4\%$  and  $\eta$  of  $21.7 \pm 0.4\%$ , respectively have been reported [3]. These types of cells are relatively economical because of less expensive and less amount of materials used for the fabrication. The fabrication of inorganic thin-films cells involves the chemical deposition technique which makes it relatively simple to manufacture. The disadvantage of the above mentioned thin film cells are: the toxicity of Cd and scarcity of Te materials which leads to lack of interest by the manufacturers for CdTe cells. Whereas for CIGS cells, the deposition process becomes more complicated due to difficulty in control over deposition process [5]. Having these issues with the technology, another type of thin-film solar cells have emerged with an advantage of

low-temperature for processing, known as amorphous silicon (a-Si) thin-film cells that has shown  $\eta$  of  $10.2 \pm 0.3\%$  [3,6].

Table 1.1 Best conversion efficiency reported for different PV technologies solar cells on laboratory scale [3].

<b>Technology</b>	<b>Cells</b>	<b>Area</b>	<b>Cell efficiency, <math>\eta</math> (%)</b>
Thin-films	CIGS	$1.044 \text{ cm}^2$ (dp)	$21.7 \pm 0.5$
	CdTe	$1.0623 \text{ cm}^2$ (ap)	$21.0 \pm 0.4$
	a-Si	$1.001 \text{ cm}^2$ (da)	$10.2 \pm 0.3$
Organic cell	Dye-sensitised cell	$1.005 \text{ cm}^2$ (da)	$11.9 \pm 0.4$
	Organic cell	$0.992 \text{ cm}^2$ (da)	$11.2 \pm 0.3$
Crystalline silicon	Multi-Si	$3.923 \text{ cm}^2$ (ap)	$22.3 \pm 0.4$
	Mono-Si (rear junction cells)	$79.0 \text{ cm}^2$ (da)	$26.7 \pm 0.5$

Abbreviations: (ap) - aperture area, (da) - designated illuminated area.

As listed in Table 1.1, the c-Si solar cells have shown highest  $\eta$  of 26.7 % among different technologies. Figure 1.1 shows, this technology also dominates most of the PV market, since it's highly compatible with the existing VLSI silicon technology and manufacturing. The record energy conversion efficiency,  $\eta$  of 26.7 % was reported for laboratory make c-Si solar cell, whereas industrial c-Si solar cells have shown  $\eta$  of 22.5 % [1]. The silicon based concentrating photovoltaic (CPV), which works on the concept of an optical concentrator system, i.e., used to focus the solar radiation into small solar cell, leads to further improvement in  $\eta$  even beyond 25 % [3]. Similarly multi-junction solar cells also give very high efficiency. But due to their high costs for design and manufacturing, they are invariably restricted to niche applications such as in space.

In conventional c-Si solar cell, various factors leads to losses, viz.: reflection from the front surface, coverage area from metal contacts, parasitic resistance and various areas of

recombination for minority charge carriers, needs to be addressed to achieve higher efficiency. In the subsequent section we will discuss and present different ways to reduce the losses due to recombination of charge carriers, hence to improve the efficiency of the c-Si solar cell.

## 1.1 Recombination mechanisms in crystalline silicon

In a semiconductor, as light falls on the Si surface a photon with enough energy will get absorbed and results in an electron to get excited from the valence band and moves to the conduction band after gaining sufficient energy. During this process a ‘hole’ is created in the valence band and thus an electron-hole pair is generated. The process is called “generation” of carriers. The exact opposite process is called “recombination” of carriers. To make high efficiency solar cell, the basic requirements are the generation of large number of free charge carriers and to minimize the recombination of these photon generated free charge carriers.

Three types of recombination mechanisms are dominant in a semiconductor material: (a) band-to-band, (b) Auger and (c) trap-assisted recombination, as shown in Figure 1.2 [7].

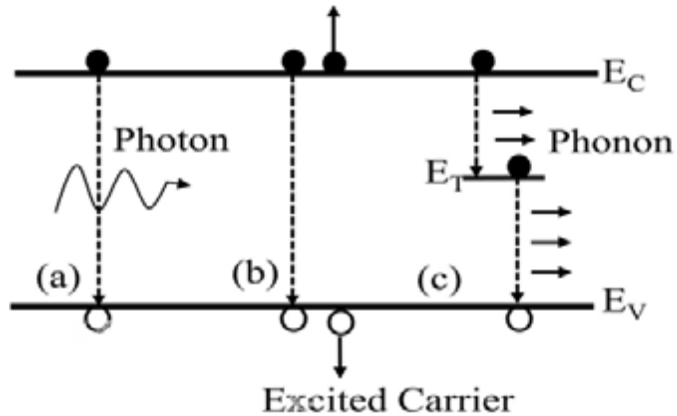


Figure 1.2 Recombination mechanisms in a semiconductor material: (a) band-to-band, (b) Auger and (c) trap-assisted recombination [7].

(a) In band-to-band recombination mechanism, an electron from the conduction band recombines with a hole in the valence band with an emission of a photon. The band-to-band recombination rate ( $R_{BtB}$ ) is expressed by eq. (1.1), considering for p-type semiconductor material,

$$R_{BtB} = B p_0 \Delta n \quad (\text{cm}^{-3} \cdot \text{s}^{-1}) \quad (1.1)$$

where,  $B$  represents the band-to-band recombination coefficient ( $\text{cm}^3.\text{s}^{-1}$ ),  $p_0$  represents the equilibrium charge carrier density ( $\text{cm}^{-3}$ ) and  $\Delta n$  represents the excess minority charge carrier density ( $\text{cm}^{-3}$ ). In direct band-gap materials the conduction band minima and the valance band maxima are directly align, hence during the recombination process an excess energy is released in the form of photon with energy equal to the band-gap energy of the material. Such kind of recombination are mostly dominating in direct band-gap semiconductor materials. Whereas in indirect band-gap material where the conduction band minima and valance band maxima are not align, the recombination process takes place in the form of phonon assisted transition. Where a phonon is lattice vibration and carries low energy and large momentum. In indirect semiconductor like Si, such kind of recombination is negligible, since the transition must be assisted with the phonon and photon.

(b) In Auger recombination, an electron from the conduction band recombines with the hole in the valance band. During this process excess energy is transferred as kinetic energy to another free electron in the conduction band, which makes it move to a higher energy state in the conduction band or similarly a hole makes a movement deeper into the valance band after gaining kinetic energy. For p-type semiconductor, Auger recombination rate ( $R_{\text{Auger}}$ ) may be expressed as eq. (1.2)

$$R_{\text{Auger}} = C_p p_0^2 \Delta n \quad (\text{cm}^3.\text{s}^{-1}) \quad (1.2)$$

where,  $C_p$  represents the Auger recombination coefficient for holes ( $\text{cm}^6.\text{s}^{-1}$ ). This type of recombination mechanism dominates mostly for the materials with higher doping concentration.

(c) In trap-assisted recombination, a free electron from the conduction band is captured in a defect level in the energy band-gap known as trap-energy ( $E_T$ ) level. This trap would then captures a hole leading to recombination. During this process the excess energy is dissipated as phonon. This recombination mechanism is described by the Shockley-Read-Hall (SRH) theory. Hence it is also known as SRH recombination [7]. The SRH recombination rate can be expressed as a function of trap densities (interface defect densities in case of recombination at the interface between materials), capture cross-section area for hole,  $\sigma_p$  and electrons,  $\sigma_n$  ( $\text{cm}^2$ ) and charge carrier density in the silicon bulk or at the surface.

The defects in the silicon bulk may be created during material processing. For example with the Czochralski (CZ) crystal growth technique, the Si wafers have more defect

density as compared to float zone (FZ) technique [8,9]. On the other hand, the surface of Si wafer is more prone to defects due to abrupt discontinuity of a crystal lattice structure, which gives rise to unsaturated bond known as dangling bond. These are actually the recombination centres at the surface which can be reduced by using different passivation technique that will be discussed later in this chapter. The SRH recombination rate ( $R_s$ ) at the surface is given by eq. (1.3).

$$R_s = \frac{s_n s_p (p_s n_s - n_i^2)}{s_n (n_s + n_{1s}) + s_p (p_s + p_{1s})} \quad (\text{cm}^{-2} \cdot \text{s}^{-1}) \quad (1.3)$$

where  $s_n$  and  $s_p$  are defined as  $s_n = \sigma_{ns} v_{th} N_{it}$  ;  $s_p = \sigma_{ps} v_{th} N_{it}$  , here  $v_{th}$  represents thermal velocity of electrons ( $\text{cm.s}^{-1}$ ),  $\sigma_n$  and  $\sigma_p$  represent capture cross-section area of electron and hole ( $\text{cm}^2$ ), respectively, here subscript ‘s’ refers to the surface quantities,  $N_{it}$  is interface state density ( $\text{cm}^{-2}$ ),  $n_s$  &  $p_s$  are electron and hole carrier densities at the surface,  $n_1$ &  $p_1$  are the statistical factors, given as follows

$$n_1 \equiv N_C \exp\left(\frac{E_T - E_C}{kT}\right); p_1 \equiv N_V \exp\left(\frac{E_C - E - E_T}{kT}\right) \quad (\text{cm}^{-3}) \quad (1.4)$$

where,  $N_C$  and  $N_V$  are effective density of states for electrons in the conduction band and holes in valence band ( $\text{cm}^{-3}$ ), respectively.  $E_C$  represents the conduction band energy (eV) and  $E_T$  represents trap-energy level (eV),  $k$  represents the Boltzmann constant which is  $1.38 \times 10^{-23} \text{ J.K}^{-1}$  and  $T$  represents absolute temperature (K).

The surface recombination velocity,  $S_r$  ( $\text{cm.s}^{-1}$ ) which is a measure of how fast the light-generated or excess charge carriers recombine at the surface of the semiconductor, is given by eq. (1.5)

$$S_r = \frac{R_s}{\Delta n_s} \quad (\text{cm.s}^{-1}) \quad (1.5)$$

where  $R_s$  represents surface SRH recombination rate ( $\text{cm}^{-2} \cdot \text{s}^{-1}$ ),  $\Delta n_s$  represents excess electron concentration ( $\text{cm}^{-3}$ ) at the semiconductor surface. From eq. (1.3) and (1.5), it is deduced that  $S_r$  can be reduced with reduction in number of  $N_{it}$  and/or by reduction in either type of charge carriers at the surface. The value of  $S_r$  can be calculated from the minority charge carrier life-time,  $\tau$  (s) as well, i.e., the average time a charge carrier spends in an excited state before recombining.

In the semiconductor the effective minority charge carrier life-time,  $\tau_{eff}$  (s), comprises the effects of all the recombination including bulk as well as surface, which is given by eq. (1.6),

$$\frac{1}{\tau_{eff}} = \left( \frac{1}{\tau_{SRH}} + \frac{1}{\tau_{Auger}} + \frac{1}{\tau_{BtB}} \right) + \frac{1}{\tau_s} \quad (s^{-1}) \quad (1.6)$$

where,  $\tau_{Auger}$  is due to Auger recombination based on impurities and defects in the material, such kind of recombination is most dominating in heavily doped materials. The  $\tau_{BtB}$  appears due to band-to-band recombination. While  $\tau_{SRH}$  appears due to SRH recombination that depends on the defects at various levels in the semiconductor material. The minority carrier life-time in bulk of semiconductor,  $\tau_{bulk}$  (s) includes the effect of all the three above mentioned recombination mechanisms. The minority carrier life-time due to recombination of charge carriers at the surface is given as  $\tau_s$  (s). In case of symmetrical structure where both the front and rear surfaces of semiconductor are passivated symmetrically, the effective surface recombination velocity ( $S_{eff}$ ) is defined using eq. (1.7) and (1.8),

$$\frac{1}{\tau_{eff}} = \frac{1}{\tau_{bulk}} + \frac{2S_{eff}}{W} \quad (s^{-1}) \quad (1.7)$$

$$S_{eff} = \frac{W}{2} \left( \frac{1}{\tau_{eff}} - \frac{1}{\tau_{bulk}} \right) \quad (cm.s^{-1}) \quad (1.8)$$

where, W represents the wafer thickness in cm. From the quasi-steady-state photo-conductance (QSSPC) technique, one can obtain the value of  $\tau_{eff}$  on the passivated semiconductor surface [10]. The value of  $\tau_{bulk}$  (s) can be measured using QSSPC technique with the application of a chemical passivation on semiconductor surface [11]. The above equation is valid for the properly passivated samples with low value of  $S_{eff}$ . Whereas for poorly passivated sample with  $S_{eff} \rightarrow \infty$ , surface recombination is limited by the diffusion of charge carriers, and the relationship is given by eq. (1.9) and (1.10) [12].

$$\frac{1}{\tau_{eff}} = \frac{1}{\tau_{bulk}} + \left( \frac{W}{2S_{eff}} + \frac{1}{D_n} \left( \frac{W}{\pi} \right)^2 \right)^{-1} \quad (s^{-1}) \quad (1.9)$$

$$S_{eff} = \frac{\pi^2 D_n W (\tau_{bulk} - \tau_{eff})}{2\pi^2 D_n \tau_{bulk} \tau_{eff} - 2W^2 (\tau_{bulk} - \tau_{eff})} \quad (cm.s^{-1}) \quad (1.10)$$

where  $D_n$  represents diffusion coefficient of electrons ( $\text{cm}^2 \cdot \text{s}^{-1}$ ). On the other hand, for asymmetrical structure like p-n junction, where emitter region is relatively doped higher as compared to the base region, the calculation of  $S_{\text{eff}}$  changes again, as defined by eq. (1.11) [13].

$$S_{\text{eff}} = \frac{J_{0e}(N_A + \Delta n)}{qn_i^2} \quad (\text{cm} \cdot \text{s}^{-1}) \quad (1.11)$$

where  $J_{0e}$  represents the emitter saturation current density ( $\text{A} \cdot \text{cm}^{-2}$ ).  $N_A$  represents the acceptor impurity concentration ( $\text{cm}^{-3}$ ) and  $n_i$  represents intrinsic concentration ( $\text{cm}^{-3}$ ) of the semiconductor material,  $q$  represents the electronic charge which is  $1.6 \times 10^{-19} \text{ C}$ . The eq. (1.11) is the simplified equation assuming that the minority carrier life-time in emitter region is much less than life-time in base region and the life-time is independent of  $\Delta n$  [13].

## 1.2 Solar cell performance parameters

The typical structure of p-n junction solar cell and current versus voltage (I-V) characteristics are shown in Figure 1.3 (a) and (b), respectively.

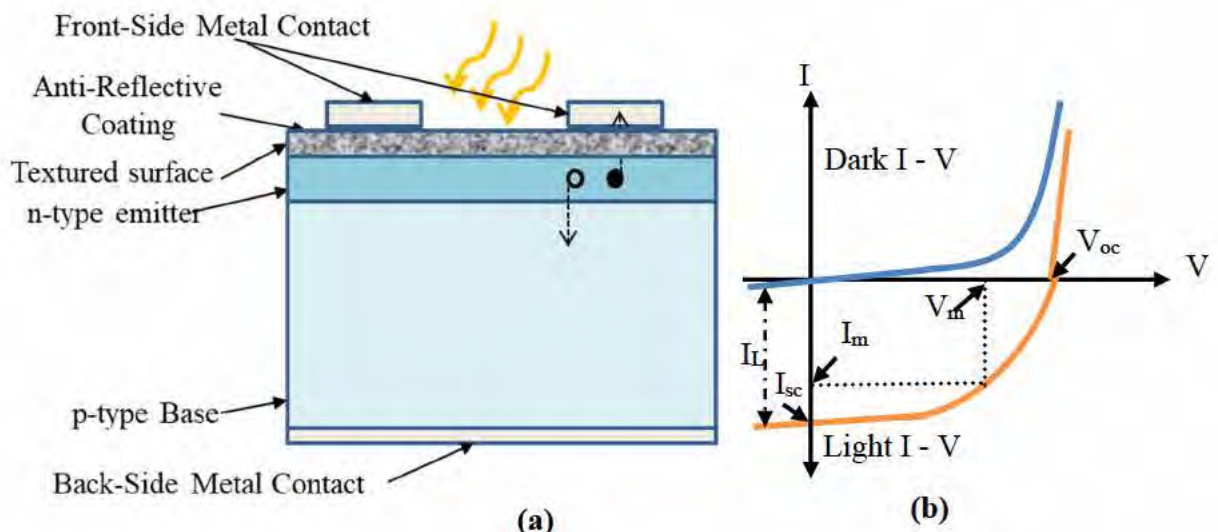


Figure 1.3 (a) Typical p-n junction solar cell structure, (b) I-V characteristics of p-n junction solar cell.

When light incident on the solar cell, the photons get absorbed in the semiconductor and generates free electron-hole pairs. At the p-n junction these carriers get separated and transported through the solar cell towards external load for the electricity generation. The I-V

characteristics of the solar cell generally appears in the IV<sup>th</sup> quadrant in the graph, as shown in Figure 1.3 (b). The total current ( $I_{total}$ ) of the p-n junction diode after illumination is given by eq. (1.12) [14].

$$I_{total} = I_0 \left( e^{qV/nkT} - 1 \right) - I_L \quad (A) \quad (1.12)$$

where V represents applied voltage (V), n represents the ideality factor which is a deviation from the ideal I-V characteristics (n = 1 for low level injection and n = 2 for high level injection).  $I_0$  represents the reverse saturation current (A), which is defined from the basic properties of the semiconductor material and the p-n junction, and is given by eq. (1.13) [14],

$$I_0 = qA \left( \frac{D_n}{L_n} n_{p0} + \frac{D_p}{L_p} p_{n0} \right) \quad (A) \quad (1.13)$$

where A represents the cross-sectional area of device ( $\text{cm}^2$ ),  $D_{(n, p)}$  represents the diffusion coefficients of electrons and holes ( $\text{cm}^2.\text{s}^{-1}$ ),  $L_{(n, p)}$  represents the diffusion lengths of electrons and holes (cm). Here diffusion length is defined as the average length a charge carrier diffuses into semiconductor before it recombines and is given by  $L_n = \sqrt{D_n \tau_n}$  where  $\tau_n$  (s) is the minority carrier life-time of electron and therefore it is related to the  $S_r$ . The terms  $n_{p0}$  represents the minority carrier electrons in the p-side under the equilibrium condition and similarly  $p_{n0}$  represents the minority carrier holes in the n-side under the equilibrium condition. To further simplify the eq. (1.13), the term reverse saturation current density ( $J_0$ ) is defined as  $I_0.A^{-1}$ , as given in eq. (1.14),

$$J_0 = J_{0e} + J_{0b} \quad (\text{A.cm}^{-2}) \quad (1.14)$$

where,  $J_{0e}$  represents emitter saturation current density ( $\text{A.cm}^{-2}$ ), which is measured using QSSPC technique on symmetrical structure [10,13] and is given by eq. (1.15),

$$J_{0e} = \frac{qn_i^2 S_{eff}}{(N_A + \Delta n)} \quad (\text{A.cm}^{-2}) \quad (1.15)$$

Hence, the reverse saturation current density is dependent on the  $S_{eff}$  value as well. In eq. (1.14), the  $J_{0b}$  represents the base saturation current density ( $\text{A.cm}^{-2}$ ), is given by eq. (1.16) [15],

$$J_{0b} = \frac{qn_i^2 D}{L_{eff} N_A} \quad (\text{A.cm}^{-2}) \quad (1.16)$$

where, D represents minority carrier diffusion coefficient ( $\text{cm}^2.\text{s}^{-1}$ ) and  $L_{\text{eff}}$  represents the effective diffusion length (cm), which depends on rear surface recombination velocity  $S_{\text{rear}}$  ( $\text{cm.s}^{-1}$ ), bulk diffusion length  $L_{\text{bulk}}$  (cm) and W (cm), is given by eq. (1.17) [15],

$$L_{\text{eff}} = L_{\text{bulk}} \frac{1 + \frac{S_{\text{rear}} L_{\text{bulk}}}{D} \tanh\left(\frac{W}{L_{\text{bulk}}}\right)}{\frac{S_{\text{rear}}}{D} + \tanh\left(\frac{W}{L_{\text{bulk}}}\right)} \quad (\text{cm}) \quad (1.17)$$

The  $I_L$  term in eq. (1.12) is known as light-generated current (A), which is defined by eq. (1.18) [14],

$$I_L = qAG(L_n + W_{\text{dep}} + L_p) \quad (\text{A}) \quad (1.18)$$

where G represents the generation rate ( $\text{cm}^{-3}.\text{s}^{-1}$ ) and  $W_{\text{dep}}$  represents the depletion width (cm). Hence the  $I_L$  represents the light current due to carriers generated within the ( $L_n + W_{\text{dep}} + L_p$ ) length.

The other important terms obtained from I-V characteristics is the short-circuit current  $I_{\text{sc}}$  (A) and open-circuit voltage  $V_{\text{oc}}$  (V), these terms are used to determine the efficiency,  $\eta$  of the solar cell, which is defined by eq. (1.19) [14],

$$\eta = \frac{I_{\text{sc}} V_{\text{oc}} \text{FF}}{P_{\text{in}}} \quad (\%) \quad (1.19)$$

where  $P_{\text{in}}$  represent the input incident radiation flux ( $\text{W.cm}^{-2}$ ) multiplied with area of incidence ( $\text{cm}^2$ ).  $I_{\text{sc}}$  represents the maximum current when load is shorted,  $I_{\text{sc}} = -I_L$  when  $V = 0$ , in eq. (1.12).  $V_{\text{oc}}$  represents the maximum voltage when load is open, i.e., with  $I = 0$ , is given by eq. (1.20) [14],

$$V_{\text{oc}} = \frac{n k T}{q} \ln \left( \frac{I_L}{I_0} + 1 \right) \quad (\text{V}) \quad (1.20)$$

The value of  $V_{\text{oc}}$  can be affected by both the  $I_L$  and  $I_0$ , where  $I_0$  depends on the properties of material like diffusion coefficient, diffusion length and  $S_{\text{eff}}$  as given in eq. (1.14), (1.15) and (1.16). Hence the value of  $S_{\text{eff}}$  eventually have impact on  $\eta$  of the solar cell, from the value of  $I_0$  in  $V_{\text{oc}}$  as defined in eq. (1.20).

The fill factor (FF) is generally expressed in percentage and is defined as the ratio of maximum power ( $I_m \times V_m$ ) to product of ( $I_{\text{sc}} \times V_{\text{oc}}$ ). Where the  $I_m$  (A) and  $V_m$  (V) from maximum power are the value of current and voltage, respectively when the cell produces

maximum power, at maximum power point (MPP). The position of MPP is normally close to the bend in I-V curve characteristics of the cell. The FF is also a measure of the squareness of the I-V curve of solar cell, which is given by eq. (1.21) [14],

$$FF = \frac{V_m I_m}{V_{oc} I_{sc}} \quad (1.21)$$

As discussed in the previous sections, the surface of the semiconductor has most recombination centres due to abrupt ending of crystal structure and defects, hence the impact of surface recombination velocity of the individual surfaces viz. front ( $S_{front}$ ) [i.e., at emitter] and rear ( $S_{rear}$ ) [i.e., at base] on the overall  $\eta$  of solar cell were simulated using PC1D simulator [16]. The p-type c-Si solar cell with the cell parameters as given in Table 1.2, was simulated using PC1D simulator. The effect of front surface recombination velocity ( $S_{front}$ ) and rear surface recombination velocity ( $S_{rear}$ ) on solar cell efficiency are shown in Figure 1.4 (a) and (b), respectively.

Table 1.2 The p-n junction c-Si solar cell parameters input to PC1D simulator to study the impact of surface recombination velocity at the front and rear surface on solar cell  $\eta$  [16].

<b>Solar cell parameters</b>	<b>Input values</b>
Cell area	1 cm <sup>2</sup>
Wafer thickness	200 $\mu$ m
Wafer resistivity	1 $\Omega$ .cm
Front surface texture	5 $\mu$ m
n <sup>+</sup> emitter doping	$5.5 \times 10^{19}$ cm <sup>-3</sup>
p-type base doping	$1.5 \times 10^{16}$ cm <sup>-3</sup>
Wafer bulk lifetime	5 ms
Anti-reflection coating	Thickness = 75 nm, Refractive index (RI) = 2
Front surface recombination velocity ( $S_{front}$ )	Varied between 1 to $10^6$ cm.s <sup>-1</sup>
Rear surface recombination velocity ( $S_{rear}$ )	Varied between 1 to $10^6$ cm.s <sup>-1</sup>

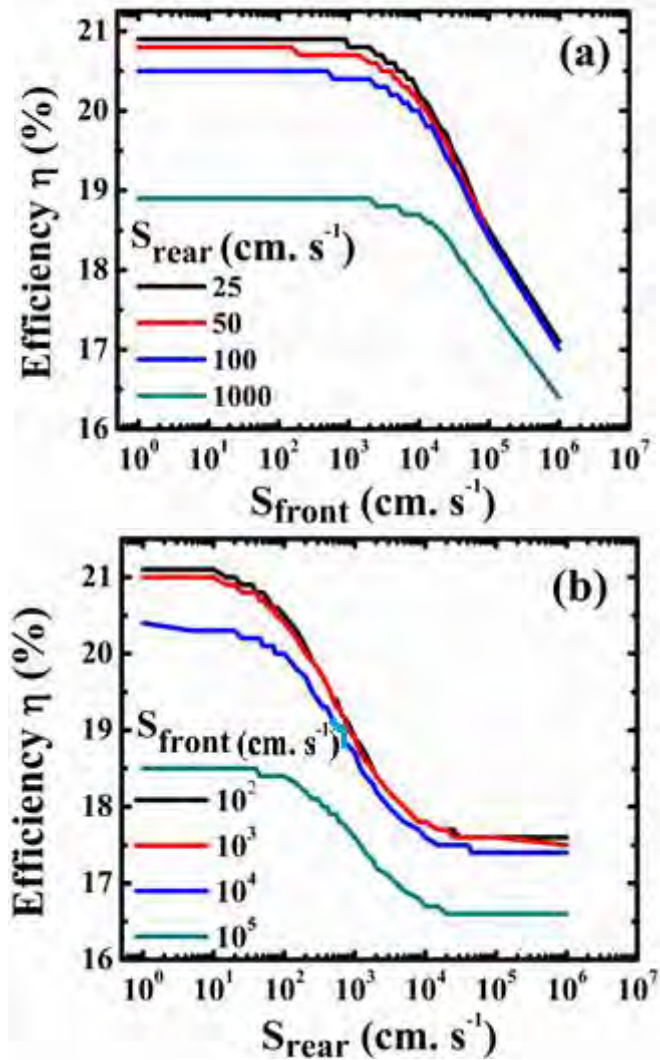


Figure 1.4 Impact of surface recombination on p-n junction solar cell efficiency  $\eta$  simulated using PC1D simulator, by (a) varying the  $S_{\text{front}}$ , while keeping  $S_{\text{rear}}$  constant (b) varying the  $S_{\text{rear}}$ , while keeping  $S_{\text{front}}$  constant.

Figure 1.4 (a) shows the effect of  $S_{\text{front}}$  on solar cell  $\eta$  (%) for different values of  $S_{\text{rear}}$  set as 25, 50, 100 and 1000 cm.s<sup>-1</sup>. The high  $\eta$  of 20.5 % is observed for cells with the values of  $S_{\text{rear}} < 100$  cm.s<sup>-1</sup> and  $S_{\text{front}} < 10^3$  cm.s<sup>-1</sup>. Figure 1.4 (b) shows the effect of  $S_{\text{rear}}$  on solar cell  $\eta$  (%) for different values of  $S_{\text{front}}$  set as  $10^2$ ,  $10^3$ ,  $10^4$  and  $10^5$  cm.s<sup>-1</sup>. An improvement in  $\eta$  from 18.5 % upto 21 % is possible for solar cell with  $S_{\text{front}} < 10^3$  cm.s<sup>-1</sup> and  $S_{\text{rear}} < 100$  cm.s<sup>-1</sup>. Since the emitter region is heavily doped in p-n junction solar cell, which results in the value of  $S_{\text{front}} \sim 10^4$  cm.s<sup>-1</sup>. Hence with the passivated rear surface ( $S_{\text{rear}} < 100$  cm.s<sup>-1</sup>), high efficiency can be achieved for this particular solar cell architecture.

## 1.3 Surface passivation of crystalline silicon

The surface passivation is a process through which the process of recombination of light generated hole-electron pair get reduced via reduction of number of recombination centres at the semiconductor surface and/or by creating electrostatic charge at surface. The two common mechanisms for surface passivation are chemical passivation and field-effect passivation as described below.

### 1.3.1 Chemical passivation

The method by which recombination centres at the surface can be reduced by decreasing the number of dangling bonds is known as chemical passivation. This can be achieved by deposition or growth of an appropriate film on the silicon surface. This will saturate the dangling bonds and hence reduce  $N_{it}$ , as shown in Figure 1.5 (a). For example, thermally grown  $\text{SiO}_2$  and hydrogenated amorphous silicon (a-Si:H) can be used as chemical passivation layers. The O or H atoms from these films make bonds with unsaturated dangling bonds and hence reduces  $N_{it}$ . Another method to improve the surface passivation is by post-deposition annealing (PDA) process in forming gas ambient (FGA). The FGA is a mixture of hydrogen and nitrogen gases, at high temperature in the range of 350-400 °C. The hydrogen from FGA diffuse through the dielectric material to make Si:H bonds at the interface to further improve the passivation quality with reduction in  $N_{it}$  [17]. The  $N_{it}$  is also referred in terms of energy density of interface states,  $D_{it}$  ( $\text{cm}^{-2} \cdot \text{eV}^{-1}$ ), i.e., number of  $N_{it}$  spread between conduction band ( $E_c$ ) and valence band ( $E_v$ ), which is given as eq. (1.22) ,

$$N_{it} = \int_{E_c}^{E_v} D_{it} dE \quad (\text{cm}^{-2}) \quad (1.22)$$

### 1.3.2 Field-effect passivation

As discussed in the previous section, the surface recombination velocity, can be reduced by preventing the minority charge carriers to reach the surface where the density of recombination centres are high. This can be implemented by creating high-low doping profile near the silicon surface, as shown in Figure 1.5 (b). Another method for reduction of surface recombination velocity by maintaining low concentration of one type of charge carrier than the other at the surface. This can be realised through the electric-field potential at the surface using an electrostatic charges like fixed oxide charges,  $Q_f$  ( $\text{cm}^{-2}$ ) of an overlying dielectric

film, as shown in Figure 1.5 (c). The electrostatic charges are usually fixed oxide charges in dielectric film or may be deposited externally through the corona charging method, which results in electrostatic potential barrier at the surface, hence results in reduction of either type of charges at the silicon surface to reduce the surface recombination velocity as explained in section 1.1.

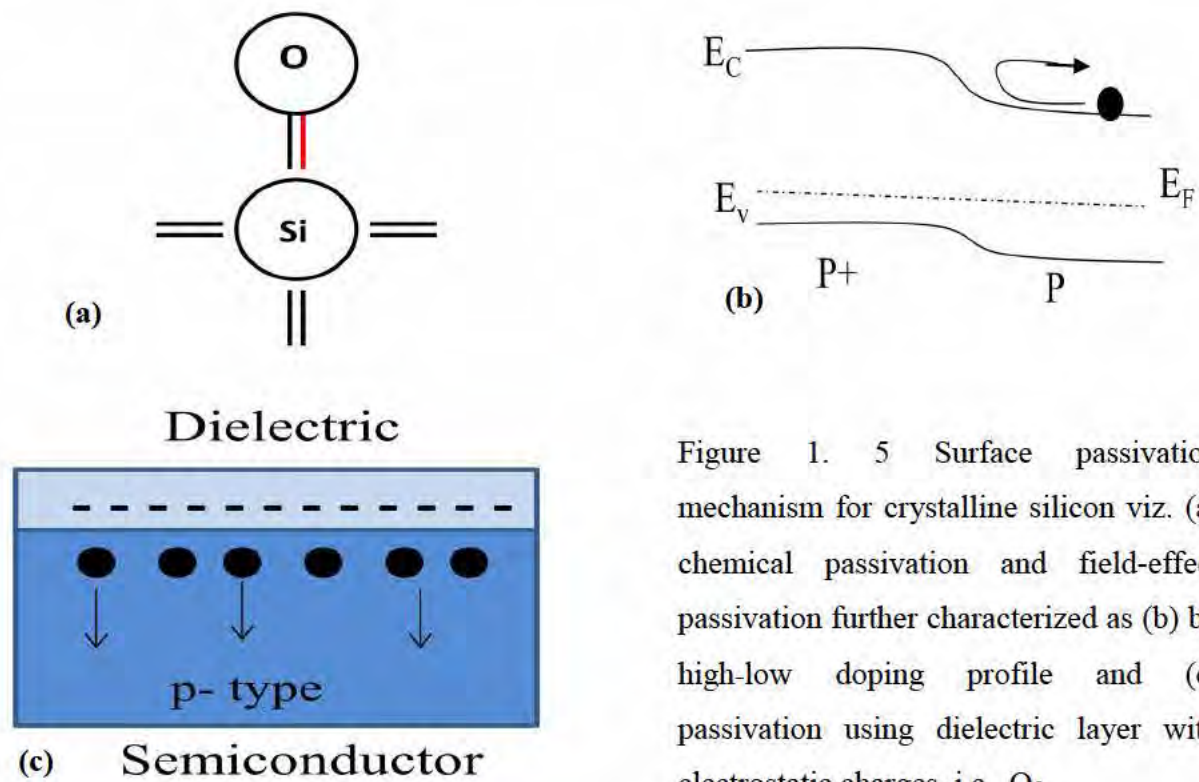


Figure 1.5 Surface passivation mechanism for crystalline silicon viz. (a) chemical passivation and field-effect passivation further characterized as (b) by high-low doping profile and (c) passivation using dielectric layer with electrostatic charges, i.e.,  $Q_f$ .

The simulation study reported by Dingemans et al., shows the impact of individual type of passivation via chemical and field-effect passivation on the value of overall  $S_{eff}$  by using eq. (1.3) and (1.5), for different values of negative  $Q_f$  and  $N_{it}$  [12]. Where the PC1D simulation tool was used to obtain the carrier densities at surface ( $n_s$ ,  $p_s$ ) under illumination, the result from the publication is shown in Figure 1.6 [12].

The simulated result shows that the value of  $S_{eff}$  is relatively high for low value of negative  $Q_f \leq 5 \times 10^{10} \text{ cm}^{-2}$ , at highly doped emitter surface. Whereas the value of  $S_{eff}$  decreases when value of negative  $Q_f$  increases beyond  $5 \times 10^{11} \text{ cm}^{-2}$ , following a  $1/Q_f^2$  relation. This effect of change in surface recombination velocity with change in fixed oxide charge density in the dielectric is known as field-effect passivation. While the result also shows, a linear change in  $S_{eff}$  values with change in number of  $N_{it}$ , the effect is known as

chemical passivation. Hence a high level of surface passivation can be achieved if both chemical as well as field-effect passivation mechanism works together [12].

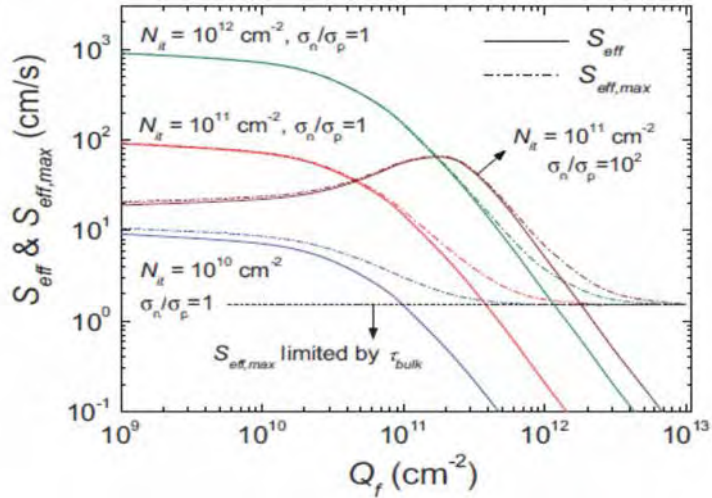


Figure 1.6 The impact of chemical and field-effect passivation on the surface recombination velocity simulated using the equations for  $S_{eff}$  and  $S_{eff,max}$ , as shown in eq. (1.3) and (1.5), for different values of negative  $Q_f$  and  $N_{it}$ . The  $n_s$  and  $p_s$  were obtained using PC1D simulator.

The values used for the defect carriers cross-sections  $\sigma_n = \sigma_p$ :  $10^{-16} \text{ cm}^2$  [12].

## 1.4 Application of different materials as surface passivation layers

### 1.4.1 Silicon dioxide ( $\text{SiO}_2$ )

The thermally grown silicon dioxide ( $\text{SiO}_2$ ), has shown a good quality of chemical passivation property on silicon solar cells due to its excellent interface property with very low  $D_{it}$  of  $10^{10} \text{ cm}^{-2} \cdot \text{eV}^{-1}$  [18,19]. The low value of  $D_{it}$  was achieved, since the film grows on Si substrate with  $\text{O}_2$  gas ambient at high processing temperature ( $900\text{-}1100$  °C) known as dry-oxidation process or in  $\text{H}_2\text{O}$  vapour ambient at relatively low temperature range ( $600\text{-}800$  °C) known as wet-oxidation process. The thermally grown  $\text{SiO}_2$  films have shown an excellent surface passivation with  $S_{eff} < 10 \text{ cm.s}^{-1}$  on both p-type and n-type silicon surfaces after PDA in FGA at  $400$  °C for 30 min [20].

The thermal stability of these  $\text{SiO}_2$  films was tested for different temperature at  $400\text{-}600$  °C (isochronal: by keeping process time constant, i.e., 3 min) and time at 1-6 min (isothermal: by keeping process temperature constant at  $550$  °C) using rapid thermal

annealing (RTA) in dry N<sub>2</sub> ambient and the S<sub>eff</sub> was seen to be degrading with time and temperature which may be due to de-passivation at Si-SiO<sub>2</sub> interface [20,21]. Johnson et al. reported a degradation of S<sub>eff</sub> value by exposure to humidity [22]. Another disadvantage of using thermally grown SiO<sub>2</sub> is the requirement of high temperature and long processing time, which may eventually increase cost of processing. Also high-temperature may degrade the τ<sub>bulk</sub>. Hence a low-temperature plasma enhanced chemical vapour deposition (PECVD) method used for SiO<sub>2</sub> film deposition, was widely investigated for silicon solar cell applications [23,24]. In another report on chemically grown SiO<sub>2</sub> using nitric acid (HNO<sub>3</sub>) was also investigated for surface passivation of solar cells [25].

#### 1.4.2 Amorphous silicon nitride (a-SiN<sub>x</sub>)

The amorphous silicon nitride (a-SiN<sub>x</sub>) film was found to be most attractive passivation layer for n-type surface, as it was already implemented as an anti-reflection coating (ARC) in silicon solar cells. The film RI can be tuned by varying the film compositions and can be easily deposited at low-temperature using PECVD technique. The PECVD deposition techniques results in hydrogenated SiN<sub>x</sub> film. The surface passivation of n-type silicon was mainly because of field-effect passivation mechanism as the film carries large number of positive Q<sub>f</sub> in the range of 10<sup>12</sup> cm<sup>-2</sup> and the hydrogen from film will incorporate the chemically passivation mechanism in the surface. The PECVD SiN<sub>x</sub> have shown good quality of surface passivation on both diffused and non-diffused Si surfaces [26]. An implied V<sub>oc</sub> of 723 mV and S<sub>eff</sub> of 2 cm.s<sup>-1</sup> was reported using as-deposited SiN<sub>x</sub> film with RI of 2.75 on the planner and non-diffused surface, whereas on textured and boron diffused surface an improvement in surface passivation was realized only after PDA at 500 °C in N<sub>2</sub> ambient for 5 min [26]. The SiN<sub>x</sub> film also shows stable surface passivation after exposure to the ultra-violet (UV) radiation [27,28].

On p-type silicon solar cells, this film was applied to passivate n-type highly doped emitter surface. However, when the same was applied on p-type rear surface, the positive charges of SiN<sub>x</sub> film is likely leading to the shunting effect due to formation of an inversion layer at rear surface [29,30]. Hence this film is not a suitable choice for passivation of p-type rear-surface.

### **1.4.3 Hydrogenated amorphous silicon (a-Si:H)**

The hydrogenated amorphous silicon (a-Si:H) can be applied as surface passivation layer by using the hydrogen atoms to saturate the dangling bond on the surface and thus minimizes the surface recombination velocity. The PECVD deposited a-Si:H was demonstrated to passivate both n and p-type silicon surfaces, with good quality of passivation achieved only after the PDA process. The quality of passivation was seen to be independent of film thickness for film thickness greater than 10 nm [31]. The disadvantage of a-Si:H film observed was the parasitic absorption in the UV-range and instability of the film after high temperature processing [32].

### **1.4.4 Aluminum oxide ( $\text{AlO}_x$ )**

As discussed earlier, a  $\text{SiN}_x:\text{H}$  film is a suitable choice for passivation of n-type surface due to positive  $Q_f$  charges, while application on p-type rear surface degrades the cell quality due to parasitic shunting effect. Hence the  $\text{AlO}_x$  film which contains negative  $Q_f$ , may be a suitable choice for passivation of p-type silicon surface, with the field-effect mechanism. The  $\text{AlO}_x$  film was successfully implemented as p-type rear-surface passivation layer for p-type silicon solar cells [12,33-35]. Various reports have shown the excellent quality of surface passivation realized using  $\text{AlO}_x$  film due to combined field-effect passivation mechanism with high number of negative  $Q_f$  and chemical passivation mechanism with low number of  $D_{it}$ .

## **1.5 Thesis motivation**

As discussed, there is much scope for research work towards an improvement in efficiency of silicon solar cells and at the same time decreasing the cost of the cell, so that one can have economically viable electricity generation through solar cells. In this thesis work, our focus is to minimize losses due to surface recombination on the p-type silicon surface with application of  $\text{AlO}_x$  film. In this work, we have examined the deposition of  $\text{AlO}_x$  films using industrial reactive sputter (RS) deposition technique with the use of pulsed-direct current (pulsed-DC) power supply source. This work carries development and optimization of process for film deposition and further the characterization of these films using different techniques to access the applicability of the film as surface passivation layer. Various in-depth studies of the film and its interface with analysis, has led us to the conclusion that the

pulsed-DC RS AlO<sub>x</sub> film is an interesting candidate for application as surface passivation layer on p-type surface.

## 1.6 Thesis outline

In this chapter we have discussed in brief different kinds of solar cell technologies. The cause of losses in the p-n junction solar cell due to carrier recombination and different surface passivation mechanism used so far for the passivation of c-Si solar cells were described. We have also discussed different materials already playing a role as passivation layer in solar cell industries. At the end, the motivation behind this research work is given in brief. In chapter 2, literature review of various reports on the applicability of the AlO<sub>x</sub> film as surface passivation layer with various properties and passivation quality, for film deposited using different techniques will be presented. The chapter will also give the details on experimental techniques used in this work. The details on systems used for various characterization and different methodology used for analysis of results will be discussed in chapter 2. In chapter 3, development and optimization process for AlO<sub>x</sub> film deposition using pulsed-DC RS technique will be discussed. The quality of the films formed will be assessed through various material and electrical characterization will be presented. In chapter 4, the impact of different PDA conditions by varying ambient and temperature, on the surface passivation quality of pulsed-DC RS AlO<sub>x</sub> film will be discussed towards the optimization of PDA process. In this chapter the detailed study of the material and interface quality using sophisticated characterization tools will also be presented. The origin and distribution of the charges in the film will be discussed in chapter 5. The chapter also gives details on the differences of the passivation result for as-deposited and annealed films. In chapter 6, the impact of different process parameters on the quality of film after application of optimized PDA condition will be presented to develop the economically viable process of the film deposition towards surface passivation application. In chapter 7, the thermal stability of the film will be presented for pulsed-DC RS AlO<sub>x</sub> film and the impact of additional SiN<sub>x</sub>:H capping layer on the thermal stability will be studied. In chapter 8, we present the conclusions of the research work with the future direction.

## **Chapter 2. Literature Review and Experimental Techniques**

### **2.1 Introduction**

As discussed in previous chapter an improvement in performance of silicon solar cells may be realised with an implementation of surface passivation layer. For example on p-type silicon solar cells, the front surface, i.e., emitter, which is normally textured to maximize the absorption of light has a-SiN<sub>x</sub> film as ARC deposited on it. The film was also used as passivation layer due to high number of positive Q<sub>f</sub> on n<sup>+</sup> emitter. Whereas rear-surface p-type base, needs a different material for passivation which must contains negative Q<sub>f</sub> to avoid parasitic shunting effect [33,36]. Since the AlO<sub>x</sub> film contains negative Q<sub>f</sub>, this becomes a potential choice for passivation of p-type silicon surface [33,36]. The AlO<sub>x</sub> film was successfully implemented as p-type rear-surface passivation layer on p-type silicon solar cells with advance structure like passivated emitter and rear cell (PERC) [95,33-35,37]. Various reports have shown that excellent surface passivation quality by AlO<sub>x</sub> film is achieved due to combined effect of field-effect mechanism (high negative Q<sub>f</sub>) and chemical passivation mechanism (low D<sub>it</sub>). Also the application of this material on n-type silicon solar cell for passivation of highly doped p<sup>+</sup> emitter surface was also explored in many reports [38-40]. Studies have shown that adding negative Q<sub>f</sub> on highly doped p-type emitter of n-type solar

cells improves the cell performance with passivation of the emitter surface. For these reasons AlO<sub>x</sub> film has become one major choice as surface passivation layer for p-type silicon [40].

In this chapter we will present a review of the published reports on the applicability of AlO<sub>x</sub> film deposited using various techniques for surface passivation layer of silicon solar cells. The review on electrical and material properties of the film, relating the passivation quality will be presented. The impact on cell parameters by using AlO<sub>x</sub> surface passivation layer will be presented for various deposition techniques.

A brief description about different systems and experimental set-ups used for the thesis work will be presented in this chapter for reference. The brief description on working principle of the various characterization tools and methodology applied for analysis of the results used in this work will also be presented later in this chapter.

## 2.2 Theoretical understanding of AlO<sub>x</sub>/c-Si interface

The origin of field-effect passivation by dielectrics is due to presence of high density of fixed oxide charges, Q<sub>f</sub> in the film. In AlO<sub>x</sub> film, it is the large density of negative Q<sub>f</sub> used for passivation of p-type c-Si surface, with repulsion of the minority carriers (i.e., electron) from the surface. The origin of these negative Q<sub>f</sub> in AlO<sub>x</sub> film deposited on c-Si was studied and reported by Matsunaga et al., using first-principles plane-wave pseudo-potential method [41]. They proposed that the presence of intrinsic defects like Al-vacancies and O-interstitials, results in origin of negative Q<sub>f</sub> charges in the film. On the other hand, Kimoto et al. reported the presence of both tetrahedrally (*T*) coordinated Al (negatively charged) and octahedrally (*O*) coordinated Al sites (positively charged) in  $\gamma$ -Al<sub>2</sub>O<sub>3</sub> film deposited using atomic layer deposition (ALD) [42], as given below



The study shows that close to the  $\gamma$ -Al<sub>2</sub>O<sub>3</sub>/c-Si interface, *T* coordinated Al bonded directly with O, seems to be more dominating which results in increase of negative Q<sub>f</sub> in the film [35,42,43]. Further increase in the negative Q<sub>f</sub> density was observed after annealing of the ALD-Al<sub>2</sub>O<sub>3</sub> film, with a concomitant formation of thin SiO<sub>2</sub> interfacial layer at Al<sub>2</sub>O<sub>3</sub>/c-Si interface [34,44,45]. The increase in negative Q<sub>f</sub> values after annealing, was due to increase in *T* coordinated Al at the interface, which results in improvement of surface passivation quality by plasma-assisted (PA)-ALD Al<sub>2</sub>O<sub>3</sub> film [44-46]. The fourier transform infra-red

spectrometer (FTIR) measurement of the film shows, after annealing the presence of the Si-O related absorbance peak intensity increases to the value similar to a good quality thermally grown  $\text{SiO}_2$  film [34]. Hence further improvement in surface passivation quality for the  $\text{AlO}_x$  films was realised by good quality of interface with low value of  $D_{it}$  after annealing and hence the combined effect of field-effect and chemical passivation mechanisms may be applied by  $\text{AlO}_x$  films [34,45-48].

## 2.3 Various techniques used to deposit $\text{AlO}_x$ film as passivation layer of c-Si surface

The  $\text{AlO}_x$  film deposited using different techniques like ALD, PECVD and RS techniques were extensively studied in c-Si solar cell applications. A report on low cost chemical deposition techniques was also studied for deposition of the  $\text{AlO}_x$  film in solar cell applications.

### 2.3.1 Atomic layer deposition

In many reports the ALD  $\text{Al}_2\text{O}_3$  film, was shown to provide excellent quality surface passivation due to combined effect of both field-effect passivation with high negative  $Q_f$  in the range of  $10^{13} \text{ cm}^{-2}$  and chemical passivation with  $D_{it}$  in the range of  $2 \times 10^{11} \text{ eV}^{-1} \cdot \text{cm}^2$  [12,34,45,48]. The two basic types of ALD techniques were mostly explored for deposition of the  $\text{Al}_2\text{O}_3$  film, viz.: thermal ALD and PA-ALD. The schematic diagram of typical thermal ALD and PA-ALD systems are shown in Figure. 2.1 (a) and (b), respectively.

In thermal ALD technique the substrate is exposed with Al precursor, i.e., tri-methylaluminum (TMA) with chemical composition of  $\text{Al}(\text{CH}_3)_3$  and after first half-cycle surface reaction the  $\text{N}_2/\text{Ar}$  gas is used to purge the by-products. After this step, the surface is exposed with the reactant, i.e., water vapour ( $\text{H}_2\text{O}$ ) to form mono-layer  $\text{Al}_2\text{O}_3$  at the substrate, followed by purging step, as shown in eq. (2.2) and (2.3). The cycle of reactions for thermal ALD technique using TMA precursor and  $\text{H}_2\text{O}$  reactant are shown in Figure 2.2 (a), which continues till the required film thickness was achieved. For thermal ALD, the heating system is used to raise the substrate temperature to the typical range of 150-250 °C for film deposition.

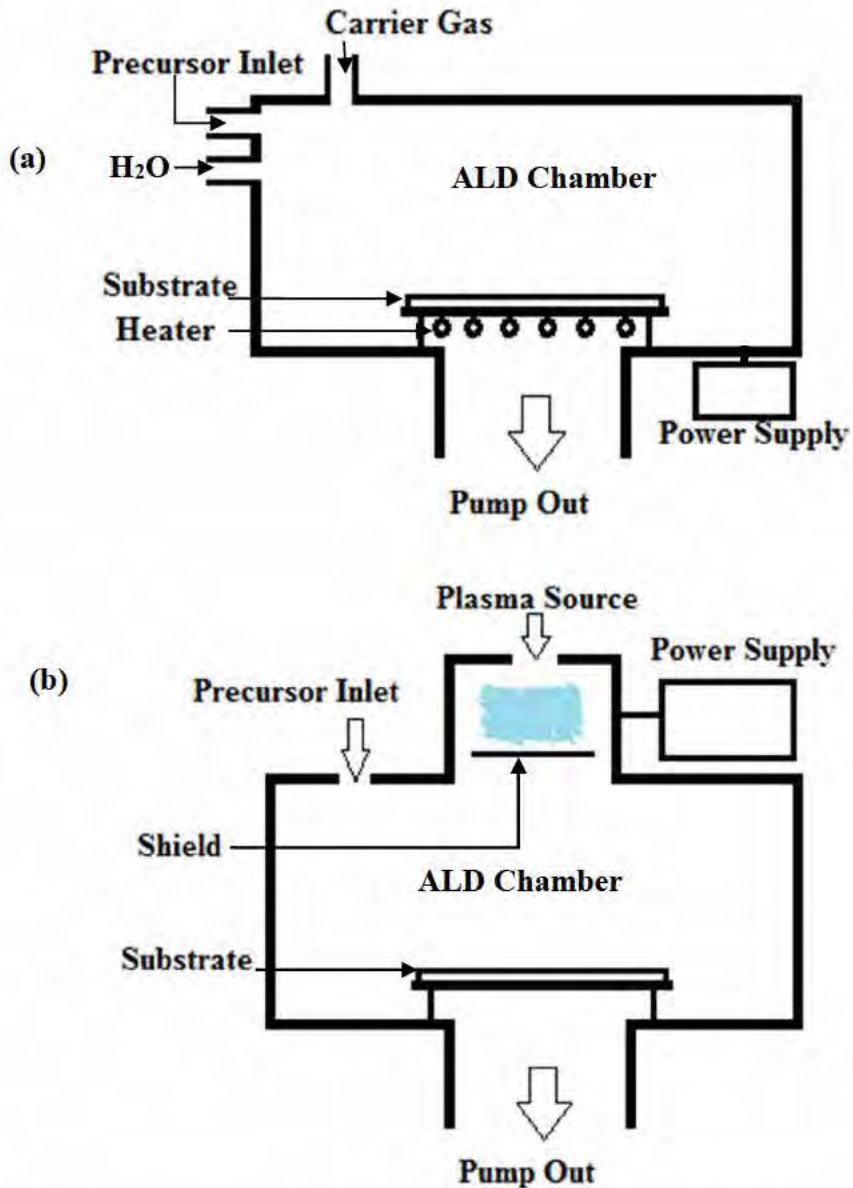
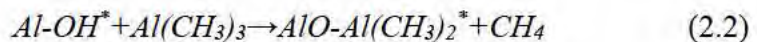
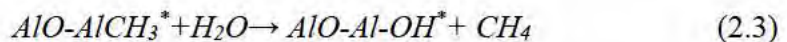


Figure 2.1 Schematic diagram of typical (a) thermal ALD and (b) plasma assisted-ALD systems [49].

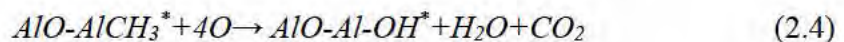
The self-limiting reactions at the surface for ALD system using TMA precursor during the first half-cycle is given as [49]:



For thermal ALD, second half-cycle reaction is



For PA-ALD, second half-cycle reaction is



In case of PA-ALD system the TMA precursor reacts in the presence of plasma from O<sub>2</sub> and deposit at the surface, as shown by self-limiting reactions in eq. (2.2) and (2.4). Due to plasma assisted deposition, the thermal energy requirement is less for PA-ALD systems. Because of high reactivity of plasma, the growth rate per cycle is also higher as compared to thermal ALD technique [50]. The reaction cycle for PA-ALD Al<sub>2</sub>O<sub>3</sub> film with TMA precursor and O<sub>2</sub> plasma reactant is shown in Figure 2.2 (b).

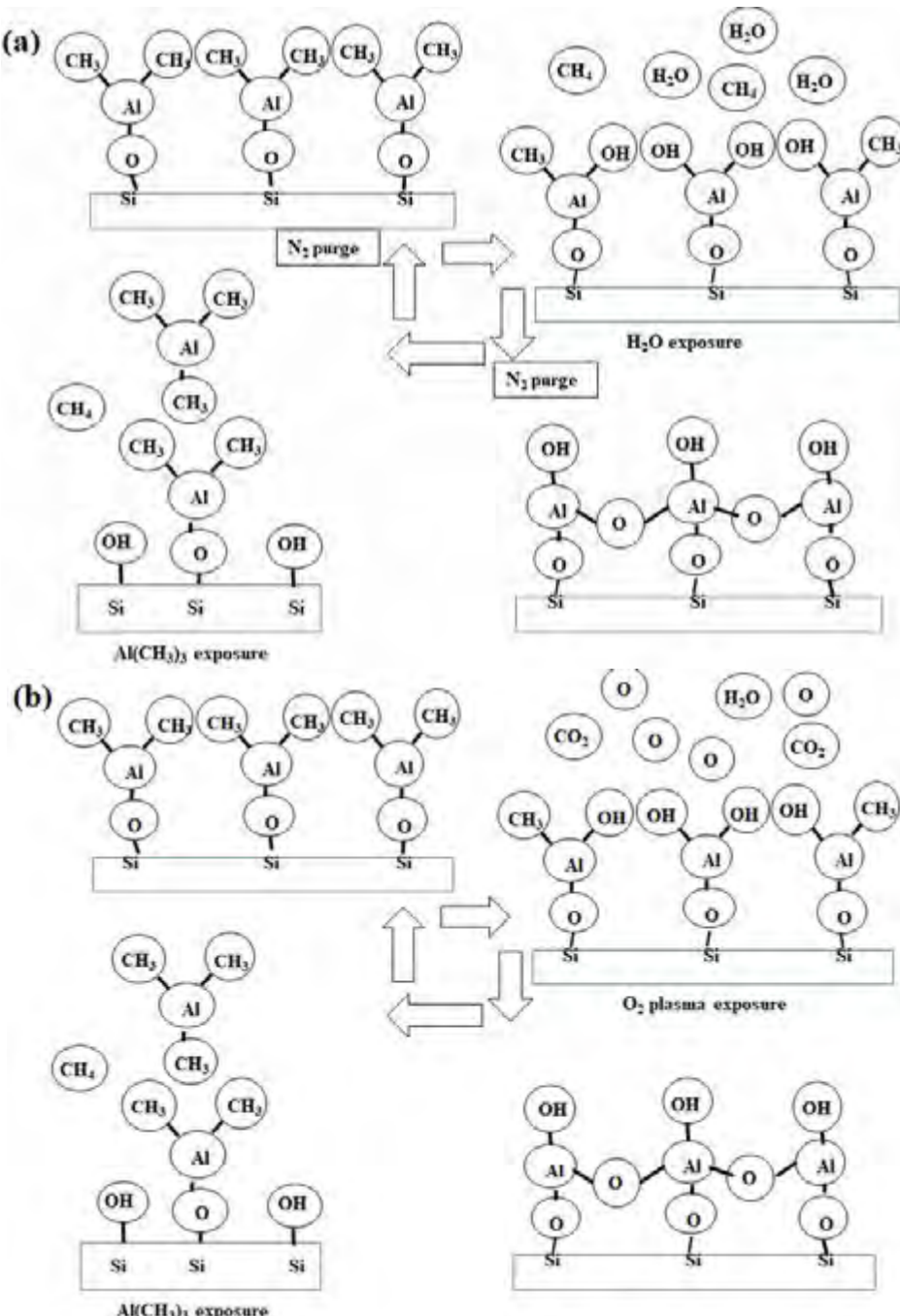


Figure 2.2 Reaction cycles for Al<sub>2</sub>O<sub>3</sub> deposition using (a) thermal ALD and (b) plasma assisted-ALD system [50].

The quality of surface passivation was investigated and compared for both thermal ALD and PA-ALD  $\text{Al}_2\text{O}_3$  films on low doped p-type silicon surface as well as highly doped  $\text{p}^+$  silicon [48,51-52]. For thermal ALD  $\text{Al}_2\text{O}_3$  film deposition on p-type floatzone (FZ) wafer exhibits good surface passivation quality with  $S_{\text{eff}}$  of  $14.5 \text{ cm.s}^{-1}$  in as-deposited condition itself, since the film deposition was carried out at high temperature ( $350^\circ\text{C}$ ). However improvement in  $S_{\text{eff}}$  to  $3 \text{ cm.s}^{-1}$  was achieved for films deposited in the substrate temperature range of  $150\text{-}200^\circ\text{C}$  and annealed at  $400^\circ\text{C}$  in  $\text{N}_2$  ambient for 10 min [52]. The film contained negative  $Q_f$  of  $2 \times 10^{12} \text{ cm}^{-2}$  and  $D_{\text{it}}$  of  $10^{11} \text{ eV}^{-1}\text{cm}^{-2}$ , after annealing [52]. As compared to thermal ALD  $\text{Al}_2\text{O}_3$  film PA-ALD  $\text{Al}_2\text{O}_3$  film, shows even better value of  $S_{\text{eff}}$  to  $2 \text{ cm.s}^{-1}$  for similar process and PDA conditions, due to an improvement in negative  $Q_f$  to  $5 \times 10^{12} \text{ cm}^{-2}$ , while the  $D_{\text{it}}$  values remains same at  $10^{11} \text{ eV}^{-1}\text{cm}^{-2}$  [52]. The report on impact of annealing on ALD  $\text{Al}_2\text{O}_3$  film shows, after annealing the  $D_{\text{it}}$  values are reported to be improved for both thermal and PA-ALD techniques, whereas the negative  $Q_f$  value seems to increase more for thermal ALD, since the PA-ALD technique shows high  $Q_f$  for as-deposited condition itself [52]. The report also shows the hydrogen content in the film is higher for thermal ALD as compared to PA-ALD technique [52]. Using PA-ALD  $\text{Al}_2\text{O}_3$  film the best value of  $S_{\text{eff}} = 2 \text{ cm.s}^{-1}$  calculated from  $\tau_{\text{eff}} = 6 \text{ ms}$ , measured on n-type c-Si surface [51,52]. Whereas on p-type c-Si surface the  $S_{\text{eff}} = 5 \text{ cm.s}^{-1}$  was reported [51,52]. The report also shows high quality surface passivation with value of surface recombination velocity on highly doped  $\text{p}^+$  emitter ( $S_{n0} = 109 \text{ cm.s}^{-1}$ ) for boron doping of  $7 \times 10^{18} \text{ cm}^{-3}$ , these value was extracted using SENTAURUS device simulation tool by feeding the measured value of  $J_{0e}$  versus dopant profile [53].

Using thermal ALD  $\text{Al}_2\text{O}_3$  film with  $\text{O}_3$  as reactant source, the value of  $J_{0e} = 33 \text{ fA.cm}^{-2}$  was reported on boron diffused  $\text{p}^+$  silicon (doping of  $2 \times 10^{19} \text{ cm}^{-3}$ ) surface with sheet resistance of  $84 \Omega.\text{sq}^{-1}$  on the  $\text{p}^+/\text{n}/\text{p}^+$  structure, this was compared with the PA-ALD  $\text{Al}_2\text{O}_3$  film with  $\text{O}_2$  plasma on similar structure which shows  $J_{0e} = 27 \text{ fA.cm}^{-2}$  [54]. On phosphorous diffused  $\text{n}^+$  emitter surface with sheet resistance  $10\text{-}100 \Omega.\text{sq}^{-1}$ , the PA-ALD  $\text{Al}_2\text{O}_3$  film used as passivation layer, results in implied- $V_{\text{oc}}$  of  $680 \text{ mV}$  and on lightly doped n-type surface the implied- $V_{\text{oc}}$  improved to  $700 \text{ mV}$  [55]. These reports suggest that ALD  $\text{Al}_2\text{O}_3$  film was promising for effectively passivating both  $\text{p}^+$  and  $\text{n}^+$  surfaces.

A conversion efficiency,  $\eta$  of  $21.2\%$  was demonstrated on p-type PERC c-Si solar cell with rear-surface passivated using PA-ALD  $\text{AlO}_x$  film (20 nm) stacked with PECVD

$\text{SiO}_x$  film (70 nm) [36]. A conversion efficiency,  $\eta$  of 23.4 % was reported on n-type c-Si solar cells on passivated emitter with rear locally diffused (PERL) structure [38,39]. The boron doped p<sup>+</sup> emitter passivated using stack of PA-ALD  $\text{Al}_2\text{O}_3$  film (30 nm) and PECVD  $\text{SiN}_x$  (40 nm) [38,39].

The ALD  $\text{Al}_2\text{O}_3$  films were also tested for passivation of the black-Si (b-Si) wafers with random structures made by dry-etching process using inductively-coupled plasma (ICP) technique, and result gives  $S_{\text{eff}} \leq 8 \text{ cm.s}^{-1}$  [56]. The ALD offers conformal deposition of the film on the irregular surface structure in this case.

The typical ALD technique was not being widely accepted by the solar industries for  $\text{AlO}_x$  film deposition because of very low rate of deposition  $< 2 \text{ nm.min}^{-1}$  [52]. To address this issue, new designs for ALD deposition tool were proposed, such as batch ALD and spatial ALD reactor, as shown in Figure 2.3 (a) and (b), respectively [57,58].

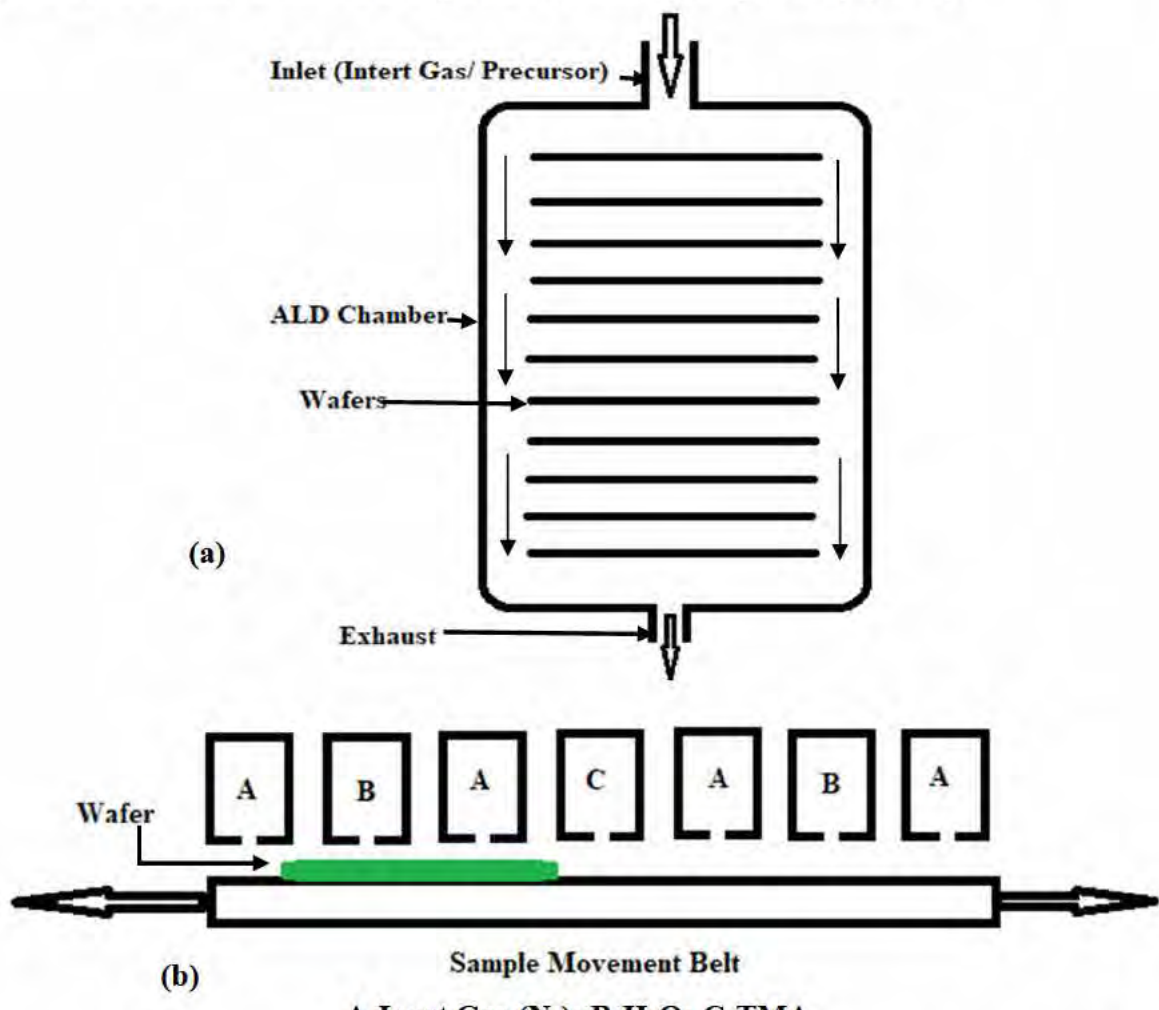


Figure 2.3 Schematic diagrams of typical (a) batch ALD reactor [57,59] and (b) spatial ALD systems [58-60] for solar industry applications.

Figure 2.3 (a) shows, a new arrangement known as batch ALD reactor with the chamber designed to process many number of wafers in one run, hence improving the throughput of the deposition tool [57,59]. The value of  $S_{eff} < 6 \text{ cm.s}^{-1}$  was reported for  $\text{Al}_2\text{O}_3$  film deposited on p-type c-Si surface using ASM batch ALD reactor with  $\text{O}_3$  used as plasma source [61]. The film has shown the negative  $Q_f$  of  $3.4 \times 10^{12} \text{ cm}^{-2}$  and  $D_{it}$  of  $1 \times 10^{11} \text{ eV}^{-1}.\text{cm}^{-2}$  on this film after PDA in  $\text{N}_2$  ambient at  $400^\circ\text{C}$  for 10 min [57,61]. Figure 2.3 (b) shows, a chamber design in which the film deposition occurs in the spatial regime that means wafers are kept on the moving belt while the precursor and oxidation cycles are reacted and exposed on the wafer surface in a sequential manner, known as spatial ALD system [58-60]. This kind of arrangement leads to a very high deposition rate of  $70 \text{ nm}.\text{min}^{-1}$  [58]. The surface passivation quality obtained by spatial ALD and thermal ALD  $\text{Al}_2\text{O}_3$  film were compared on p-type Czochralski (CZ) c-Si wafer ( $1\text{-}3 \Omega.\text{cm}$ ). The result shows for spatial ALD  $\text{Al}_2\text{O}_3$  film, similar level of surface passivation are achieved for film thickness  $> 10 \text{ nm}$  for similar process and PDA conditions [62]. The same report shows high level of surface passivation,  $S_{eff}$  of  $2.9 \text{ cm.s}^{-1}$  using spatial ALD  $\text{Al}_2\text{O}_3$  film deposited on n-type FZ c-Si wafer ( $2.4 \Omega.\text{cm}$ ), i.e., slightly higher as compared to  $S_{eff}$  of  $1.9 \text{ cm.s}^{-1}$  using thermal ALD  $\text{Al}_2\text{O}_3$  film of same thickness (30 nm). These films were annealed in rapid thermal processing (RTP) at  $835^\circ\text{C}$  for 1-2 s [62]. The deposition rate of  $72 \text{ nm}.\text{min}^{-1}$  was reported for this particular spatial ALD system, i.e., very high as compared to conventional ALD system [62].

The value of negative  $Q_f$  and  $D_{it}$  for spatial ALD  $\text{Al}_2\text{O}_3$  film, were reported by Werner et al. in two different reports [58,63]. The spatial ALD  $\text{Al}_2\text{O}_3$  film deposition at the rate of  $30 \text{ nm}.\text{min}^{-1}$ , on n-type CZ c-Si wafer ( $4 \Omega.\text{cm}$ ) without any PDA, shows the mid-gap  $D_{it} = 7 \pm 1 \times 10^{10} \text{ eV}^{-1}.\text{cm}^{-2}$ , i.e., assessed through quasi-static and high-frequency C-V measurement techniques for film thickness of 10 nm [63]. On another report the negative  $Q_f$  of  $4 \pm 1 \times 10^{12} \text{ cm}^{-2}$  extracted using corona discharge method for spatial ALD  $\text{Al}_2\text{O}_3$  film (30 nm) deposited on p-type FZ c-Si ( $1.3 \Omega.\text{cm}$ ) wafer was reported [58]. For this sample, the maximum value  $S_{eff,max} = 47 \text{ cm.s}^{-1}$  at  $\Delta n = 10^{15} \text{ cm}^{-3}$  was reported after PDA in  $\text{N}_2$  ambient at  $350^\circ\text{C}$  for 15 min [58]. This implies that the films deposited by spatial ALD technique possess good quality and are suitable for surface passivation application [58,63].

### 2.3.2 Plasma enhanced or assisted chemical vapor deposition

The PECVD technique was widely used in solar cell manufacturing industries for the deposition of  $\text{SiN}_x$  film applied as ARC. The schematic diagram of a typical parallel plate

capacitively coupled PECVD system is shown in Figure 2.4. The  $\text{Al}_2\text{O}_3$  film deposited using TMA precursor and  $\text{N}_2\text{O}$  or  $\text{O}_2$  may be used as reactants with Ar plasma in this technique [64].

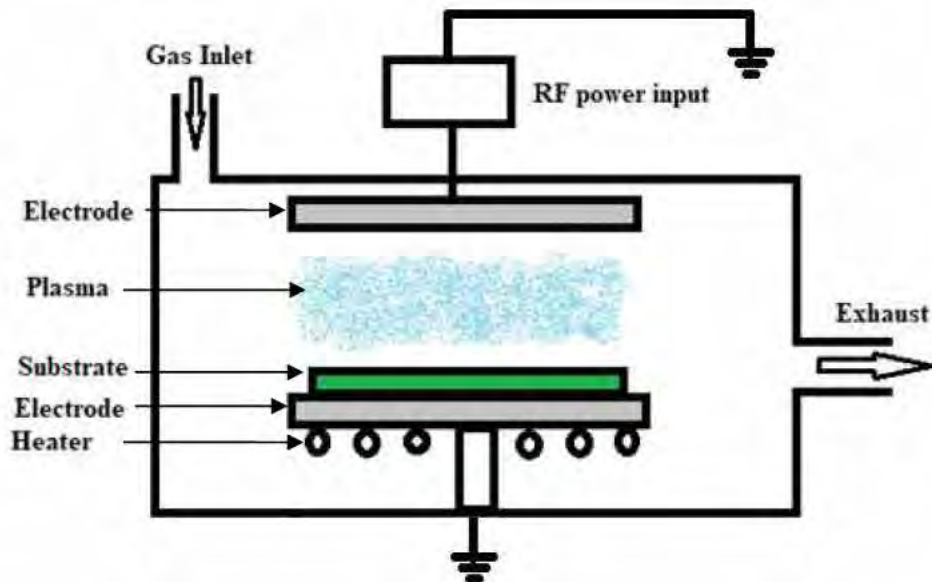


Figure 2.4 Schematic diagram of typical PECVD system [64].

The PECVD  $\text{Al}_2\text{O}_3$  shows  $S_{\text{eff}} < 1 \text{ cm.s}^{-1}$  on n-type c-Si surface for high deposition rate of  $5 \text{ nm.min}^{-1}$  using this technique. The film was deposited at  $200^\circ\text{C}$  substrate temperature and annealed at  $400^\circ\text{C}$  in  $\text{N}_2$  for 10 min, as reported by Dingemans et al. [52]. The PECVD tools with pulsed flow of TMA precursor and  $\text{O}_2$  plasma used to deposit  $\text{Al}_2\text{O}_3$  film with high deposition rate  $> 30 \text{ nm.min}^{-1}$ , has shown high quality surface passivation  $S_{\text{eff}} < 1 \text{ cm.s}^{-1}$  [65]. The film was deposited on n-type FZ c-Si wafer, with substrate temperature varied between  $50\text{-}300^\circ\text{C}$  during deposition and PDA was carried out in  $\text{N}_2$  ambient at  $400^\circ\text{C}$  for 10 min [65].

Saintcast et al. explored very high deposition rate for  $\text{Al}_2\text{O}_3$  film deposition using PECVD system by Roth & Rau, which is already used in solar industries for  $\text{SiN}_x$  film deposition. The system uses TMA precursor and  $\text{N}_2\text{O}$  and Ar as reactant gases, for  $\text{Al}_2\text{O}_3$  film deposition [66]. The deposition was done on large substrate which shows about  $100 \text{ nm.min}^{-1}$  static deposition rate, showing fairly low  $S_{\text{eff}}$  of  $10 \text{ cm.s}^{-1}$  on low-resistivity p-type c-Si [66]. Film deposited at substrate temperature of  $300^\circ\text{C}$  and annealed at  $400^\circ\text{C}$  in FGA ambient for 25 min [66].

A high conversion efficiency,  $\eta$  of 21.5 % was reported on p-type PERC solar cell structure with rear-surface passivated by using PECVD Al<sub>2</sub>O<sub>3</sub> film [36]. An improvement in solar cell efficiency was related to an improved  $V_{oc}$  of 684 mV after rear surface passivation using PECVD Al<sub>2</sub>O<sub>3</sub> film, i.e., similar to the value of  $V_{oc}$  obtained for thermal SiO<sub>2</sub> film passivated silicon solar cells [36,37]. The as-deposited PECVD Al<sub>2</sub>O<sub>3</sub> film was shown to contain very high negative  $Q_f$  of  $2 \times 10^{12} \text{ cm}^{-2}$ , since the film deposition was carried out at 300 °C, whereas an improvement in  $D_{it}$  to  $3 \times 10^{11} \text{ eV}^{-1} \cdot \text{cm}^{-2}$  was realized after PDA in FGA ambient at 425 °C for 15 min [37,67]. This film was applied as rear-surface passivation layer on p-type solar cells, which resulted in reverse saturation current density of the base ( $J_{0b}$ ) = 52 fA.cm<sup>-2</sup> [36]. In another report by Saintcast et al., the value of reverse saturation current density of the emitter ( $J_{0e}$ ) =  $9.5 \pm 0.7 \text{ fA.cm}^{-2}$  was shown on boron doped p<sup>+</sup> emitter with sheet resistance  $120 \Omega \cdot \text{sq}^{-1}$  and PECVD Al<sub>2</sub>O<sub>3</sub> passivation film was used to passivate the planner wafer [68].

The PECVD tool, discussed above is capacitively coupled type, while an inductively coupled plasma (ICP) CVD system was also explored for the AlO<sub>x</sub> film deposition report by Vieth et al. [69]. The 30 nm thick ICP-CVD AlO<sub>x</sub> film was applied as rear surface passivation of p-type PERC silicon solar cell, resulted in  $S_{eff}$  of  $9 \text{ cm.s}^{-1}$  after annealing at 425 °C on p-type FZ c-Si wafer ( $1.4 \Omega \cdot \text{cm}$ ) [69]. The film contains high value of negative  $Q_f$  of  $4.5 \times 10^{12} \text{ cm}^{-2}$  and mid-gap  $D_{it}$  of  $11.0 \pm 4.0 \times 10^{11} \text{ eV}^{-1} \cdot \text{cm}^{-2}$ , which is quite high as compared to the typical PECVD and ALD techniques discussed so far [69]. The technique has shown deposition rate of  $5 \text{ nm.s}^{-1}$ , as a result of high plasma density during deposition. In this technique, the TMA precursor was used along with O<sub>2</sub> process gas for film deposition. The PERC structure with rear surface passivated using ICP-CVD AlO<sub>x</sub>/SiN<sub>x</sub> layer shows  $\eta$  of 20.1 % [69].

The AlO<sub>x</sub> films deposited by ALD and PECVD techniques, shows an improvement in surface passivation quality after PDA in FGA or N<sub>2</sub> ambient at typical annealing temperature between 350-450 °C. The reason for an improvement in passivation quality was mostly related to good quality interface with the reduction in  $D_{it}$  value, i.e., activation of chemical passivation mechanism. In all these reports the most commonly used Al precursor was TMA, which results in incorporation of 2-7 % hydrogen in the film during deposition, and this hydrogen transports towards the interface during PDA process and hence results in improvement in AlO<sub>x</sub>/c-Si interface [70-72].

The disadvantage of above techniques, are use of TMA precursor which is pyrophoric in nature, hence the safety equipment are required to protect from any hazards. In addition to this, the precursor itself is very expensive. Hence adding the costs of safety equipment and chemical made the overall  $\text{AlO}_x$  films deposition quite expensive. Thus the low cost reactive sputter deposition techniques were explored for  $\text{AlO}_x$  film deposition for its application as surface passivation layer in c-Si solar cells.

### 2.3.3 Reactive sputter deposition technique

As discussed in previous sections, for industrial relevance one has to consider a system which gives higher deposition rate and process film with low cost, and a solution lies in the technique called RS deposition. The schematic diagram of typical RS system using radio frequency (RF) power source is shown in Figure 2.5.

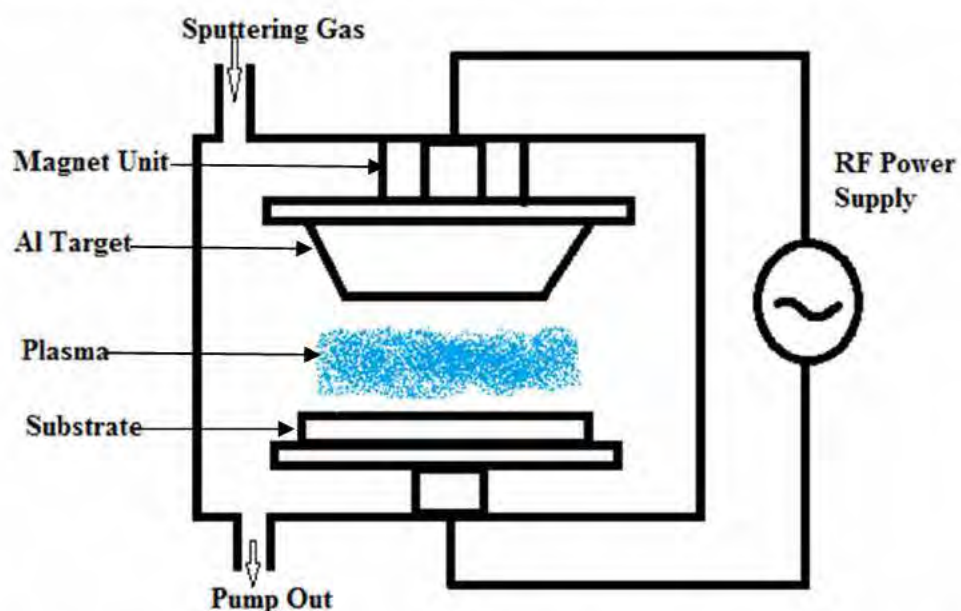


Figure 2.5 Schematic diagram of typical reactive sputter system using RF power supply [73,74].

In a typical RS deposition technique, the  $\text{AlO}_x$  film deposition is carried out using the RF power supply source, where high purity aluminium target is sputtered in  $\text{O}_2$  reactive gas ambient, using Ar as sputter gas [73,74]. The technique has advantage that it does not require expensive chemical precursors for the film deposition.

There are several reports published on the application of RS deposited AlO<sub>x</sub> film as surface passivation layer of c-Si [75-79]. The report by Li et al., shows the as-deposited film contains negative Q<sub>f</sub> of  $8.6 \times 10^{11} \text{ cm}^{-2}$ , which is lower compared to the ALD and PECVD techniques [75]. While an improvement in negative Q<sub>f</sub> to  $3.4 \times 10^{12} \text{ cm}^{-2}$  and D<sub>it</sub> to  $4 \times 10^{12} \text{ eV}^{-1} \cdot \text{cm}^{-2}$  was realized after PDA of the RS AlO<sub>x</sub> film at 400 °C in N<sub>2</sub> ambient for 30 min [75].

As mentioned in many report, for AlO<sub>x</sub> film deposited on c-Si, the PDA process results in improvement of surface passivation quality with an increase in negative Q<sub>f</sub> and decrease in D<sub>it</sub> [34,43,48,67,76]. Agostinelli et al., reported such improvement in passivation quality after PDA was due to formation of thin interfacial oxide (SiO<sub>x</sub>), that results in increase of negative Q<sub>f</sub> [35]. Li et al., studied an impact of different PDA conditions on RS deposited AlO<sub>x</sub> film deposited on low resistivity p-type c-Si wafer. The τ<sub>eff</sub> of 290 μs was measured on film after annealing in FGA ambient at 400 °C for 60 min, which results in low S<sub>eff</sub> of 54 cm.s<sup>-1</sup>. The same report shows τ<sub>eff</sub> of 200 μs was measured on the film annealed in N<sub>2</sub> ambient at 400 °C for 60 min, which results in S<sub>eff</sub> of 74 cm.s<sup>-1</sup> [75]. This indicates an annealing in FGA ambient results in relatively good surface passivation quality as compared to N<sub>2</sub> ambient, the reason stated as the modification of interfacial quality due to presence of hydrogen in FGA ambient [75]. Since hydrogen can be incorporated in this film through PDA ambient only, as the RS AlO<sub>x</sub> film deposition was carried out in high purity O<sub>2</sub> and Ar gases by reactively sputtering of high purity Al target [73,74,77].

Very high quality of surface passivation by RS AlO<sub>x</sub> film with S<sub>eff</sub> of 8 cm.s<sup>-1</sup> was reported by Zhang et al. on n-type c-Si surface. The film was deposited at process pressure of 5 mTorr and deposition power of 220 W (i.e., power density of 4.82 W.cm<sup>-2</sup>). The film was annealed in N<sub>2</sub> ambient at 425 °C for 30 min [78]. Krugel et al. reported the cell performance of p-type local-fired contact (LFC) PERC solar cells, using rear surface passivation of RS AlO<sub>x</sub> capped with SiN<sub>x</sub> film and shows an improvement in η by ~ 1 % as compared to Al-back surface field (BSF) solar cells [79]. An efficiency η of 20.1 % was reported on p-type PERC solar cell, using RS AlO<sub>x</sub> film applied as rear-surface passivation layer [33]. In this case the solar cell contacts were made using shadow mask with Al evaporation at the back [33]. The RS AlO<sub>x</sub> film used in this cells, showed S<sub>eff</sub> of 35 cm.s<sup>-1</sup> measured on 1 Ω.cm p-type FZ c-Si surface [33,75].

Untila et al. reported  $\text{AlO}_x$  film deposition using ultrasonic chemical spray pyrolysis method, gives very high deposition rate of  $130 \text{ nm} \cdot \text{min}^{-1}$  at a deposition temperature of  $500^\circ\text{C}$ . The  $S_{\text{eff}}$  of  $70 \text{ cm} \cdot \text{s}^{-1}$  was reported on highly doped  $p^+$  ( $10^{20} \text{ cm}^{-3}$ ) c-Si surface using this technique [80].

There are different reports available on high temperature stability of  $\text{AlO}_x$  film deposited using ALD, PECVD and RS techniques, for the typical firing temperature up to  $850^\circ\text{C}$ . Since the firing process at such temperature is required to activate the contacts in screen-printed c-Si solar cells. Various reports shows degradation in the passivation quality of these films for PECVD and RS techniques, after firing at such high temperature [33]. However the film deposited using ALD technique, has shown an acceptable surface passivation quality after firing process on screen-printed c-Si solar cells [33,81]. The degradation of passivation quality for ALD and PECVD  $\text{Al}_2\text{O}_3$  films after firing process was related to the effusion of hydrogen from the film [67,70,71]. To improve the high-temperature stability of  $\text{AlO}_x$  film, a stack structure of  $\text{AlO}_x/\text{SiN}_x$  or  $\text{AlO}_x/\text{SiO}_x$  was introduced on the silicon solar cells [82-84].

## 2.4 Experimental techniques

In this section of the chapter we will discuss about various experimental techniques, systems and methodology used during this work. The sample preparation methods used for different experiments will also be presented in brief in this section.

### 2.4.1 Electrical characterization

The thin dielectric films deposited on silicon surface were characterized electrically for the assessment of electrical behaviour viz. interfacial properties, electrical charges in the films, breakdown voltage, as well as uniformity using capacitance versus voltage (C-V), conductance versus voltage (G-V) and current versus voltage (I-V) measurements performed on metal oxide semiconductor (MOS) structure, as shown in Figure 2.6. Keithley 4200 semiconductor characterization system (SCS) was used for these measurements.

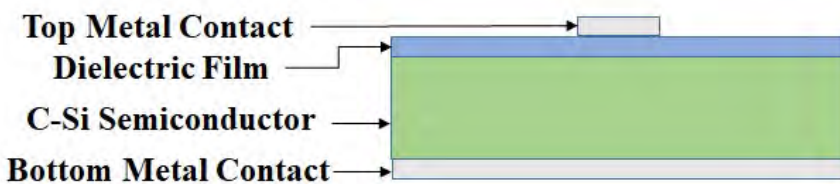


Figure 2.6 MOS capacitor structure for electrical characterization of the dielectric film.

The MOS structure was fabricated by depositing the dielectric film to be characterized on p-type CZ c-Si wafers. The wafers were cleaned before film deposition by standard Radio Corporation of America (RCA) cleaning procedure which involves the standard cleaning SC-I to remove organic contamination and SC-II to remove metal contamination. These were followed by immersing wafer in 2 % hydrofluoric (HF) acid followed by rinsing in de-ionized (DI) water and N<sub>2</sub> drying. The detailed process conditions used for film deposition will be discussed in coming chapters of the thesis, under experimental details. The metal contacts in MOS capacitors were deposited using thermal evaporation of aluminum (Al), the top contact was made using shadow mask of nominal diameter = 200 μm followed by bottom contact with blanket Al deposition. The native oxide on the backside of the wafers were etched using dilute HF before the deposition of Al on the backside.

The electrical measurements were performed on the MOS capacitors, by supplying small alternate current (AC) voltage superimposed on direct current (DC) voltage to the top gate contact while the bottom contact was grounded. The impedance was measured for different values of DC voltages, and the capacitance and conductance were extracted from the impedance. The resultant C-V and G-V plot for a typical MOS device is shown in Figure 2.7.

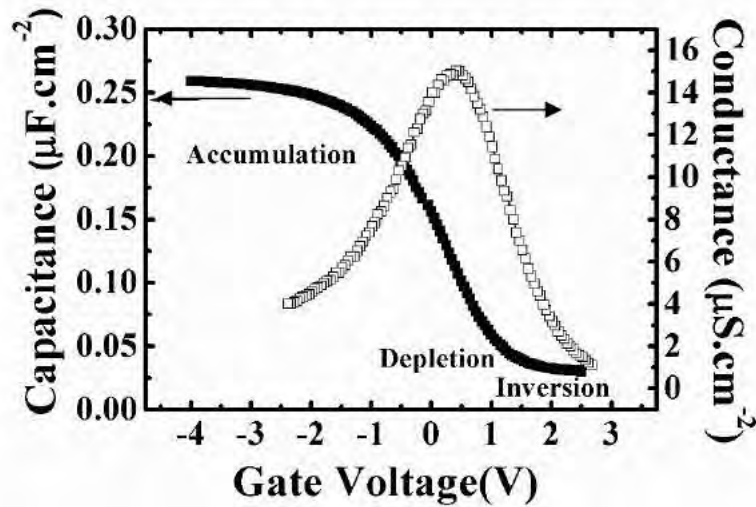


Figure 2.7 The high frequency C-V and G-V plot for the dielectric film measured on MOS capacitor at frequency,  $f = 100$  kHz.

The dielectric film thickness,  $T_{ox}$  (nm), can be measured from the C-V plot using the eq. (2.5),

$$T_{ox} = \frac{\epsilon_{ox}}{C_{acc}} \quad (\text{nm}) \quad (2.5)$$

where,  $\epsilon_{ox}$  represents relative permittivity (dielectric constant) of the oxide ( $\text{F.cm}^{-1}$ ), and  $C_{acc}$  represents value of accumulation capacitance, which is the maximum capacitance value in the C-V plot ( $\mu\text{F.cm}^{-2}$ ). The permittivity of the material is given as eq. (2.6),

$$\epsilon = \epsilon_r \epsilon_0 \quad (2.6)$$

where,  $\epsilon_r$  represent relative permittivity of the dielectric also defined as dielectric constant, and  $\epsilon_0$  represents permittivity of free space =  $8.854 \times 10^{-14} \text{ F.cm}^{-1}$ .

In this case we will assess the electrical property of  $\text{Al}_2\text{O}_3$  film which has high dielectric constant,  $\epsilon_{r-AlOx}$  of 9 [85], hence the equivalent oxide thickness (EOT) in nm, can be extracted from the C-V plot, which is defined as equivalent  $\text{SiO}_2$  (with  $\epsilon_{r-SiO2} = 3.9$ ) thickness required to achieve the similar value of maximum capacitance density for high dielectric constant material, calculated using eq. (2.7) [7,86],

$$EOT = \frac{3.9}{\epsilon_{r-AlO}} T_{ox} \quad (\text{nm}) \quad (2.7)$$

where  $\epsilon_{r-AlOx}$  represents the dielectric constant of  $\text{AlO}_x$  film, and  $T_{ox}$  represents the film thickness (nm) measured using spectroscopic ellipsometer (SE).

The other parameters such as acceptor doping concentration  $N_A$  may be extracted using following set of eq. (2.8) to (2.11), assuming a uniform doping in the semiconductor [86].

$$X_{d,max} = \sqrt{\frac{4\epsilon_s \phi_B}{qN_A}} \quad (\text{cm}) \quad (2.8)$$

where,  $X_{d,max}$  is maximum depletion length (cm) extracted from the C-V plot using eq. (2.9),

$$C_{S min}^{HF} = \frac{\epsilon_s}{X_{dmax}} \quad (\mu\text{F.cm}^{-2}) \quad (2.9)$$

where  $C_{S min}^{HF}$  is extracted from high- frequency C-V plot using the eq. (2.10),

$$\frac{1}{C_{S min}^{HF}} = \frac{1}{C_{min}} - \frac{1}{C_{acc}} \quad (2.10)$$

where,  $C_{min}$  represents the minimum value of capacitance in  $\mu\text{F.cm}^{-2}$  in C-V plot. In eq. (2.8), and eq. (2.9) the  $\epsilon_s$  represents the relative permittivity of silicon = 11.68 and the  $\phi_B$  represents the bulk potential, defined as difference between potential of doped and intrinsic silicon.

$$\phi_B = \frac{kT}{q} \ln \frac{N_A}{n_i} \quad (\text{V}) \quad (2.11)$$

The flat-band voltage ( $V_{FB}$ ) represents the voltage at which capacitance value equals the flat-band capacitance ( $C_{FB}$ ), and is extracted using the eq. (2.12) [86],

$$\frac{1}{C_{FB}} = \frac{1}{C_{acc}} + \frac{1}{C_{S,FB}} \quad (2.12)$$

where,  $C_{S,FB}$  represents semiconductor flat-band capacitance, extracted using eq. (2.13),

$$C_{S,FB} = \frac{\epsilon_s}{L_D} \quad (2.13)$$

where,  $L_D$  represent extrinsic debye length in cm, which is the characteristic screening length, is given by eq. (2.14) [86],

$$L_D = \sqrt{\frac{kT\epsilon_s}{q^2 N_A}} \quad (\text{cm}) \quad (2.14)$$

Another important electrical parameter is the fixed oxide charge density,  $Q_f$  which can be extracted from high frequency C-V plot, by determining shift in mid-gap voltage from the ideal value,  $\Delta V_{MG}$  (V), using eq. (2.15) [86],

$$Q_f = - \left( \frac{\Delta V_{MG} C_{acc}}{q} \right) \quad (\text{cm}^{-2}) \quad (2.15)$$

where  $\Delta V_{MG} = V_{MG} - V_{MG,\text{ideal}}$ , the  $V_{MG}$  is the voltage value corresponding to the mid-gap capacitance ( $C_{MG}$ ) in C-V plot, is given by eq. (2.16),

$$\frac{1}{C_{MG}} = \frac{1}{C_{acc}} + \frac{1}{C_{S,MG}} \quad (2.16)$$

where,  $C_{S,MG}$  represents semiconductor mid-gap capacitance, extracted using eq. (2.17),

$$C_{S,MG} = \frac{\epsilon_s}{\sqrt{2L_D}} \frac{1}{\left( \frac{q\phi_B}{kT} - 1 \right)^{1/2}} \quad (2.17)$$

The ideal  $V_{MG}$  ( $V_{MG,\text{ideal}}$ ) is defined as the  $V_{MG}$  when the fixed charge density is zero, which is calculated using eq. (2.18)

$$V_{MG,ideal} = \phi_{MS} + \phi_B + \frac{qN_A X_{MG}}{C_{acc}} \quad (\text{V}) \quad (2.18)$$

where,  $\phi_{MS}$  represents work-function difference, between metal ( $\phi_M$ ) and semiconductor ( $\phi_S$ ), is extracted using eq. (2.19), from the C-V plot [86],

$$\phi_{MS} = \phi_M - \phi_S = \phi_M - \left( \chi + \frac{E_{BG}}{2q} + \phi_B \right) \quad (V) \quad (2.19)$$

where,  $\chi$  is known as electron affinity for Si and is given as  $q\chi = 4.05$  eV,  $\phi_M$  is the work function of Al metal gate = 4.1 eV and  $E_{BG}$  represent band-gap energy of Si = 1.1 eV. The  $X_{MG}$  in eq. (2.18), represents depletion width at mid-gap (cm).

The  $D_{it}$  is extracted from the high frequency G-V plot, shown in Figure 2.7, using single frequency conductance approximation technique, as given in eq. (2.20) [87].

$$D_{it} = \frac{2}{qA} \frac{G_{max}/\omega}{\left(G_{max}/\omega C_{acc}\right)^2 + \left(1 - C_{max}/C_{acc}\right)} \quad (\text{cm}^{-2} \cdot \text{eV}^{-1}) \quad (2.20)$$

where, A represents the area of capacitor ( $\text{cm}^2$ ),  $\omega = 2\pi f$  represents measurement angular frequency ( $\text{rad.s}^{-1}$ ),  $G_{max}$  represents the value of peak conductance and  $C_{max}$  represents the value of capacitance at the voltage corresponding to  $G_{max}$  in G-V plot. Through electrical characterization, the two important parameters  $Q_f$  and  $D_{it}$  of the dielectric film and its interface with silicon are obtained. For these measurements 8 number of devices were measured from each sample.

Another important quality of the dielectric material is the breakdown voltage, which is obtained from the I-V measurement. Figure 2.8, shows the current density versus voltage (J-V) graph for a MOS capacitor measured using Keithley 4200 SCS, by linear voltage sweep.

The voltage at which the gate current increase abruptly is identified as the breakdown voltage,  $V_{BD}$  (V). To investigate the uniformity of the film over the wafer, in terms of breakdown voltage, measurements were performed on 20 devices at different locations on the samples.

The breakdown is known to follow the Weibull distribution. Figure 2.9 shows the Weibull plot of the effective breakdown field ( $E_{BD}$ )  $\text{V.cm}^{-1}$ , is given as eq. (2.21) [7],

$$E_{BD} = \frac{V_{BD}}{EOT} \quad (\text{V.cm}^{-1}) \quad (2.21)$$

where,  $V_{BD}$  is breakdown voltage in V and EOT is equivalent oxide thickness in cm as defined in eq. (2.7). The Weibull distribution plot for  $E_{BD}$  of 20 MOS capacitor devices, tested on a wafer is shown in Figure 2.9.

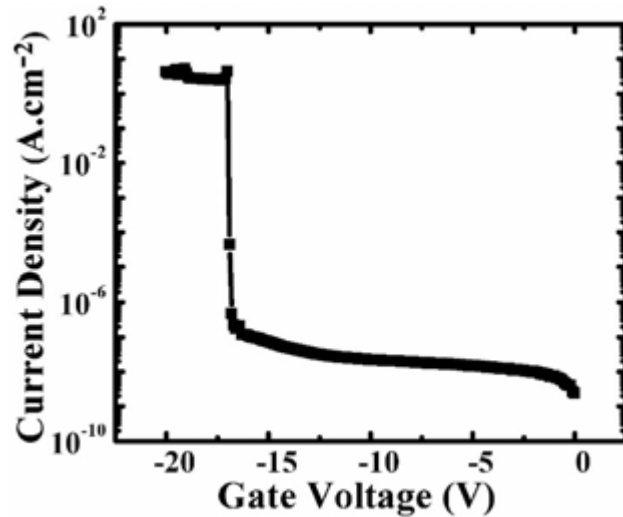


Figure 2.8 The J-V plot for the dielectric film measured on MOS capacitor.

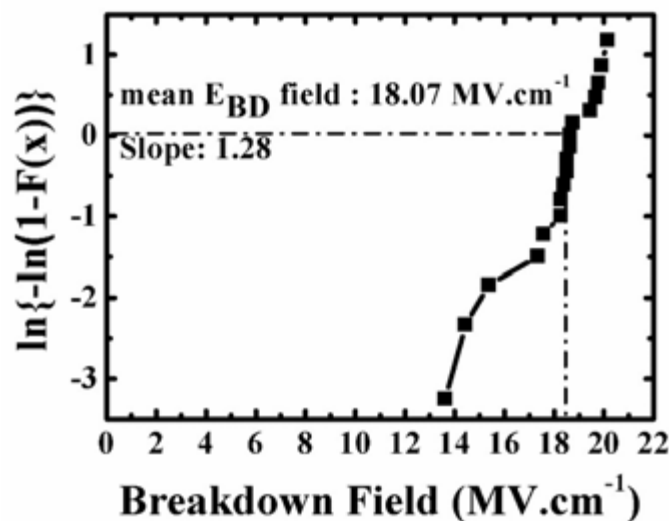


Figure 2.9 The Weibull distribution plot of the  $E_{BD}$  for 20 MOS capacitor devices tested on a wafer [7].

The mean  $E_{BD}$  for the entire sample is defined as, the effective field below which 63.2 % of the devices are expected to fail. Also the slope of the Weibull distribution estimated by linear fit shows the uniformity in the film. High value of slope means a more uniform film, as most of the devices will breakdown at nearly the same voltage.

The above electrical characteristics are used in this thesis work for assessing the electrical behaviour of the dielectric film for different experimental conditions during process optimization. Material characteristics of the film which may influence the properties of the

dielectric and its interface with Si are investigated using different systems are discussed in the next section.

### 2.4.2 Material characterization

In this section we will discuss about the material characterization systems used in this work to assess different parameters of the dielectric film, viz. film thickness, film density, topography and uniformity, elemental composition and chemical bonding of the film and most importantly interfacial property.

#### (a) Spectroscopic ellipsometer

In this work Sentech SE, model number SE800 was used to measure film thickness ( $T_{ox}$ ) and refractive index (RI), through change in polarization of the incident light on sample [88]. The typical schematic diagram of SE is shown in Figure 2.10.

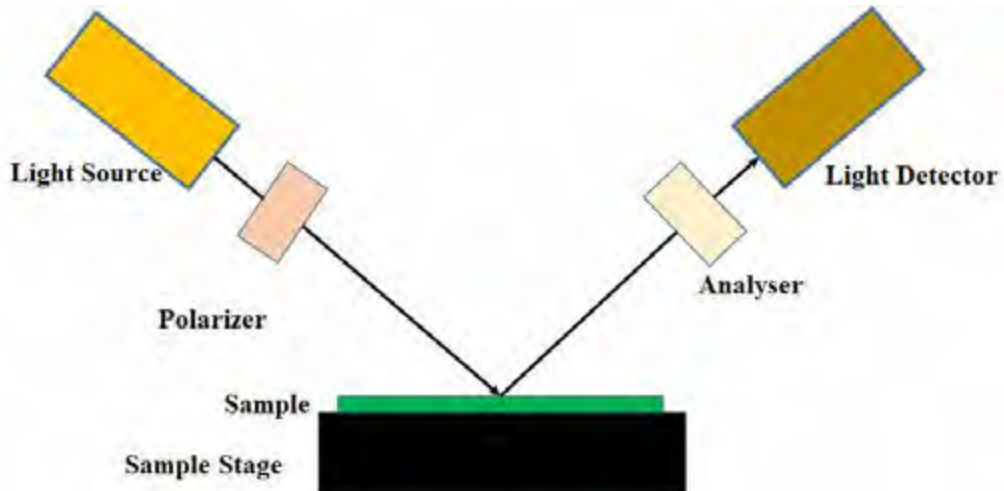


Figure 2.10 Typical schematic diagram and working principle of spectroscopic ellipsometer.

The system has a light source, i.e., xenon (Xe) arc lamp which is used to produce light in the wavelength range of 350-850 nm. The sampling point under the test sample, are focused manually on the sample stage (or chuck). The light from the Xe light source, passes through the polarizer is incident on the sample. The polarizer is used here to linearly polarize the incident light. The linearly polarized incident light, after interacting with the sample, reflects back and becomes elliptically polarized. The change in intensity and orientation of the reflected elliptically polarized light after interaction, are analysed through the analyser and light detector. This optical result generated through SE, is compared to the existing available model defined in the material library and fitted using the software provided with the system.

The system is capable of measuring the film property like  $T_{ox}$  and RI of the material. Such measurement was performed at very initial level of the experiment after film deposition to assess the thickness and uniformity. The RI value is noted and reported at wavelength,  $\lambda = 635$  nm. The value of RI can give qualitative information about film density and stoichiometry.

### (b) X-ray reflectometer

In this work, the Bruker make D8 DISCOVER diffractometer equipped with multilayer mirror used in X-ray reflectometer (XRR) mode for the measurement. This is a non-destructive measurement technique for extraction of film properties like thickness, surface roughness and film density [89]. The typical schematic diagram of XRR system is shown in Figure 2.11.

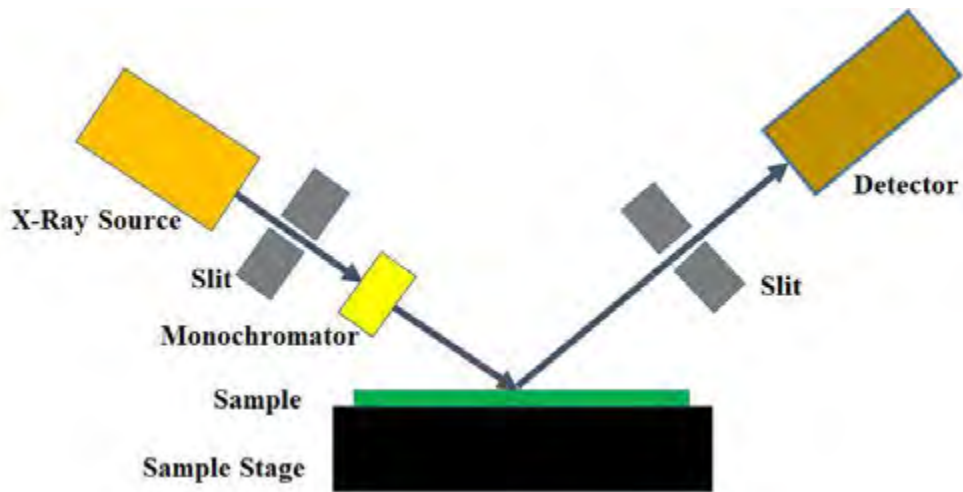


Figure 2.11 Typical schematic diagram and working principle of X-ray reflectometer.

The Cu K $\alpha$  X-ray source produce beam with photon energy  $E = 8047$  eV, which travels through the slit and monochromator to focus a narrow and parallel monochromatic beam on sample. In XRR, the beam is incident on sample at very small angles ( $< 0.5^\circ$ ), so as to probe into few nanometres at the surface. The reflected beam from the sample is collected through the slit to the detector. The main principle of XRR exists in total external reflection as a result of beam incident on the sample below the critical angle ( $\alpha_c$ ). Where the value of  $\alpha_c$  depends on material property such as electron density, the classical electron radius ( $r_e = 2.81 \times 10^{-18}$  m) and wavelength of X-ray beam. The X-ray beam after reflecting from the surface at grazing angle (i.e.,  $< \alpha_c$ ), produces total external reflection. The intensity of the reflected beam is normalized to the surface and plotted against the incident angle in the

logarithmic scale [89]. This reflectivity graph is fitted by using Parratt formalism to obtain the parameters such as film thickness, film density and surface roughness [90]. The intensity of oscillations in reflectivity graph gives information about the film thickness, i.e., more oscillations means thicker the film. While the film density is obtained through the amplitude of the oscillations in reflectivity graph, i.e., high amplitude of the oscillations means higher film density. The surface roughness is assessed through the decay of the reflectivity graph, i.e., fast decay in plot represents rough surface of the film.

### (c) Atomic force microscope

The atomic force microscope (AFM), used in this work is Veeco-Digital Instruments make Nanoscope IV. The system is used to assess the surface roughness and topography through the three dimensional image of the film surface [88]. The typical AFM setup, is shown in Figure 2.12.

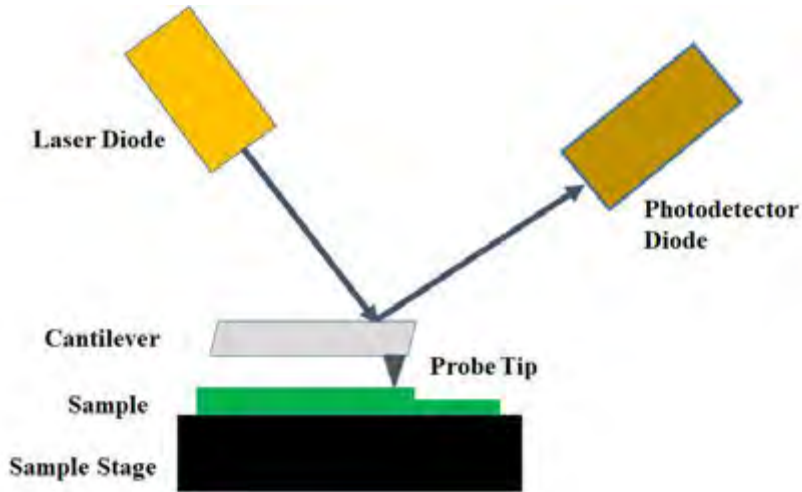


Figure 2.12 Typical schematic diagram of atomic force microscope.

As shown in Figure 2.12, the typical AFM system consists of a light source (laser diode), and probe tip attached to the cantilever and photodetector. The cantilever is typically made of Si or  $\text{SiN}_x$ , connected with a sharp probe tip. The cantilever is oscillated up and down close to its resonance frequency. When the probe tip with constant oscillation and frequency comes close to different surface, the electro-dynamic force of interaction between the probe tip and the surface starts to act. This interaction results in change in amplitude of cantilever's oscillation, and at the same time, the feedback controller is used to maintain the oscillation amplitude constant [88]. Thus an AFM image is generated using the intermittent contact between the probe tip and surface. The most commonly used AFM measurement technique is

beam-deflection type, as shown in Figure 2.12. The laser diode generated light beam incident on the cantilever, after interaction of probe tip and surface, the cantilever makes an angular displacement as per vertical and lateral movement of probe tip on sample. The light reflected from the cantilever is collected using the photodetector, and is used to detect the surface topography. The AFM works on both contact and contact-less mode. In this work we have used the contact mode to assess the topography of the sample surface.

#### (d) X-ray photoelectron spectroscope

In this work the X-ray photoelectron spectroscope (XPS) characterization system is used to assess the film and interfacial property in terms of film composition and elemental profile [88]. We have used Thermo-VG Scientific make Multilab 2000 XPS system for the measurements to be discussed in chapters 4 and 6, whereas ULVAC-PHI make, PHI 5000 Versa Probe-II for measurements to be discussed in chapter 5. The typical schematic diagram of XPS measurement system is shown in Figure 2.13.

As shown in Figure 2.13, the XPS system comprises of X-ray source, which is Mg K $\alpha$  source with photon energy of  $E = 1253.6$  eV, i.e., used in this work. The surface of sample placed in sample stage is irradiated with the X-ray beam using high energy photon, which is transferred to the core-level electrons. After this interaction the electron at core-level gets excited due to high energy photon and ejected with some kinetic energy (KE). These ejected electrons are known as photo emitted electrons. The KE of photo emitted electrons depends on the X-ray and binding energy (BE) of the atoms to the orbit. The electron detector at the receiving end, will analyse the BE of the atoms using the eq. (2.22),

$$BE = h\nu - KE - \varphi \quad (\text{eV}) \quad (2.22)$$

where,  $\varphi$  represents the work function that depends on the spectrometer and material.

By analysing the KE of the photo-emitted electrons from the atoms, the BE can be determined, which is a unique property of each element. Hence the type of elements in the film can be determined. The analyser in the system will provide the information on the different elements present in the sample surface. The resultant XPS spectrum is the plot between number of photo-emitted electrons and BE.

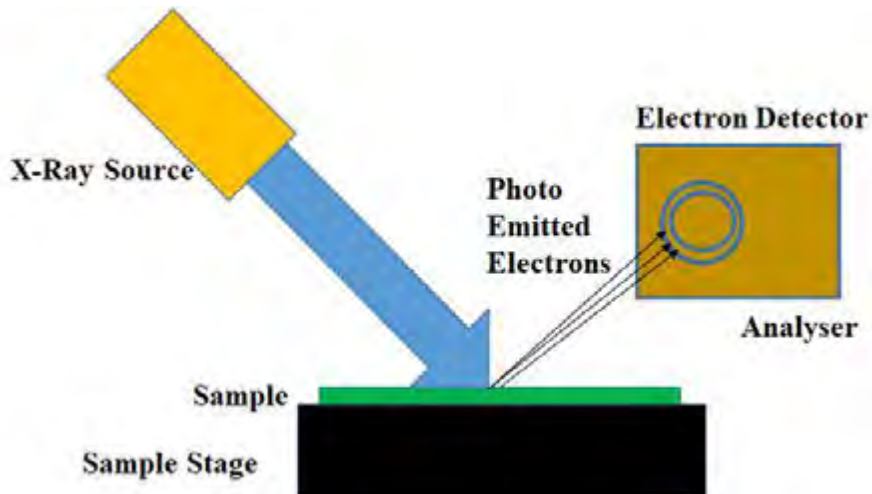


Figure 2.13 Typical schematic diagram and working principle of X-ray photoelectron spectrometer.

The XPS peaks are the characteristic peak of the elements present in film. To assess the chemical composition of the film, the area under these characteristic peak will be obtained with respect to each other to obtain the relative percentage of each element present in the film/volume of the material studied. The elemental depth profile is assessed by bombarding the surface with  $\text{Ar}^+$  ions at specific time and power, and obtaining the XPS spectrum after each bombardment steps. The depth profile consist of atomic concentration (%) of each elements plotted against depth (nm).

#### (e) Transmission electron microscope

In this work the JEOL make JEM 2100F, transmission electron microscope (TEM) was used for high resolution imaging of thin films to assess the crystalline and interfacial property. The typical schematic diagram of TEM system is shown in Figure 2.14 [88].

This system uses very high energy electron beam, which is incident into the ultra-thin sample. The interaction between these electrons and atoms results in some unscattered electron transmission, while some scattered electrons that are both elastic and inelastic in nature.

The unscattered electrons transmitted through the thin sample, were focused into an image plane through electromagnetic lens to create magnified image of the sample. This image shows the film properties such as thickness, interface, crystal orientation and grain boundaries [88].

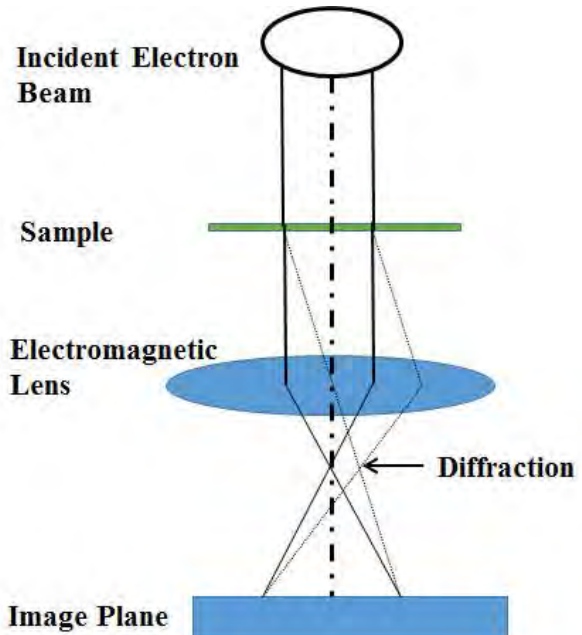


Figure 2.14 Typical schematic diagram and working principle of transmission electron microscope.

Since TEM operates on transmission of high energy electrons through the ultra-thin sample, therefore it requires a sample preparation method to achieve the sample thickness in the range of 100-150 nm for measurement.

The elastically scattered electrons were used to obtain the diffraction pattern of the sample to access information about crystal structure. These scattered electrons deflected in particular angle were focused in back-focal plane of the objective lens to form a diffraction pattern [88].

#### (f) Electron energy loss spectroscopy

The electron energy loss spectroscopy (EELS) is one of the operation mode in TEM system to obtain information about electronic state and chemical bonding in the film. In this work we have used FEI TITAN 80-300 kV TEM system at International Centre for Materials Science, Jawaharlal Nehru Centre for Advanced Scientific Research, Bengaluru. The system was operated in EELS mode and operated in extraction voltage of 300 kV, to acquire the measurements. As discussed in the previous section, when high energy electron beam incident on ultra-thin sample, some of the electrons gets transmitted (in TEM mode) through the sample while some gets scattered due to interaction with atoms. The inelastically scattered electrons cause loss of energy for an incident electrons on the sample. By collecting the

information on the number of electrons versus energy loss, the EELS spectrum is generated, which is compared with the known samples to determine the chemical bonding between elements [88,91].

In this work the zero-loss peak was removed from the EELS spectrum, by subtracting the reflected tail of the negative part of the zero-loss intensity. While the low-loss region between 1-50 eV in EELS spectrum, consists a series of broad features related to inelastic scattering with valence electron that is used to determine the  $E_{BG}$  in film. The EELS spectrum in the range of 50-200 eV, is known as energy loss near edge spectra (ELNES) which are “edges” due to electrons that lost energy in vacancies present in deep core-level of atoms. This corresponds to the binding energy of the respective shell which is used to determine the composition of the film [91].

### (g) Fourier transform infra-red spectroscope

In this work the Perkin Elmer make (Spectrum BX II), Fourier transform infra-red spectroscope (FTIR) was used to assess the chemical bonding of the material through infrared spectrum. The typical schematic diagram of FTIR spectroscope system is shown in Figure 2.15.

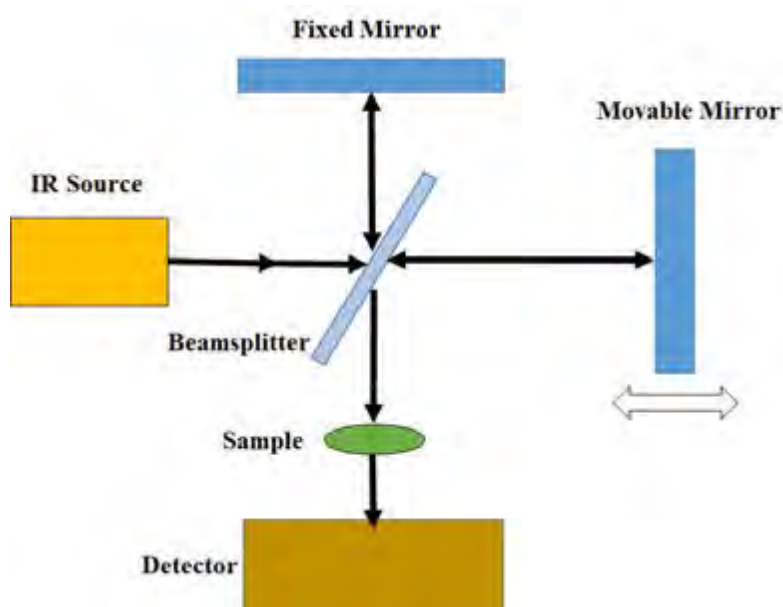


Figure 2.15 The typical schematic diagram of Fourier transform infra-red spectroscope.

Figure 2.15 shows, the FTIR system which comprises of an IR light source, a unit called Michelson interferometer and detector [88]. The Michelson interferometer unit consists

of beamsplitter, fixed mirror and moving mirror. The unit splits the light beam from IR light source into two separate beams, one of which is reflected by a fixed mirror and other by moving mirror. The process of beam splitting and combining after reflection from both the mirrors, create time difference in same optical path, hence the interference signals are generated. The mathematical Fourier transform method is applied on these interference signals to obtain the resultant spectra in terms of wave number. The main advantage of Michelson interferometer is that the resultant spectra were obtained with high accuracy and fast data acquisition. In this system broad-band IR radiation incidents on the sample, where some of the light gets reflected while other gets absorbed. The difference in intensity of light incident after interaction with sample, is plotted as function of wavelength. The absorbance spectrum is plotted against wave number ( $\text{cm}^{-1}$ ) in the range of 400 to 4000  $\text{cm}^{-1}$  in this work. The spectra shows different absorbance peaks at specific frequencies which is related to chemical bonding in the sample using Beer-Lambert Law, as given below in eq. (2.23) [88].

$$A = a(\lambda)bc \quad (2.23)$$

where,  $A$  represents absorbance,  $a (\lambda)$  represents wavelength dependent molar absorption coefficient ( $\text{L.mol}^{-1}.\text{cm}^{-1}$ ) and  $b$  represents path length (cm),  $c$  represents concentration of chemical bonds ( $\text{mol.L}^{-1}$ ). In absorbance spectrum, each absorbance peak at particular wavelength represents the characteristics of chemical bonding between the specific elements. And the broadness of absorbance peak is related to information about strong bonding between elements.

#### (h) Ultra violet-visible-near infrared spectroscope

In this work the Perkin Elmer make Lambda 950 model, ultra violet-visible-near infrared spectroscope (UV-Vis-NIR) is used to assess the  $E_{\text{BG}}$  of the film through the optical absorption spectrum generated by system. The typical block diagram of UV-Vis-NIR spectroscope showing different units in the system is shown in Figure 2.16.

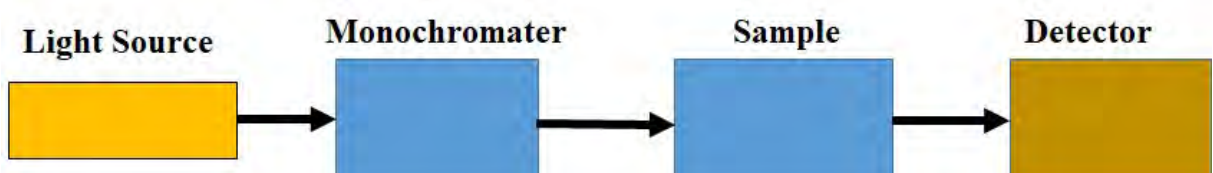


Figure 2.16 The typical block diagram of UV-Vis-NIR spectroscope showing different units in system.

As shown in Figure 2.16, the system comprises of light source to generate the light in the range of UV-Vis and NIR range as the name suggests. The light is then passed through a monochromator, which is used to send single wavelength light at a time to the sample by filtering out the others from light source. In this system, the sample holder is designed to hold one reference sample and one actual sample. The reference sample is normally the un-deposited piece of quartz wafer, while the actual sample has film deposited on other piece of same quartz wafer. In the detector, the change in intensity of light ( $I$ ) after interaction with the film is compared to the intensity of light from the reference sample ( $I_0$ ). The absorbance ( $A$ ) is defined by eq. (2.24) [92],

$$A = -\log \left( \frac{I}{I_0} \right) \quad (2.24)$$

The band-gap of the material is known as the difference between the minimum of conduction band and maximum of valance band in material. From the absorbance plot, the value of  $E_{BG}$  can be extracted using the Tauc method [93]. Under this method, the  $(\alpha E)^2$  is plotted against  $E$  and the line crossing the x-axis of the exponential gives the estimated  $E_{BG}$  of the film. Here  $\alpha$ , is defined as absorption coefficient given by eq. (2.25),

$$\alpha = \frac{A(hv - E_{BG})^n}{hv} \quad (\text{cm}^{-1}) \quad (2.25)$$

where,  $A$  is constant,  $E = hv$  represents the energy, which is Planck's constant ( $h$ ) multiplied by the frequency of vibration ( $v$ ) from the incident beam and  $n$  represents the index which is 1/2 for direct allowed transition material and 2 for indirect allowed transition material like silicon.

### 2.4.3 Opto-electronic characterization

Under opto-electronic characterization, we measure the minority carrier life-time ( $\tau$ ) of the film under study by optical means. This is carried out using Sinton WCT-120 system, which uses the quasi-steady-state photoconductance (QSSPC) method for measuring the  $\tau$  of film [11]. The typical schematic diagram of life-time measurement system is shown in Figure 2.17.

As shown in Figure 2.17, the system uses flash light source which causes a short and slow pulse from lamp to be incident on the sample through the IR pass filter. The minority carrier life-time of value  $< 100 \mu\text{s}$ , is measured using QSSPC mode with high accuracy, while moderate to high values were also measured effectively. The quasi-steady-state condition is

achieved by keeping the pulse time lower than  $\tau$ . The photo conductance decay w.r.t. time is measured using the inductive-coupled electronics attached inside sample stage, to determine the excess carrier density  $\Delta n$  using the following eq. (2.26) [94],

$$\Delta n = \frac{\Delta\sigma}{qW(\mu_n + \mu_p)} \quad (\text{cm}^{-3}) \quad (2.26)$$

where,  $\Delta\sigma$  represents excess photoconductance (S), W represents sample thickness (cm),  $\mu_n$  and  $\mu_p$  are electron and hole mobilities  $\{\text{cm}^2 \cdot (\text{V.s})^{-1}\}$ , respectively.

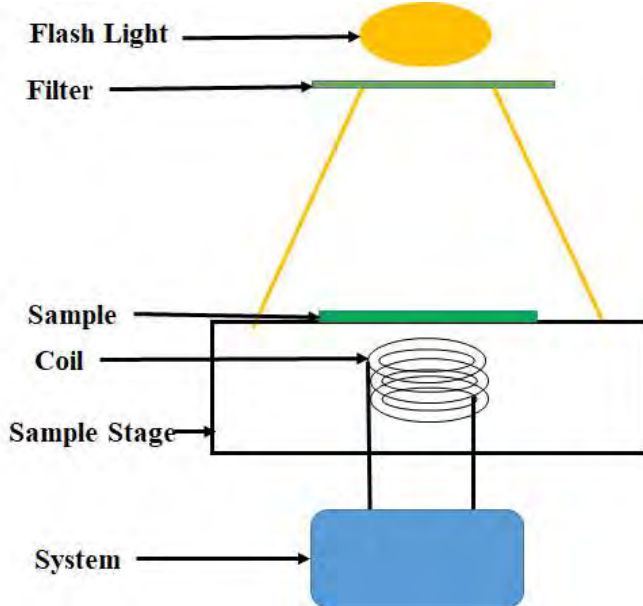


Figure 2.17 The typical schematic diagram of life-time measurement system [11].

The effective minority carrier lifetime  $\tau_{eff}$  (s) by QSSPC method, is assessed by using the following eq. (2.27),

$$\tau_{eff}(\Delta n) = \frac{\Delta n(t)}{G(t) - \frac{\partial \Delta n(t)}{\partial t}} \quad (\text{s}) \quad (2.27)$$

where,  $G(t)$  represents the generation rate for electron-hole pairs ( $\text{cm}^{-3} \cdot \text{s}^{-1}$ ), which is determined by using the light intensity on a calibrated detector,  $\Delta n(t)$  represents time-dependent average of excess carrier density. Since the  $\tau_{eff}$  is a measure of recombination at front & rear surfaces and bulk life-time, this is also defined as eq. (2.28),

$$\frac{1}{\tau_{eff}(\Delta n)} = \frac{1}{\tau_{bulk}(\Delta n)} + \frac{S_{front}(\Delta n) + S_{rear}(\Delta n)}{W} \quad (\text{s}^{-1}) \quad (2.28)$$

In eq. (2.28),  $S_{\text{front/rear}}$  are surface recombination velocities for front and rear surface and  $\tau_{\text{bulk}}(\Delta n)$  represents the bulk lifetime at  $\Delta n$ . When both the front and rear surfaces are passivated symmetrically with same film, the effective surface recombination velocity,  $S_{\text{eff}}$  can be determined using eq. (2.29) as given below [11,95],

$$S_{\text{eff}} = \frac{W}{2} \left( \frac{1}{\tau_{\text{eff}}} - \frac{1}{\tau_{\text{bulk}}} \right) \quad (\text{cm.s}^{-1}) \quad (2.29)$$

The same was also discussed in chapter 1, section 1.2. The  $\tau_{\text{bulk}}$  was measured on silicon wafer by immersing the wafer in Iodine-Methanol (IM) solution [95]. The solution was prepared with 1.18 g of Iodine mixing in 50 mL of Methanol. After having obtained the value of  $\tau_{\text{bulk}}$ , the  $S_{\text{eff}}$  can be determined by using eq. (2.29) at particular value of  $\Delta n$ , which is applicable for symmetrically passivated structure. This procedure for measurement of  $\tau_{\text{eff}}$  and determining  $S_{\text{eff}}$  is followed for all the experiments stated in this thesis. If there is any change in the procedure, it will be mentioned explicitly in the experiment section of the respective chapters.

## 2.5 Summary

In this chapter we have reviewed the existing literature on  $\text{AlO}_x$  film synthesized by different techniques and application of film as the surface passivation of c-Si wafers for solar cell applications. The typical values of  $S_{\text{eff}}$  and power conversion efficiencies achieved so far by  $\text{AlO}_x$  film synthesized using ALD, PECVD and RS technique are revised in this chapter. Also the review on film applied as rear or front passivation layer in p-type and n-type c-Si solar cells, respectively are documented. The typical values of fixed oxide charge and interface density that results in good passivation of silicon surface using  $\text{AlO}_x$  are also documented.

As discussed in section 2.3.3, the  $\text{AlO}_x$  film deposited using RS technique have already shown its applicability as surface passivation layer in solar cells. Since the technique uses Al metal target reactively sputtered in high purity Ar and  $\text{O}_2$  gases, makes it more viable for industrial application due to simple setup. As also discussed the RS  $\text{AlO}_x$  film is capable of passivating both n-type and p-type surface very effectively with  $S_{\text{eff}}$  of  $8 \text{ cm.s}^{-1}$  and  $35 \text{ cm.s}^{-1}$ , respectively [75,78]. The  $\eta$  of 20.1 % was measured on p-type PERC cell with rear surface passivated using RS  $\text{AlO}_x$  [79]. Hence with considering the applicability of this technique on solar industries, we have explored the development of high quality  $\text{AlO}_x$  film for

surface passivation of p-type c-Si. To further achieve the cost factor of the processing, the RS system with pulsed-DC power supply was used in this work. The details on the system will be discussed in the chapter 3. The work involves process development and optimization to achieve the good quality of surface passivation in terms of higher number of negative  $Q_f$  and low  $D_{it}$ , which are the most basic requirements to achieve the field-effect and chemical passivation, respectively by the film. Various characterization techniques viz. electrical, material and optical discussed in this chapter were used to access the film property.

In the next chapter, we will discuss the proposed work on the development and optimization of  $\text{AlO}_x$  films by using pulsed-DC RS technique. The various characterization and analysis of the results will be presented in chapter 3.

# **Chapter 3. Pulsed-DC Reactive Sputter Deposited AlO<sub>x</sub> Film**

## **3.1 Introduction**

In RS PVD technique, a high purity metal is sputtered by heavy ions in reactive gas ambient for deposition of compound film on the substrate [74]. This technique may have a remarkable importance in the field of solar cell industries due to the goals set to achieve green energy and provide cheaper energy to the peoples. The PECVD system was widely used in solar cell industries, as high-quality of surface passivation was reported by AlO<sub>x</sub> films deposited using this technique. However the PECVD technique used for film deposition may not full-fulfill the green energy criteria, as the TMA precursor with chemical composition of Al(CH<sub>3</sub>)<sub>3</sub> has carbon in it [96,97]. This chemical precursor is expensive and requires extra equipment for safe handling of such hazardous chemical. Hence adding all this to the cost of passivated solar cell. In one of the report by Dingemans et al., a cost-cutting solution to make ALD AlO<sub>x</sub> films cheaper was proposed by using low purity solar grade TMA precursor for solar cells [12]. Whereas the well-known RS technique uses pure metal and elemental gases for film deposition, could be advantageous due to potentially low cost for processing. As discussed in chapter 2, the RS AlO<sub>x</sub> films were also successfully implemented as surface passivation layer of c-Si solar cells [33,75,78]. The RS deposition systems discussed in reports are with RF power source that work at high frequency of 13.56 MHz and hence require an impedance matching network. While in this work we propose to use pulsed-DC

power supply source in RS deposition system, which works at relatively low frequencies and hence does not need an impedance matching network.

Even though ALD AlO<sub>x</sub> films have shown the better surface passivation quality with  $S_{eff} < 6 \text{ cm.s}^{-1}$  as compared to RS AlO<sub>x</sub> films with  $S_{eff} < 35 \text{ cm.s}^{-1}$  on p-type surface. These films were implemented and tested on the PERC solar cell structures as rear-surface passivation layer, that resulted in the  $V_{oc}$  of 662 mV and 651 mV, with corresponding cell  $\eta$  of 21.4 % and 20.1 % for ALD AlO<sub>x</sub> and RS AlO<sub>x</sub> film, respectively [33,98]. The advantage of RS technique, is high deposition rate and hence the processing would be faster as compared to ALD technique. In the subsequent sections of this chapter we will discuss in detail the pulsed-DC RS deposition technique with the process development to achieve high quality AlO<sub>x</sub> film.

## 3.2 Pulsed-DC reactive sputter deposition technique

In this work, AlO<sub>x</sub> film was deposited by sputtering of high purity aluminum target with 99.9995 % purity using Ar as sputtering gas and O<sub>2</sub> as reactive gas. Ar is used here as plasma source to generate heavy Ar<sup>+</sup> ions for sputtering of metal atoms from the target. Figure 3.1 (a) and (b) shows schematic diagram of typical sputter deposition system, and the pulsed-DC waveform of the power supply used this system, respectively.

The high purity Al target is connected to the cathode, where pulsed-DC power source supplies continuous negative and positive voltage pulses ( $V_p$ ) and the substrate is connected to the anode which is grounded. For this RS system during the negative voltage supply the target surface is sputtered in the reactive gas ambient for  $\tau_{ON}$  time, hence the compound film gets deposited on the substrate. Having a small positive voltage (i.e., pulse reversal) during the  $\tau_{OFF}$  time, causes neutralization of the built-up charges which is created due to the formation of dielectric compound layer on the metal target surface. With pulse reversal a continuous reactive sputtering of metal target is possible in an arc free environment, which is another advantage of using the pulsed-DC power supply [99,100]. The negative peak amplitude of  $V_p$  is 80 % of total  $V_p$  during  $\tau_{ON}$  time, whereas positive peak amplitude of  $V_p$  is 20 % of total applied voltage during  $\tau_{OFF}$  time. The voltage and current are the measure of applied process power, which is reported to determine the plasma condition inside chamber [74].

This system also has magnet connected to the chamber near the cathode that is used for the proper confinement of the plasma close to the substrate, hence deposition rate improves through secondary ionizations [101].

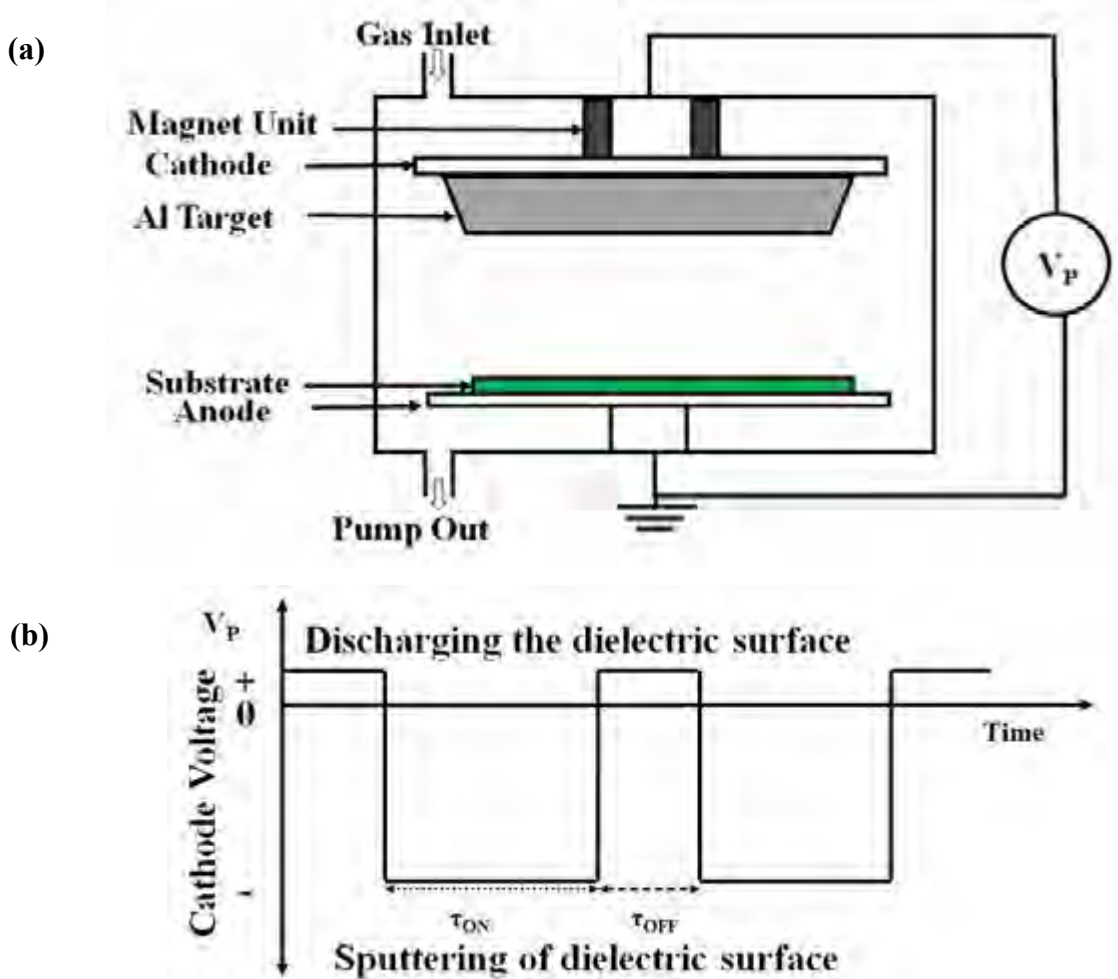


Figure 3.1 (a) Schematic diagram of the reactive sputtering system and (b) waveform of pulsed-DC power supply with  $V_p$ . Time  $\tau_{ON}$  is target surface sputtering time and  $\tau_{OFF}$  is the time when charges at the target surface get neutralized.

The pulsed-DC RS system with applied  $V_p$  is shown in Figure 3.1, the process development and optimization involves understanding the effect of various process variables in the system to achieve the required film quality by fine tuning them. In the following we will discuss various process parameters of the system with their impact on the film quality from the available reports.

### **(a) Process power**

The applied power during film deposition, cause direct impact on the rate of sputtering. With high process power, the rate of  $\text{Ar}^+$  ions hitting the target surface are high and cause more atoms to sputter off the target surface, hence increases the deposition rate. However with high power the roughness on the substrate surface also increases as the high energy accelerated  $\text{Ar}^+$  ions hit the surface as well [74]. In this report the process power is also referred as power density (PD) in  $\text{W.cm}^{-2}$ , i.e., applied power per unit area.

### **(b) Process time**

The process time is a measure of time during which the process power is applied to the metal target with process gas for reactive sputtering. Usually in PVD processes more process time is preferable as it allows the reactive species to settle down at the substrate surface and the incoming species could fill up the voids. The less process time may lead to porous film structure, which again depends on the applied process power [74].

### **(c) Process pressure**

The property of the reactive sputtered film may be varied by changing the process pressure during deposition. The process pressure is the measure of reactive  $\text{O}_2$  and sputter  $\text{Ar}$  gas flow rates inside chamber. In the reactive sputter deposition system, the gas composition (i.e., partial pressure) is very crucial element, as very low flow of  $\text{O}_2$  gas may lead to non-stoichiometric film while very high flow of  $\text{O}_2$  gas may lead to decrease in deposition rate due to poisoning of target [99]. The study also shows, for low process pressure the deposited film can have high compressive stress whereas with high process pressure this stress can be tensile [102].

### **(d) Substrate temperature**

In the pulsed-DC RS system the substrate temperature can be varied between the room temperature to 320 °C. The property of the film can also be changed with high temperature deposition, as with heated surface the knock-on atoms penetrates deep into the film and trapped into interstitial and vacancies which results in the denser film [74,103]. However at very high temperature the back-sputtering of the deposited film may also occur which may results in peeling-off of the film from substrate after deposition [74].

### (e) Pulsed-DC power supply

As shown in Figure 3.1 (b), the pulsed-DC type power supply used in this system, also has several variables for process optimization such as, pulse frequency, pulse reversal time and duty cycle. The optimal pulse frequency depends on the type of material to be sputtered. Keeping very low pulse frequency may damage the deposited film due to arcing in the chamber by formation of thick insulating layer at the metal target surface. The term  $\tau_{ON}$  is the time corresponds to sputtering of the target surface with negative power supplied to cathode and  $\tau_{OFF}$  is the time corresponds to positive power supplied to the cathode to compensate the surface charges which built-up during the reactive sputtering. The  $\tau_{OFF}$  is also known as reverse time. The optimal value of pulse reversal should be selected, since large duration of  $\tau_{OFF}$ , may cause the  $\text{Ar}^+$  ions to get repelled from the cathode and cause damage in deposited film on substrate [99,100]. The term duty cycle (%) is defined as the ratio of  $\tau_{ON}$  to total time ( $\tau_{ON} + \tau_{OFF}$ ). The pulsed-DC power supply variables are kept constant as pulse frequency = 100 kHz, reverse time = 3  $\mu\text{s}$  and duty cycle = 70 %, for all the experiments carried out in this work.

The development and optimization of process was carried out by varying various parameters as discussed above for good quality  $\text{AlO}_x$  film deposition. The quality of the film for different process variables are assessed using material characterization and electrical characterization, which will be discussed in subsequent sections.

## 3.3 Experimental details

The  $\text{AlO}_x$  film was deposited on  $5 \Omega\cdot\text{cm}$  p-type CZ c-Si (100) wafers by pulsed-DC RS technique in PVD chamber of Applied Materials ENDURA cluster tool. The wafers were cleaned using standard RCA cleaning process before film deposition, as discussed in chapter 2, section 2.4.1. The process chamber was pumped down to the base pressure of  $7 \times 10^{-8}$  torr before film deposition. For electrical characterization, the MOS capacitor structures were fabricated with the thermally evaporated Al using shadow mask of diameter of 200  $\mu\text{m}$  as top metal gate and blanket Al was evaporated on backside for back contact. These MOS capacitors were subsequently subjected to FGA (5 %  $\text{H}_2$  in  $\text{N}_2$ ) at 420 °C for 20 min to improve the metal-semiconductor contact resistance and also the film quality may improve with reduction of dangling bonds using hydrogen atoms. This process is also known as post-metallization annealing (PMA). During the  $\text{AlO}_x$  film deposition certain power supply

parameters were kept constant as discussed in previous section. The process variable such as process power, gas flow and deposition time for experiments are mentioned explicitly in the respective section of this chapter.

### 3.4 Hysteresis behaviour

The behaviour of the cathode voltage in the RS system was observed as the reactive O<sub>2</sub> gas flow rate was varied from minimum to a certain value and subsequently retracing the flow to the minimum value. Figure 3.2 shows the hysteresis behavior observed at three different applied process PD namely: 0.69, 1.3 and 2.07 W.cm<sup>-2</sup>. The O<sub>2</sub> flow was varied from 5 sccm onwards by keeping Ar flow rate constant at 10 sccm during these process. The cathode voltage was monitored directly from the system. This process was carried out at room temperature. The plot of cathode voltage versus O<sub>2</sub> flow rate is shown in Figure 3.2 for different PD.

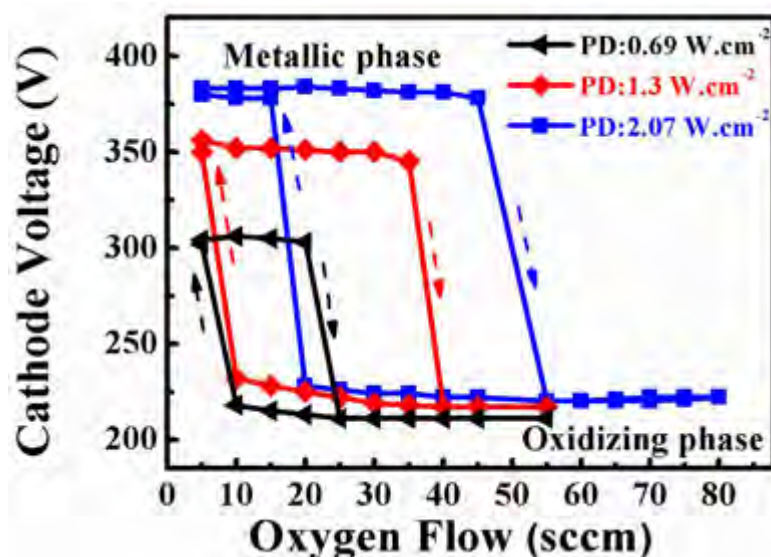


Figure 3.2 Hysteresis behaviour of cathode voltage as a function of oxygen (O<sub>2</sub>) flow rate for different PD conditions in pulsed-DC RS system. The arrows indicate the forward and reverse direction of variation of O<sub>2</sub> flow.

In the pulsed-DC RS system the metal target retains its metallic property at low O<sub>2</sub> flow as the reactive species concentration in the chamber is still low. As the O<sub>2</sub> flow increases, the target surface starts to react with O<sub>2</sub> resulting in the formation of compound oxide layer at the target surface. This oxide layer would be charged by electrons from the plasma and hence causes a sudden drop in the cathode voltage. The initial target condition

with high cathode voltage is called “metallic phase” and sudden drop in the cathode voltage is called “oxidized phase” in forward direction of O<sub>2</sub> flow as shown in Figure 3.2. During the retrace, i.e., lowering of the O<sub>2</sub> flow rate in reverse direction, it is observed that the cathode voltage remains low until the oxide layer on the target surface gets completely sputtered-off. As the O<sub>2</sub> flow becomes sufficiently low the cathode voltage rises back to the initial high value, i.e., the target surface regains the metallic property with very low or almost no availability of any reactive gas species [100,101,104]. Since the critical O<sub>2</sub> flow for the reverse direction in the hysteresis curve is less than the forward direction, a hysteresis behavior is observed.

In the RS system, the AlO<sub>x</sub> film deposition is carried out in the oxidized phase with low cathode voltage value in the forward direction of the hysteresis curve, where the O<sub>2</sub> flow rate value is chosen close to the knee point for stable film deposition [99,101]. As shown in Figure 3.2, the critical O<sub>2</sub> flow required for film deposition is observed to be different for different process power. At high deposition power a high rate of O<sub>2</sub> flow is required to get the oxide film deposition.

## 3.5 Material characterization

To obtain the material characteristics, the following systems were used: Sentech SE-800 for thickness and RI measurement, Bruker D8 discover diffractometer used in XRR mode to obtain film density, thickness and surface roughness of the film, Thermo VG scientific make Multilab 2000 XPS was used in the surface scanning mode to obtain the film composition, Veeco-Digital Instruments (Nanoscope IV) AFM was used for measuring surface roughness of the film in contact mode. The results of these analysis are discussed in the subsequent sections.

### 3.5.1 Film density and surface morphology

The film density and morphology were obtained for the AlO<sub>x</sub> film deposited at three different PD viz. 0.69, 1.3 and 2.07 W.cm<sup>-2</sup>. The deposition time for these are kept same at 300 s for all the experiments. These films are annealed in RTP system at 900 °C in oxygen ambient for 1 min. Figure 3.3 (a) and (b), shows the thickness and RI of films measured using SE, respectively.

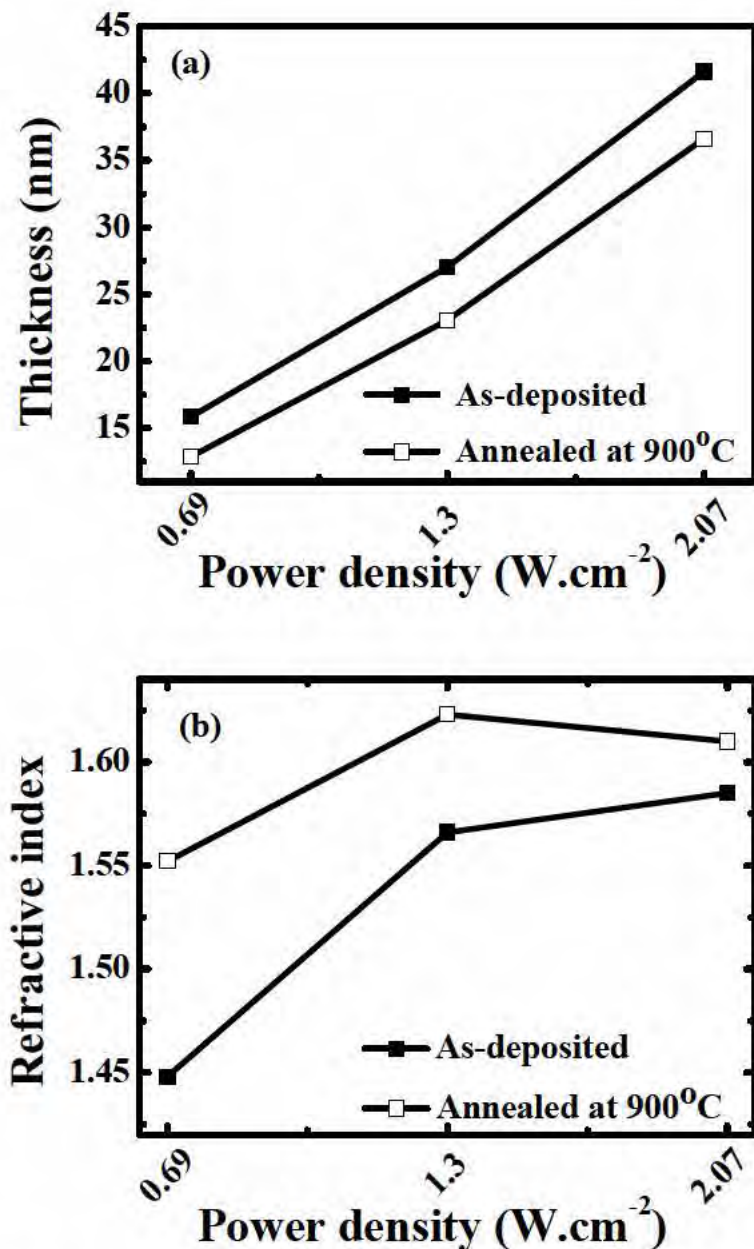


Figure 3.3 (a) Thickness and (b) RI of as-deposited and annealed  $\text{AlO}_x$  film deposited at different PD.

From Figure 3.3 (a), the deposition rate can be deduced using film thickness which shows a linear increase in deposition rate with process power. The high deposition rate of  $8 \text{ nm}.\text{min}^{-1}$  was obtained for film deposited at high PD of  $2.07 \text{ W.cm}^{-2}$ . The thickness of the annealed film is reduced by 4 nm than as-deposited film, which is consistent for each process PD depositions. In Figure 3.3 (b), the RI of these films increases after annealing, which signifies an increase in film density. After annealing the value of  $\text{RI} = 1.62$  was measured at a wavelength of  $632.8 \text{ nm}$  using SE, on high PD deposited film. The RI observed here is lower

than that reported for crystalline  $\text{Al}_2\text{O}_3$  film, i.e.,  $\text{RI} = 1.76$  at  $632.8 \text{ nm}$  [105]. However for solar cell applications the value of  $\text{RI} = 1.62$  that is typical value for amorphous  $\text{AlO}_x$  films, is acceptable [12].

The film density and surface roughness for different film deposited at different PD were assessed using XRR system using  $\text{Cu K}\alpha$  energy source ( $E = 8047 \text{ eV}$ ). The result was further analysed using Parratt formalism to extract the surface roughness and thickness of as-deposited  $\text{AlO}_x$  film from the reflectivity graph [90], are shown in Figure 3.4.

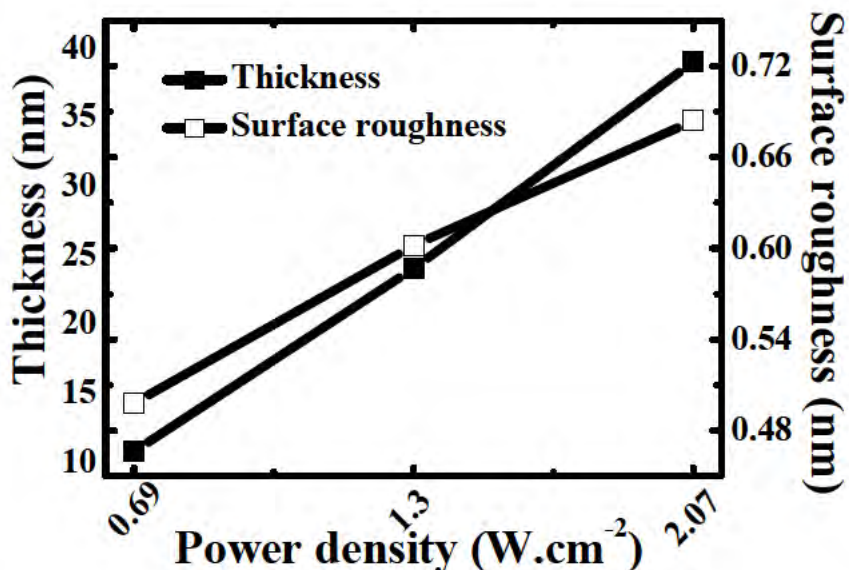


Figure 3.4 Surface roughness and thickness of as-deposited  $\text{AlO}_x$  film measured by XRR and extracted using Parratt formalism for different PD conditions.

The  $\text{AlO}_x$  film thickness and surface roughness seem to increase almost linearly with process power. The increase in surface roughness with power, may be due to the fact that high power cause fast collisions of the ions onto the substrate with high energy and hence leads to more damage on the film surface [74]. We have noticed here, the thickness of film measured by XRR shows about 3 nm less value as compared to the thickness obtained by SE measurement, as in Figure 3.3 (a). Such difference in thicknesses measured using these techniques was also reported by Wasserman et al. [106]. The thickness measured using SE is obtained from the shape and intensity of elliptically polarized light reflected from the interface separating the two mediums with different RI and in XRR technique, the difference in two interfaces separated by different electron densities were measured [107].

The film density for pulsed-DC RS AlO<sub>x</sub> film deposited at different PD conditions, obtained using XRR measurement for as-deposited and annealed film in RTP at 900 °C for 1 min, are shown in Figure 3.5.

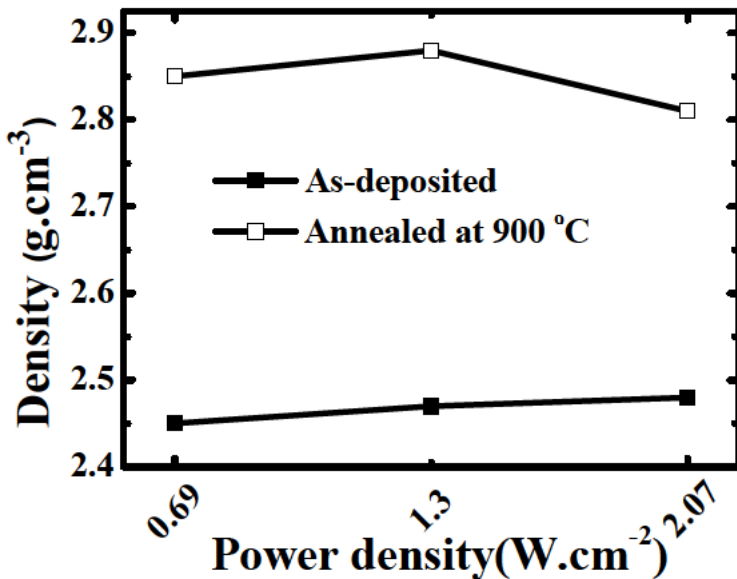


Figure 3.5 The film density for AlO<sub>x</sub> obtained by XRR measurement using Parratt formulism for film deposited at different PD.

The value of film density seems independent of process power, however the density seems to increase after annealing. The film density for as-deposited AlO<sub>x</sub> = 2.45 g.cm<sup>-3</sup>, increases to 2.88 g.cm<sup>-3</sup> after annealing. This result is in line with the RI values obtained for the annealed film as shown in Figure 3.3 (b), i.e., an increase in RI values relating to improvement in the film density after annealing. The value of film density for this film is relatively lower than the reported values for crystalline stoichiometric Al<sub>2</sub>O<sub>3</sub> film which is between 3.95-4.1 g.cm<sup>-3</sup> [108].

The surface morphology for this film was also obtained using Veeco-Digital Instruments (Nanoscope IV) make AFM for film deposited at low PD of 0.69 W.cm<sup>-2</sup>. The surface roughness measured in contact mode for films deposited at different gas flow ratios, viz. with Ar:O<sub>2</sub> flow ratios of 2:5 and 3:5, are shown in Figure 3.6 (a) and (b), respectively.

The film deposited at low power shows very good surface with roughness value of root mean square (RMS) = 3.2 Å, as shown in Figure 3.6 (a), for Ar:O<sub>2</sub> flow ratio of 2:5, i.e., Ar = 10 sccm and O<sub>2</sub> = 25 sccm.

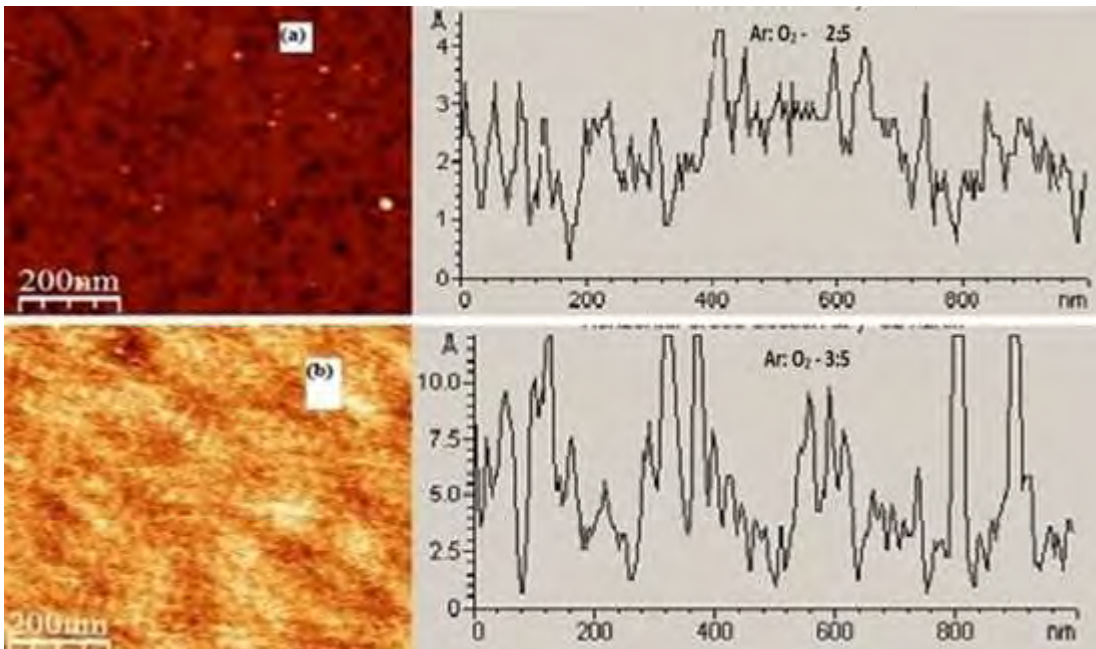


Figure 3.6 Contact mode AFM measurement of  $\text{AlO}_x$  films deposited with  $\text{Ar}:\text{O}_2$  flow ratio of (a) 2:5 and (b) 3:5, and PD of  $0.69 \text{ W.cm}^{-2}$ .

In Figure 3.6 (b), an increase in surface roughness to RMS value of  $10 \text{ \AA}$  with increase in  $\text{Ar}:\text{O}_2$  flow ratio of 3:5, i.e.,  $\text{Ar} = 15 \text{ sccm}$  and  $\text{O}_2 = 30 \text{ sccm}$ , is observed. Since an increase in Ar flow, may cause more  $\text{Ar}^+$  ions bombarding the surface, hence may results in relatively higher roughness of the deposited film. The roughness values obtained using AFM technique is lower as compared to result obtained from XRR measurement, since the surface morphology obtained by AFM is in contact mode whereas by XRR measurement the extracted roughness values depend mostly on the Parratt model fitting, hence the surface morphology obtained using AFM technique is more reliable.

### 3.5.2 Film composition

The composition of the film was measured by Thermo VG Scientific make Multilab 2000 XPS using  $\text{Mg K}\alpha$  radiation source (1253.6 eV). The XPS measurement was done on  $\text{AlO}_x$  film deposited at low PD of  $0.69 \text{ W.cm}^{-2}$  for different  $\text{O}_2$  gas flow of 25 sccm and 30 sccm, keeping Ar flow of 10 sccm constant for both experiments. The  $\text{Al 2p}$  and  $\text{O 1s}$  spectra of XPS measurements are shown in Figure 3.7 (a) and (b), respectively.  $\text{Al 2p}$  and  $\text{O 1s}$  spectra along with Gaussian curve fitting for single peak after baseline correction are shown in Figure 3.7. The fitted curve is shown as smooth blue colored lines in both the figures.

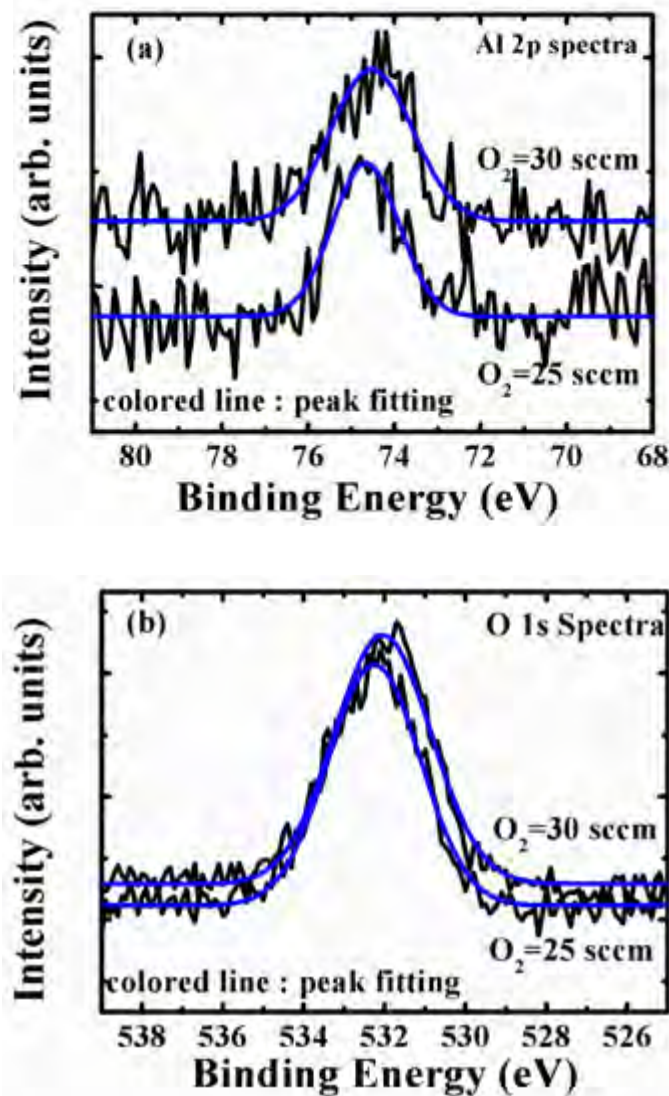


Figure 3.7 (a) Al 2p spectra (b) O 1s spectra of  $Al_xO_y$  films for different  $O_2$  flow ratio measured using XPS.

The O/Al ratio of 1.48 was observed for  $AlO_x$  film deposited using Ar: $O_2$  ratio of 2:5 (i.e.,  $O_2 = 25 \text{ sccm}$  and Ar = 10 sccm) which seems to be closer to stoichiometric  $Al_2O_3$  film. This value of  $O_2 = 25 \text{ sccm}$ , is slightly higher than the knee point in the forward direction of  $O_2$  flow on the hysteresis curve for film deposited at low PD of  $0.69 \text{ W.cm}^{-2}$ , as shown in Figure 3.2. The O/Al ratio of 1.7 was observed for Ar: $O_2$  ratio of 1:3 (i.e.,  $O_2 = 30 \text{ sccm}$  and Ar = 10 sccm), this means the film became O rich with higher  $O_2$  flow rate during deposition.

In conclusion the deposited film would achieve stoichiometric  $Al_2O_3$ , if the  $O_2$  flow rate is chosen close to the knee point in the forward sweep of hysteresis plot. A similar trend

was also reported by Olsson et al., with stoichiometric  $\text{Al}_2\text{O}_3$  film was achieved when deposition was carried out in oxidized mode close to knee point [109].

### 3.5.3 Deposition rate and optical property

The thickness and RI of the film were measured using Sentech SE-800 followed by curve fitting using SpectraRay software by Sentech GmbH. Figure 3.8 shows, the deposition rate and RI obtained for  $\text{AlO}_x$  film deposited at PD of  $0.69 \text{ W.cm}^{-2}$  with different  $\text{O}_2$  flow.

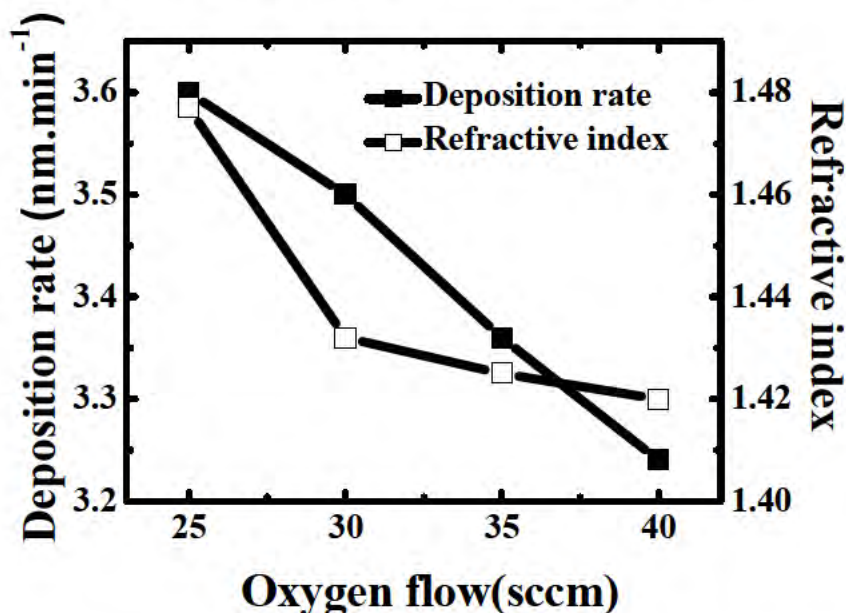


Figure 3.8 Deposition rate and RI of  $\text{AlO}_x$  film for different  $\text{O}_2$  flow rate, keeping the Ar flow constant at 10 sccm and PD at  $0.69 \text{ W.cm}^{-2}$ .

The deposition rate is observed to be decreasing with increase in  $\text{O}_2$  flow rate. The increase in reactive gas flow increases the process pressure inside the chamber during deposition, which causes a decrease in mean free path and hence the rate of sputtering. Another reason also supports result of the decrease in deposition rate, as the high reactive gas ( $\text{O}_2$ ) inside the chamber makes the metal target surface to oxidize by formation of compound layer and hence secondary electron emission coefficient is higher, which further decrease the sputtering of metal surface as the compound surface lowers the reaction at the target [74,101]. The RI of 1.478 is observed for  $\text{Ar}:\text{O}_2$  of 2:5, whereas the value of RI goes down a little for higher  $\text{O}_2$  flow. This may be due to changes in the composition of the film or the density of the film.

### 3.6 Electrical characterization

To assess the electrical properties of the film, MOS capacitors were fabricated with AlO<sub>x</sub> film deposited under the process conditions mentioned in section 3.3. The high frequency C-V measurements (at  $f = 100$  kHz) of MOS capacitors were carried out using Keithley 4200 semiconductor characterization system, and the results are shown in Figure 3.9. The AlO<sub>x</sub> film  $T_{ox}$  of 18 nm was measured using SE for film deposited at PD of  $0.69 \text{ W.cm}^{-2}$  with Ar:O<sub>2</sub> of 2:5 and deposition time of 300 s.

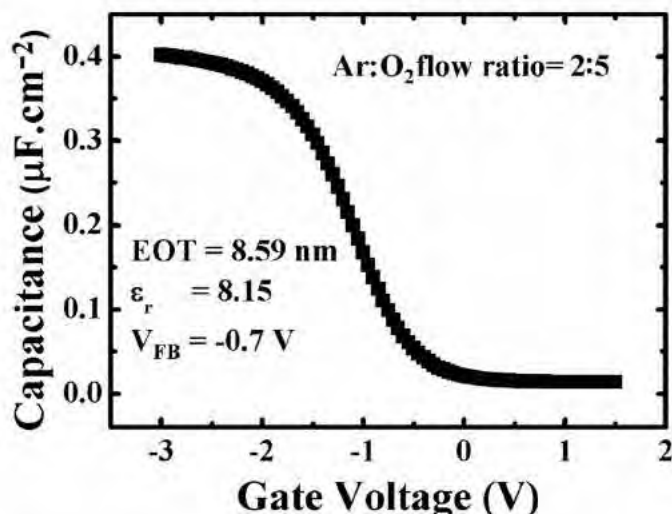


Figure 3.9 High frequency C-V characteristics curve of a typical MOS capacitor for AlO<sub>x</sub> film deposited at PD of  $0.69 \text{ W.cm}^{-2}$  and Ar:O<sub>2</sub> flow of 2:5.

Various parameters extracted from the high frequency C-V plot, are dielectric constant of AlO<sub>x</sub> film  $\epsilon_{r,\text{AlO}_x} = 8.15$  and EOT = 8.59 nm, obtained using eq. (2.5) and eq. (2.7), respectively [86]. The value of  $V_{FB} = -0.7$  V is extracted using different parameters of high frequency C-V using eq. (2.12) to eq. (2.14), in chapter 2.

The high frequency C-V measurement of AlO<sub>x</sub> film deposited at two different PD of  $0.69 \text{ W.cm}^{-2}$  and  $1.3 \text{ W.cm}^{-2}$  are shown in Figure 3.10. The film deposited at O<sub>2</sub> = 25 sccm for PD of  $0.69 \text{ W.cm}^{-2}$  and O<sub>2</sub> = 55 sccm for PD of  $1.3 \text{ W.cm}^{-2}$ , i.e., close to knee point on hysteresis curve for respective power as shown in Figure 3.2, while keeping Ar flow = 10 sccm for both conditions. The deposition time was kept 300 s for both the experiments. The inset in Figure 3.10, shows the normalized C/C<sub>acc</sub> curves. The shift in  $V_{FB}$  values is observed more towards the positive value for high process power (i.e., PD of  $1.3 \text{ W.cm}^{-2}$ ) as compared to PD of  $0.69 \text{ W.cm}^{-2}$  for AlO<sub>x</sub> film deposition.

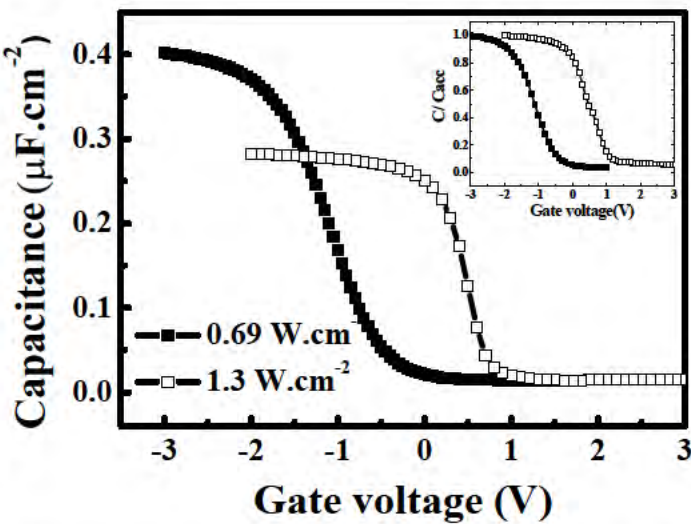


Figure 3.10 High frequency C-V plot of  $\text{AlO}_x$  MOS capacitor with films deposited at PD of  $0.69 \text{ W.cm}^{-2}$  and  $1.3 \text{ W.cm}^{-2}$ . The inset shows the normalised  $C/C_{\text{acc}}$  curve for both conditions to assess shift in  $V_{\text{FB}}$ .

The  $Q_f$  values can be extracted using eq. (2.15) from high-frequency C-V curve, by assessing the  $\Delta V_{\text{MG}}$  [86], as discussed in chapter 2, section 2.4.1. The values of EOT,  $\epsilon_{\text{r-AlO}_x}$ ,  $V_{\text{FB}}$  and negative  $Q_f$  extracted from the high frequency C-V measurement at different PD conditions are given in Table 3.1.

Table 3.1 The extracted values of EOT,  $\epsilon_{\text{r-AlO}_x}$ ,  $V_{\text{FB}}$  and  $Q_f$  from high frequency C-V measurement for  $\text{AlO}_x$  film deposited at different PD.

Power density ( $\text{W.cm}^{-2}$ )	EOT (nm)	$\epsilon_{\text{r-AlO}_x}$	$V_{\text{FB}}$ (V)	Negative $Q_f$ ( $\text{cm}^{-2}$ )
0.69	8.59	8.15	-0.7	$3.5 \times 10^{11}$
1.3	12.44	8.93	0.8	$2.88 \times 10^{12}$

The as-deposited film at high PD of  $1.3 \text{ W.cm}^{-2}$  has more negative  $Q_f$  of  $2.88 \times 10^{12} \text{ cm}^{-2}$  as compared to low PD deposited film which has negative  $Q_f$  of  $3.5 \times 10^{11} \text{ cm}^{-2}$ . The value of negative  $Q_f$  of  $1.7 \times 10^{12} \text{ cm}^{-2}$  for as-deposited  $\text{Al}_2\text{O}_3$  film by PECVD process was reported by Kania et al. [67]. The increased  $Q_f$  to  $3.1 \times 10^{12} \text{ cm}^{-2}$  was shown after annealing in FGA at  $425 \text{ }^{\circ}\text{C}$  for 25 min for this PECVD  $\text{AlO}_x$  film. In our case the as-deposited film deposited at PD of  $1.3 \text{ W.cm}^{-2}$  shows negative  $Q_f$  of  $2.88 \times 10^{12} \text{ cm}^{-2}$ , which is comparable to

those reported by PECVD AlO<sub>x</sub> film after PDA. Hence pulsed-DC RS AlO<sub>x</sub> film deposited at PD of 1.3 W.cm<sup>-2</sup>, shows an applicability as surface passivation layer on p-type surface of c-Si solar cells by field-effect passivation mechanism.

The film was also tested for robustness and leakage using I-V measurement of MOS capacitors, by application of gate voltage sweeps. The film was deposited at PD of 0.69 W.cm<sup>-2</sup> with Ar:O<sub>2</sub> flow ratio of 2:5 and deposited time of 300 s. The I-V measurements were performed on 20 different devices on the same wafer and the breakdown voltage was noted for each device. The Weibull distribution plot of E<sub>BD</sub> is shown in Figure 3.11 (a). In Figure 3.11 (b), the gate current density versus gate voltage (J-V) plot is shown for one of the MOS capacitors to assess the leakage current.

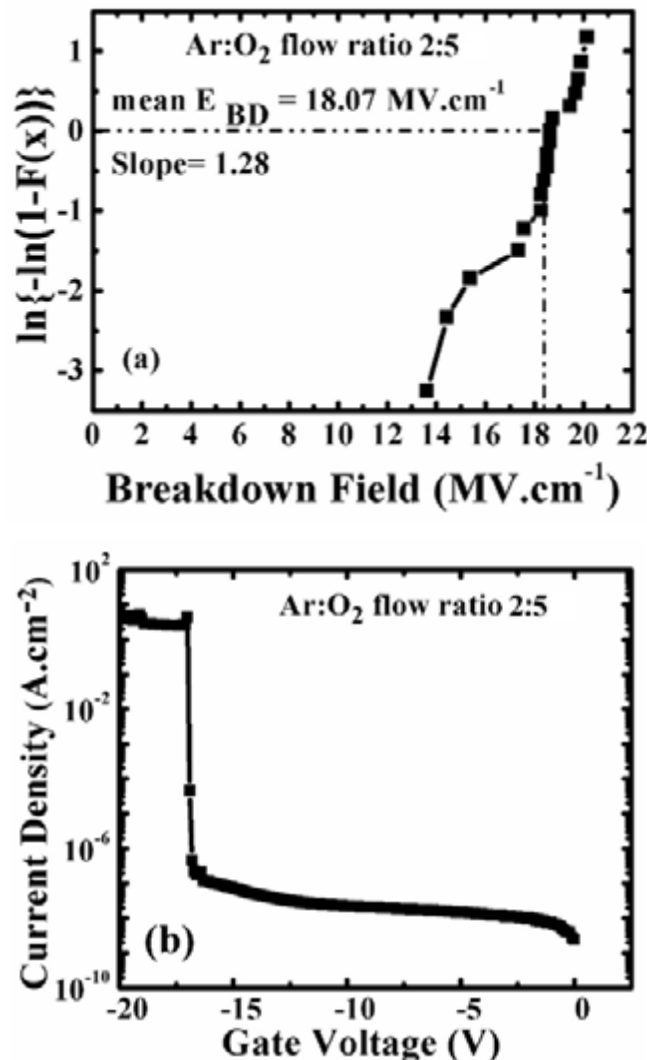


Figure 3.11 (a) Weibull distribution plot of E<sub>BD</sub> and (b) J-V plot for MOS capacitor with AlO<sub>x</sub> film deposited using Ar:O<sub>2</sub> gas flow ratio of 2:5.

In this work with the film deposited using 70 % O<sub>2</sub> flow ratio, we have obtain mean E<sub>BD</sub> of 18.07 MV.cm<sup>-1</sup> for film thickness of 17.97 nm (EOT = 8.59 nm), as shown in Figure 3.11 (a). An E<sub>BD</sub> of 7.4 MV.cm<sup>-1</sup> was reported by Seino et al. for pulsed-DC RS AlO<sub>x</sub> film, with film physical thickness of 50 nm and deposited using 70% O<sub>2</sub> flow ratio [110]. The comparison of E<sub>BD</sub> values for respective EOT obtained and reported by various RS deposition techniques and metal-organic chemical vapor deposition (MOCVD) technique are given in Table 3.2 [111,112].

Table 3.2 Comparison of the E<sub>BD</sub> for AlO<sub>x</sub> film deposited using different methods from the published report.

Reference	Deposition method	EOT (nm)	E <sub>BD</sub> (MV.cm <sup>-1</sup> )
[112]	MOCVD	5.5	19.3
	RF reactive sputtering	6.3	14.1
[110]	Pulsed-DC reactive sputtering	*50	**7.4
This work	Pulsed-DC reactive sputtering	8.59	18.07

\*Physical thickness

\*\*Breakdown field = breakdown voltage/physical thickness

The E<sub>BD</sub> obtained by our optimized process with low power deposition is comparable to the values reported for films deposited by MOCVD Al<sub>2</sub>O<sub>3</sub> film and is better than the RS deposited Al<sub>2</sub>O<sub>3</sub> film [111,112]. From Figure 3.11 (b), low leakage current density of  $3 \times 10^{-9}$  A.cm<sup>-2</sup> is observed at gate voltage of -5 V for the film with EOT of 8.59 nm, which is similar to the leakage current obtained for MOCVD deposited stoichiometric Al<sub>2</sub>O<sub>3</sub> films [111]. This film was applied as inter-poly dielectric (IPD) layer in the flash memory applications [111]. Thus the film developed during the thesis and reported in this chapter may be also implemented as IPD layer for flash memory applications [113].

### 3.7 Summary

In this chapter we have reported the development and optimization of process for deposition of AlO<sub>x</sub> film using a pulsed-DC RS technique. The various material and electrical characteristics were used towards the optimization of the process. The electrical properties measured for the film indicate its potential to be applied as surface passivation layer on p-type

c-Si surface with high negative  $Q_f$  of  $2.88 \times 10^{12} \text{ cm}^{-2}$  when deposited at high power (i.e., PD = 1.3 W.cm<sup>-2</sup>). With the low PD optimized process, a stoichiometric Al<sub>2</sub>O<sub>3</sub> film were obtained at O<sub>2</sub> flow rate chosen close to knee point at forward hysteresis behaviour of the system. The same process have shown mean E<sub>BD</sub> of 18.07 MV.cm<sup>-1</sup> and dielectric constant  $\epsilon_{r-AlOx}$  of 8.15 for EOT of 8.59 nm for this AlO<sub>x</sub> film. The film may be also applied as IPD layer in flash memory applications due to low leakage and high breakdown field. The high deposition rate at high PD deposition, makes pulsed-DC RS technique a suitable choice for industrial purpose. This technique makes an attractive low cost option. In the subsequent chapters we will discuss in detail the pulsed-DC RS AlO<sub>x</sub> film applicability for the surface passivation of p-type c-Si using suitable characterization techniques. The impact of various process parameters and PDA process on the film and interface quality will be analysed and discussed with the use of more sophisticated measurement tools.

## **Chapter 4. Optimization of Post-Deposition Annealing for the Improvement of Passivation**

### **4.1 Introduction**

One of the mechanisms for surface passivation by  $\text{AlO}_x$  film on p-type silicon is the repulsion of electrons from the surface by the negative  $Q_f$  present in the  $\text{AlO}_x$  film, causing field-effect passivation. An improvement in interface quality during deposition or after PDA process leads to reduction in number of  $D_{it}$ , causing chemical passivation and hence further improves the surface passivation quality [35,45]. The origin of negative  $Q_f$  in  $\text{Al}_2\text{O}_3$  film was proposed by Kimoto et al., which says the presence of both  $T$  and  $O$  coordinated Al in the  $\gamma\text{-Al}_2\text{O}_3$  film and  $T$  coordinated Al are present at the  $\text{Al}_2\text{O}_3/\text{c-Si}$  interface [42]. The films were deposited by ALD process on c-Si wafer and the Al-coordination was probed using EELS [42]. On the other hand Hoex et al. reported, an increase in negative  $Q_f$  in PA-ALD  $\text{Al}_2\text{O}_3$  film after PDA, due to the formation of a very thin ( $\sim 2$  nm) interfacial oxide ( $\text{SiO}_2$ ) layer at  $\text{Al}_2\text{O}_3/\text{c-Si}$  interface [44]. From the published reports, the necessity of PDA process for enhancing the passivation effect by  $\text{AlO}_x$  film synthesized using different techniques was very clear, since the PDA process cause an improvement in field-effect passivation and/or chemical passivation [34,35,58,70,75,76,114,115]. The PDA was mainly carried out in  $\text{N}_2$ , forming gas (forming gas anneal-FGA) or air ambient at the temperature range of 300-550 °C for annealing time between 10-60 min [34,35,39,70,76,115-117].

For PA-ALD and PECVD  $\text{Al}_2\text{O}_3$  films an improvement in surface passivation with  $S_{\text{eff}} < 5 \text{ cm.s}^{-1}$  was reported after annealing of film. However as discussed in chapter 2, these films contain 2-7 % hydrogen [52]. Hence the improvement in surface passivation quality after PDA was related to diffusion of hydrogen from the film to the interface, that improves chemical passivation [36,72,117]. For RS  $\text{AlO}_x$  film, Li et al. reported  $S_{\text{eff}}$  of 16 and 14  $\text{cm.s}^{-1}$  after PDA in  $\text{N}_2$  and FGA ambient at 400 °C, respectively [75]. Since the RS deposited  $\text{AlO}_x$  film was not expected to contain hydrogen as discussed in earlier chapter, hence hydrogen may be introduced into the film during the PDA process to improve the surface passivation quality.

In this chapter we will discuss the impact of different PDA conditions on pulsed-DC RS  $\text{AlO}_x$  film for surface passivation application. The film and interface quality is assessed through electrical characterization of the MOS capacitor and material characterizations like cross-sectional TEM and depth resolved XPS. The surface passivation quality was measured using minority carrier life-time tester. The details of the instruments were provided in chapter 2.

## 4.2 Experimental details

As discussed in chapter 3, the  $\text{AlO}_x$  film deposited at PD of 1.3  $\text{W.cm}^{-2}$  has shown high density of negative  $Q_f$  compared to low PD deposited film. Hence we have optimized different PDA conditions on the film deposited at high PD of 1.3  $\text{W.cm}^{-2}$ . The other process parameters for film were set as: Ar flow = 15 sccm,  $\text{O}_2$  flow = 55 sccm, and deposition time = 300 s. The film deposition was carried out at room temperature. For electrical characterization MOS capacitors were fabricated on 5  $\Omega.\text{cm}$  p-type (100) CZ c-Si wafer. The  $\text{AlO}_x$  films were deposited on RCA cleaned wafers as discussed in chapter 2, section 2.4.1. Subsequently the samples were subjected to PDA in a quartz furnace in three different ambients: (i) high purity  $\text{N}_2$  gas, (ii) mixture of  $\text{N}_2 + \text{O}_2$  gas (in 79:21 ratio to mimic dry air), and (iii) FGA with 8 % hydrogen in  $\text{N}_2$ , and three different temperatures set at: 420 °C, 470 °C and 520 °C. The annealing time of 20 min was used for all the experimental conditions. The MOS capacitors fabrication steps with  $\text{AlO}_x$  dielectric film were discussed in chapter 2, section 2.4.1.

For these  $\text{AlO}_x$  films surface passivation quality was assessed by minority carrier life-time measurements by Sinton Consulting WCT-120 life-time tester. Symmetrical structures were prepared with film deposited on both sides of RCA cleaned p-type FZ c-Si (100) wafers

with resistivity of  $7.8 \Omega\text{cm}$ . The material characterization of these films were carried out using, JEOL make JEM 2100F cross-sectional TEM and elemental analysis of the film using Thermo Scientific make MultiLab 2000 XPS. The Sentech SE-800 SE was used for thickness and RI measurement. Keithley 4200 SCS was used for C-V and G-V measurements.

### 4.3 Electrical characterization

The high frequency C-V and G-V characteristics of the MOS capacitor with as-deposited film and film annealed in FGA are shown in Figure 4.1 (a) and (d),  $N_2$  are shown in Figure 4.1 (b) and (e) and  $N_2 + O_2$  ambient are shown in Figure 4.1 (c) and (f) at different temperatures namely  $420^\circ\text{C}$ ,  $470^\circ\text{C}$  and  $520^\circ\text{C}$ , respectively. The annealing time for all the PDA conditions are 20 min. The measurement frequency was  $f = 100 \text{ kHz}$ .

The different parameters extracted from the high frequency C-V characteristic plot as discussed in chapter 2. The EOT of  $\text{AlO}_x$  film in the range of 12.7-13.6 nm were extracted using eq. (2.7), for all the PDA conditions which is in line with the process control of the deposition process. Figure 4.1 (a), (b) and (c) shows after annealing the C-V curve shifts to the right, i.e., positive shift in  $V_{FB}$  value. This indicates an increase in negative  $Q_f$  after PDA of  $\text{AlO}_x$  film.

From the G-V curve in Figure 4.1 (d), (e) and (f) shows the peak conductance is observed to reduce after annealing, indicating a decrease in value of  $D_{it}$ . This implies that the interface quality has improved after annealing in a way suitable for passivation of p-type c-Si surfaces.

The negative  $Q_f$  and  $D_{it}$  are extracted using C-V and G-V characteristics, respectively, are quantified using methods described in section 2.4 of chapter 2. The value of  $Q_f$  is extracted from  $\Delta V_{MG}$  of C-V plot, using eq. (2.15) and the  $D_{it}$  is extracted from the G-V plot using eq. (2.20) [87].

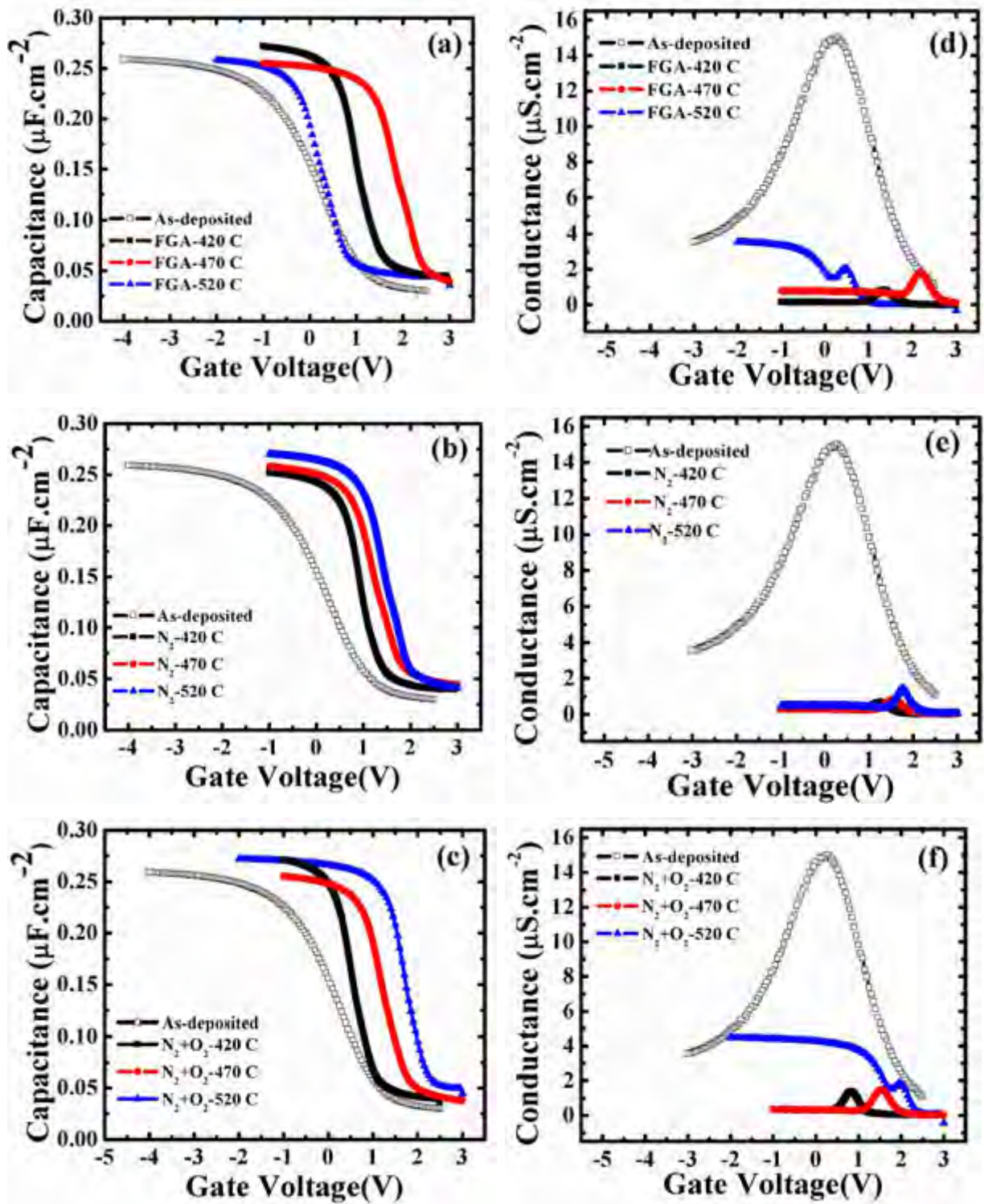


Figure 4.1 The C-V and G-V characteristics plot of MOS capacitors measured at  $f = 100$  kHz for as-deposited  $\text{AlO}_x$  film and after annealing in FGA {(a), (d)},  $\text{N}_2$  {(b), (e)} and  $\text{N}_2 + \text{O}_2$  {(c), (f)} ambient at  $420^\circ\text{C}$ ,  $470^\circ\text{C}$  and  $520^\circ\text{C}$  for 20 min.

Figures 4.2 (a) and (b) shows the extracted values of the negative  $Q_f$  and  $D_{it}$  for as-deposited and annealed  $\text{AlO}_x$  film at different conditions, respectively. The error-bar shows the spread of data over a sample for at least five devices from each experimental split. The centreline of the box shows the mean value while the upper and lower ends of the boxes are high and low values of the parameters. As shown in Figure 4.2 (a), the negative  $Q_f$  of  $4 \times 10^{12} \text{ cm}^{-2}$  is obtained for as-deposited  $\text{AlO}_x$  film. While after annealing, the value of negative  $Q_f$  increases and saturates to  $6 \times 10^{12} \text{ cm}^{-2}$  for PDA temperature of  $470^\circ\text{C}$  and above in  $\text{N}_2$  and  $\text{N}_2 + \text{O}_2$  ambient. The negative  $Q_f$  of these films are comparable to the value reported for PA-ALD  $\text{Al}_2\text{O}_3$  film [34,58,116] and slightly higher than that reported for RF reactive sputtered  $\text{AlO}_x$  films [75].

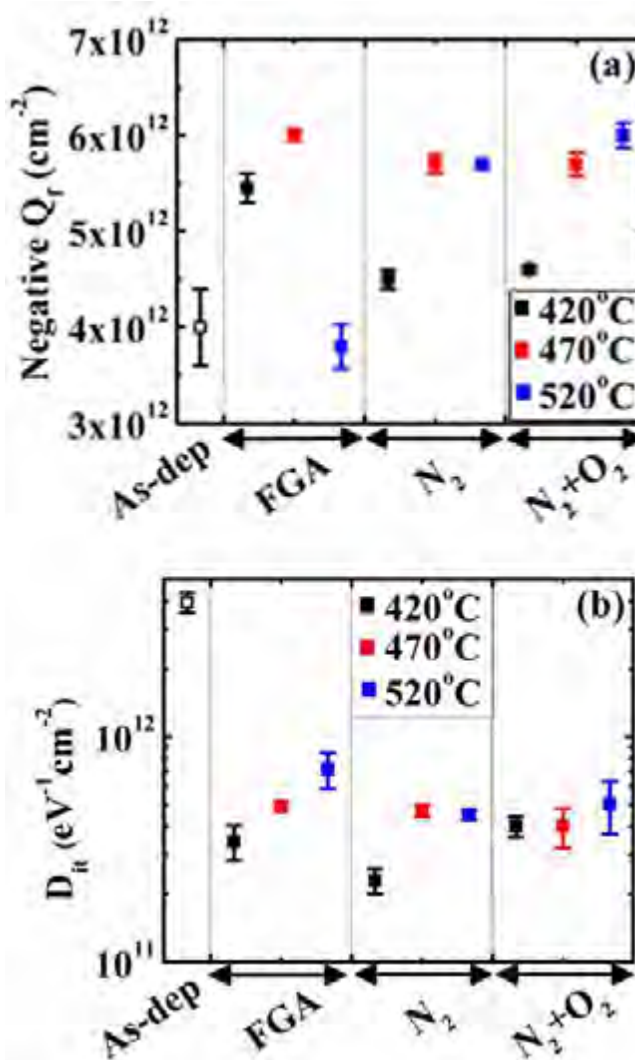


Figure 4.2 Extracted value of (a) negative  $Q_f$  and (b)  $D_{it}$  from MOS capacitors for as-deposited and annealed  $\text{AlO}_x$  film in different PDA conditions.

In report by Krugel et al. only marginal difference in the negative  $Q_f$  values were shown after annealing of RF reactive sputtered  $\text{AlO}_x$  films [79]. For FGA annealed film, the value of negative  $Q_f$  is observed to drop down significantly for higher temperature ( $520^\circ\text{C}$ ) annealing, whereas at low temperatures the trend looks similar to that of other annealing ambients. In fact the value of negative  $Q_f$  for FGA film at  $520^\circ\text{C}$  is slightly lower than that observed for as-deposited film. The trend of negative  $Q_f$  values after annealing in FGA is quantitatively similar to that reported by Benick et al. in PA-ALD  $\text{Al}_2\text{O}_3$  films [116]. The report also showed that the value of negative  $Q_f$  obtained at  $425^\circ\text{C}$  annealing temperature is higher than that for higher temperature annealing at  $550^\circ\text{C}$ , the ambient for annealing was air [116]. The presence of Al vacancies or O interstitials in the film causes negative  $Q_f$  in the film, according to Miyajima et al. [76]. Kimoto et al. [42], shows the Al atoms occupy  $T$  coordinated Al sites and hence results in negative  $Q_f$  in the film. These results along with the results by Benick et al. suggests that the structural modification may be responsible for the suppression or reduction of negative  $Q_f$  at high annealing temperatures ( $\sim 500^\circ\text{C}$ ) due to the presence of hydrogen in the film [116]. The source of hydrogen in the PA-ALD  $\text{Al}_2\text{O}_3$  film is the hydrogen from precursor. However in our work, the PDA with FGA is the only source of hydrogen that could diffuse through the  $\text{AlO}_x$  film during annealing.

The values of  $D_{it}$  extracted from the G-V plot of  $\text{AlO}_x$  film annealed in different PDA conditions are shown in Figure 4.2 (b). The value of  $D_{it}$  is observed to decrease nearly by one order of magnitude after annealing, resulting in improved  $\text{AlO}_x/\text{c-Si}$  interface. The  $D_{it}$  values observed here were less than the values reported for RF reactive sputtered films used as surface passivation application [75]. For PDA in  $\text{N}_2$  ambient, the lowest  $D_{it}$  of  $2 \times 10^{11} \text{ cm}^{-2}.\text{eV}^{-1}$  is obtained at an annealing temperature of  $420^\circ\text{C}$ , whereas for high temperature annealing a slight increase in the value of  $D_{it}$  to  $4 \times 10^{11} \text{ cm}^{-2}.\text{eV}^{-1}$  is observed. Similar behaviour is observed for PDA in  $\text{N}_2 + \text{O}_2$  ambient with the mean  $D_{it}$  value appearing to be independent of annealing temperature. The improvement in  $D_{it}$  after PDA in  $\text{N}_2$  and  $\text{N}_2 + \text{O}_2$  ambients, can be attributed to oxidation of interface by diffusion of oxygen from the  $\text{AlO}_x$  film or oxygen from PDA ambient during the annealing [75]. With FGA annealing the reduction in  $D_{it}$  values can be explained by the passivation of dangling bonds at the interface using atomic hydrogen. However, the high temperature ( $520^\circ\text{C}$ ) annealing, cause degradation of the interface quality with increase in  $D_{it}$  value, which can be related to the effusion of hydrogen from the interface [116].

## 4.4 Surface passivation

The  $\tau_{\text{eff}}$  was measured using WCT-120 lifetime tester and corresponding value of  $S_{\text{eff}}$  was calculated using eq. (2.29), in section 2.4.3 of chapter 2. The  $\tau_{\text{bulk}}$  of 1.4 ms is measured on p-type FZ (100) wafer of resistivity  $7.8 \Omega\text{cm}$  (2 inch) by immersing the RCA cleaned wafer in iodine-methanol (IM) solution (i.e., 1.18 g of iodine in 50 mL of methanol) [95]. Other method includes application of PECVD SiN<sub>x</sub> film as passivation layer, was proposed by Schmidt et al., to accurately determine the value of  $\tau_{\text{bulk}}$  on mono-Si wafers with doping density of  $10^{14}\text{-}10^{17} \text{ cm}^{-3}$  [118].

Kerr et al. proposed the generalized parameterization method to calculate the upper limit of  $\tau_{\text{bulk}}$  for mono-Si with specific doping density [119]. Here the FZ wafers of resistivity  $7.8 \Omega\text{cm}$  (measured using 4-probe) with doping density of  $1.75 \times 10^{15} \text{ cm}^{-3}$ , estimated from the resistivity versus doping concentration plot by Thurber et al. [120]. Hence in this work upper limit of  $\tau_{\text{bulk}} = 30 \text{ ms}$  at excess minority carrier density,  $\Delta n$  of  $4 \times 10^{14} \text{ cm}^{-3}$  was calculated using generalized parameterization method. Since the value of  $\tau_{\text{bulk}}$  estimated using generalized parameterization method by Kerr et al. is different than the measured  $\tau_{\text{bulk}} = 1.4 \text{ ms}$  for same specification of silicon substrate [119], hence we have also investigated the sensitivity of  $S_{\text{eff}}$  value to  $\tau_{\text{bulk}}$  value for different  $\tau_{\text{eff}}$  values, extracted using eq. (2.29). The results are shown in Figure 4.3.

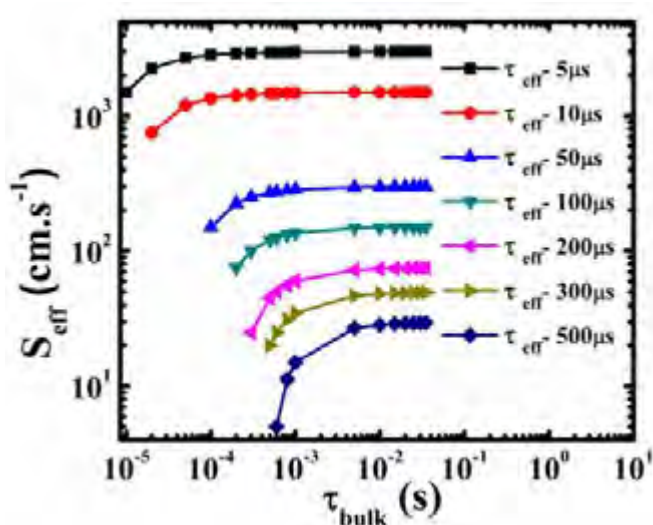


Figure 4.3 Study of relation between  $S_{\text{eff}}$  and  $\tau_{\text{bulk}}$  for different values of  $\tau_{\text{eff}}$ , extracted using eq. (2.29).

The result shows that the value of  $S_{\text{eff}}$  is most sensitive to the value of  $\tau_{\text{bulk}}$  in lower range  $< 10$  ms for  $\tau_{\text{eff}} = 300 \mu\text{s}$  and above, whereas at higher range of  $\tau_{\text{bulk}} > 30$  ms the value of  $S_{\text{eff}}$  seems to be nearly independent of  $\tau_{\text{bulk}}$ .

The measured  $\tau_{\text{eff}}$  on as-deposited and annealed AlO<sub>x</sub> film in different PDA conditions using life-time tester are shown in Figure 4.4 (a) and the corresponding calculated value of  $S_{\text{eff}}$  using eq. (2.29) are shown in Figure 4.4 (b).

As shown in Figure 4.4 (a), as-deposited AlO<sub>x</sub> the  $\tau_{\text{eff}}$  of  $0.1 \mu\text{s}$  at  $\Delta n = 4 \times 10^{14} \text{ cm}^{-3}$  is measured, while significant improvement in value of  $\tau_{\text{eff}}$  is observed on annealed films. The best value of  $\tau_{\text{eff}} = 0.35 \text{ ms}$  is observed on N<sub>2</sub> + O<sub>2</sub> annealed film at 520 °C for 20 min, at  $\Delta n = 4 \times 10^{14} \text{ cm}^{-3}$ . The film annealed in FGA ambient at 520 °C, has shown very poor  $\tau_{\text{eff}} < 0.1 \mu\text{s}$ .

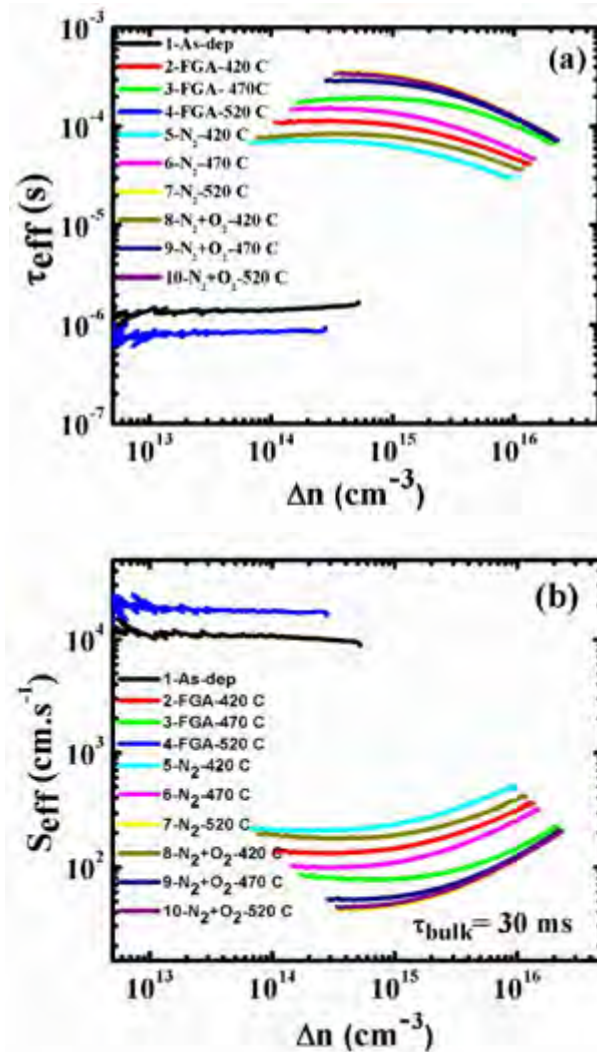


Figure 4.4 (a) The  $\tau_{\text{eff}}$  measured and (b) corresponding calculated value of  $S_{\text{eff}}$  on as-deposited AlO<sub>x</sub> film and after annealing in different PDA conditions.

Based on the hypothesis explained before, the value of  $S_{\text{eff}}$  calculated using eq. (2.29) with upper limit,  $\tau_{\text{bulk}} = 30$  ms on p-type c-Si wafer with resistivity  $7.8 \Omega\text{cm}$  [119], shown in Figure 4.4 (b). The result shows an improvement in the surface passivation after annealing, with the reduction of  $S_{\text{eff}}$  by 2 orders of magnitude compared to as-deposited film.

The comparison of  $S_{\text{eff}}$  values calculated for  $\tau_{\text{bulk}}$  measured in IM solution using life-time tester and for upper limit of  $\tau_{\text{bulk}}$  using generalized parameterization reported by Kerr et al., is given in Table 4.1 [95,119]. The  $\text{AlO}_x$  film is annealed in  $\text{N}_2 + \text{O}_2$  ambient at  $520^\circ\text{C}$  for 20 min. The  $\tau_{\text{eff}} = 0.35$  ms is measured on the symmetrical structure of  $\text{AlO}_x$  film passivated p-type c-Si using life-time tester.

Table 4.1 The value of  $S_{\text{eff}}$  for  $\text{AlO}_x$  film annealed in  $\text{N}_2 + \text{O}_2$  ambient at  $520^\circ\text{C}$ , with  $\tau_{\text{bulk}}$  measured in IM solution [95] and estimated using upper limit by generalized parameterization [119] at  $\Delta n = 4 \times 10^{14} \text{ cm}^{-3}$ .

Methods	$\tau_{\text{bulk}}$ (ms)	Measured* $\tau_{\text{eff}}$ (ms)	Calculated $S_{\text{eff}}$ ( $\text{cm. s}^{-1}$ )
Measured* on p-type FZ ( $7.8 \Omega\text{cm}$ ) wafer by immersing in IM solution	1.4	0.35	32
Upper limit of $\tau_{\text{bulk}}$ using generalized parameterization by Kerr et al. [119]	30	0.35	42

\*Measured using life-time tester

In Figure 4.5, the minimum value of  $S_{\text{eff}}$  at  $\Delta n$  of  $4 \times 10^{14} \text{ cm}^{-3}$  calculated using the upper limit of  $\tau_{\text{bulk}} = 30$  ms and measured  $\tau_{\text{eff}}$  on as-deposited film and film annealed in different PDA conditions are shown.

As shown in Figure 4.5, the minimum  $S_{\text{eff}}$  of  $42 \text{ cm.s}^{-1}$ , is observed on annealed  $\text{AlO}_x$  film in  $\text{N}_2 + \text{O}_2$  or  $\text{N}_2$  ambient at temperature  $520^\circ\text{C}$  for 20 min. For PDA in  $\text{N}_2 + \text{O}_2$  ambient, the  $S_{\text{eff}}$  is observed to decrease with annealing temperature. The improvement in surface passivation can be further related to an increase in negative  $Q_f$  hence field-effect passivation, as shown in Figure 4.2 (a). Similar trend in minimum  $S_{\text{eff}}$  value to annealing temperature is observed for PDA in  $\text{N}_2$  ambient as well.

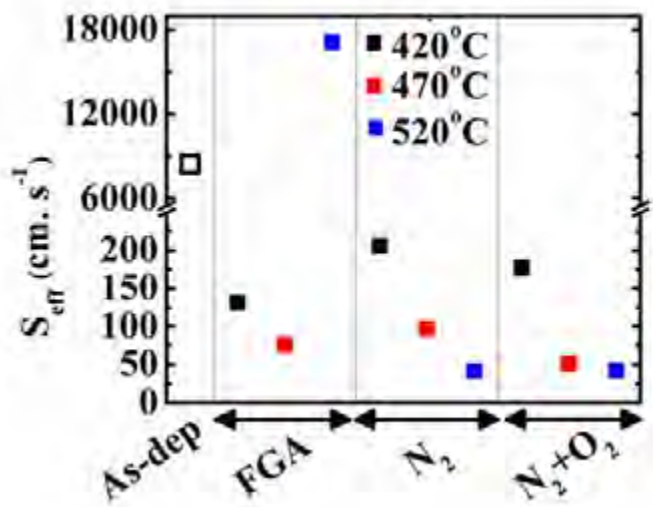


Figure 4.5 Minimum value of  $S_{\text{eff}}$  at  $\Delta n$  of  $4 \times 10^{14} \text{ cm}^{-3}$  for as-deposited  $\text{AlO}_x$  film and after PDA of  $\text{AlO}_x$  film in different conditions.

However PDA in FGA ambient, shows improvement in  $S_{\text{eff}}$  value for annealing temperature upto 470 °C and further at higher temperature (i.e., 520 °C), a significant degradation is observed. As discussed in section 4.3, this sample shows the lowest negative  $Q_f$  of  $4 \times 10^{12} \text{ cm}^2$  and the highest  $D_{it}$  of  $3.8 \times 10^{12} \text{ eV}^{-1}\text{cm}^2$  at high temperature annealing among the PDA samples. The poor surface passivation can be attributed to the effusion of hydrogen from film at such high temperature and hence increase of dangling bonds [46,61,121]. In subsequent section the material characterization and interfacial property will be discussed to infer the reason for differences in passivation quality for different PDA conditions.

## 4.5 Material characterization

### 4.5.1 Cross-sectional imaging by TEM

Cross-sectional TEM images of these films were obtained to gain better insight into  $\text{AlO}_x/\text{c-Si}$  interface. Figure 4.6 (a) and (b) shows the cross-sectional TEM images of as-deposited  $\text{AlO}_x$  film and annealed  $\text{AlO}_x$  film in  $\text{N}_2 + \text{O}_2$  ambient at 520 °C for 20 min.

Figure 4.6 (a), shows thick interfacial layer (IL) at  $\text{AlO}_x/\text{c-Si}$  interface with thickness of 8.2 nm, and the  $\text{AlO}_x$  layer on IL with thickness of 21.4 nm is observed on as-deposited film. After annealing the film, thickness of IL = 8.4 nm and the  $\text{AlO}_x$  layer on IL with

thickness of 19.9 nm are observed, in Figure 4.6 (b). Thus no significant effect of PDA is observed on the thickness of the IL and AlO<sub>x</sub> layer. For ALD deposited Al<sub>2</sub>O<sub>3</sub> film very thin (1-2 nm) IL was reported at the AlO<sub>x</sub>/c-Si interface after PDA [34]. Y. Jin et al. reported thick IL of 4 nm for electron cyclotron resonance (ECR) sputter deposited Al<sub>2</sub>O<sub>3</sub> film, which is significantly thicker than ALD or PECVD Al<sub>2</sub>O<sub>3</sub> film [34,121]. The thickness of IL observed in our experiment is significantly higher than those reported elsewhere.

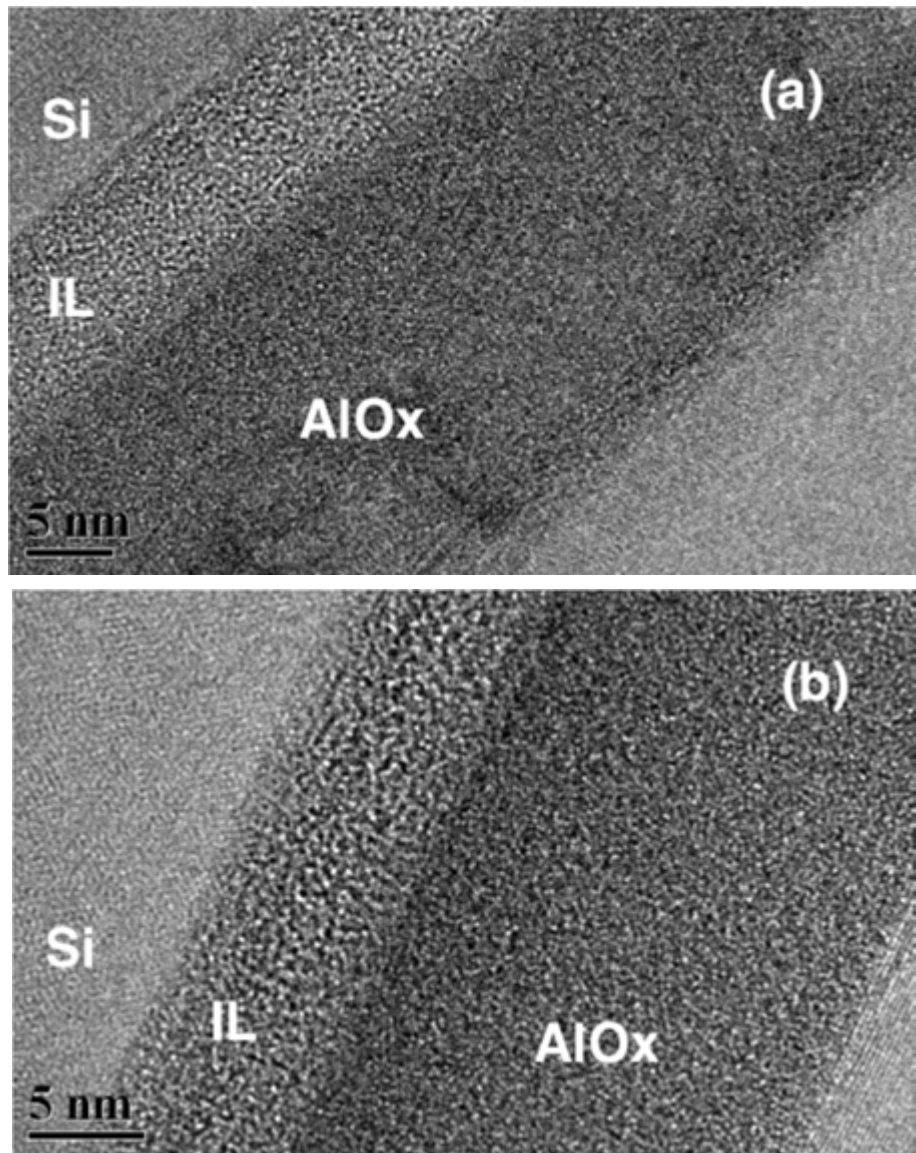


Figure 4.6 Cross-sectional TEM image of (a) as-deposited AlO<sub>x</sub> film deposited on c-Si and (b) AlO<sub>x</sub> film annealed in N<sub>2</sub> + O<sub>2</sub> gas at 520 °C for 20 min.

The presence of IL was suggested as the key to improvement in passivation quality by AlO<sub>x</sub> film on the Si surface [34,122,123]. Dingemans et al. demonstrated the effect of

different thickness of interfacial  $\text{SiO}_2$  layer intentionally deposited on c-Si and subsequently capped with ALD  $\text{Al}_2\text{O}_3$  film, on the quality of surface passivation by ALD  $\text{Al}_2\text{O}_3$  film [124]. The report shows the surface field was decreasing with an increase in  $\text{SiO}_2$  layer thickness, as the positive  $Q_f$  in  $\text{SiO}_2$  may screen a part of the negative  $Q_f$  at the  $\text{SiO}_2/\text{Al}_2\text{O}_3$  interface [124].

#### 4.5.2 Elemental analysis by XPS

The elemental depth-resolved profile using XPS measurement for  $\text{AlO}_x$  film annealed in  $\text{N}_2 + \text{O}_2$  ambient at 520 °C for 20 min, is shown in Figure 4.7. Using elemental depth-resolved profile, the elemental profile and composition in IL and  $\text{AlO}_x$  layer can be obtained in terms of atomic concentration (%). As discussed in previous section, the IL = 8.4 nm was found on  $\text{N}_2 + \text{O}_2$  annealed film, hence using the XPS depth-profile technique the composition of thick IL in  $\text{AlO}_x$  /c-Si interface will be analysed.

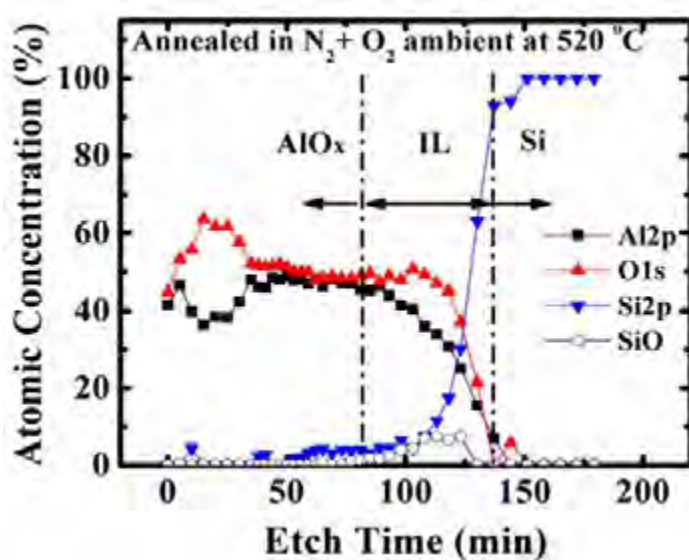


Figure 4.7 Atomic concentration of Al 2p, O 1s and Si 2p elemental depth-profiles of  $\text{AlO}_x$  film deposited on c-Si for annealing in  $\text{N}_2 + \text{O}_2$  ambient at 520 °C for 20 min.

As shown in Figure 4.7, the atomic concentration (%) determined from Al 2p, O 1s and Si 2p emissions obtained using depth-resolved XPS measurement are plotted as a function of etch time. The film shows O concentration of approximately 60 atomic % and Al concentration of approximately 40 atomic %, near the top surface in the  $\text{AlO}_x$  layer, which indicates stoichiometry  $\text{Al}_2\text{O}_3$  film with O/Al ratio of 1.5 after PDA. While in the bulk of  $\text{AlO}_x$  layer, the atomic concentrations of O and Al are almost equal and O/Al ratio became approximately 1. As we go deeper, a gradual decrease in Al concentration and increase in Si concentration are observed along with a constant O concentration. The oxidized state of Si

(SiO) is observed in this region. This transition region can be identified as the IL. Hence it can be concluded that the composition in IL is in the form of aluminum silicate.

Close to the c-Si/IL interface the aluminum silicate became Si rich and close to the IL/AlO<sub>x</sub> layer interface it became Al rich. The stoichiometric Al<sub>2</sub>O<sub>3</sub> film close to the surface is due to re-oxidation of the surface during PDA in N<sub>2</sub> + O<sub>2</sub> ambient at 520 °C. Kimoto et al. analysed the composition of ALD deposited AlO<sub>x</sub> film by using EELS and showed that the composition of IL is aluminum silicate (AlSiO<sub>x</sub>) at the interface [42]. In the RS technique, two processes occur simultaneously during the initial stage of deposition (i) the oxidation of the Si surface by oxygen radicals and ions from the plasma and (ii) deposition of aluminum oxide compound. The intermixing of deposited layers and the layer already present on the substrate during the sputtering process are because of high energy particles arriving at the substrate and hence may lead to formation of AlSiO<sub>x</sub> layer [125]. As the deposition proceeds, the oxidation of silicon stops beyond a certain IL thickness as the oxidants would have to penetrate through already deposited layer.

## 4.6 Summary

In this chapter we have investigated the role and importance of PDA process in the surface passivation quality of pulsed-DC RS AlO<sub>x</sub> film deposited on p-type c-Si. The best value of S<sub>eff</sub> = 42 cm. s<sup>-1</sup> is obtained for the film annealed in N<sub>2</sub> or N<sub>2</sub> + O<sub>2</sub> ambient at high temperature of 520 °C for 20 min. The reasons for improved surface passivation is also assessed through electrical characterization of these films, which has shown an increase in negative Q<sub>f</sub> to about  $6 \times 10^{12}$  cm<sup>-2</sup> and decrease in D<sub>it</sub> to about  $4 \times 10^{11}$  eV<sup>-1</sup> cm<sup>-2</sup> after PDA. From the results we have also observed a degradation in surface passivation quality after high temperature annealing in FGA at 520 °C. The D<sub>it</sub> remained similar to that of the as-deposited film. For the same condition, a significant decrease in Q<sub>f</sub> is observed. That means that the passivation of low doped p-Si surface by pulsed-DC RS AlO<sub>x</sub> film is dominantly field-effect passivation mechanism. The TEM and depth-resolved XPS analysis reveals the presence of thick IL with the composition of AlSiO<sub>x</sub> for pulsed-DC RS AlO<sub>x</sub> film deposited on c-Si. In the next chapter the origin and distribution of the Q<sub>f</sub> in the AlO<sub>x</sub> film will be explored using EELS and other measurement techniques. The reason for difference in passivation quality by AlO<sub>x</sub> film after high temperature annealing in N<sub>2</sub> + O<sub>2</sub> and FGA ambients will be investigated using XPS analysis.

## **Chapter 5. Origin and Distribution of Charges in AlO<sub>x</sub> Film Deposited on c-Si by Pulsed-DC Reactive Sputtering**

### **5.1 Introduction**

As discussed in the previous chapters, one of the mechanisms for surface passivation of p-type c-Si by pulsed-DC RS AlO<sub>x</sub> film is field-effect passivation by repulsion of electrons from the surface using negative Q<sub>f</sub> present in the film [35,45]. Further improvement in surface passivation is possible due to chemical passivation mechanism with reduction in D<sub>it</sub> values after PDA [35,45]. The level of surface passivation is evaluated by estimating S<sub>eff</sub> from the measured  $\tau_{eff}$  on passivated wafers. Kimoto et al. studied the ALD Al<sub>2</sub>O<sub>3</sub> film deposited on c-Si (001), using EELS to determine elemental coordination and interfacial property of the film [42]. The study, shows presence of both *T* and *O* coordinated Al in the  $\gamma$ -Al<sub>2</sub>O<sub>3</sub> film. The bonding structure of the *T* (i.e., AlO<sub>4</sub>) and *O* (AlO<sub>6</sub>) coordinated Al, are shown in Figure 5.1 (a) and (b), respectively [126].

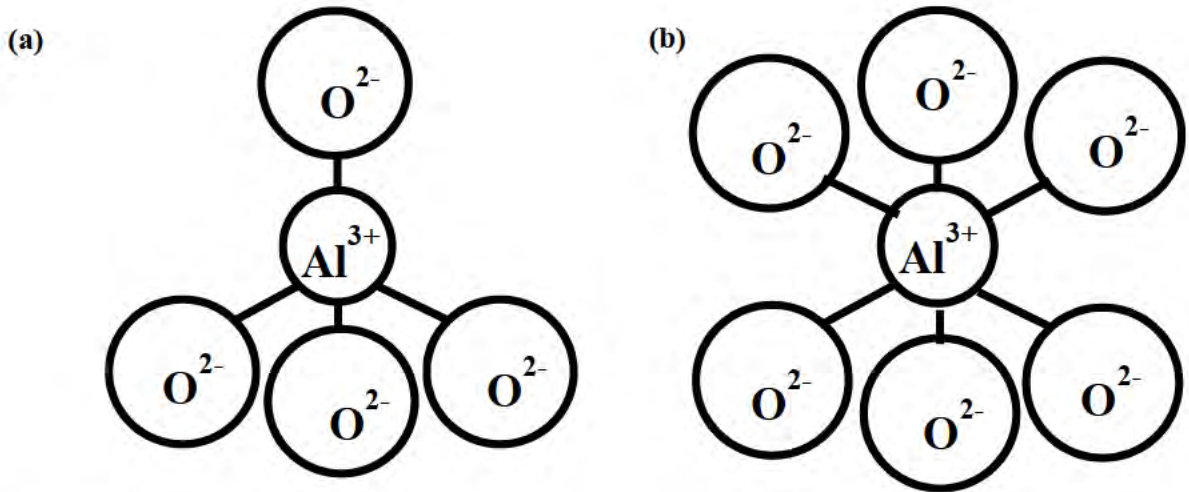


Figure 5.1 (a) Tetrahedral ( $T$ ) structure of  $\text{Al}^{3+}$  coordinated with four  $\text{O}^{2-}$  ions and (b) octahedral ( $O$ ) structure of  $\text{Al}^{3+}$  coordinated with six  $\text{O}^{2-}$  ions [126].

M. Mbila identified two basic soil clay mineral structures, known as silicon tetrahedron ( $\text{SiO}_4$ ) and Al octahedron ( $\text{AlO}_6$ ) [126]. The  $\text{SiO}_4$  also known as orthosilicate anion, consists of all four oxygen ions shared equally with silicon ion while leaving behind excess negative charges. These negative charges will get neutralized after bonding of these oxygen ions with other silicon ions in the structure. During the soil weathering process, the  $\text{Al}^{3+}$  ion substitutes for  $\text{Si}^{4+}$  in the basic structure as shown in Figure 5.1 (a), which is also called isomorphous substitution. The  $T$  structure of soil which used to carry the effective positive charge, turns into net negative charged  $T$  coordinated structure after isomorphous substitution process of replacing  $\text{Si}^{4+}$  with  $\text{Al}^{3+}$  [126]. The study by S.W. Bailey, also reported an apical oxygen results in net negative charge for the  $T$  structure after  $\text{Al}^{3+}$  substitutes for  $\text{Si}^{4+}$  [127]. Figure 5.1 (b) shows, the  $O$  structure of  $\text{AlO}_6$ , with each aluminum ion sharing positive 0.5 charge with bonded oxygen ions and each oxygen ions has remaining negative 1.5 charge to be neutralized by bonding with other Al ions [126].

Kimoto et al. showed EELS study for ALD deposited  $\text{Al}_2\text{O}_3$ , where 5 nm thick  $\text{Al}_2\text{O}_3$  film were deposited at 300 °C using TMA precursor and  $\text{H}_2\text{O}$  reactant on Si (001) wafer [42]. The film was annealed using RTA process at 750 °C in  $\text{Ar} + \text{O}_2$  mixture (1 %). The EELS spectra shows the peak intensity of  $T$  coordinated Al at 78.2 eV was higher near the  $\text{Al}_2\text{O}_3/\text{c-Si}$  interface, and decreases gradually towards the surface of  $\text{Al}_2\text{O}_3$  layer [42]. The  $O$  coordinated Al peak at 79.7 eV was high towards the surface of  $\text{Al}_2\text{O}_3$  layer. It was also reported that, near the interface Si L<sub>2,3</sub>

peak was chemically shifted by 5 eV towards high energy. This peak was related to the silicate present in the form of  $\text{SiO}_4$  ( $T$ ) or amorphous  $\text{SiO}_2$ . The intensity of peak at 105 eV, was decreasing towards the surface of  $\text{Al}_2\text{O}_3$  layer. Hence the presence of Si in the form of silicate ( $\text{SiO}_4$ ) at the interface, results in formation of aluminium silicate at the interfacial layer [42]. Similarly Hoex et al. studied the origin of negative  $Q_f$  in 30 nm thick  $\text{Al}_2\text{O}_3$  film deposited using thermal ALD and PA-ALD at 200 °C on n-type c-Si (100) wafer. The film was annealed in  $\text{N}_2$  ambient at 400 °C for 30 min to activate the surface passivation [128]. The result also confirmed the presence of peaks related to  $T$  and  $O$  coordinated Al in both thermal ALD and PA-ALD  $\text{Al}_2\text{O}_3$  films. After annealing the  $T$  coordinated Al peak becomes quite significant near the interface, for both deposition methods, which supports the finding of increase in number of negative  $Q_f$  after PDA. The result also indicates the formation of about 0.8 nm thick interfacial  $\text{SiO}_2$  for thermal ALD, while for PA-ALD the interfacial oxide layer thickness was about 2 nm [128]. Both the reports suggest that study of  $\text{AlO}_x/\text{c-Si}$  interface is very important in analysing the origin and distribution of  $Q_f$ .

As discussed in chapter 4, the IL at  $\text{AlO}_x/\text{c-Si}$  interface by pulsed-DC RS technique is thicker (8.4 nm) than ALD and PECVD  $\text{Al}_2\text{O}_3$  interface. The IL was identified as  $\text{AlSiO}_x$  using XPS measurements. The good quality surface passivation with  $S_{\text{eff}}$  of  $42 \text{ cm.s}^{-1}$  was observed for film annealed in  $\text{N}_2 + \text{O}_2$  ambient at 520 °C for 20 min, whereas in same condition with FGA ambient leads to degradation in the surface passivation quality. Dingemans et al., correlated degradation of surface passivation in FGA annealing at high temperature to the effusion of hydrogen from the PA-ALD  $\text{Al}_2\text{O}_3$  film [72]. In this case, the film is not expected to contain hydrogen, as high purity Al target was sputtered using Ar and  $\text{O}_2$  as sputtering and reactive gas in vacuum system [74].

In this chapter, we will explore the origin and distribution of  $Q_f$  in the pulsed-DC RS  $\text{AlO}_x$  film using spatially resolved EELS. We further study the interface quality in more detail by analysing the XPS data for different intermediate oxide states of Si 2p in different samples under study. The FTIR spectroscope measurement of film will be discussed to analyse the type of chemical bonding between elements present in the film. The study of film property using EELS and UV-Vis-NIR spectroscope will be presented to determine the  $E_{\text{BG}}$  of the film.

## 5.2 Experimental details

The pulsed-DC RS AlO<sub>x</sub> films were deposited on RCA cleaned 5 Ω.cm p-type (100) CZ c-Si wafer, as discussed in chapter 2, section 2.4.1. The optimized process parameter as discussed in chapter 3, was used for AlO<sub>x</sub> film deposition at room temperature, using PD of 1.3 W.cm<sup>-2</sup> and Ar flow rate of 15 sccm and O<sub>2</sub> flow rate of 55 sccm, with deposition time of 300 s. Subsequently two samples were annealed in N<sub>2</sub> + O<sub>2</sub> (79:21) ambient, and FGA ambient with 8 % hydrogen at 520 °C for 20 min.

High resolution EELS spectrum for these samples were collected using FEI TITAN 80-300 kV TEM operating at an extraction voltage of 300 kV. A gun monochromator was used to obtain a resolution as good as 180 meV in energy loss for a dispersion of 0.01 eV/channel. The Al L<sub>2,3</sub> (onset ~ 73 eV) and Si L<sub>2,3</sub> (onset ~ 99 eV) energy loss near edge spectra (ELNES) were measured using a dispersion of 0.03 eV/channel. The plural scattering background was removed by using power law method. The measurement was done at 12 different spots in the samples starting from the c-Si substrate, IL and AlO<sub>x</sub> region in the sample. The EELS spectra were collected in the low-loss region to study the E<sub>BG</sub> of the film. A dispersion of 0.01 eV/ channel was used for low-loss EELS acquisition. The zero-loss peak was removed by subtracting the reflected tail of the negative part of the zero-loss intensity. The single scattering distribution was then extracted by Fourier-log deconvolution method.

The distribution of intermediate oxidation states of Si in the IL for different annealing samples were studied using depth-resolved XPS measurement. The ULVAC-PHI make XPS measurements system with model PHI 5000 Versa Probe-II was used in this work. The XPSPEAK 4.1 software was used for curve fitting and Shirley background correction was applied before the analysis of the XPS spectrum [129].

The optical absorption coefficient ( $\alpha$ ) was calculated using Kramers-Kronig analysis [130]. The Perkin Elmer make Lambda 950 model UV-Vis-NIR spectroscope with an integrating sphere was used in transmission mode, to measure the E<sub>BG</sub> of AlO<sub>x</sub> film deposited on quartz wafer [131,132]. Perkin Elmer make (Spectrum BX II) FTIR spectroscope was used to analyze chemical

properties in terms of chemical bonding and coordination by measuring the absorbance spectra in the wide wavelength range in normal transmission mode.

### 5.3 EELS measurements

The cross-sectional TEM image with different sampling spots for EELS measurements with corresponding EELS intensity spectra at each sampling spot of pulsed-DC RS AlO<sub>x</sub> film are shown in Figure 5.2 (a,b,c) and Figure 5.2 (d,e,f), respectively. The TEM image and EELS spectra of as-deposited AlO<sub>x</sub> film is shown in Figure 5.2 (a) and (d), respectively. The TEM image and EELS spectra of annealed AlO<sub>x</sub> film in N<sub>2</sub> + O<sub>2</sub> ambient is shown in Figure 5.2 (b) and (e), respectively and similarly for FGA annealed AlO<sub>x</sub> film is shown in Figure 5.2 (c) and (f), respectively.

For as-deposited film the *T* and *O* peaks of Al L<sub>2,3</sub> signal spectra are positioned at 70 and 74 eV respectively, in the AlO<sub>x</sub> region as shown in Figure 5.2 (d) [133]. While the *T* and *O* peaks of Al L<sub>2,3</sub> signal spectra are shifted to higher energy values and positioned at 73.3 and 76.3 eV, in the IL region, respectively as shown in Figure 5.2 (d), which can be attributed to an increase in oxidization state [134]. As noticed the *T* and *O* peaks are seen separately in this sample. The Si L<sub>2,3</sub> signal is present at 99.4 eV which also extends till about 2 nm in the IL region [44,128,134,135]. Whereas no strong signal corresponding to SiO<sub>2</sub>, is seen on as-deposited AlO<sub>x</sub> film spectra, since the film was deposited at room temperature and film obtained is a sub-stoichiometric oxide of Al [136]. The XPS analysis will be presented later in this chapter to support this observation.

The EELS spectra for annealed film in N<sub>2</sub> + O<sub>2</sub> is shown in Figure 5.2 (e). For annealed films the *T* and *O* signal peaks are inseparable in the bulk of the AlO<sub>x</sub> region, and the *T* coordinated Al L<sub>2,3</sub> peak is positioned at 70 eV. Whereas in the IL region, the *T* and *O* peaks are seen separately with shift in energy to high value at 75 eV and 76.9 eV, respectively [44,128,134,135]. A peak at 106.2 eV corresponds to the oxidation state of Si is present throughout the IL region and the Si L<sub>2,3</sub> signal peak at 99.2 eV is present in c-Si region [44,128]. The formation of SiO<sub>2</sub> at IL region is due to the diffusion of excess O from annealing ambient through the AlO<sub>x</sub> region at high temperature exposure [134,135].

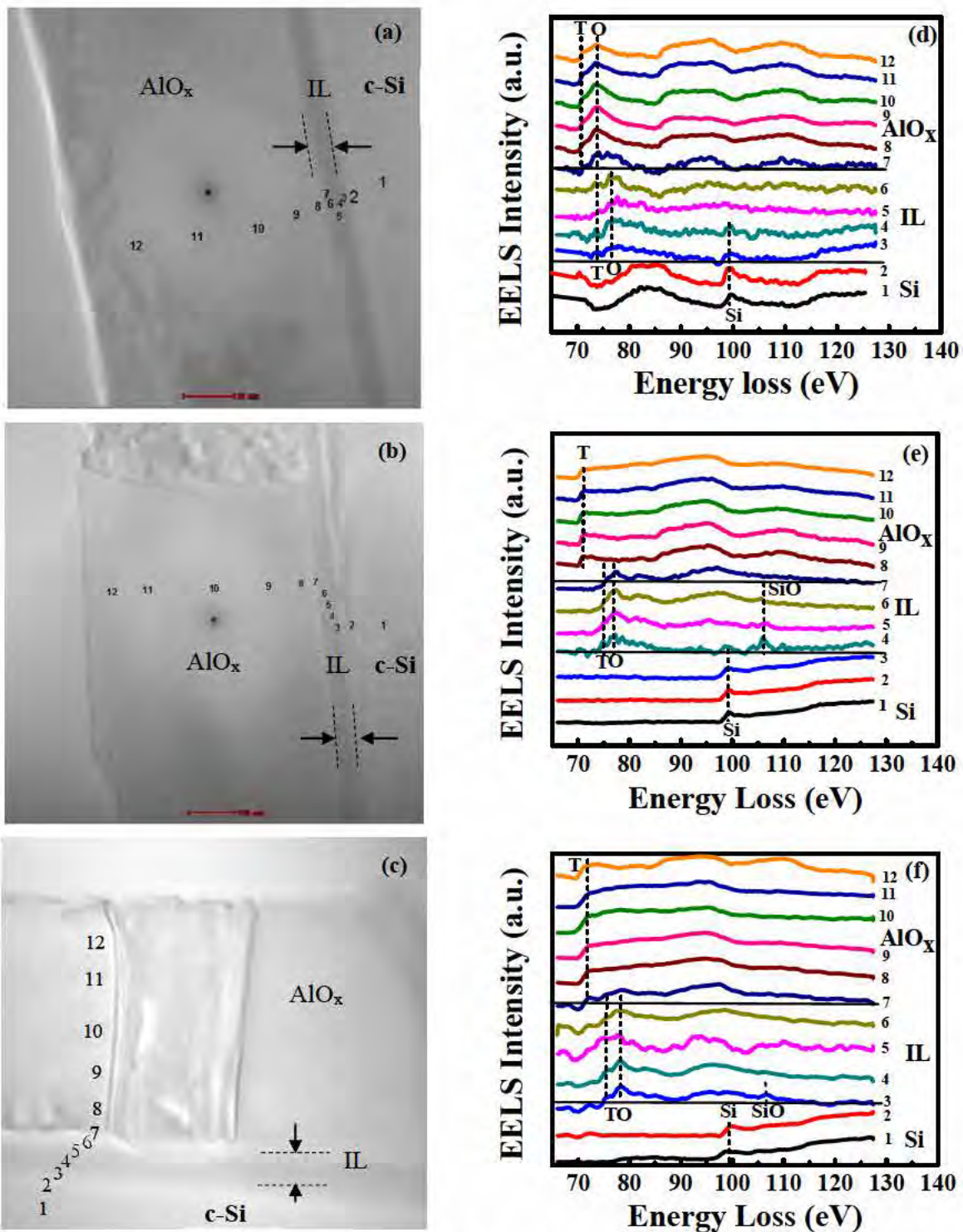


Figure 5.2 (a,b,c) Cross-sectional TEM image of  $\text{AlO}_x$  films with different scanning spots and (d,e,f) corresponding EELS spectrum. (a,d) as-deposited film, (b,e) film annealed in  $\text{N}_2 + \text{O}_2$  ambient, and (c,f) in FGA ambient at 520 °C.

The EELS spectra for FGA annealed film is shown in Figure 5.2 (f). As also discussed above, the *T* and *O* signal peaks are inseparable in the bulk of the  $\text{AlO}_x$  region for this annealing condition as well. The *T* coordinated Al  $\text{L}_{2,3}$  peak is positioned at 71.6 eV in bulk of  $\text{AlO}_x$  region, while in the IL region, the separate *T* and *O* peaks are seen to be shifted to higher energy and positioned at 75.6 eV and 77.9 eV respectively [44,128,134,135]. A peak corresponding to  $\text{SiO}_2$  at 106.2 eV is present at IL only for about 1 nm from the c-Si surface and Si  $\text{L}_{2,3}$  signal is present in c-Si [44,128]. A very thin  $\text{SiO}_2$  layer at c-Si/IL interface can be attributed to the diffusion of oxygen from  $\text{AlO}_x$  layer to the interface during high temperature annealing [134,135].

The *T/O* peak intensity ratios at different sampling points in the  $\text{AlO}_x$  and IL region of as-deposited film and in IL region of annealed film is plotted for three samples to assess the distribution of  $Q_f$  at the interface, as shown in Figure 5.3.

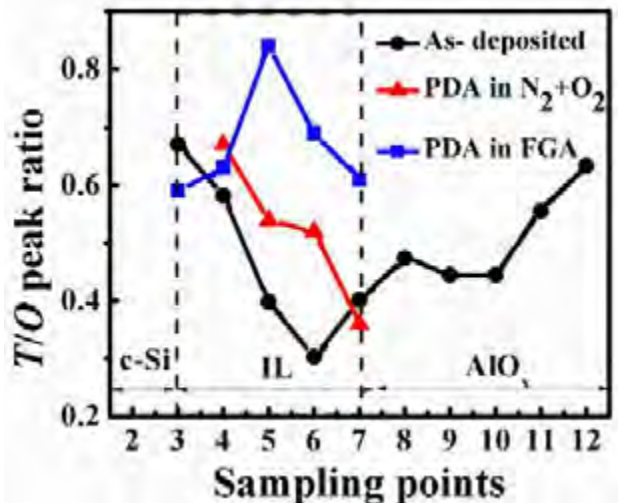


Figure 5.3 The *T/O* peak intensity ratios at different sampling points in the  $\text{AlO}_x$  and IL regions of the as-deposited film, and in IL region of the annealed  $\text{AlO}_x$  film.

It is observed that the value of *T/O* peak intensity ratio is increasing for annealed films in the IL region, the similar trend was also reported by Hoex et al. for PA-ALD  $\text{Al}_2\text{O}_3$  film deposited on c-Si [44,128]. An increase in *T/O* peak intensity ratio signifies that the *T* coordinated Al is dominating at the IL region. For the FGA annealed sample, the *T/O* ratio is seen to peak in the middle of the IL region and then decreases towards the c-Si surface. For the  $\text{N}_2 + \text{O}_2$  annealed sample, the *T/O* ratio is seen to be consistently increasing towards the c-Si surface. At the IL/ $\text{AlO}_x$

interface, the  $T/O$  ratio for the FGA annealed sample is seen to be marginally lower than both the as-deposited and  $N_2 + O_2$  annealed sample. As proposed by Kimoto et al., the increase in  $T/O$  ratio is attributed to the increase in negative  $Q_f$  [42], these observations are consistent with the trends in the negative  $Q_f$  presented in Figure 4.2.

## 5.4 Exploration of intermediate oxidation states using XPS

The depth-profile of Al 2p, O 1s and Si 2p elements using XPS measurement of as-deposited  $AlO_x$  film and films annealed in  $N_2 + O_2$  and FGA ambient at 520 °C are shown in Figure 5.4 (a), (b) and (c), respectively.

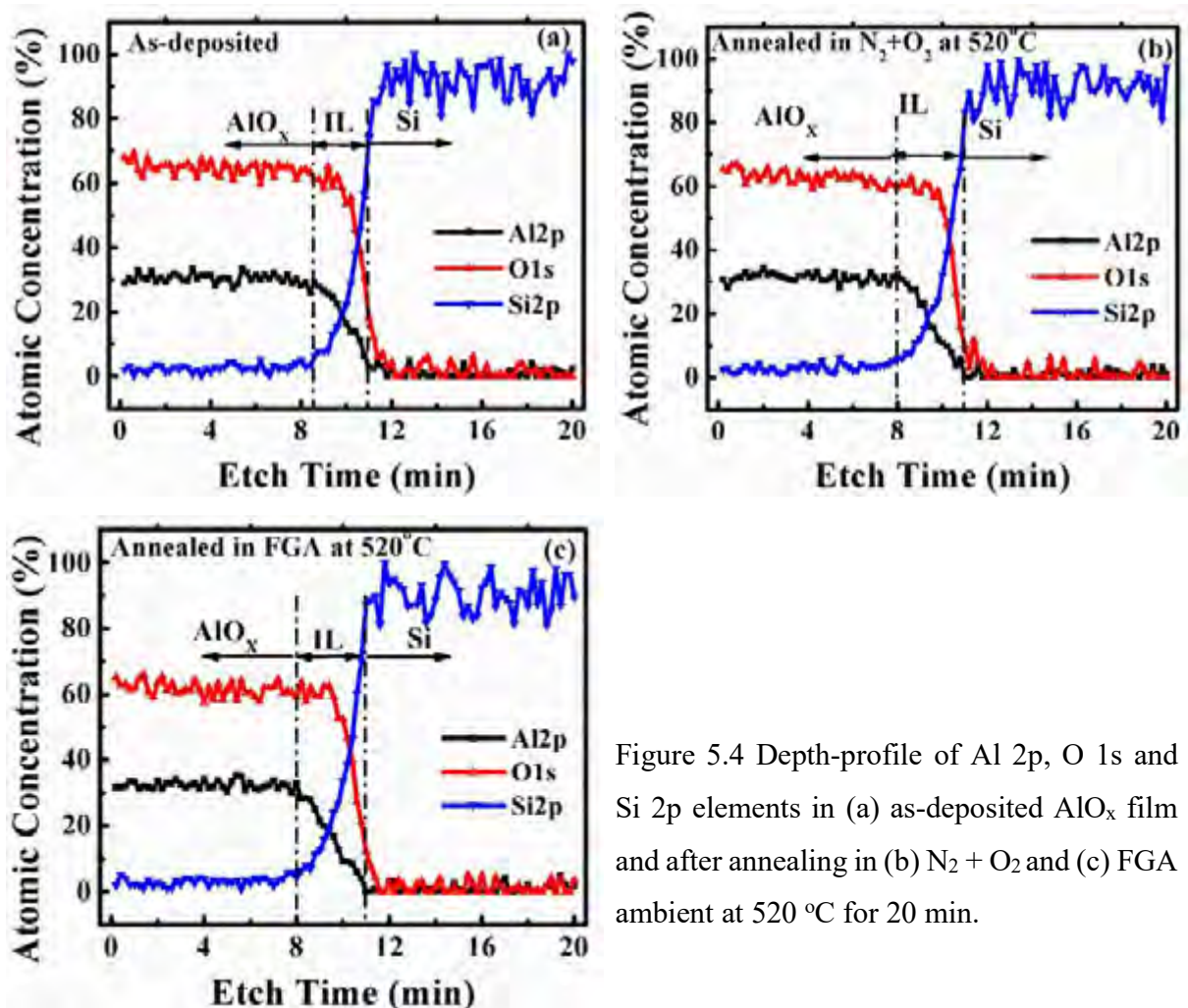
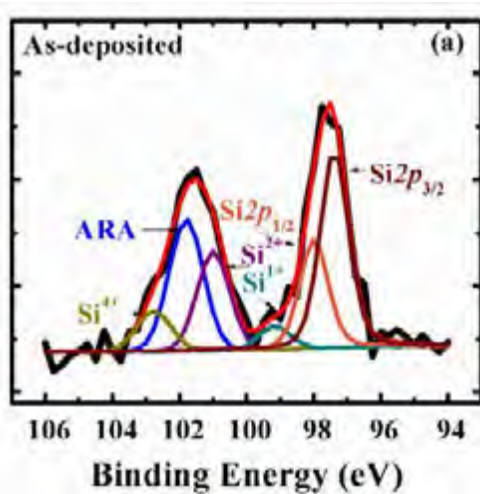


Figure 5.4 Depth-profile of Al 2p, O 1s and Si 2p elements in (a) as-deposited  $AlO_x$  film and after annealing in (b)  $N_2 + O_2$  and (c) FGA ambient at 520 °C for 20 min.

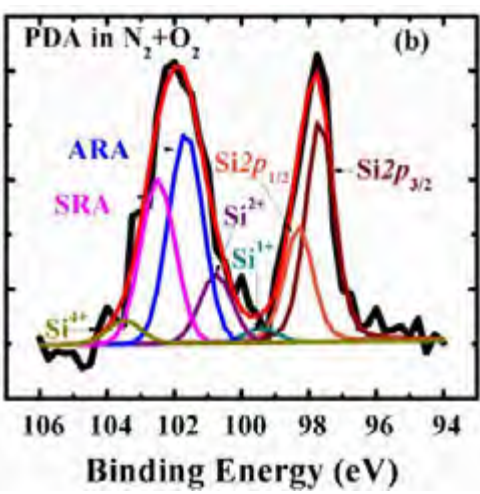
In the bulk of the  $\text{AlO}_x$  region near top surface, the concentration of O is between 60-70 atomic (%) and Al concentration is between 35-38 atomic (%), this indicates a sub-stoichiometric, oxygen rich film. In the IL region, a gradual decrease in Al and O concentration and increase in Si concentration are observed. As also discussed in chapter 4, the composition in the IL is in the form of aluminum silicate.

To gain better insight on the chemical composition w.r.t. distribution of intermediate oxidation states of Si  $2p$  in the IL region of these films, XPS data were studied in more details. Different intermediate oxidation states are termed as  $\text{Si}^{n+}$ , where  $n = 1, 2, 4$ , i.e.,  $\text{Si}^{1+}$  as  $\text{Si}_2\text{O}$ ,  $\text{Si}^{2+}$  as  $\text{SiO}$ , and  $\text{Si}^{4+}$  as  $\text{SiO}_2$  are used here to fit the Si  $2p$  signal [137]. The XPS spectra of Si  $2p$  fitted for different intermediate oxidation states in the IL region (at 46\_Depth Level) of  $\text{AlO}_x/\text{c-Si}$  for as-deposited film and film annealed in  $\text{N}_2 + \text{O}_2$  and FGA ambients at 520 °C are shown in Figure 5.5 (a), (b) and (c), respectively. The Si  $2p$  spectra was fitted using XPSPEAK 4.1 software, where the baseline correction was applied using Shirley integration method and the FWHM and GL was kept constant during the peak fitting [129]. As shown in Figure 5.5, the spectra of Si  $2p$  for as-deposited and films annealed in  $\text{N}_2 + \text{O}_2$  and FGA were fitted for 46\_depth level at IL region of  $\text{AlO}_x/\text{c-Si}$ , while the other depth level spectra fitting are not shown here.

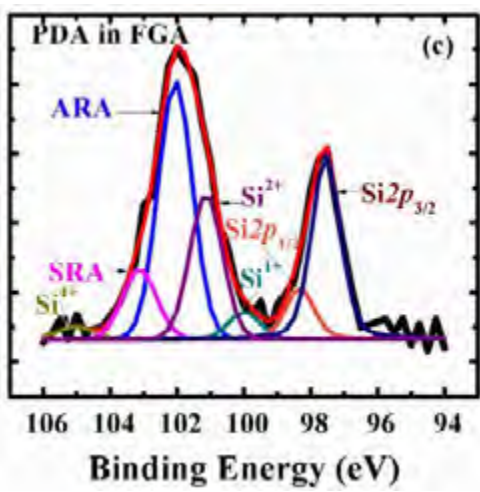
As shown in Figure 5.5, the Si  $2p$  spectra for different samples are fitted with different peaks which are identified as  $\text{Si}^0$  (bulk Si),  $\text{Si}^{1+}$ ,  $\text{Si}^{2+}$  and  $\text{Si}^{4+}$ . While the peaks marked as aluminium-oxygen rich aluminosilicate (ARA) and silicon-oxygen rich aluminosilicate (SRA) are also identified in between the binding energy of 101.5 to 103 eV, as different forms of aluminosilicate [138]. It was also reported by Zhang et al. that the Si  $2p$  peak at 102.66 eV may appear either due to  $\text{SiO}_x$  or Si-O-Al [139]. The peak position (eV) and corresponding peak area fitted by XPSPEAK 4.1 software is also given in Table next to Figure 5.5 (a), (b) and (c). The core level Si  $2p$  spectrum, i.e.,  $\text{Si}^0$  (bulk Si) state can be further decomposed into two peaks  $\text{Si } 2p_{1/2}$  and  $\text{Si } 2p_{3/2}$  with the intensity ratio 1:2 and a spin-orbit splitting of 0.63 eV. The same FWHM of 1 eV with Gaussian-Lorentzian (GL) of 25 % for fitting these peaks [137,140,141]. The silicon intermediate oxide states are fitted using pure Gaussian peak with full width at half maximum (FWHM) of 1.1, 1.15 and 1.2 eV for  $\text{Si}^{1+}$ ,  $\text{Si}^{2+}$  and  $\text{Si}^{4+}$ ,respectively and GL of 0 %. The oxide peaks named as ARA and SRA in between  $\text{Si}^{2+}$  and  $\text{Si}^{4+}$  was fitted using FWHM of 1.2 eV and GL of 0 %.



Peak	Position (eV)	Area
Si 2p <sub>3/2</sub>	97.357	1059.288
Si 2p <sub>1/2</sub>	97.959	666.101
Si <sup>1+</sup>	99.128	135.494
Si <sup>2+</sup>	100.942	521.225
ARA	101.762	835.331
Si <sup>4+</sup>	102.745	254.974



Peak	Position (eV)	Area
Si 2p <sub>3/2</sub>	97.67	1214.813
Si 2p <sub>1/2</sub>	98.300	630.897
Si <sup>1+</sup>	99.420	79.487
Si <sup>2+</sup>	100.760	382.564
ARA	101.660	1231.724
SRA	102.490	963.232
Si <sup>4+</sup>	103.490	139.202



Peak	Position (eV)	Area
Si 2p <sub>3/2</sub>	97.545	1574.969
Si 2p <sub>1/2</sub>	98.324	438.768
Si <sup>1+</sup>	99.989	229.070
Si <sup>2+</sup>	101.129	1280.476
ARA	102.050	2376.485
SRA	103.118	644.394
Si <sup>4+</sup>	105.041	120.117

Figure 5.5 The Si 2p XPS spectra fitted for different intermediate oxidation states in the IL region of  $AlO_x/c-Si$  for as-deposited and annealed  $AlO_x$  films. The spectra is shown for only at one depth level (46\_Depth Level) for clarity.

As shown in Figure 5.5, the core-level peak of Si  $2p$  spectrum, i.e.,  $\text{Si}^0$  (bulk Si), was decomposed into two peaks  $\text{Si } 2p_{1/2}$  and  $\text{Si } 2p_{3/2}$  present at different binding energy (eV). Such decomposition of  $\text{Si}^0$  at various depth level in the bulk of Si, IL and  $\text{AlO}_x$  region was performed for different samples. In Figure 5.6, the peak position of  $\text{Si } 2p_{3/2}$  was obtained through fitting at different #\_Depth Level in  $\text{AlO}_x$  film, IL and c-Si region are shown for different samples.

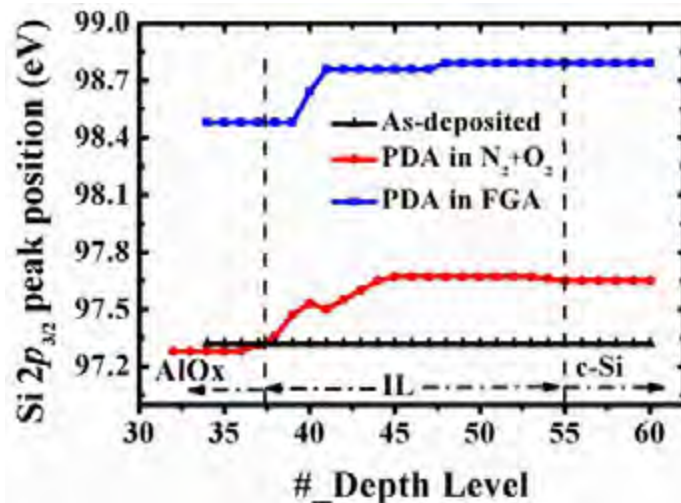


Figure 5.6 The  $\text{Si } 2p_{3/2}$  peak position of  $\text{Si}^0$  (bulk) for core level  $\text{Si } 2p$  at different #\_Depth Level for as-deposited  $\text{AlO}_x$  film and after annealing in  $\text{N}_2 + \text{O}_2$  and FGA ambients at 520 °C.

As shown in Figure 5.6, the peak position of  $\text{Si } 2p_{3/2}$  seems to be shifting to high energy value for annealed samples. The abrupt shift of entire  $\text{Si } 2p_{3/2}$  spectrum by 0.3 eV was observed for FGA annealed sample in the IL region, which may be related to the presence of atomic H from the annealing ambient [142]. The similar result was reported by Gunther et al., which shows a shift in core-level  $\text{Si } 2p$  by 0.3 eV towards higher energy as atomic H saturates dangling “Si-” bonds, from the atomic deuterium annealing of  $\text{SiO}_2$  film (5 nm) grown on Si [142]. Another report by Himpel et al., studied the effect of  $\text{H}_2$  ambient annealing in 3 nm  $\text{SiO}_2$  film grown on Si substrate, which shows the distribution of intermediate oxidation states remains un-affected by  $\text{H}_2$  annealing [141]. As shown in Figure 5.6, for  $\text{N}_2 + \text{O}_2$  annealed film, the shift of  $\text{Si } 2p_{3/2}$  spectrum is not as abrupt as FGA annealed film and while the overall shift is also low, the reason behind this difference is not very clear at this point. The observation on core-level shift to improvement in interface quality after annealing is consistent with the result of  $D_{it}$  reduction for annealed films as shown in Figure 4.2 in previous chapter.

Similarly, in the IL region of as-deposited and annealed  $\text{AlO}_x$  films, the position of intermediate oxidation states in-terms of shift in binding energy with respect to reference peak Si  $2p_{3/2}$  at various #\_Depth Level are shown in Figure 5.7 (a), (b) and (c), respectively.

Figure 5.7 shows, the binding energy peak shift are in the range of 2-6.5 eV for different intermediate oxidation states with respect to core-level Si  $2p_{3/2}$  peak, for all the samples. This shift to higher energy was related to oxidation of Si [143]. As shown in Figure 5.7 (b) and (c), the distribution of oxide states are relatively smooth for annealed films as compared to as-deposited  $\text{AlO}_x$  film which is more scattered, in Figure 5.7 (a). The smooth distribution of oxide states can be attributed to saturation of dangling “Si-” bonds by hydrogen present in FGA ambient and oxygen present in  $\text{N}_2 + \text{O}_2$  ambient after annealing in 520 °C, as also discussed earlier.

Figure 5.7, the distribution of  $\text{Si}^{4+}$  (i.e.,  $\text{SiO}_2$ ) state is present throughout IL for as-deposited and FGA annealed samples, whereas in  $\text{N}_2 + \text{O}_2$  annealed film the  $\text{Si}^{4+}$  is seen only in smaller segment of the IL. This may partly explain the reason for less number of negative  $Q_f$  in as-deposited and FGA annealed film. Since the  $\text{SiO}_2$  has positive  $Q_f$  which compensates the negative  $Q_f$  in  $\text{AlO}_x$  film and hence decreases the net negative  $Q_f$  in  $\text{AlO}_x$  film for as-deposited and FGA annealed samples [144].

The relative contribution of individual intermediate oxidation states present in the IL region of as-deposited and annealed  $\text{AlO}_x$  films, are given in Table 5.1. The data shows, contribution of  $\text{Si}^0$  (i.e., Si  $2p_{3/2}$ ) in as-deposited  $\text{AlO}_x$  film is relatively higher by ~ 2 % as compared to both the annealed films. This support the result of EELS spectra in Figure 5.2 (d), which shows the presence of Si L<sub>2,3</sub> signal at 99.4 eV throughout the IL of as-deposited film. The  $\text{Si}^{1+}$  (i.e.,  $\text{Si}_2\text{O}$ ) oxidation state contribution is observed to be slightly higher by 1-2 % in as-deposited and FGA annealed  $\text{AlO}_x$  film as compared  $\text{N}_2 + \text{O}_2$  annealed film. The contribution of  $\text{Si}^{2+}$  (i.e.,  $\text{SiO}$ ) is about 4 % higher in as-deposited and  $\text{N}_2 + \text{O}_2$  annealed film as compared to FGA annealed film. The contribution of  $\text{Si}^{4+}$  (i.e.,  $\text{SiO}_2$ ) is about two times higher in as-deposited and FGA annealed  $\text{AlO}_x$  film as compared to  $\text{N}_2 + \text{O}_2$  annealed  $\text{AlO}_x$  film, as discussed earlier, the contribution of  $\text{Si}^{4+}$  leads to reduction of net negative  $Q_f$ . The sub-oxides states known as ARA and SRA, the contribution of ARA higher in  $\text{N}_2 + \text{O}_2$  annealed film by ~ 5 % and the contribution of SRA is higher in FGA annealed film by ~ 15-20 % as compared to  $\text{N}_2 + \text{O}_2$  annealed and as-deposited films.

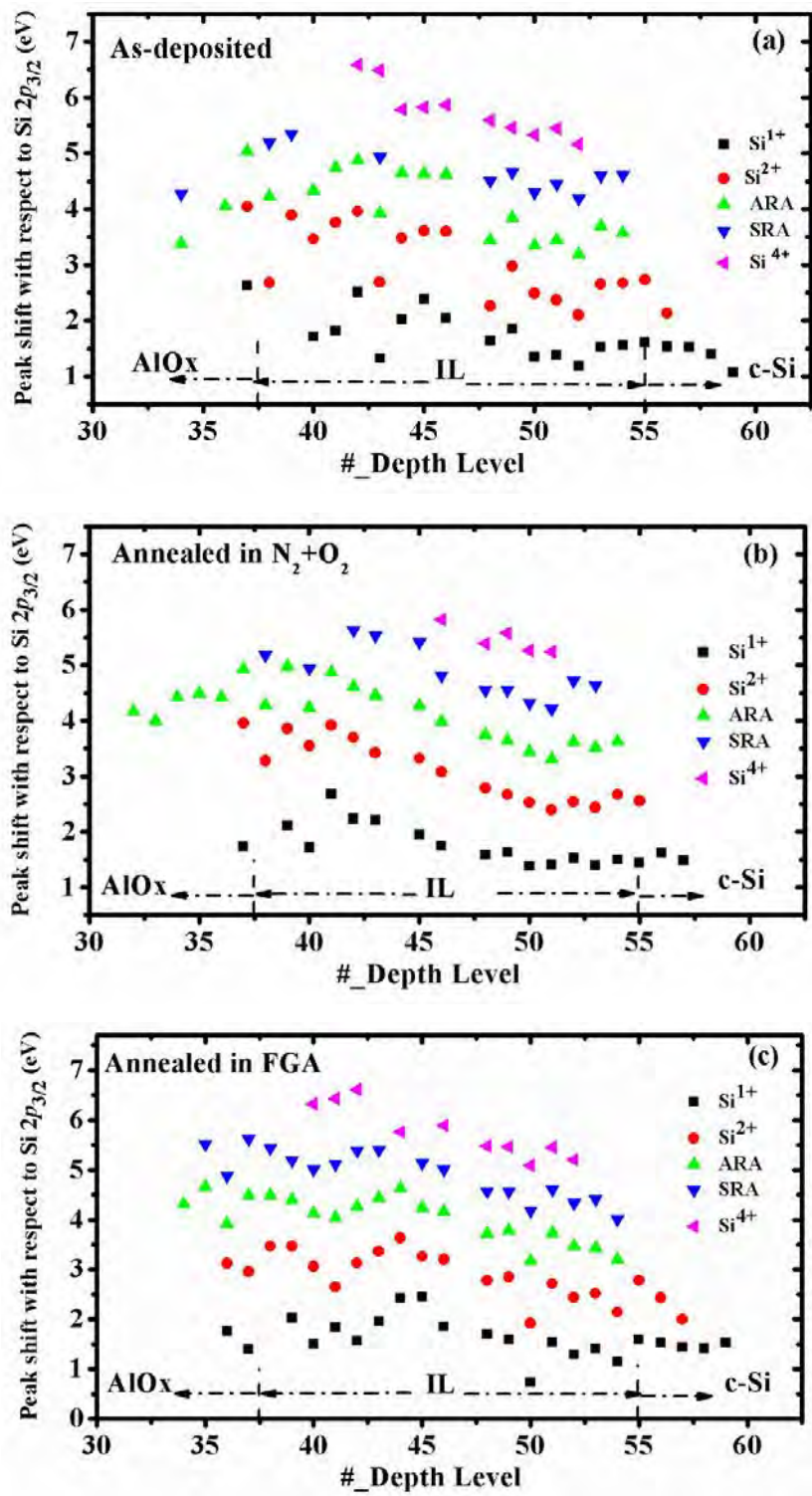


Figure 5.7 Different intermediate oxidation states in-terms of shift in binding energy (eV) with respect to Si  $2p_{3/2}$  peak at #\_Depth Level in IL of (a) as-deposited  $AlO_x$  film and  $AlO_x$  film (b) annealed in  $N_2 + O_2$  ambient and (c) FGA ambient at  $520^{\circ}C$ .

Table 5.1 The relative contribution of intermediate oxidation states for different samples.

Samples	Relative contribution of intermediate oxidation states for different samples (%)					
	Si <sup>0</sup>	Si <sup>1+</sup>	Si <sup>2+</sup>	ARA	SRA	Si <sup>4+</sup>
<b>As-deposited</b>	34.95	33.02	34.57	24.8	30.03	40.16
<b>PDA in N<sub>2</sub> + O<sub>2</sub></b>	32.63	32.7	34.72	39.7	25.54	20.47
<b>PDA in FGA</b>	32.42	34.29	30.71	35.5	44.43	39.37

Figure 5.8 (a) and (b), shows the relative contribution and distribution of ARA and SRA sub-oxide states in different samples at #\_Depth Level in the IL region, respectively. For N<sub>2</sub> + O<sub>2</sub> annealed AlO<sub>x</sub> film, ARA is enhanced and the SRA states is suppressed at IL near AlO<sub>x</sub> region. The presence of aluminum silicate at the interface of AlO<sub>x</sub>/c-Si was also discussed in chapter 4.

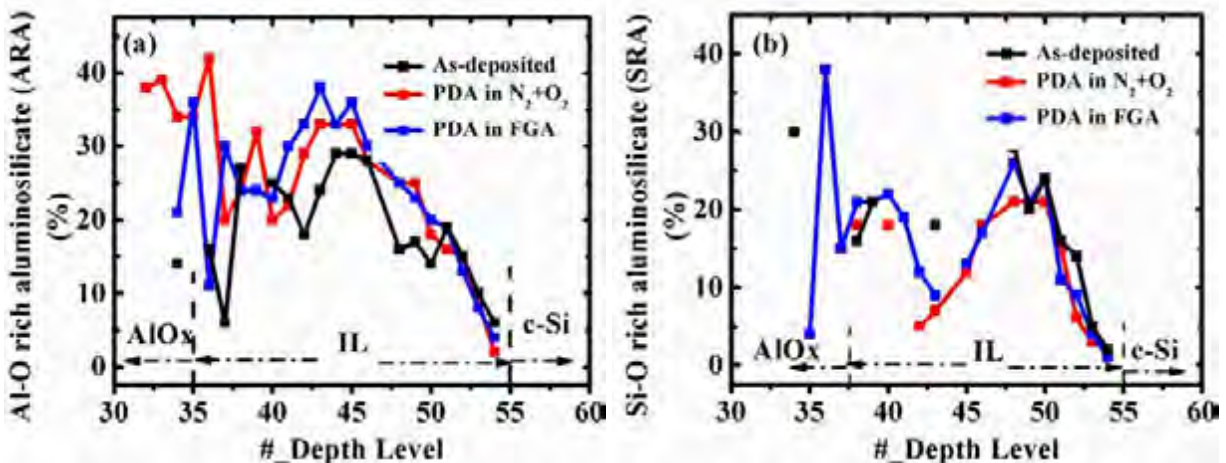


Figure 5.8 The presence (%) and distribution of (a) Al-O rich aluminosilicate (ARA) and (b) Si-O rich aluminosilicate (SRA) sub-oxide states in different samples at #\_Depth Level in the IL region.

## 5.5 FTIR investigation of the films

The absorbance spectra are obtained using FTIR spectroscope in the normal transmission mode at the 4000-450 cm<sup>-1</sup> wave number range for different samples, as shown in Figure 5.9.

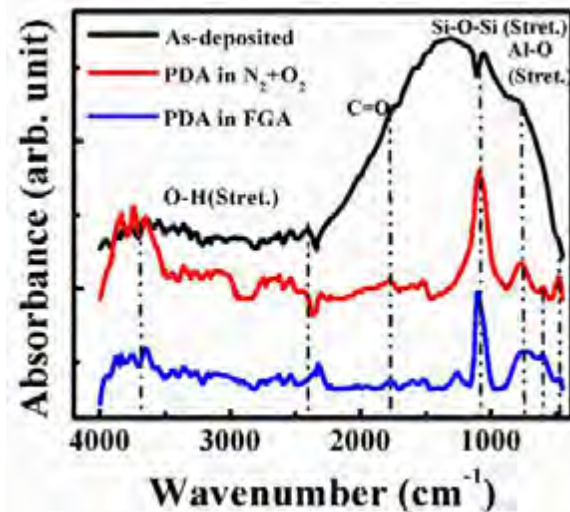


Figure 5.9 Absorbance spectra for as-deposited and annealed AlO<sub>x</sub> film in N<sub>2</sub> + O<sub>2</sub> and FGA ambient at 520 °C, using FTIR measurement. “Stret.” stands for stretching mode.

The background spectra was subtracted using same un-deposited c-Si wafer prior to measurement, so that the absorbance spectra shows vibration peaks related to deposited film only. The peak position and corresponding peak assignment for as-deposited and annealed samples are given in Table 5.2.

The broad peak at 480 cm<sup>-1</sup> corresponds to Al-O stretching are present in all three samples, with asymmetrical structure for as-deposited and FGA annealed AlO<sub>x</sub> film, while it is symmetrical and sharp for N<sub>2</sub> + O<sub>2</sub> annealed AlO<sub>x</sub> film [145]. The broadness in the spectra is related to motion of both Al and O elements, whereas the sharpness of spectra is related to O motion only [146-150]. An asymmetrical peak at 600 cm<sup>-1</sup> corresponding to Si is also present in all samples [135]. The feature peak positioned at 630 cm<sup>-1</sup> are present in both the annealed samples, which are related to O-Al-O bending mode [135,146,151]. The peak at 750 cm<sup>-1</sup> corresponds to Al-O stretching mode of condensed AlO<sub>4</sub> tetrahedra, present in N<sub>2</sub> + O<sub>2</sub> annealed AlO<sub>x</sub> film and the asymmetrical and broader peak for as-deposited and FGA annealed films is seen [147,148].

Table 5.2 The peak position and respective chemical bonds associated with it, for as-deposited and annealed AlO<sub>x</sub> film in N<sub>2</sub> + O<sub>2</sub> and FGA ambient at 520 °C.

Peak position (cm <sup>-1</sup> )	Chemical bond	Sample and peak type			References
		As-deposited	N <sub>2</sub> + O <sub>2</sub>	FGA	
480	Al-O Stret. mode	Asym	Sym	Asym	145
630	O-Al-O bending mode	No	Sym	Asym	135,146,151
750	Al-O Stret. mode ['condensed' Tetrahedral AlO <sub>4</sub> ]	Asym	Sym	Asym	135,144,147 ,148
1090	Si-O-Si	No	Sym	Sym	135,144
1062	Si-O-Si	Asym	No	No	135,144

\*Stret. : stretching mode, Asym.: asymmetric peak, Sym.: symmetric, No: not present.

A sharp and symmetrical peak at 1090 cm<sup>-1</sup> corresponds to Si-O-Si stretching mode is observed for annealed films. The appearance of peak at 1090 cm<sup>-1</sup> (Si-O-Si stretching mode), shows that an interfacial oxide is found at the AlO<sub>x</sub>/c-Si interface, as a result of diffusion of oxygen from AlO<sub>x</sub> film or diffusion of excess oxygen present in PDA ambient which reacts with the c-Si surface [135]. For as-deposited AlO<sub>x</sub> film, the broad asymmetric peak is positioned at 1060 cm<sup>-1</sup> can be attributed to the lack of formation of Si-O bond at the interface [134,135]. From the FTIR measurement the presence of interface in the form of silicate is confirmed and the peak positioned at 750 cm<sup>-1</sup> related to Al-O stretching mode of condensed AlO<sub>4</sub> tetrahedra for all the three samples are evident from this experiment.

## 5.6 Band-gap energy measurement using low-loss EELS spectra

The EELS can be used to assess the E<sub>BG</sub> of the film in low-loss regime < 10 eV with a high spatial resolution, as shown in Figure 5.10 [131,132]. Since the EELS spectra consists of zero-loss peak at 0 eV, which seems more intense due to elastically scattered electrons through atomic nuclei interaction causing very small energy loss. The intense energy distribution at zero-loss peak was mainly due to electron source, hence need to be removed by subtracting the reflected tail of the

negative part of the zero-loss intensity [130]. The single scattering distribution was then extracted by Fourier-log deconvolution method [91]. This energy distribution at low energy are due to inelastic scattering by electrons from conduction and valance bands. The  $E_{BG}$  is calculated by the equation used for traditional semiconductors, as shown in eq. (5.1) [132],

$$\alpha = A(E - E_{BG})^n/E \quad (5.1)$$

where,  $\alpha$  is optical absorption coefficient which was calculated using Kramers-Kronig analysis [130],  $A$  is a constant,  $E = h\nu$  represents photon energy and  $n = 1/2$  for allowed direct transition. The  $E_{BG}$  for different samples can be obtained from the x-axis intercept of the linear fit between  $(\alpha \cdot E)^2$  versus  $E$  plots, are shown in Figure 5.10 [132,152].

Figure 5.10 (a,b,c), shows the low-loss EELS spectra for  $E_{BG}$  measurement in  $\text{AlO}_x$  bulk region, whereas Figure 5.10 (d,e,f), shows low-loss EELS spectra for  $E_{BG}$  measurement in IL region of as-deposited  $\text{AlO}_x$  film and film annealed in  $\text{N}_2 + \text{O}_2$  and in FGA at  $520^\circ\text{C}$ , respectively. It was reported that the low-loss EELS measurement may underestimate the value of  $E_{BG}$  due to the Cerenkov radiation effect [153-155]. To negate the effect of Cerenkov radiation, Gu et al. reported  $E_{BG}$  values for film thicknesses  $< 0.5 \lambda$ , here  $\lambda$  is the mean free path of the electron in the material [131]. In these experiments the low-loss EELS spectra was acquired for thickness between  $0.2 \lambda$  to  $0.4 \lambda$ , hence the Cerenkov radiation effects will not be very significant. The same method and experimental conditions were also tested successfully in  $\text{ZnO}$  and  $\text{ZnO}_{1-x}\text{S}_x$  alloys to obtain accurate  $E_{BG}$  values [156,157].

For the as-deposited  $\text{AlO}_x$  film the  $E_{BG}$  of 2.6 eV is measured at  $\text{AlO}_x$  region by low-loss EELS method, as shown in Figure 5.10 (a). After annealing of  $\text{AlO}_x$  film in  $\text{N}_2 + \text{O}_2$  and FGA ambient, an increase in the  $E_{BG}$  value of  $\text{AlO}_x$  region to 4.4 eV is shown in Figure 5.10 (b,c). This value of  $E_{BG}$  measured is relatively lower than the reported  $E_{BG}$  of 8.7 eV for  $\alpha\text{-Al}_2\text{O}_3$  [158]. However trends similar to those shown in Figure 5.10 were reported by Rose et al., which showed a low  $E_{BG}$  of 2.6 eV for ultra-thin amorphous  $\text{Al}_2\text{O}_3$  film formed by  $\text{Ar}/\text{O}_2$  plasma exposure on Al film grown on CoAl (100) substrate and an increase in  $E_{BG}$  value to 4.5 eV for well-ordered  $\text{Al}_2\text{O}_3$  film, after annealing at elevated temperature in the oxygen ambient [159,160]. This may suggest a structural modification of the  $\text{AlO}_x$  film after annealing at high temperature.

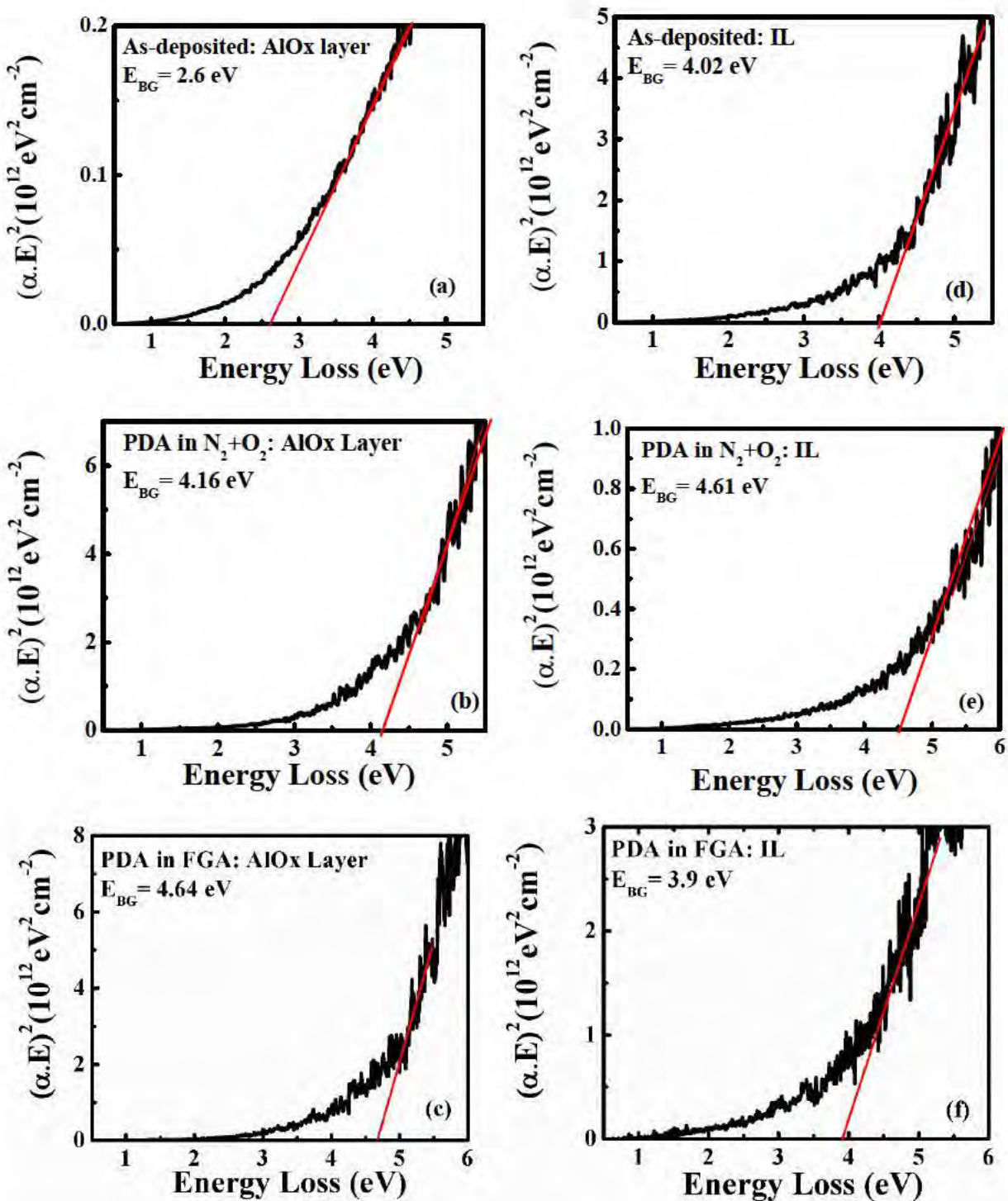


Figure 5.10 The  $E_{BG}$  measured using low-loss EELS spectra at the AlO<sub>x</sub> layer (a,b,c) and IL region (d,e,f) for: (a,d) as-deposited film, (b,e) film annealed in N<sub>2</sub> + O<sub>2</sub> and (c,f) FGA ambient at 520 °C.

While the value of low  $E_{BG}$  for RS  $\text{AlO}_x$  film to 4.4 eV as compared to  $E_{BG}$  of 8.7 eV for  $\alpha\text{-Al}_2\text{O}_3$  may be related to the defects induced in band-gap of the film [160]. As discussed in chapter 3, section 3.5, the film density of  $2.88 \text{ g.cm}^{-3}$  were obtained using XRR measurement technique after annealing, i.e., also low as compared to crystalline stoichiometric  $\text{Al}_2\text{O}_3$  film density ( $3.95\text{-}4.1 \text{ g.cm}^{-3}$ ) [108]. Hence low film density may be related to the porosity of the film which results in low  $E_{BG}$  for this film [161].

The  $E_{BG}$  is also obtained for the IL using the low-loss EELS measurement technique with high spatial resolution, shown in Figure 5.10 (d,e,f). The  $E_{BG}$  of IL (i.e., 4.02 eV) is relatively higher as compared to the  $E_{BG}$  of  $\text{AlO}_x$  layer for as-deposited film. This can be explained by bonding between Al, O and Si that may results in band gap widening, as reported by Reiche et al. [162].

## 5.7 Band-gap energy measurement using UV-Vis-NIR spectroscope

The UV-Vis-NIR measurements were performed on  $\text{AlO}_x$  films deposited on quartz wafer in normal transmission mode. Figure 5.11 (a,b,c), shows the Tauc plot of  $(\alpha E)^2$  versus E to acquire the  $E_{BG}$  value of the as-deposited and annealed  $\text{AlO}_x$  film in  $\text{N}_2 + \text{O}_2$  and FGA ambients at  $520^\circ\text{C}$  [94]. It should be noted that the  $E_{BG}$  obtained using UV-Vis-NIR spectroscopy gives detail of complete dielectric film deposited on quartz wafer, unlike the EELS technique where the  $E_{BG}$  can be assessed in different regions of the dielectric film as discussed earlier. However since the film is deposited in quartz for UV-Vis-NIR analysis, the IL layer in this case would be different from that in the sample analysed using EELS. So we would compare only the  $E_{BG}$  of the  $\text{AlO}_x$  obtained by the two techniques. From Figure 5.11, the  $E_{BG}$  for different samples can be obtained from the x-axis intercept of the linear fit between  $(\alpha.E)^2$  versus E plots.

As shown in Figure 5.11 (a), for the as-deposited  $\text{AlO}_x$  film, an  $E_{BG}$  of 3.5 eV is obtained. Similar to the result of EELS, the UV-Vis-NIR measurement also shows an increase in the  $E_{BG}$  value to 4.3-4.4 eV after annealing of  $\text{AlO}_x$  film in  $\text{N}_2 + \text{O}_2$  and FGA ambients, as shown in Figure 5.11 (b) and (c), respectively. The discussion on structural modification of the  $\text{AlO}_x$  film after annealing at high temperature, stand here as well.

The  $E_{BG}$  values obtained using the techniques mentioned for as-deposited film and the film annealed in  $N_2 + O_2$  and FGA ambients are given in Table 5.3, for comparison. The as-deposited film shows low  $E_{BG}$  of 2.5 eV as compared to annealed film, which also suggest the modification of the film after annealing and so as the improvement in the film quality. With the low-loss EELS spectra the  $E_{BG}$  between 4-4.5 eV is obtained for individual regions, i.e.,  $AlO_x$  and IL. The  $E_{BG}$  between 4.2-4.4 eV is measured by UV-Vis-NIR spectroscopy for the  $AlO_x$  film after PDA, which is lower than the value reported for stoichiometric amorphous  $Al_2O_3$  film, i.e., 8.7 eV [163].

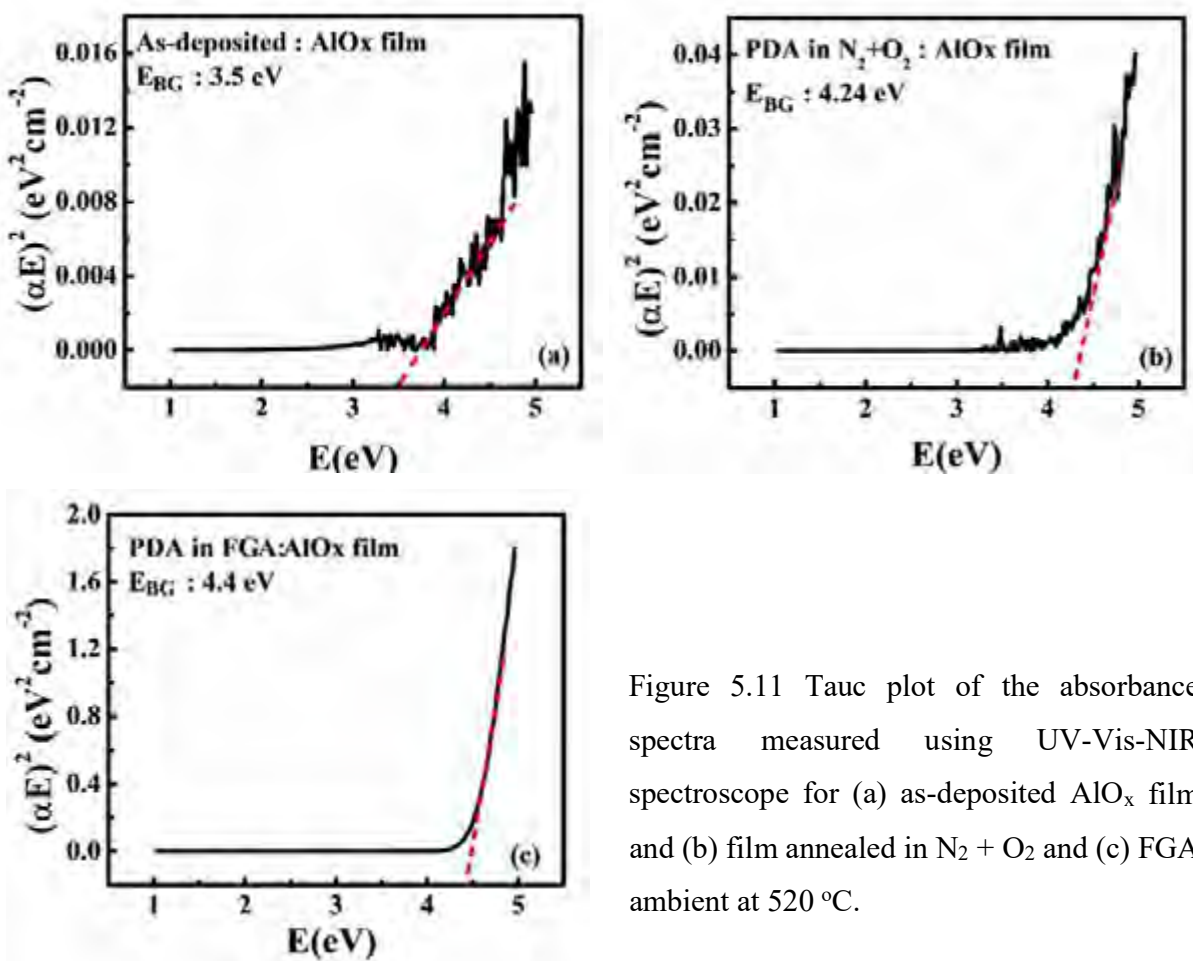


Figure 5.11 Tauc plot of the absorbance spectra measured using UV-Vis-NIR spectroscope for (a) as-deposited  $AlO_x$  film and (b) film annealed in  $N_2 + O_2$  and (c) FGA ambient at 520 °C.

Table 5.3 Values of AlO<sub>x</sub> film E<sub>BG</sub>, measured using low-loss EELS spectra and UV-Vis-NIR spectroscope for as-deposited and annealed films in N<sub>2</sub> + O<sub>2</sub> and FGA ambients at 520 °C.

Samples	Low-loss EELS measurement	UV-Vis-NIR measurement
As-deposited	2.6 eV	3.5 eV
PDA in N <sub>2</sub> +O <sub>2</sub>	4.0 eV	4.2 eV
PDA in FGA	4.6 eV	4.4 eV

## 5.8 Conclusion

In this chapter we have studied the origin and distribution of Q<sub>f</sub> in the pulsed-DC RS AlO<sub>x</sub> film deposited on p-type c-Si, using EELS measurement technique. It is observed that T and O coordinated Al L<sub>2,3</sub> peaks are present in this AlO<sub>x</sub> film. From the EELS measurement, the shift in T and O peaks of Al L<sub>2,3</sub> to higher energy for all the three samples are observed in the IL region of at AlO<sub>x</sub>/c-Si interface. The peak at 106.2 eV is present throughout the IL region, which is corresponding to the oxidation state of Si. In this films, the T/O peak intensity ratio in the IL region is observed to increase after annealing, which signifies an improvement in negative Q<sub>f</sub> values. Similar observation was also reported by Hoex et al. on PA-ALD Al<sub>2</sub>O<sub>3</sub> film deposited on c-Si [44,128]. However in our case, the increase in T/O peak intensity ratio is higher in the middle of the IL region for FGA annealed film, as compared to N<sub>2</sub> + O<sub>2</sub> annealed film. While the T/O peak intensity ratio is higher at the IL/c-Si interface for the N<sub>2</sub> + O<sub>2</sub> film. From this result, it may be concluded that the fixed charge distribution in the FGA and N<sub>2</sub> + O<sub>2</sub> films are significantly different.

Through XPS measurement, the distribution of intermediate oxidation states of Si 2p in the IL region of these films are studied in detail. The following intermediate oxidation states are identified at the IL region: Si<sup>1+</sup> (Si<sub>2</sub>O), Si<sup>2+</sup> (SiO) and Si<sup>4+</sup> (SiO<sub>2</sub>) with the peak shifts between 2 to 6.5 eV with respect to core-level (Si<sup>0</sup>), i.e., Si 2p<sub>3/2</sub> for all the samples, as a result of oxidation of the Si elements. Two significant peaks are identified between the binding energy of 102 eV-103 eV, named as ARA and SRA, can be a combination of Al-O-Si elements. The presence of Si<sup>4+</sup> (i.e., SiO<sub>2</sub>) related peak in as-deposited and FGA annealed AlO<sub>x</sub> films are higher as compared to

$\text{N}_2 + \text{O}_2$  annealed film, which may partly explains the reason of reduction in net negative  $Q_f$  in  $\text{AlO}_x$  film.

From the FTIR measurement the peak positioned at  $750\text{ cm}^{-1}$  related to Al-O stretching mode of condensed  $\text{AlO}_4$  tetrahedra are present in all the three samples. A sharp and symmetrical peak at  $1090\text{ cm}^{-1}$ , corresponding to Si-O-Si stretching mode, is observed for annealed films. For as-deposited  $\text{AlO}_x$  film, the broad asymmetric peak positioned at  $1060\text{ cm}^{-1}$  can be attributed to the lack of formation of Si-O bond at the interface.

The  $E_{BG}$  obtained for these films using both low-loss EELS spectra and UV-Vis-NIR spectroscopy, which shows a relatively low  $E_{BG}$  of  $2.6\text{ eV}$  for as-deposited  $\text{AlO}_x$ . After annealing, the  $E_{BG}$  of the film improves to  $4.5\text{ eV}$ , which also suggest the modification and improvement of the film quality after annealing. However the value of  $E_{BG}$  measured is relatively lower than the  $8.7\text{ eV}$  reported for  $\alpha\text{-Al}_2\text{O}_3$  [163], which may be related to low film density of  $2.88\text{ g.cm}^{-3}$  for this film and hence the porosity in the film results in low  $E_{BG}$  [161].

In the next chapter we will discuss the optimization of different process conditions by varying different process parameters in the pulsed-DC RS system, and assess the film behaviour by applying the optimized PDA conditions which is proved as most important process to activate the passivation quality of these films.

# **Chapter 6. Impact of Deposition Process Conditions on the Quality and Interface between Pulsed-DC Reactive Sputtered AlO<sub>x</sub> and Silicon**

## **6.1 Introduction**

In this chapter we have investigated the impact of various process conditions on the AlO<sub>x</sub> film deposited on p-type c-Si towards the application as surface passivation layer after optimized PDA process. As stated in earlier chapters, high quality of surface passivation is related to activation of both field-effect and chemical passivation, which is achieved after the PDA process. Hence the optimized PDA condition as discussed in chapter 4, i.e., annealing in N<sub>2</sub> + O<sub>2</sub> ambient at 520 °C for 20 min was applied on the AlO<sub>x</sub> film for different process conditions. The process parameters investigated are (i) the power density, (ii) substrate temperature, and (iii) the process gas used during film deposition.

The experimental details are as follows: the films were deposited on RCA cleaned p-type silicon wafers as discussed in chapter 2, section 2.4.1. The electrical and material characterization were performed on the film deposited on p-type (100) CZ c-Si wafers with resistivity of 5 Ω.cm. For life-time measurements the films were deposited on both the sides of double-sided polished p-type (100) FZ c-Si wafer with resistivity of 7.8 Ω. cm. The τ<sub>eff</sub> was measured using Sinton WCT-120 life-time tester. Sentech SE-800 was used for thickness and

RI measurement. The cross-sectional imaging was carried out using JEOL make JEM 2100F TEM. The elemental analysis of the film was carried out using Thermo Scientific make MultiLab 2000 XPS. The MOS capacitors fabrication steps with  $\text{AlO}_x$  dielectric film were discussed in chapter 2, section 2.4.1. Keithley 4200 SCS was used for C-V and G-V measurements.

## 6.2 Impact of process power density

The  $\text{AlO}_x$  films were deposited at PD between  $0.13$  and  $1.3 \text{ W.cm}^{-2}$ , keeping the gas flow rate constant at Ar of  $10 \text{ sccm}$  and  $\text{O}_2$  of  $55 \text{ sccm}$  for these depositions. Since the variable for this experiment was PD, i.e., varied from  $0.13$  and  $1.3 \text{ W.cm}^{-2}$ , the  $\text{O}_2$  flow =  $55 \text{ sccm}$  was selected based on knee point of forward hysteresis curve for maximum PD of  $1.3 \text{ W.cm}^{-2}$ , as discussed in chapter 3, section 3.4. The Ar flow rate =  $10 \text{ sccm}$  was selected, based on the observation of good quality  $\text{AlO}_x$  film with low surface roughness as discussed in chapter 3 section 3.5.1. The  $T_{\text{ox}}$  of the  $\text{AlO}_x$  films measured using SE for various PD conditions are between  $17$ - $20 \text{ nm}$ . The deposition time set for  $\text{PD} = 0.13 \text{ W.cm}^{-2}$  as  $40 \text{ min}$ , for  $\text{PD} = 0.27 \text{ W.cm}^{-2}$  as  $25 \text{ min}$ ,  $\text{PD} = 0.41 \text{ W.cm}^{-2}$  as  $20 \text{ min}$ ,  $\text{PD} = 0.69 \text{ W.cm}^{-2}$  as  $8 \text{ min}$  and  $\text{PD} = 1.3 \text{ W.cm}^{-2}$  as  $4 \text{ min}$ . Figure 6.1(a), (b) and (c), shows the thickness of the film, deposition rate and RI of the film for different PD conditions.

Figure 6.1 (a) shows, the  $T_{\text{ox}}$  measured using SE for different PD conditions for as-deposited and annealed films. The value of  $T_{\text{ox}} = 16.8 \text{ nm}$  is obtained on low  $\text{PD} = 0.13 \text{ W.cm}^{-2}$  deposited  $\text{AlO}_x$  film and high  $\text{PD} = 1.3 \text{ W.cm}^{-2}$  deposition results in  $T_{\text{ox}} = 20 \text{ nm}$ . Since for this experiment, our focus was to obtain same thickness for all PD conditions, hence the deposition time was set as mentioned earlier. The effect of annealing on these shows almost same thickness for as-deposited and PDA films for all PD values.

Figure 6.1 (b) shows deposition rate for different PD conditions. In this case, as the thickness of the film is almost same for all the PD conditions, while the deposition time is varied. Hence the deposition rate was obtained as  $T_{\text{ox}}$  divided by the deposition time for each PD conditions. The deposition rate is observed to increase with process power, as similar trend was also discussed in chapter 3 for pulsed-DC RS technique. The highest deposition rate of  $5 \text{ nm}.\text{min}^{-1}$  was observed for film deposited at high PD of  $1.3 \text{ W.cm}^{-2}$ .

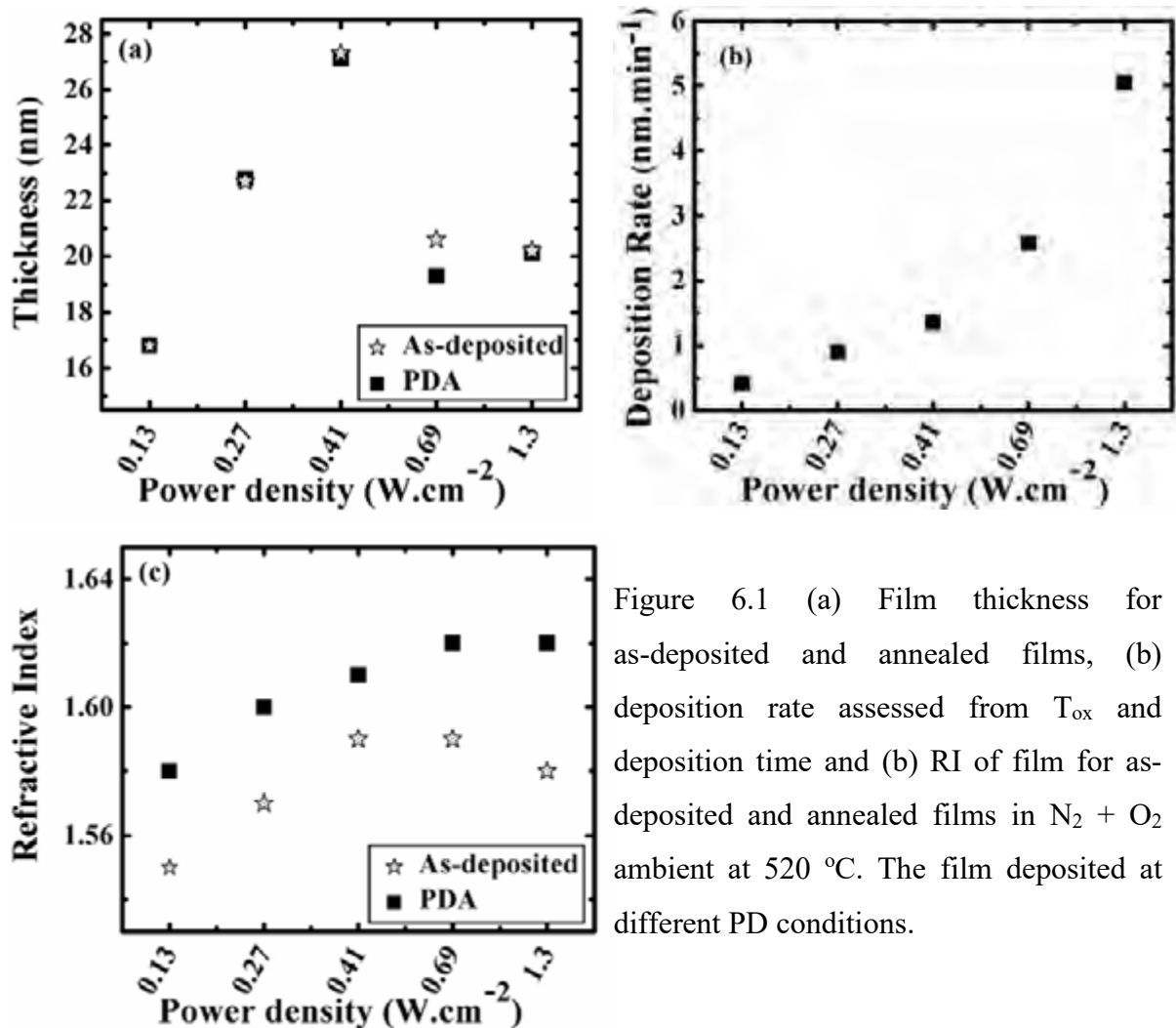


Figure 6.1 (a) Film thickness for as-deposited and annealed films, (b) deposition rate assessed from  $T_{ox}$  and deposition time and (b) RI of film for as-deposited and annealed films in  $N_2 + O_2$  ambient at 520 °C. The film deposited at different PD conditions.

This deposition system shows reasonably high rate of deposition with cost-effective film deposition. Dingemans et al. reported that  $\text{AlO}_x$  thickness in the range of 3 nm is adequate for passivation of p-type c-Si surfaces [12]. From this perspective, high power deposition looks attractive as high throughput could be used in an industrial application. However, Zang et al., reported that high power deposition in RF reactive sputtering process degrades the passivation performance of RS  $\text{AlO}_x$  films [78].

Figure 6.1 (c) shows the value of RI is improving with applied power. Since the high power process, results in  $\text{Ar}^+$  ions to accelerate with high energy, so that more atoms are sputtered from the target surface and deposited on the substrate. Further improvement in the RI value to 1.6 was observed after PDA of these films, due to improvement in film density or change in film composition, as discussed in chapter 3.

### 6.2.1 Electrical characterization

The films are characterized electrically for different PD conditions, to obtain the values of negative  $Q_f$  and  $D_{it}$  for as-deposited and annealed samples using MOS capacitors. Figure 6.2 (a) and (b) shows the C-V characteristics of the  $\text{AlO}_x$  film deposited at different PD conditions and after annealing in  $\text{N}_2 + \text{O}_2$  ambient at  $520^\circ\text{C}$  for 20 min, respectively. Figure 6.2 (c) and (d) shows, G-V characteristics of the as-deposited and annealed  $\text{AlO}_x$  film deposited at different PD conditions, respectively. These measurements were carried out at a frequency of 100 kHz.

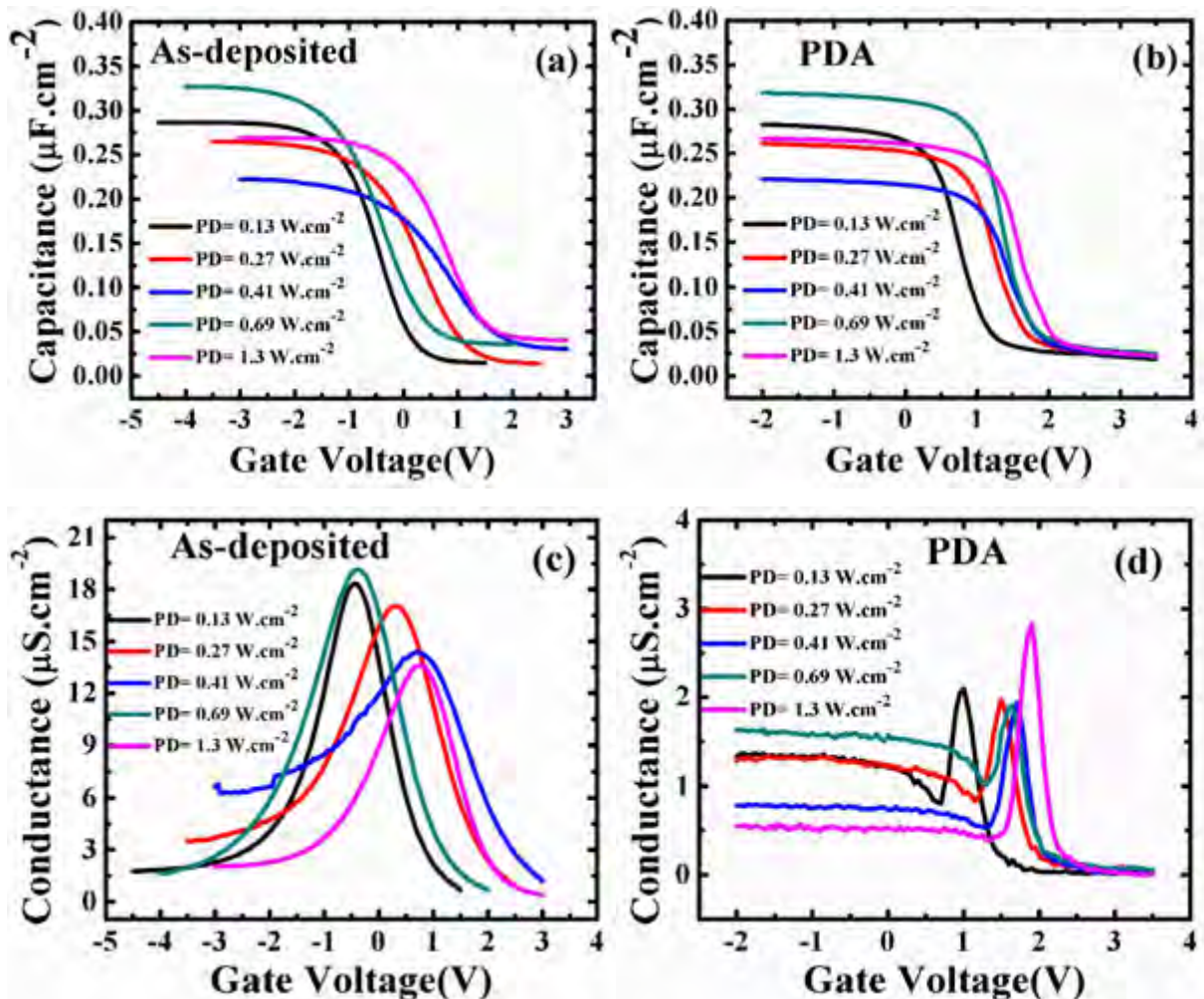


Figure 6.2 (a,b) The C-V and (c,d) G-V characteristics of MOS capacitor with film deposited at different PD between  $0.13-1.3 \text{ W} \cdot \text{cm}^{-2}$ . Film are annealed in  $\text{N}_2 + \text{O}_2$  ambient at  $520^\circ\text{C}$  for 20 min.

As shown in Figure 6.2 (a) and (b), the C-V plot for as-deposited films and annealed films deposited at different PD conditions, respectively. The difference in the  $C_{acc}$  is observed

due to difference in  $T_{ox}$  of the film. Figure 6.2 (a), shows positive shift of  $V_{FB}$  value by 0.33 V for film deposited at high PD = 1.3 W.cm<sup>-2</sup> as compared to low PD = 0.13 W.cm<sup>-2</sup> deposition, attributed to increase in negative  $Q_f$  with process power for as-deposited condition. Whereas in Figure 6.2 (b), the more positive shift of  $V_{FB}$  for annealed films was observed after annealing. As shown in Figure 6.2 (c) and (d), the conductance peak is observed to reduce significantly after annealing, which signifies an improvement in interfacial quality with reduction of  $D_{it}$  values.

The values of negative  $Q_f$  obtained from C-V plot using eq. (2.15) and the  $D_{it}$  extracted from G-V plot using eq. (2.20), are shown in Figure 6.3 (a) and (b), respectively for both as-deposited and annealed films deposited at different PD conditions.

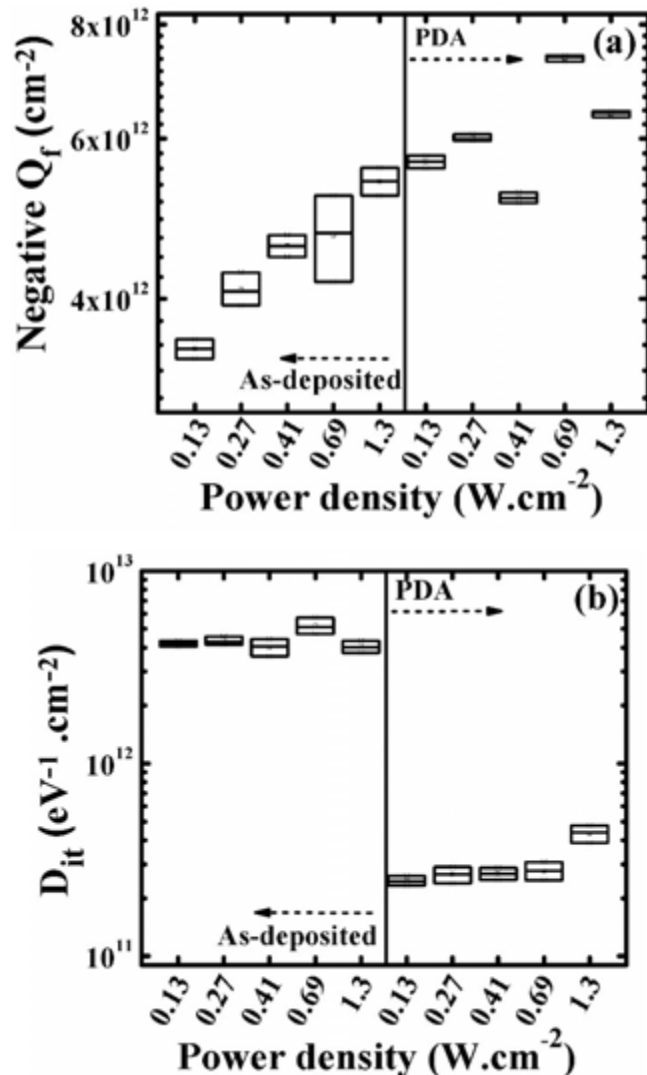


Figure 6.3 Extracted values of (a) negative  $Q_f$  and (b)  $D_{it}$  for AlO<sub>x</sub> film deposited at different PD conditions. The film was annealed in N<sub>2</sub> + O<sub>2</sub> ambient at 520 °C for 20 min.

As shown in Figure 6.3 (a), the negative  $Q_f$  value is observed to be increasing monotonously with process power for as-deposited film, with high value of negative  $Q_f = 5 \times 10^{12} \text{ cm}^{-2}$  is observed at high PD deposition. After PDA the value of negative  $Q_f$  increases further to  $5.5 \pm 1.5 \times 10^{12} \text{ cm}^{-2}$  with the tighter distributions for all PD conditions. Figure 6.3 (b) shows, the values of  $D_{it}$  is in the range of  $3 \pm 1 \times 10^{12} \text{ cm}^{-2} \cdot \text{eV}^{-1}$  for as-deposited  $\text{AlO}_x$  film and after annealing the  $D_{it}$  decreases to  $2 \pm 3 \times 10^{11} \text{ cm}^{-2} \cdot \text{eV}^{-1}$  shows an improvement in interfacial quality. However a small increase in value of  $D_{it}$  is observed at high PD deposition of  $1.3 \text{ W.cm}^{-2}$  as compared to low PD deposition after annealing.

## 6.2.2 Surface passivation

The impact of process power on the quality of surface passivation is assessed using life-time tester by measuring  $\tau_{eff}$  and calculating  $S_{eff}$  using eq. (2.29), where upper limit of  $\tau_{bulk} = 30 \text{ ms}$  is used from generalized parameterization proposed by Kerr et al. [119] as discussed in chapter 4. Figure 6.4 (a) and (b) shows the measured  $\tau_{eff}$  and calculated  $S_{eff}$  in as-deposited and annealed  $\text{AlO}_x$  films. The film was deposited at PD of  $0.13 \text{ W.cm}^{-2}$  and  $1.3 \text{ W.cm}^{-2}$ , with process time of 40 min and 4 min, respectively. The annealing of film was carried out in  $\text{N}_2 + \text{O}_2$  ambient at  $520^\circ\text{C}$  for 20 min.

As shown in Figure 6.4 (a) and (b), the result shows significant improvement obtained in terms of surface passivation quality with very low value of  $S_{eff} = 30 \text{ cm.s}^{-1}$  for film deposited at high PD of  $1.3 \text{ W.cm}^{-2}$  after annealing, whereas low PD of  $0.13 \text{ W.cm}^{-2}$  deposited film seems not so effective with value of  $S_{eff} = 107 \text{ cm.s}^{-1}$  after annealing. These result of surface passivation improvement with increase in power is contradictory to the surface passivation results shown for RF reactive sputtered  $\text{AlO}_x$  film by Zhang et al. [78]. The report shows a degradation in surface passivation quality with increase in process power, where the  $\text{AlO}_x$  film was deposited at  $220 \text{ W}$  (i.e., PD of  $4.82 \text{ W.cm}^{-2}$ ) [78]. The results presented in this work indicates that good surface passivation quality can be achieved with high deposition rate by using pulsed-DC RS technique with high PD deposition of  $\text{AlO}_x$  film.

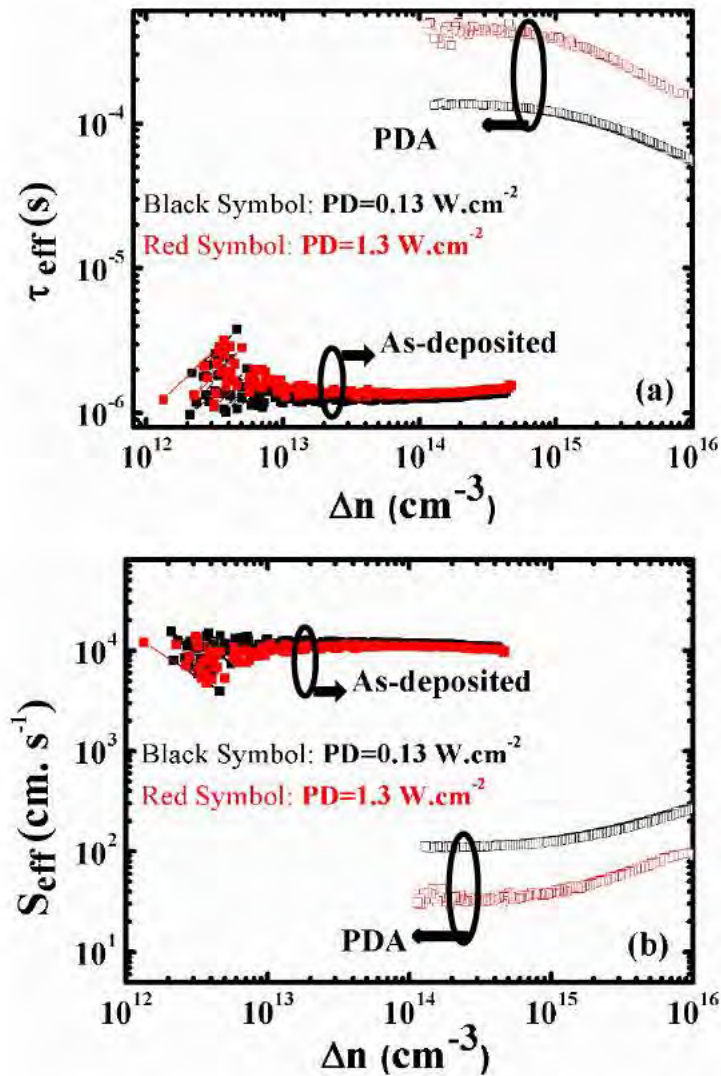


Figure 6.4 (a) Measured  $\tau_{\text{eff}}$  and (b) corresponding  $S_{\text{eff}}$  on as-deposited and annealed films deposited at  $\text{PD} = 0.13 \text{ W.cm}^{-2}$  and  $1.3 \text{ W.cm}^{-2}$ .

### 6.2.3 Physical characterization of the films

The cross-sectional TEM image of as-deposited  $\text{AlO}_x$  film deposited at low  $\text{PD} = 0.13 \text{ W.cm}^{-2}$  is shown in Figure 6.5. In this case the film deposited at low  $\text{PD} = 0.13 \text{ W.cm}^{-2}$ , and result show the IL thickness of 5.8 nm and  $\text{AlO}_x$  region thickness of 10.9 nm. A significantly thick IL is seen for as-deposited film at the interface of  $\text{AlO}_x/\text{c-Si}$  for low PD deposition. The IL layer is formed by the oxidation of the Si by the oxygen species present in the plasma. The intermixing of silicon oxide and deposited aluminum oxide due to ion bombardment leads to formation of thick IL [125]. Since the low PD deposition shows, lower deposition rate as compared to others condition, hence the time available for oxidation of Si at the interface is large, which may result in formation of relatively thick IL.

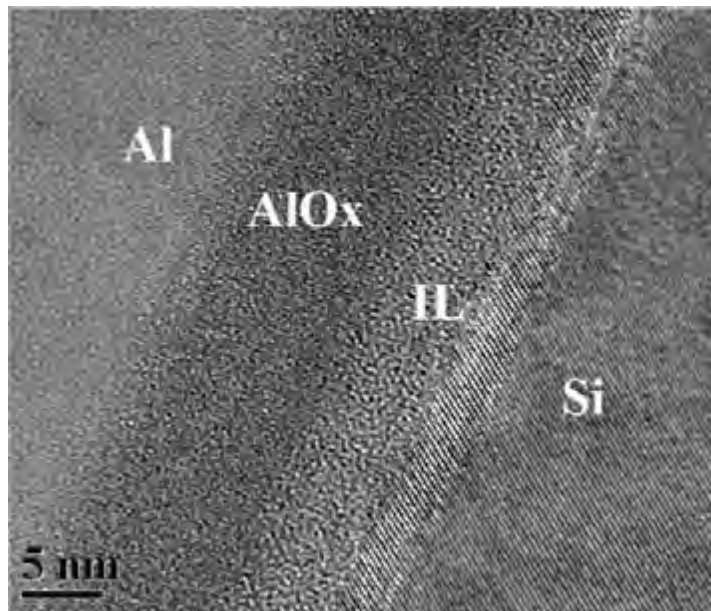


Figure 6.5 Cross-sectional TEM image of as-deposited  $\text{AlO}_x$  film deposited at low PD of 0.13  $\text{W.cm}^{-2}$ .

The depth-profile of Al 2p, O 1s and Si 2p elemental measured using depth-resolved XPS measurement technique for as-deposited and annealed  $\text{AlO}_x$  films, deposited at low PD = 0.13  $\text{W.cm}^{-2}$  and high PD = 1.3  $\text{W.cm}^{-2}$  are shown in Figures 6.6 (a,c) and (b,d), respectively. The atomic concentration (%) is plotted as a function of etch time (min).

Figure 6.6 (a) and (c) shows the depth-profile of as-deposited films deposited at low PD = 0.13  $\text{W.cm}^{-2}$  and high PD = 1.3  $\text{W.cm}^{-2}$ , respectively. It is found that the atomic ratio of O/Al is approximately 1 in the  $\text{AlO}_x$  region for these films. In Figure 6.6 (b) and (d), the depth-profile of annealed films in same deposition conditions, respectively, shows the atomic concentration of O 1s found to be increasing at the  $\text{AlO}_x$  region, hence the atomic ratio of O/Al increases for annealed films. Since the annealing was done in  $\text{N}_2 + \text{O}_2$  ambient at 520 °C, the O from the annealing ambient may diffuse into the film during the process and hence results in increase of O/Al atomic ratio. The annealed film at high PD of 1.3  $\text{W.cm}^{-2}$  also shows stoichiometric  $\text{Al}_2\text{O}_3$  is achieved with atomic O/Al ratio ~ 1.5 in the  $\text{AlO}_x$  region. In the IL region, a peak corresponding to  $\text{SiO}$  at 103 eV was observed in all the samples. The concentration of  $\text{SiO}$  profile for low PD deposition in the IL region is increasing significantly after annealing. In the IL region of all samples, the gradual decrease in Al and O atomic concentration with increase in Si atomic concentrations suggests the IL is in the form of aluminum silicate.

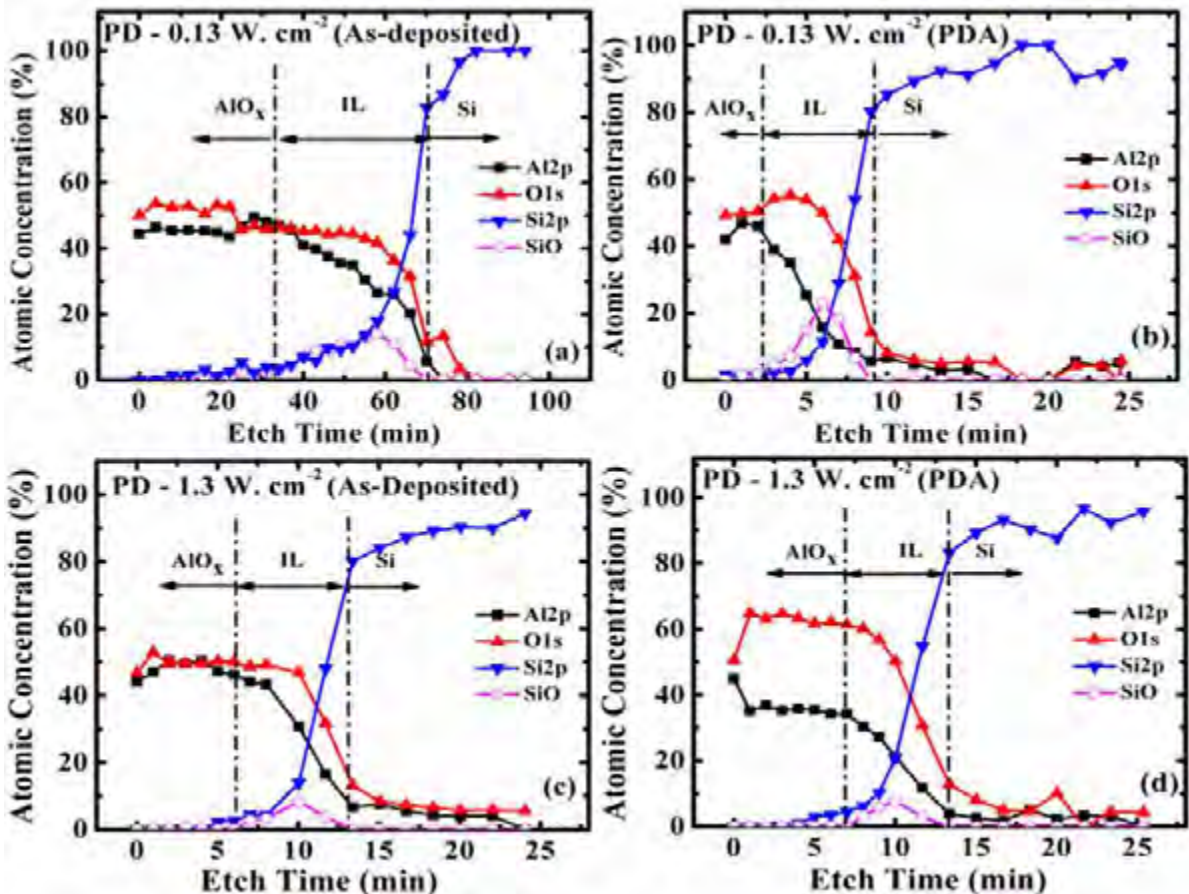


Figure 6.6 Atomic concentration of Al 2p, O 1s and Si 2p elemental depth-profiles for (a) as-deposited and (b) annealed  $\text{AlO}_x$  films deposited at low PD of  $0.13 \text{ W. cm}^{-2}$  and (c) as-deposited and (d) annealed  $\text{AlO}_x$  films deposited at high PD of  $1.3 \text{ W. cm}^{-2}$ .

In the IL region, relatively higher concentration of  $\text{SiO}$  bonding = 20 % atomic concentration is observed at low PD deposited film, whereas high PD deposition leads to 8 % less  $\text{SiO}$  concentration. This shows consistency in result with relatively thick IL for low PD deposition that low deposition rate gives sufficient time for the growth of  $\text{SiO}_x$  and intermixing with the  $\text{AlO}_x$  in IL region. For high PD deposited film, the deposition rate is higher which may result in more abrupt transition in material composition and so result in relatively thin IL layer with higher Al than the low PD deposition.

Since the high PD =  $1.3 \text{ W.cm}^{-2}$  deposited  $\text{AlO}_x$  film gives best value of surface passivation after annealing, as presented in section 6.2.2 and with high deposition rate. This means that pulsed-DC RS technique is more appropriate for high throughput processing of high quality sputtered  $\text{AlO}_x$  film as compared to RF reactive sputtering system.

### 6.3 Impact of substrate temperature during deposition

The impact of different substrate temperatures during film deposition on the quality of AlO<sub>x</sub> film was assessed through electrical characterization. In the pulsed-DC RS system used for the investigations in this thesis, the substrate temperature can be varied from room temperature (RT) to 320 °C. For this experiment the substrate temperature during deposition viz. RT, 100 °C, 200 °C and 320 °C, and different PD deposition viz.: 0.13, 0.69 and 1.3 W.cm<sup>-2</sup>, was used for film deposition while keeping Ar flow of 10 and O<sub>2</sub> flow of 55 sccm. The deposition time for PD = 0.13 W.cm<sup>-2</sup> was 40 min, PD = 0.69 W.cm<sup>-2</sup> was 8 min and PD = 1.3 W.cm<sup>-2</sup> was 4 min, to achieve similar thickness for all PD conditions. The film was annealed in optimized PDA condition in N<sub>2</sub> + O<sub>2</sub> ambient at 520 °C for 20 min, as discussed in chapter 4.

The film thickness and RI measured for different film with above experimental details using SE are shown in Figure 6.7 (a) and (b).

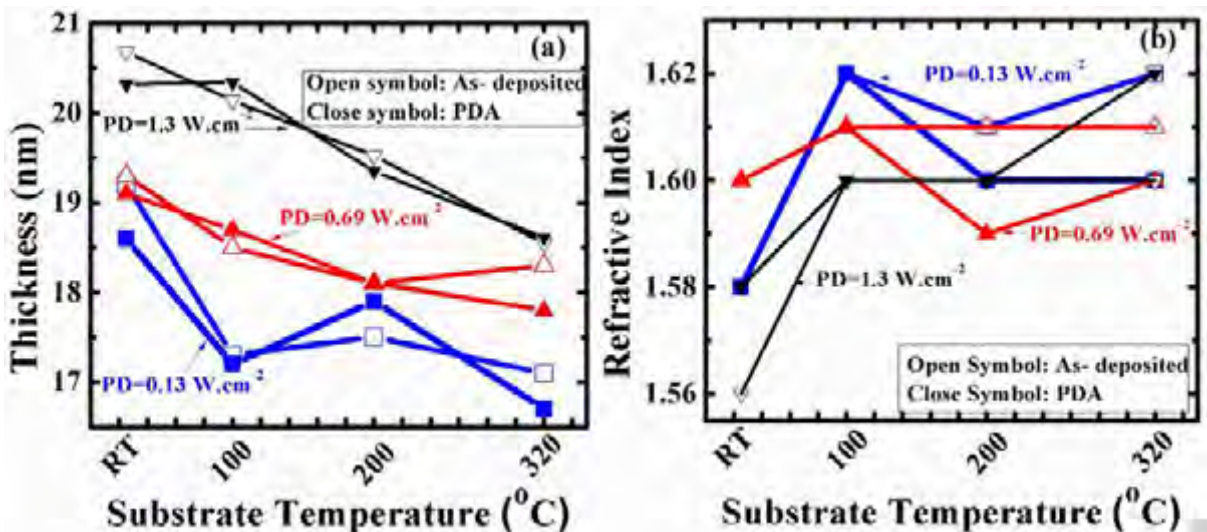


Figure 6.7 (a) Thickness and (b) RI measured by SE for film deposited with different PD conditions and substrate temperature of RT, 100 °C, 200 °C and 320 °C. Open symbol: as-deposited film and close symbol: annealed film.

From Figure 6.7 (a), it is observed that the thickness of film is decreasing with increase in substrate temperature, which is very significant for high PD deposition whereas at low PD deposition the difference seems less. With high temperature on the substrate, the knock-on atoms may penetrate deep into the film and gets trapped into interstitial and vacancies hence results in denser film [74,103]. The reduction in thickness can be related to densification of film [103].

Figure 6.7 (b) shows the value of RI is improved for film deposited at high substrate temperature as compared to RT deposition. The RI values for high temperature deposition films are in the range of 1.59-1.62, which signifies an improvement in film density. However no clear trend in value of RI is visible for substrate temperature  $> 100$  °C.

The AlO<sub>x</sub> film deposited at high PD of 1.3 W.cm<sup>-2</sup> is electrically characterized for different substrate temperature depositions, the deposition time was 4 min, while keeping Ar flow of 10 sccm and O<sub>2</sub> flow of 55 sccm. The film was annealed in optimized PDA condition in N<sub>2</sub> + O<sub>2</sub> ambient at 520 °C for 20 min. Figures 6.8 (a) and (b) shows extracted values of negative Q<sub>f</sub> and D<sub>it</sub> using eq. (2.15) and (2.20), respectively for as-deposited films and Figures 6.8 (c) and (d) for annealed films.

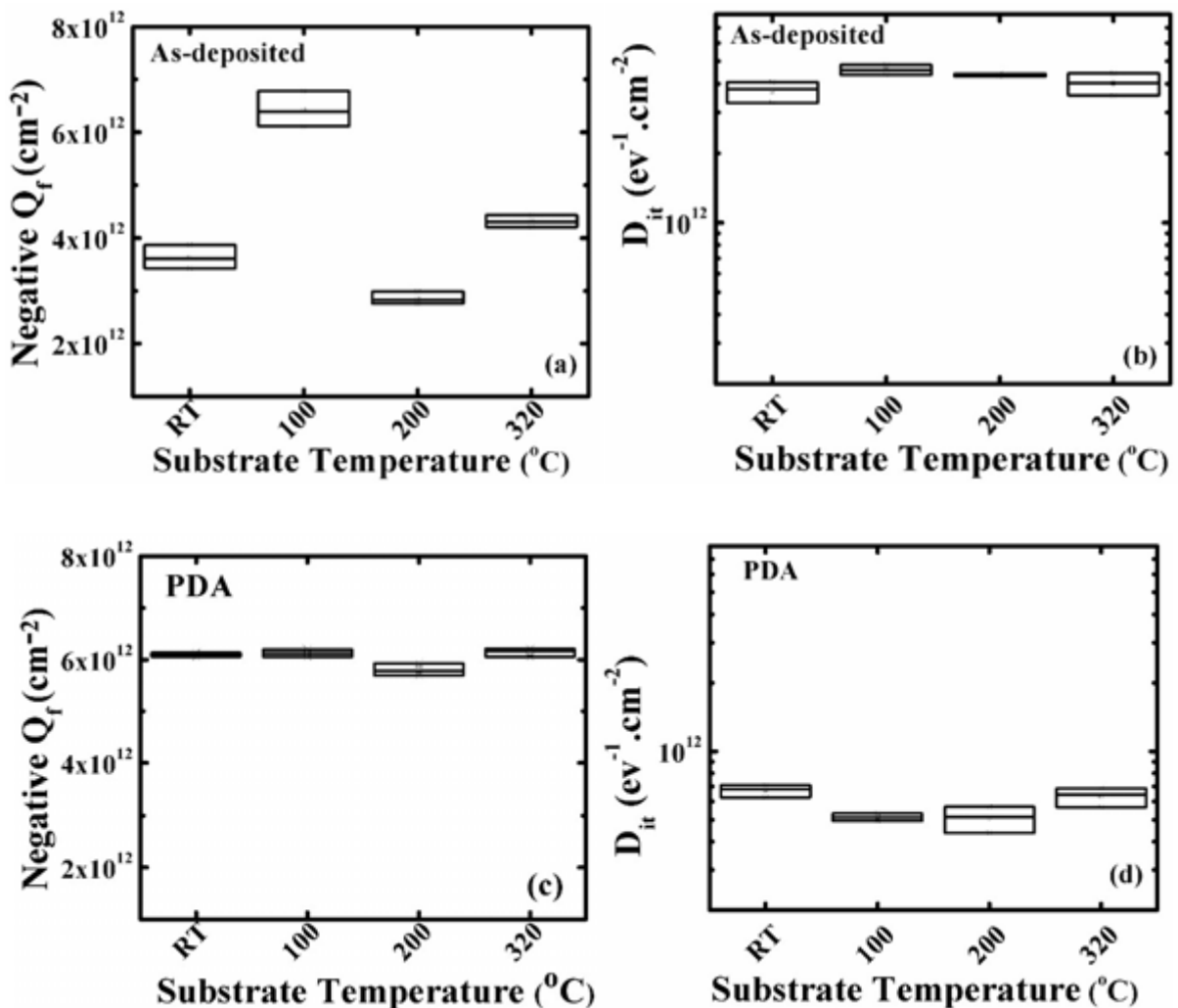


Figure 6.8 Extracted values of negative Q<sub>f</sub> (a,c) and D<sub>it</sub> (b,d) from C-V and G-V characteristics plot of MOS capacitor with AlO<sub>x</sub> film deposited at different substrate temperature.

Figure 6.8 (a) shows, high value of negative  $Q_f$  in the range of  $2.5 \pm 3.7 \times 10^{12} \text{ cm}^{-2}$  is observed in as-deposited film deposited at different substrate temperature. The negative  $Q_f$  increases to  $5.8 \pm 0.3 \times 10^{12} \text{ cm}^{-2}$  after annealing in  $\text{AlO}_x$  film deposited at different substrate temperature, as shown in Figure 6.8 (c).

Figure 6.8 (b) and (d) shows the values of  $D_{it}$  extracted from G-V characteristics plot for as-deposited and annealed  $\text{AlO}_x$  film deposited at different substrate temperature, respectively. As shown in Figure 6.8 (b), the  $D_{it}$  values are in the range of  $3 \pm 1 \times 10^{12} \text{ cm}^{-2} \cdot \text{eV}^{-1}$ , for as-deposited films and improves significantly to  $5 \pm 2 \times 10^{11} \text{ cm}^{-2} \cdot \text{eV}^{-1}$ , after annealing for these films.

From the experiment, we can conclude that pulsed-DC RS film deposited at RT is good enough to maintain the film quality as desired for surface passivation of p-type c-Si wafer after activation of passivation using optimized PDA condition. This would result in a simpler system for commercial applications.

## 6.4 Impact of process gas

This experiment was performed to observe the impact of changing the process gas used during deposition, while keeping process pressure constant at 3.5 mTorr during deposition. Two experiments were carried out: (i) an optimized recipe with Ar of 10 sccm as sputter gas and O<sub>2</sub> of 55 sccm as reactive gas and (ii) only O<sub>2</sub> of 65 sccm used during film deposition. The film was deposited at PD = 1.3 W.cm<sup>-2</sup> with deposition time of 4 min for both the processes. The films were subjected to optimized PDA condition, i.e., in N<sub>2</sub> + O<sub>2</sub> ambient at 520 °C for 20 min as discussed in chapter 4. Figures 6.9 (a) and (b) show the thickness and RI of the film for these process conditions, are measured by SE.

The result shows, the thickness for  $\text{AlO}_x$  film deposited using only O<sub>2</sub> gas is 1 nm less as compared to the process gas with Ar + O<sub>2</sub> mixture. The presence of excessive reactive gas (O<sub>2</sub>) in the chamber leads to relatively slow reaction at surface of the Al target that lowers the deposition rate. As discussed in chapter 3, in the RS system the Al target forms a compound surface after O<sub>2</sub> exposure, which results in slow sputter rate as compared to the metal surface. The state of low deposition rate is called as poisoned surface at target with formation of thick oxidized layer [74,101,109].

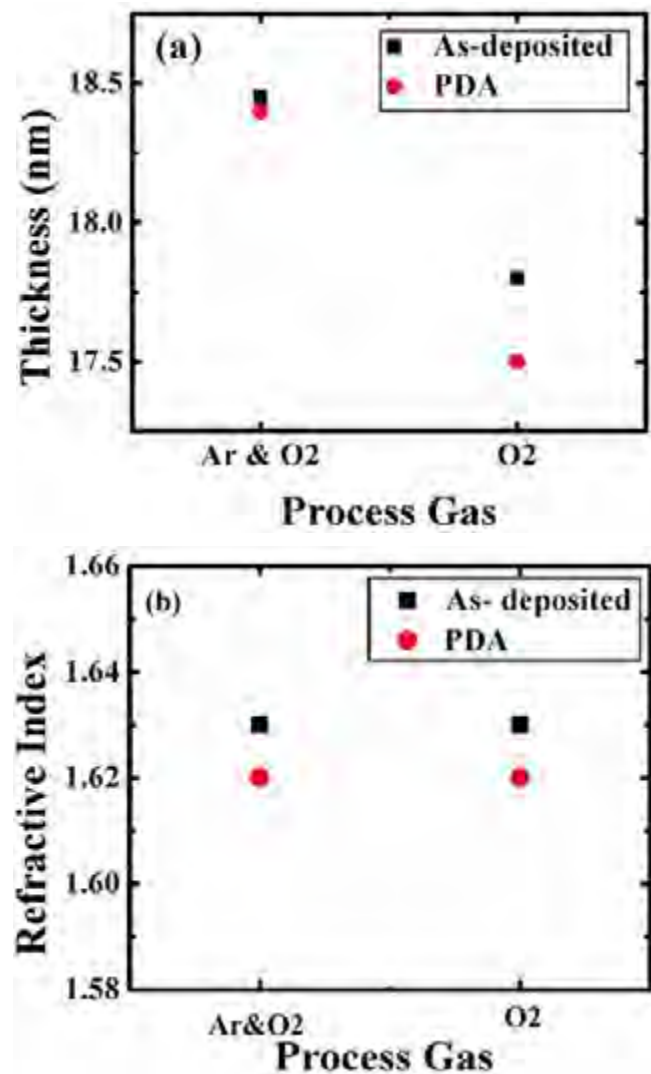


Figure 6.9 (a) Thickness and (b) RI values measured by using SE for different process gases used during film deposition.

For process with Ar used as sputter gas during deposition, make use of heavy Ar<sup>+</sup> ions to sputter the metal surface and hence results in relatively high rate of deposition. Figure 6.9 (b), shows the value of RI = 1.63 for as-deposited film, which is independent of the process gas. The annealed film shows value of RI = 1.62 for both the process gases.

The films were characterized electrically using MOS capacitors fabricated using AlO<sub>x</sub> film deposited by Ar + O<sub>2</sub> and only O<sub>2</sub> process gas. The negative Q<sub>f</sub> extracted from C-V characteristics plot and D<sub>it</sub> extracted from G-V characteristics plot for both as-deposited and annealed conditions are shown in Figures 6.10 (a) and (b), respectively. The negative Q<sub>f</sub> calculated using eq. (2.15) and D<sub>it</sub> calculated using eq. (2.20), respectively from chapter 2.

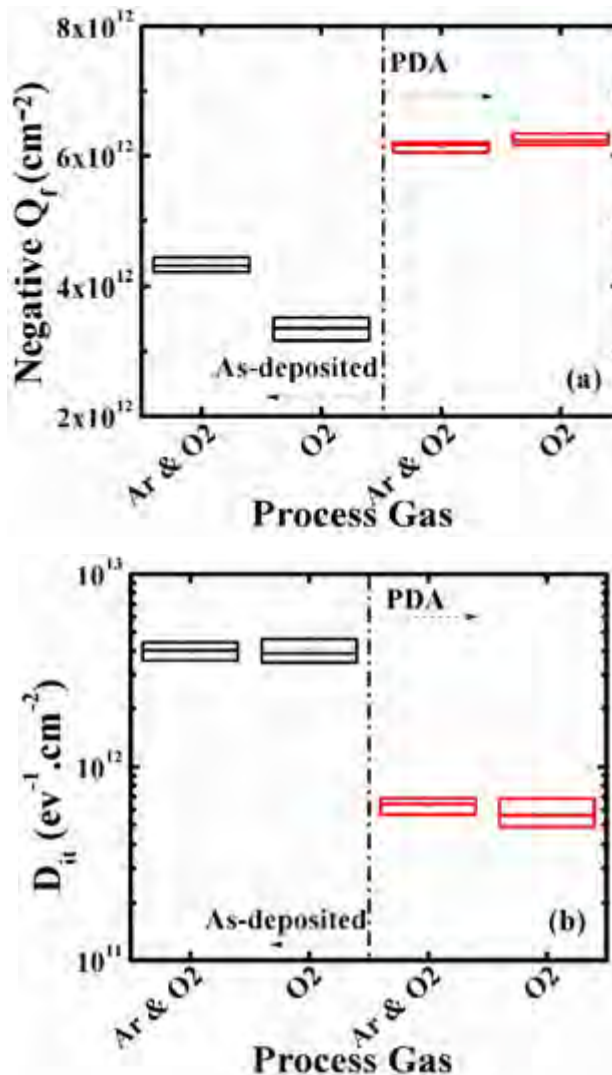


Figure 6.10 Extracted values of (a) negative  $Q_f$  and (b)  $D_{it}$  from C-V and G-V MOS characteristics plot for  $AlO_x$  films deposited using different process gas viz.:  $Ar \& O_2$  and  $O_2$  only and keeping process pressure = 3.5 mTorr.

As shown in Figure 6.10 (a), the value of negative  $Q_f$  is slightly lower for the as-deposited film processed using  $O_2$  gas only. However after PDA, the value is approximately the same  $6.2 \times 10^{12} \text{ cm}^{-2}$  for both the process conditions. The value of  $D_{it} = 3.5 \times 10^{12} \text{ cm}^{-2} \cdot \text{eV}^{-1}$  seems to be independent of the process gas for as-deposited film, as shown in Figure 6.10 (b). An improvement in the value of  $D_{it}$  to  $5 \times 10^{11} \text{ cm}^{-2} \cdot \text{eV}^{-1}$  is observed for both the process conditions after annealing. From electrical characterization it is observed that the difference in value of negative  $Q_f$  and  $D_{it}$  is almost negligible after the annealing process, hence we may select the process with  $O_2$  gas as  $Ar$  is much more expensive than  $O_2$ , for the processes with long deposition time. For long deposition time the target poisoning may lead to low

deposition rate or arcing [74]. With only O<sub>2</sub> gas used as process gas for deposition periodic target conditioning, i.e., sputtering-off target surface with no reactive gas, may be required to avoid decrease in deposition rate during the processes [74].

## 6.5 Summary

In this chapter we have discussed the impact of various process parameters on the quality of pulsed-DC RS AlO<sub>x</sub> film. The optimized PDA process were applied on these films for further characterization. The impact of following process parameters on the film was studied:

- i. Process power density: The PD was varied between 0.13 to 1.3 W.cm<sup>-2</sup>, keeping the other parameters constant. The study shows that with high PD of 1.3 W.cm<sup>-2</sup> deposition rate as high as 5 nm.min<sup>-1</sup> was obtained. The values of negative Q<sub>f</sub> obtained were in the range of  $5.5 \pm 1.5 \times 10^{12}$  cm<sup>-2</sup> and D<sub>it</sub> of  $2 \pm 3 \times 10^{11}$  cm<sup>-2</sup>.eV<sup>-1</sup> for various PD depositions. The films were characterized further to access the surface passivation quality, which shows very low value of S<sub>eff</sub> = 30 cm.s<sup>-1</sup> for film deposited at high PD of 1.3 W.cm<sup>-2</sup> after annealing, whereas low PD deposited film seems not so effective with value of S<sub>eff</sub> = 107 cm.s<sup>-1</sup> after annealing. Hence with high PD deposition we have found an improvement in the surface quality with higher rate of deposition (higher throughput).
- ii. Substrate temperature: For these study the deposition of the film was carried out at different substrate temperature between RT to 320 °C, while keeping the other process parameters constant. The thickness of the films seems to be decreasing with increase in substrate temperature, as higher mobility of the deposited particles was attained on the heated surface leading to an improvement in film density. The improvement in RI value of the film after high temperature deposition, also shows an improvement in film density. These films were electrically characterized for assessment of film property after as-deposited and annealed conditions. The film deposited at high PD of 1.3 W.cm<sup>-2</sup> and annealed in N<sub>2</sub> + O<sub>2</sub> at 520 °C for 20 min, gives the negative Q<sub>f</sub> in the range of  $5.8 \pm 0.3 \times 10^{12}$  cm<sup>-2</sup> and D<sub>it</sub> values are in the range of  $5 \pm 2 \times 10^{11}$  cm<sup>-2</sup>.eV<sup>-1</sup> with high temperature depositions. These values are similar to values obtained for RT deposited film after annealing. Hence we can conclude that film deposited at RT is good enough to maintain the film quality as desired for surface passivation application on p-type c-Si after PDA.

iii. Process gas: Here we have studied the impact of process gas used for film deposition while keeping the process pressure constant at 3.5 mTorr during deposition. The optimized process with Ar and O<sub>2</sub> used as process gases was compared to process using only O<sub>2</sub> as process gas for film deposition. The process PD of 1.3 W.cm<sup>-2</sup> with deposition time of 4 min was used in both the conditions. The T<sub>ox</sub> for AlO<sub>x</sub> film deposited using only O<sub>2</sub> gas is 17.5 nm versus 18.5 nm for Ar + O<sub>2</sub> mixture, a decrease of 5%. The RI of the films were 1.62 and independent of the process gas. From electrical characterization it is observed that after PDA the difference in value of negative Q<sub>f</sub>  $6.2 \times 10^{12}$  cm<sup>-2</sup> and D<sub>it</sub>  $5 \times 10^{11}$  cm<sup>-2</sup>.eV<sup>-1</sup> is almost negligible. Hence we may select the process with O<sub>2</sub> gas as Ar is much more expensive than O<sub>2</sub>, with periodic target conditioning process to be carried out once a while to avoid target poisoning.

In this chapter the process optimization steps were discussed with changing the process parameters in the system. In the next chapter, we will discuss the high temperature stability of the film, as this is important property of the film in terms of application on c-Si solar cells. The solar cell process involve the firing process for activation of screen-printed contacts with high temperature exposure in the range of 800 °C for few seconds. Hence the film should show stability to high temperature as well. The study and behaviour of pulsed-DC RS AlO<sub>x</sub> film for high temperature exposure will be presented in the next chapter.

## **Chapter 7. Thermal Stability of Passivation for Pulsed-DC Reactive Sputtered AlO<sub>x</sub> Film**

### **7.1 Introduction**

For the purpose of implementing AlO<sub>x</sub> film on silicon solar cells as surface passivation layer, one of the important criteria is that the passivation should be stable when the solar cell goes through high temperature processing. The stability against high temperature exposure is required due to the process step called “firing” which is used to activate the contacts by processing the cells to temperatures above 800 °C for a few seconds, especially in industrial screen-printed silicon solar cells [82]. The reports suggest degradation in surface passivation quality for PA-ALD Al<sub>2</sub>O<sub>3</sub> film after this step, due to the effusion of hydrogen from the film [72]. The effusion of large amount of hydrogen from the film cause blistering in ALD and PECVD Al<sub>2</sub>O<sub>3</sub> film after high temperature firing step [67,83]. It was also reported that the blistering is the main cause of degradation in surface passivation quality, by causing shunting in the solar cells and hence overall performance of cells degrade [67]. The stability against UV exposure is required especially when the film is applied on front surface passivation layer, for n-type silicon solar cells with p<sup>+</sup> emitter [164]. Hezel et al. reported that after UV exposure to the film, the  $\tau_{\text{eff}}$  is improving as a result of an increase in value of negative Q<sub>f</sub> [164]. The humidity exposure to the

PA-ALD Al<sub>2</sub>O<sub>3</sub> film on the other hand cause degradation in surface passivation quality as studied by Liang et al. [165]. In this chapter, we address the issue of thermal stability as the main passivation mechanism in the case of pulsed-DC sputter deposited AlO<sub>x</sub> is field-effect passivation. The passivation of p+ emitter would require chemical passivation [12], hence the application of this film may be limited to passivation of low doped p-type silicon surface as in the case of PERC solar cell structures.

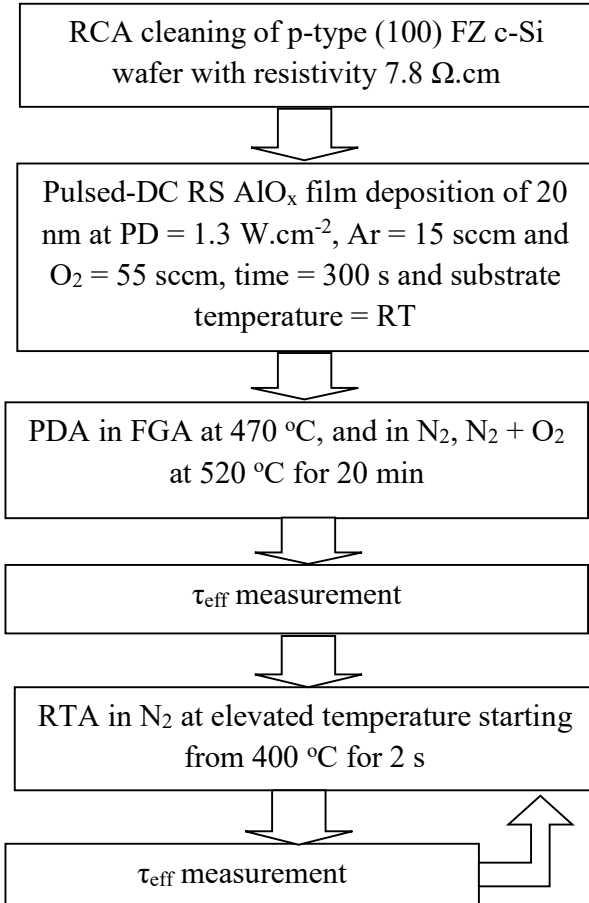
It was reported that the thermal stability of the AlO<sub>x</sub> film can be improved by the application of a capping layer, typically SiN<sub>x</sub>:H film [82,83,165-167]. Dingemans et al. reported excellent surface passivation quality with S<sub>eff</sub> of 3 cm.s<sup>-1</sup> (measured τ<sub>eff</sub> of 4.6 ms) for the stack structure of Al<sub>2</sub>O<sub>3</sub> (30 nm) capped with SiN<sub>x</sub>:H (70 nm) [82]. The Al<sub>2</sub>O<sub>3</sub> film was deposited on 2 Ω.cm n-type c-Si using remote plasma ALD process and the SiN<sub>x</sub>:H was deposited by PECVD technique at a temperature of 400 °C. The improvement in surface passivation quality after SiN<sub>x</sub>:H film capping layer was due to diffusion of hydrogen from the SiN<sub>x</sub>:H film to the PA-ALD Al<sub>2</sub>O<sub>3</sub> film upon exposure to high temperature during the firing step [82]. Kania et al. reported that the improvement in surface passivation for stack structure was related to the reduction in the density of D<sub>it</sub> by one order of magnitude [67]. Richter et al. reported practical application of AlO<sub>x</sub>/SiN<sub>x</sub>:H stack structure on p<sup>+</sup>nn<sup>+</sup> solar cells fabricated using 1 Ω.cm FZ silicon wafer and demonstrated an efficiency η of 20.8 %. In this case thickness of SiN<sub>x</sub>:H film was 70 nm, as the same thickness was optimized for ARC in cells [39,83].

In this chapter we will discuss the thermal stability of single layer pulsed-DC RS AlO<sub>x</sub> film and later the stack structure with inductively coupled plasma CVD (ICP-CVD) SiN<sub>x</sub>:H film as capping layer.

## 7.2 Experimental details

The details of sample preparation and process for the two experiments viz.: single layer AlO<sub>x</sub> and stack structure of AlO<sub>x</sub>/SiN<sub>x</sub>:H are shown in Figure 7.1 (a) and (b), respectively.

**(a) Single layer AlO<sub>x</sub> film**



**(b) Stack structure AlO<sub>x</sub>/SiN<sub>x</sub>:H**

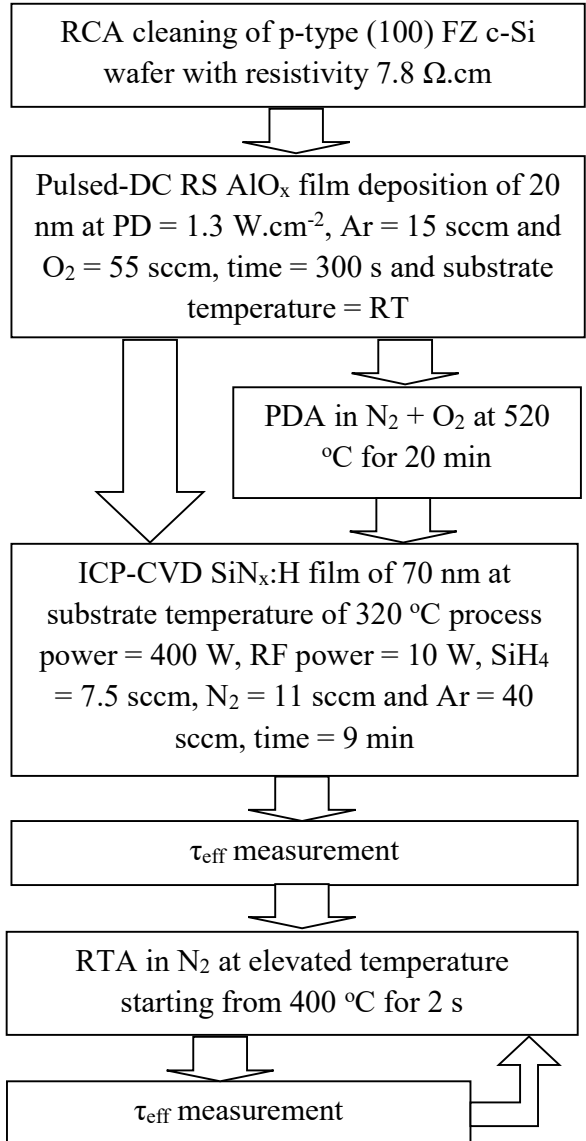


Figure 7.1 Sample preparation for  $\tau_{\text{eff}}$  measurement of (a) single layer AlO<sub>x</sub> film and (b) stack structure of AlO<sub>x</sub>/SiN<sub>x</sub>:H layer for thermal stability study.

For these experiments the optimized process condition with PD = 1.3 W.cm<sup>-2</sup>, Ar flow = 15 sccm and O<sub>2</sub> flow = 55 sccm, deposition time of 300 s were used for AlO<sub>x</sub> film deposition at room temperature on RCA cleaned p-type (100) c-Si wafer. The p-type CZ wafer with resistivity of 5 Ω.cm was used for electrical characterization and p-type FZ wafer with resistivity of 7.8 Ω.cm was used for life-time measurements of the film. First experiment includes the study

of single layer pulsed-DC RS AlO<sub>x</sub> film stability which was annealed in different PDA conditions. As shown in Figure 7.1 (a), for thermal study of single layer AlO<sub>x</sub> film, the different films under study were annealed with PDA conditions as discussed in chapter 4, i.e., FGA at 470 °C, and N<sub>2</sub>, N<sub>2</sub> + O<sub>2</sub> PDA at 520 °C for 20 min. As shown in Figure 7.1 (b), second experiment includes the study of AlO<sub>x</sub>/SiN<sub>x</sub>:H stack structure for two sets of samples (i) with SiN<sub>x</sub>:H film deposited on as-deposited AlO<sub>x</sub> film and (ii) with SiN<sub>x</sub>:H film deposited on annealed AlO<sub>x</sub> film (i.e., PDA in N<sub>2</sub> + O<sub>2</sub> ambient at 520 °C for 20 min).

The 70 nm thick SiN<sub>x</sub>:H film with RI of 2 was deposited using ICP-CVD system. The deposition was carried out at substrate temperature of 320 °C, using process power of 400 W and RF power of 10 W. Deposition time of 9 min was used to achieve the required thickness and RI for the film. The SiH<sub>4</sub> gas of 7.5 sccm, N<sub>2</sub> gas of 11 sccm and Ar gas of 40 sccm flow rates were used for the SiN<sub>x</sub>:H film deposition, at the chamber pressure of 6 mTorr. More details on the ICP-CVD SiN<sub>x</sub>:H film deposition and property can be found in report by Sandeep S.S. et al. [168].

The electrical characterization of single layer AlO<sub>x</sub> and AlO<sub>x</sub>/SiN<sub>x</sub>:H stack were carried by MOS capacitors fabrication, the details are discussed in chapter 2, section 2.4.1. Keithley 4200 SCS was used for C-V and G-V measurements, at measurement frequency of 100 kHz. For lifetime measurements, a symmetrical structure was used with film deposited on both sides of p-type (100) FZ c-Si wafers (resistivity of 7.8 Ω.cm). For thermal stability study, the sample were exposed to high temperature by RTA process in AnnealSys As-One150 system, at elevated temperature starting from 400 °C to 700 °C for exposure time = 2 s, in N<sub>2</sub> ambient and subsequently the  $\tau_{\text{eff}}$  was measured by Sinton Consulting WCT-120 life-time tester. The S<sub>eff</sub> was calculated from  $\tau_{\text{eff}}$  and  $\tau_{\text{bulk}}$  using eq. (2.29). For the S<sub>eff</sub> calculation, the upper limit of  $\tau_{\text{bulk}} = 30$  ms was used by generalized parametrization reported by Kerr et al. [119]. Sentech SE-800 SE for thickness and RI measurement.

### 7.3 Thermal stability of single layer pulsed-DC RS AlO<sub>x</sub> film

The value of S<sub>eff</sub> evaluated from measured  $\tau_{\text{eff}}$  at  $\Delta n = 10^{15} \text{ cm}^{-3}$  for the AlO<sub>x</sub> films after RTA treatments at various temperatures are shown in Figure 7.2.

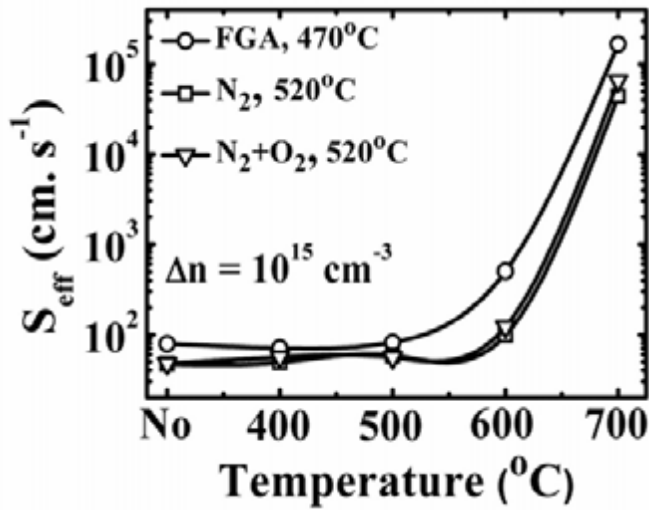


Figure 7.2 Thermal stability of  $\text{AlO}_x$  film subjected to high temperature exposure in RTA in  $\text{N}_2$ . The films were subjected to various PDA conditions. The  $S_{\text{eff}}$  was measured at  $\Delta n = 10^{15} \text{ cm}^{-3}$ .

As shown in Figure 7.2, the single layer  $\text{AlO}_x$  annealed at different PDA conditions are degrading at the firing temperature higher than 600 °C. While comparing the different samples, the sample subjected to PDA in FGA is less robust to those subjected to PDA in  $\text{N}_2$  and  $\text{N}_2 + \text{O}_2$  ambients. The thermal stability obtained for the single layer  $\text{AlO}_x$  film annealed in  $\text{N}_2$  and  $\text{N}_2 + \text{O}_2$  ambient is also not adequate for the screen-printed solar cell applications, as the requirement is stability against temperature in the range of 800 °C. On the other hand, this film shows adequate stability to be applied as passivation layer on PERC solar cells with Ni/Cu contacts, since the firing temperature requirement are in the range of 500 °C or lower [83,166].

The ALD and PECVD  $\text{Al}_2\text{O}_3$  films are reported to have relatively better thermal stability for single layer [37,82,83]. Dingemans et al., studied the thermal stability of PA-ALD  $\text{Al}_2\text{O}_3$  film, 30 nm film was deposited on both sides of n-type FZ (100) c-Si wafer ( $2 \Omega.\text{cm}$ ) at 200 °C using TMA precursor and annealed at 425 °C for 30 min in  $\text{N}_2$  ambient. The firing step was performed in standard industrial belt furnace at temperature  $> 800$  °C for few seconds, the result shows  $S_{\text{eff}} < 14 \text{ cm.s}^{-1}$  on this film, which concludes that the film was stable for application in screen-printed solar cells [82]. Kania et al., studied the thermal stability of PECVD  $\text{Al}_2\text{O}_3$  film deposited on both sides of p-type FZ (100) c-Si wafer ( $1 \Omega.\text{cm}$ ) using industrial PECVD SiNA-system by Roth & Rau [67]. The 50 nm thick  $\text{Al}_2\text{O}_3$  film was deposited using TMA precursor, with  $\text{N}_2\text{O}$  and Ar gases. The deposition temperature in range of 300-400 °C. The result showed  $\tau_{\text{eff}} = 2 \text{ ms}$  for film

annealed in FGA at temperature of 400 °C for 25 min, and thermal stability was tested at firing temperature of 900 °C in fast firing chain belt oven, which results in decrease in  $\tau_{\text{eff}}$  to 0.85 ms [67]. The study also showed that the film is stable till 750 °C, with  $\tau_{\text{eff}} = 2$  ms [67]. In this case thermal stability for single layer pulsed-DC RS AlO<sub>x</sub> film after PDA in N<sub>2</sub> and N<sub>2</sub> + O<sub>2</sub> ambient at 520 °C results in similar behaviour.

## 7.4 Thermal stability of AlO<sub>x</sub>/SiN<sub>x</sub>:H stack structure

As reported in the literature, the thermal stability of AlO<sub>x</sub> surface passivation layer can be improved by incorporating SiN<sub>x</sub>:H capping layer on top of the oxide. Dingemans et al. reported, an excellent quality of surface passivation with  $\tau_{\text{eff}}$  of 4.6 ms for the stack structure of 70 nm PECVD SiN<sub>x</sub>:H film deposited on 30 nm PA-ALD AlO<sub>x</sub> film [82]. The cause for degradation in surface passivation quality after high temperature exposure was assessed using thermal effusion transient measurements, which shows that the film loses both hydrogen as well as oxygen during the firing process. By applying a capping layer of PECVD SiN<sub>x</sub>:H film, the loss of hydrogen was prevented with diffusion of hydrogen into the AlO<sub>x</sub> layer. The report also shows that the post firing degradation of surface passivation can be prevented by annealing the stack structure again. Kania et al. reported that the improvement in surface passivation for stack structure was related to an improvement in chemical passivation with decrease in the value of D<sub>it</sub> [67]. The AlO<sub>x</sub>/SiN<sub>x</sub>:H stack structure was also reported as the best choice for passivation of p<sup>+</sup> boron doped emitter layer on n-type silicon solar cell [39,83,169,170]. The ALD or PECVD deposited AlO<sub>x</sub> films shows the formation of blisters were due to effusion of hydrogen from film for thickness > 10 nm after firing [82], while another report suggests the blister formation in ALD Al<sub>2</sub>O<sub>3</sub> film were due to tensile residual stress for thickness > 10 nm [170]. The issue of blistering seems to be resolved for earlier case with J<sub>0e</sub> of 25 fA.cm<sup>-2</sup> observed for the stack structure [39,82], since the high hydrogen content in the SiN<sub>x</sub>:H film reduces the gradient of hydrogen concentration and thus reducing the diffusion of the same from AlO<sub>x</sub> layer [67,72]. Also, with capping layer the AlO<sub>x</sub> layer may be protected from the tensile residual stress, hence resolving the issue of blister formation during firing process [171]. Similar result was observed by Dattagupta et al., for PECVD deposited AlO<sub>x</sub>/SiN<sub>x</sub>:H stack structure with low J<sub>0e</sub> of 6 and 45 fA.cm<sup>-2</sup> on 220 and 30 Ω.sq<sup>-1</sup> p<sup>+</sup> boron doped emitter [169]. The implementation of stack structure on the rear-surface

passivation of ion implanted p-type PERC solar cell was investigated by Wu et al., and they reported a cell  $\eta$  of 20.14 % for champion cell with  $V_{oc} = 661$  mV and  $J_{sc} = 38.88$  mA.cm $^{-2}$  [170].

#### 7.4.1 Electrical characterization

The high-frequency C-V and G-V characteristic plots for single layer and stack structure measured at  $f = 100$  kHz, are shown in Figure 7.3 (a) and (b), respectively. Two sets of samples were prepared, (i) as-deposited and annealed AlO<sub>x</sub> film and (ii) stack structure with SiN<sub>x</sub>:H deposited on as-deposited and annealed AlO<sub>x</sub> film. The process flow is shown in Figure 7.1 (a) and (b).

As shown in Figure 7.3 (a), the difference in  $C_{acc}$  is due to the difference in effective dielectric thickness between the samples. Similar to result as observed earlier for single layer AlO<sub>x</sub> film, a positive shift in  $V_{FB}$  after annealing is observed in this experiment also. In the case of AlO<sub>x</sub>/SiN<sub>x</sub>:H, a positive shift in  $V_{FB}$  value is observed for the sample with as-deposited AlO<sub>x</sub> film capped with SiN<sub>x</sub>:H. The difference between as-deposited and annealed  $V_{FB}$  values for single layer AlO<sub>x</sub> film is  $\Delta V_{FB} = 1.17$  V, which is higher compared to  $\Delta V_{FB}$  of 0.26 V for stack structure with SiN<sub>x</sub>:H film deposited on as-deposited and annealed AlO<sub>x</sub> films.

As shown in Figure 7.3 (b), the G-V characteristic of different samples, the improvement in interface property is observed for annealed AlO<sub>x</sub> film as discussed in earlier chapters. Again capping as-deposited AlO<sub>x</sub> film with SiN<sub>x</sub>:H film shows improvement in interfacial property which is similar to annealed AlO<sub>x</sub> film.

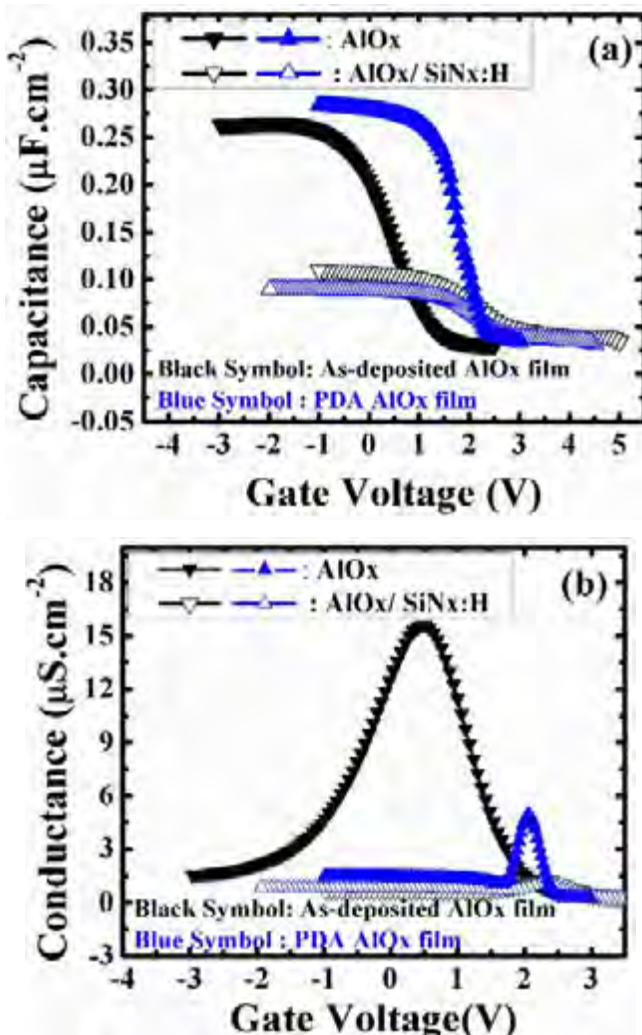


Figure 7.3 (a) The C-V and (b) G-V characteristics plot for AlO<sub>x</sub> film (close symbol) and AlO<sub>x</sub>/SiN<sub>x</sub>:H stack structure (open symbol). Black color: as-deposited AlO<sub>x</sub> film and blue color: annealed AlO<sub>x</sub> film.

Since the ICP-CVD SiN<sub>x</sub>:H capping layer was deposited at high temperature of 320 °C and with SiH<sub>4</sub> gas, this may results in improvement of interfacial quality with saturating the dangling bonds by hydrogen present in the system during deposition at such temperature. The values of negative Q<sub>f</sub> and D<sub>it</sub> for both samples extracted using eq. (2.15) and eq. (2.20), from C-V and G-V characteristics plot are shown in Figure 7.4 (a) and (b), respectively.

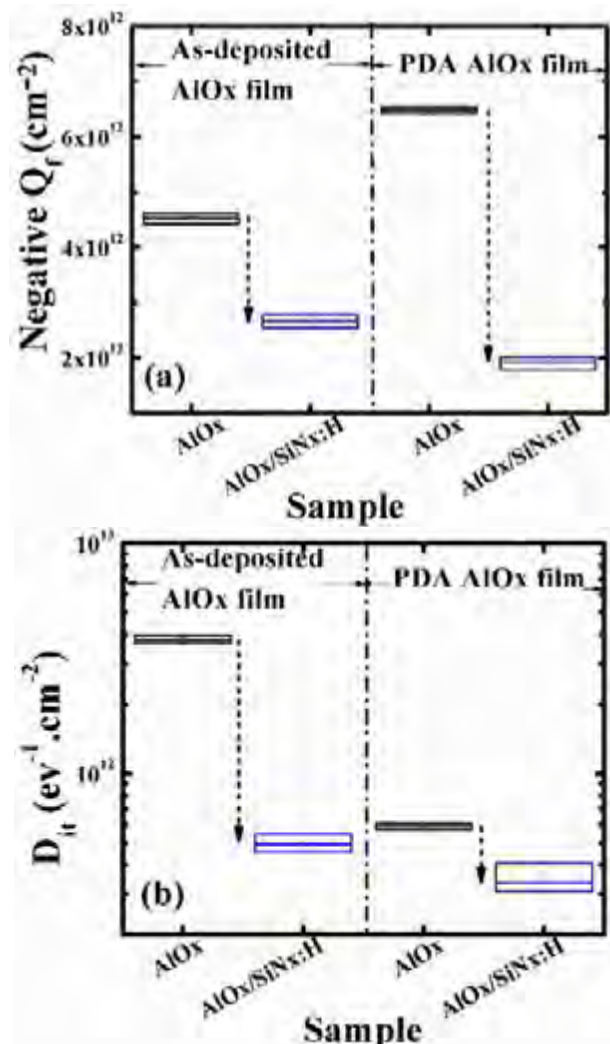


Figure 7.4 Extracted values of (a) negative  $Q_f$  and (b)  $D_{it}$  from C-V and G-V characteristics, respectively, for single layer AlO<sub>x</sub> film (black color) and AlO<sub>x</sub>/SiN<sub>x</sub>:H stack structure (blue color). The results are shown for as-deposited and annealed AlO<sub>x</sub> film.

For single layer AlO<sub>x</sub> film, the value of negative  $Q_f$  increases significantly after PDA. For stack structure, after deposition of SiN<sub>x</sub>:H, the  $Q_f$  is observed to decrease. The similar result was observed for FGA annealing of the AlO<sub>x</sub> film at 520 °C, reported in chapter 4. The reason for this change can be twofold: (i) The diffusion of hydrogen from the SiN<sub>x</sub>:H during deposition to the AlO<sub>x</sub>/c-Si interface influencing the structural modifications responsible for the change in negative charges at this interface. A similar situation exist in the case of annealing in FGA ambient. (ii) The AlO<sub>x</sub>/c-Si interface contains negative  $Q_f$ , while the SiN<sub>x</sub>:H film consists of positive  $Q_f$ .

charges, as reported by Aberle et al. [172]. Hence it is possible that the negative  $Q_f$  in  $\text{AlO}_x$  film are compensated by the positive  $Q_f$  in  $\text{SiN}_x:\text{H}$  film and results in net reduction of negative  $Q_f$  in the stack structure. The reduction is more in case of sample with  $\text{SiN}_x:\text{H}$  film deposited on annealed  $\text{AlO}_x$  film. Similar result was also reported by Kania et al., that shows a reduction in negative  $Q_f$  after deposition of  $\text{SiN}_x:\text{H}$  on annealed PECVD  $\text{AlO}_x$  film [67].

Figure 7.4 (b) shows the values of  $D_{it}$  for these samples. An improvement in  $D_{it}$  values after annealing of single layer  $\text{AlO}_x$  film is observed, similar to the result as discussed in chapter 4. The value of  $D_{it}$  is observed to reduce after deposition of  $\text{SiN}_x:\text{H}$  film on both as-deposited  $\text{AlO}_x$  film and annealed  $\text{AlO}_x$  film. This may suggest an improvement in interfacial quality could be possible without any PDA process, since the deposition of  $\text{SiN}_x:\text{H}$  film on as-deposited  $\text{AlO}_x$  film results in reduction of  $D_{it}$ . For ICP-CVD  $\text{SiN}_x:\text{H}$  film, the  $\text{SiH}_4$  was used as process gas and deposition temperature was kept as  $320\text{ }^\circ\text{C}$ , hence the atomic hydrogen in the film may be used to passivate the dangling bonds in this case [168]. The high temperature deposition of  $\text{SiN}_x:\text{H}$  film, acts as annealing process of  $\text{AlO}_x$  film. Therefore the stack structure shows improved interfacial quality even with as-deposited  $\text{AlO}_x$  film.

#### 7.4.2 Surface passivation

In Figures 7.5 (a) and (b), the  $\tau_{eff}$  measured using life-time tester and corresponding  $S_{eff}$  calculated using eq. (2.29) are shown for single layer annealed  $\text{AlO}_x$  film (PDA  $\text{AlO}_x$  film) and stack structure with  $\text{SiN}_x:\text{H}$  film deposited on annealed  $\text{AlO}_x$  film (PDA  $\text{AlO}_x/\text{SiN}_x:\text{H}$  stack). The  $S_{eff}$  was calculated from  $\tau_{eff}$  and upper limit of  $\tau_{bulk} = 30\text{ ms}$  by generalized parameterization on low-resistivity silicon wafer [119], as discussed in chapter 4.

Figure 7.5 (a) shows that the  $\tau_{eff}$  decreases after the  $\text{AlO}_x$  film capped with  $\text{SiN}_x:\text{H}$  film. This results in high value of  $S_{eff}$  for stack structure, i.e.,  $400\text{ cm.s}^{-1}$  as compared to  $S_{eff} = 40\text{ cm.s}^{-1}$  for single layer  $\text{AlO}_x$  at  $\Delta n = 10^{15}\text{ cm}^{-3}$ , as shown in Figure 7.5 (b). The degradation in the surface passivation quality for stack structure, can be related to decrease in negative  $Q_f$ , i.e., reduction of effect of field-effect passivation mechanism. This was also discussed in previous chapters, that the field-effect passivation mechanism is dominating for pulsed-DC RS  $\text{AlO}_x$  film, with high density of negative  $Q_f$  on p-type c-Si surface.

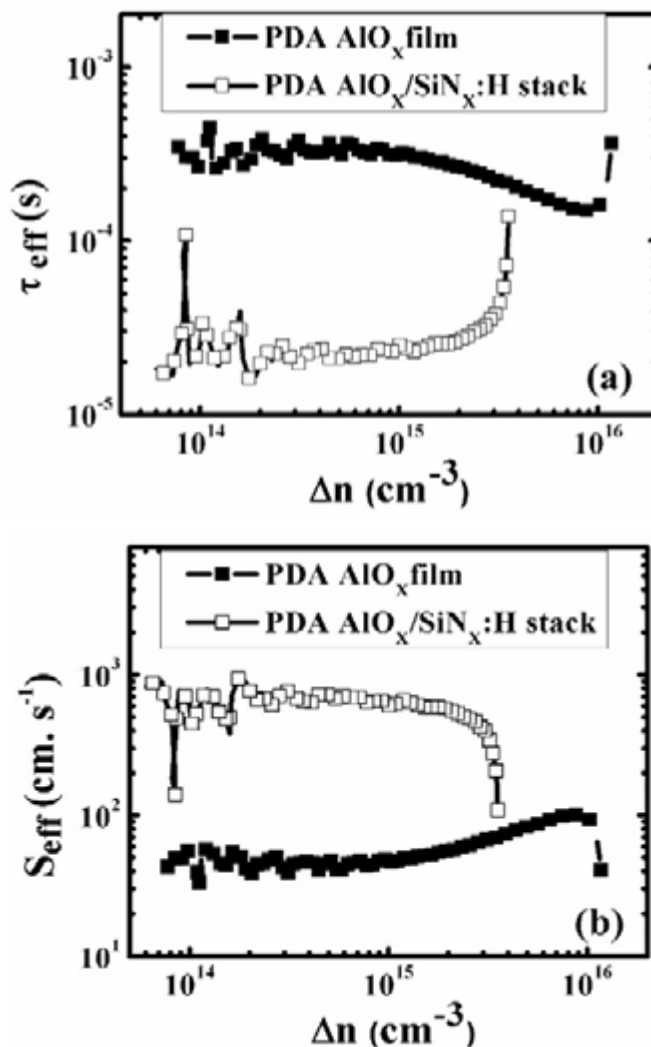


Figure 7.5 (a) Measured  $\tau_{\text{eff}}$  and (b) corresponding  $S_{\text{eff}}$  value on p-type c-Si (FZ) wafer for single layer annealed  $\text{AlO}_x$  film (close symbols) and stack structure  $\text{AlO}_x/\text{SiN}_x:\text{H}$  (open symbols) with the  $\text{AlO}_x$  film annealed before  $\text{SiN}_x:\text{H}$  deposition.

The above results shows, after application of ICP-CVD  $\text{SiN}_x:\text{H}$  capping layer, the reduction of negative  $Q_f$  is leading to degradation of surface passivation quality.

The thermal stability of the single layer and stack structure, are tested for firing stability with exposure to high temperature for 2 s using RTA process as discussed in experimental details. Figure 7.6 shows the minimum values of  $S_{\text{eff}}$  at  $\Delta n = 4 \times 10^{14} \text{ cm}^{-3}$  for samples fired at different temperatures upto 700 °C in steps of 100 °C for 2 s.

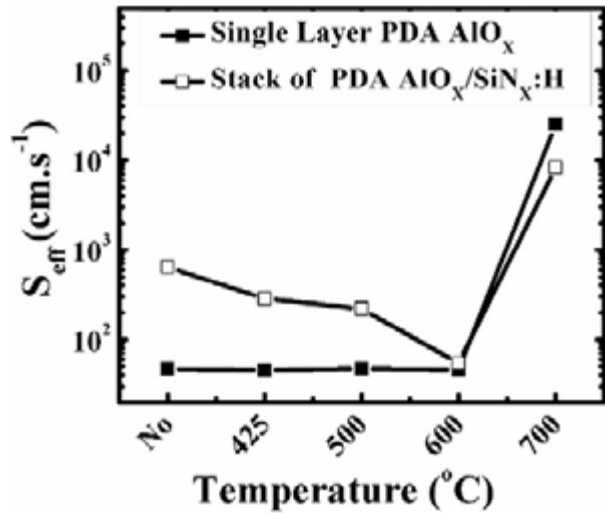


Figure 7.6 Thermal stability for single layer  $\text{AlO}_x$  film (close symbol) and  $\text{AlO}_x/\text{SiN}_x:\text{H}$  stack structure (open symbol) at different firing temperatures using RTA process. The  $\text{AlO}_x$  film was annealed in  $\text{N}_2 + \text{O}_2$  ambient at  $520^\circ\text{C}$  for 20 min for both the cases.

Figure 7.6 shows, the  $S_{\text{eff}}$  of the stack structure is higher than the single layer  $\text{AlO}_x$  film without any firing process. As the samples exposed to firing temperature, the  $S_{\text{eff}}$  for the single layer passivation remains unchanged between  $420^\circ\text{C}$  to  $600^\circ\text{C}$  and degrades further at higher temperature exposure. Whereas the stack structure shows improvement in passivation quality with firing temperature till  $600^\circ\text{C}$  and degradation after exposure of any higher temperature. The result shows, the passivation using the stack is never better than the single layer  $\text{AlO}_x$  film at any firing temperature. Since the stack structure with high temperature may lead to dissociation of the Si–H bonds at the interface may and hence may lead to degradation of interface quality. While another possible explanation is based on the study of different PDA conditions on surface passivation of  $\text{AlO}_x$  film, as discussed in chapter 4, shows the significant degradation in passivation quality for film annealed in FGA ambient at high temperature was due to reduction of negative  $Q_f$ . In this case for stack structure, the hydrogen may be diffusing from  $\text{SiN}_x:\text{H}$  film into the  $\text{AlO}_x$ , hence may also cause reduction in the negative  $Q_f$  at such high temperature. The experiment shows even with application of  $\text{SiN}_x:\text{H}$  capping layer the high temperature degradation remains same for both single layer and stack structure for pulsed-DC RS  $\text{AlO}_x$  film.

## 7.5 Summary

In this chapter, we have discussed the thermal stability of pulsed-DC RS AlO<sub>x</sub> film for firing temperature as required by industrial screen-printed solar cell fabrication process. The films subjected to PDA in N<sub>2</sub> and N<sub>2</sub> + O<sub>2</sub> ambients have shown better thermal stability as compared to films annealed in FGA. The film has shown degradation in passivation for firing at 700 °C, which is lower than the typical firing temperatures used for industrial screen-printed solar cell manufacturing. The film, however, may be used as passivation layer on PERC cells with Ni/Cu contact where the firing temperature in the range of 500 °C or less. Further experiment on thermal stability of stack structure with AlO<sub>x</sub> film capped by ICP-CVD SiN<sub>x</sub>:H was conducted, as various reports suggested an improvement in firing stability for such stack structure. The result from this experiments show a decrease in the net negative Q<sub>f</sub> while marginal improvement in D<sub>it</sub> values were observed for the stack structure assessed using electrical characterization. The stack structure is tested for stability at different firing temperature using RTA process. The result has shown improvement in S<sub>eff</sub> value till firing temperature of 600 °C and post that the passivation quality of stack degrades in similar manner as single layer AlO<sub>x</sub> film. Hence with this experiment we can conclude the additional film does not improve the surface passivation quality of pulsed-DC RS AlO<sub>x</sub> film on p-type c-Si, unlike the ALD and PECVD AlO<sub>x</sub> films reported elsewhere.

## Chapter 8. Conclusions and Future Work

In this work we have investigated the applicability of pulsed-DC RS AlO<sub>x</sub> film for surface passivation of p-type c-Si. We have shown the process development of AlO<sub>x</sub> film deposition using pulsed-DC RS technique in industrial PVD system of ENDURA by Applied Materials Inc. in chapter 3. While the film has shown electrical robustness with mean E<sub>BD</sub> of 18.07 MV.cm<sup>-1</sup> for film EOT of 8.59 nm and  $\epsilon_{r\text{-AlO}_x}$  of 8.15. Using this characteristics of the film it was applied and tested as IPD layer in flash memory applications.

The value of negative Q<sub>f</sub> of  $2.88 \times 10^{12} \text{ cm}^{-2}$  was obtained in as-deposited AlO<sub>x</sub> film at high PD of 1.3 W.cm<sup>-2</sup> on p-type c-Si wafer. With the application of optimized PDA process in N<sub>2</sub> + O<sub>2</sub> ambients at 520 °C for 20 min, the best value of S<sub>eff</sub> = 31 cm.s<sup>-1</sup> was observed on p-type FZ c-Si (7.8 Ω.cm) wafer. Through electrical measurements an improvement in surface passivation was related to an increase in negative Q<sub>f</sub> to  $6 \times 10^{12} \text{ cm}^{-2}$  and reduction in D<sub>it</sub> values to  $2.3 \times 10^{11} \text{ eV}^{-1}.\text{cm}^{-2}$ . The film deposited at high PD of 1.3 W.cm<sup>-2</sup>, resulted in high deposition rate of 5 nm.min<sup>-1</sup>. Hence the high quality surface passivation may be realised using this deposition technique with high throughput.

Through material characterization presence of thick IL of 8.2 nm with the composition of aluminum silicate was observed using cross-sectional TEM and depth-resolved XPS measurements. The presence of both *T* and *O* coordinated Al, with *T* coordinated Al increasing near the IL after annealing was observed for this film using EELS measurement technique. The dominating *T* coordinated Al results in increase of negative Q<sub>f</sub> in AlO<sub>x</sub> film. From the FTIR measurement a symmetrical peak at 1090 cm<sup>-1</sup>, corresponding to Si-O-Si

stretching mode, was observed on annealed films, resulting in improvement in interfacial quality.

The film annealed in optimized PDA condition has shown slow gradual degradation in passivation quality for firing temperature of upto 700 °C. Which is lower than typical firing temperature for industrial screen-printed solar cell, hence the film may be applicable as passivation layer on PERC cells with Ni/Cu contact where the firing temperature is in the range of 500 °C or less.

## 8.1 Future direction

With pulsed-DC RS AlO<sub>x</sub> film, we have obtained the S<sub>eff</sub> of 31 cm. s<sup>-1</sup> on p-type FZ c-Si surface deposited using optimized process conditions and annealed in optimized PDA conditions. The thermal stability against firing temperature has shown that the film is stable upto 700 °C. Since the thermal stability of stack structure with AlO<sub>x</sub> film capped using ICP-CVD SiN<sub>x</sub>:H does not seems to improve the firing stability, hence the proposal to test the hydrogen diffusion hypothesis could be pursued in further research.

The integration of pulsed-DC RS AlO<sub>x</sub> film as rear surface passivation layer on c-Si solar cells is required to assess the cell performance. The film may be integrated as rear-surface passivation layer in advance cell structure known as “PERC” structure, as shown in Figure 8.1.

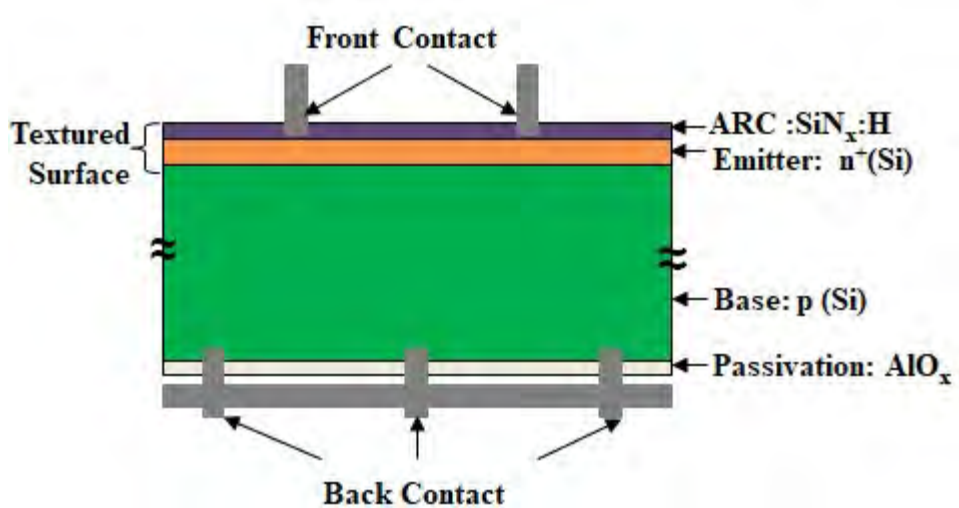


Figure 8.1 Typical p-type c-Si PERC solar cell with rear-surface passivated using AlO<sub>x</sub> film.

In Figure 8.2, shows the proposed process flow for fabrication of advance PERC structure p-type c-Si solar cells with pulsed-DC RS AlO<sub>x</sub> film integrated as rear-surface passivation layer.

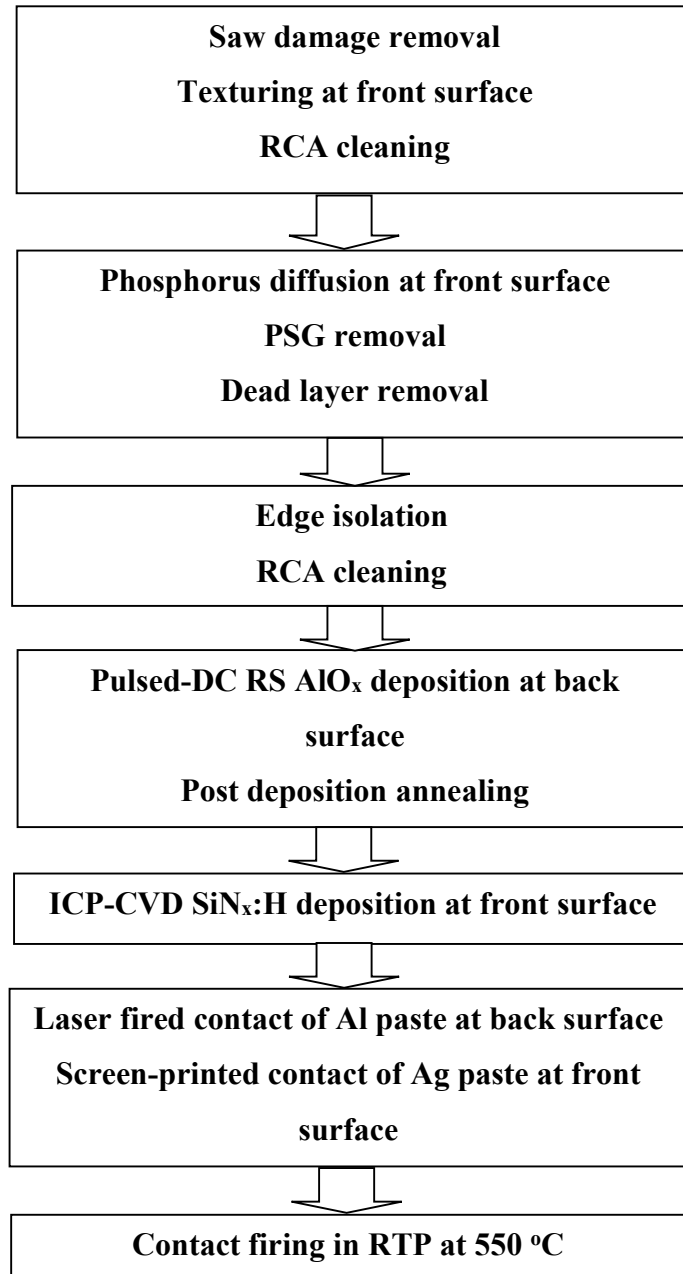


Figure 8.2 Proposed process flow for fabrication of PERC structure p-type c-Si solar cell using AlO<sub>x</sub> film as rear-surface passivation layer.

The initial sample preparation involved, saw damage removal followed by texturing of the front surface of the wafer to reduce the reflection of light, followed by RCA cleaning of the wafer. The p-n junction can be formed by phosphorus doping in diffusion furnace to form

$n^+$ -emitter on p-type base. After formation of p-n junction, the phosphor silicate glass (PSG) and dead layer on the surface, should be removed before proceeding for edge isolation process. The wafer needs another RCA cleaning process to remove any metallic residue on the wafer before film deposition. The pulsed-DC RS  $\text{AlO}_x$  film deposited on the rear-surface and optimized PDA process applied after film deposition to activate the surface passivation of rear-surface. The ICP-CVD  $\text{SiN}_x:\text{H}$  film is then deposited on front surface  $n^+$  emitter to serve as ARC. Since the film contains positive fixed charges, it also act as emitter-surface passivation layer. The contacts formation process involves, the Al paste to be locally fired using laser at back surface and the Ag paste by screen printing technique at front surface. The contact firing process will be performed to activate the contacts.

## References

- [1] ITRPV, 2017, “International technology roadmap for photovoltaic 2016 results,” 8<sup>th</sup> ed., March, 2017.
- [2] Solar Industry Technology Report 2015-2016, Canadian Solar, October, 2016.
- [3] M. A. Green, Y. Hishikawa, E. D. Dunlop, D. H. Levi, J. Hohl-Ebinger, and A. W. Y. Ho-Baillie, “Solar cell efficiency tables (version 51),” *Prog. Photovolt: Res. Appl.*, vol. 26, pp. 3-12, 2018.
- [4] A. Hagfeldt, G. Boschloo, L. Kloo, and H. Pettersson, “Dye-sensitized solar cells,” *Chem. Rev.*, vol. 110, pp. 6595-6663, 2010.
- [5] R. Noufi and K. Zweibel, “High-efficiency CdTe and CIGS thin-film solar cells: highlights and challenges,” In Proc. of IEEE 4<sup>th</sup> World Conference on Photovoltaic Energy Conversion, 2006, pp. 317-320.
- [6] X. Deng and Eric A. Schiff, “Amorphous silicon-based solar cells,” in *Handbook of Photovoltaic Science and Engineering*, A. Luque and S. Hegedus, Eds., Chichester, UK: John Wiley Sons, 2003, pp. 505-565.
- [7] D. K. Schroder, *Semiconductor Material and Device Characterization*, 3<sup>rd</sup> ed., Hoboken, NJ: IEEE press, 2006.
- [8] S. M. Sze, *VLSI Technology*, 2<sup>nd</sup> ed., New York: McGraw Hill, 1988.
- [9] S. K. Gandhi, *VLSI Fabrication Principles: Silicon and Gallium Arsenide*, 2<sup>nd</sup> ed., New York: John Wiley & Sons Inc., 1994.
- [10] J. Schmidt, “Measurement of differential and actual recombination parameters on crystalline silicon wafers,” *IEEE Trans. Electron Devices*, vol. 46, no. 10, pp. 2018-2025, 1999.
- [11] R. A. Sinton and A. Cuevas, “Contactless determination of current–voltage characteristics and minority carrier lifetimes in semiconductors from quasi-steady-state photo conductance data,” *Appl. Phys. Lett.*, vol. 69, no. 17, pp. 2510-2512, 1996.
- [12] G. Dingemans and W.M.M. Kessels, “Status and prospects of Al<sub>2</sub>O<sub>3</sub>-based surface passivation schemes for silicon solar cells,” *J. Vac. Sci. Technol. A*, vol. 30, pp. 040802-1-040802-27, 2012.
- [13] C. Reichel, F. Granek, J. Benick, O. Schultz-Wittmann, and S. W. Glunz, “Comparison of emitter saturation current densities determined by injection-dependent lifetime spectroscopy in high and low injection regimes,” *Prog. Photovolt: Res. Appl.*, vol. 20, pp. 21-30, 2010.

- [14] C.S. Solanki, *Solar Photovoltaic: Fundamental, Technologies and Applications*, 2<sup>nd</sup> ed., India: Prentice Hall, 2011.
- [15] A. Wolf, D. Biro, J. Nekarda, S. Stumpp, A. Kimmerle, S. Mack, and R. Preu, “Comprehensive analytical model for locally contacted rear surface passivated solar cells,” *J. Appl. Phys.*, vol. 108, pp. 124510-124513, 2010.
- [16] P. A. Basore and D. A. Clugston, *PCID Version 5.9*, Sydney, Australia: University of New South Wales, 2003.
- [17] S. Olibet, E. Vallat-Sauvain, and C. Ballif, “Model for a-Si:H/c-Si interface recombination based on the amphoteric nature of silicon dangling bonds,” *Phys. Rev. B*, vol. 76, pp. 035326-1-035326-14, 2007.
- [18] J. H. Zhao, A. Wang, P. P. Altermatt, and M. A. Green, “24.5% efficiency silicon PERT cells on MCZ substrates and 24.7% efficiency PERL cells on FZ substrates,” *Prog. Photovolt: Res. Appl.*, vol. 7, pp. 471-474, 1999.
- [19] M. A. Green, “The path to 25% silicon solar cell efficiency: history of silicon cell evolution,” *Prog. Photovolt: Res. Appl.*, vol. 17, pp. 183-189, 2009.
- [20] H. Jin, K. J. Weber, and A. W. Blakers, “Depassivation of Si-SiO<sub>2</sub> interface following rapid thermal annealing,” In Proc. of IEEE 4<sup>th</sup> World Conference on Photovoltaic Energy Conversion, 2006, pp. 1078-1080.
- [21] A. F. Thomson and K. R. McIntosh, “Degradation of oxide-passivated silicon,” In Proc. of 24<sup>th</sup> European Photovoltaic Solar Energy Conference, 2009, pp. 959-964.
- [22] L. P. Johnson, K. R. McIntosh, B. S. Richards, H. Jin, B. Paudyal, and E. Klampaftis, “Characterisation of Si-SiO<sub>2</sub> interface after humidity exposure,” In Proc. of Australia and New Zealand Solar Energy Society Conference, Canberra, Australia, 2006.
- [23] M. Hofmann, S. Janz, C. Schmidt, S. Kambor, D. Suwito, N. Kohn, J. Rentsch, R. Preu, and S. W. Glunz, “Recent developments in rear-surface passivation at Fraunhofer ISE,” *Sol. Energy Mater. Sol. Cells*, vol. 93, pp. 1074-1078, 2009.
- [24] B. Hoex, F. J. Peeters, M. Creatore, M. A. Blauw, W. M. M. Kessels, and M. C. M. van de Sanden, “High-rate plasma-deposited SiO<sub>2</sub> films for surface passivation of crystalline silicon,” *J. Vac. Sci. Technol. A*, vol. 24, pp. 1823-1830, 2006.
- [25] V. D. Mihailetti, Y. Komatsu, and L. J. Geerligs, “Nitric acid pretreatment for the passivation of boron emitters for n-type base silicon solar cells,” *Appl. Phys. Lett.*, vol. 92, pp. 063510-1-063510-3 2008.

- [26] F. W. Chen, T. A. Li, and J. E. Cotter, “PECVD silicon nitride surface passivation for high-efficiency n-type silicon solar cells,” In Proc. of IEEE 4<sup>th</sup> World Conference on Photovoltaic Energy Conversion, 2006, pp. 1020-1023.
- [27] T. Lauinger, J. Moschner, A. G. Aberle, and R. Hezel, “UV stability of highest-quality plasma silicon nitride passivation of silicon solar cells,” In Proc. of 25<sup>th</sup> IEEE Photovoltaic Specialists Conference, 1996, pp. 417-420.
- [28] M. Tucci, L. Serenelli, S. De Iuliis, and M. Izzi, “Characeterisation of SiN<sub>x</sub>/a-Si:H crystalline silicon surface passivation under UV light exposure,” *Thin solid films*, vol. 515, pp. 7625-7628, 2007.
- [29] S. Dauwe, L. Mittelstadt, A. Metz, and R. Hezel, “Experimental evidence of parasitic shunting in silicon nitride rear surface passivated solar cells,” *Prog. Photovolt: Res. Appl.*, vol. 10, pp. 271-278, 2002.
- [30] S. Dauwe, J. Schmidt, and R. Hezel, “Very low surface recombination velocities on p- and n-type silicon wafers passivated with hydrogenated amorphous silicon films,” In Proc. of 29<sup>th</sup> IEEE Photovoltaic Specialists Conference, 2002, pp. 1246-1249.
- [31] J. Mitchell, D. Macdonald, and A. Cuevas, “Plasma-enhance chemical vapour deposition of a-Si:H to provide surface passivation of c-Si surface at low temperature,” In Proc. of 22<sup>nd</sup> European Photovoltaic Solar Energy Conference, 2007, pp. 928-931.
- [32] T. A. Li, F. W. Chen, A. Cuevas, and J. E. Cotter, “Thermal Stability of Microwave PECVD Hydrogenated Amorphous Silicon as Surface Passivation of N-type Heterojunction Solar Cells,” In Proc. of 22<sup>nd</sup> European Photovoltaic Solar Energy Conference, 2007, pp. 1326-1331.
- [33] J. Schmidt, F. Werner, B. Veith, D. Zielke, R. Bock, V. Tiba, P. Poodt,, F. Roozeboom, A. Li, A. Cuevas, and R. Brendel, “Industrially Relevant Al<sub>2</sub>O<sub>3</sub> Deposition Techniques for the Surface Passivation of Si Solar Cells,” In Proc. of 25<sup>th</sup> European Photovoltaic Solar Energy Conference, 2010, pp. 1130-1133.
- [34] B. Hoex, S. B. S. Heil, E. Langereis, M. C. M. Van de Sanden, and, W. M. M. Kessels, “Ultralow surface recombination of c-Si substrates passivated by plasma-assisted atomic layer deposited Al<sub>2</sub>O<sub>3</sub>,” *Appl. Phys. Lett.*, vol. 89, pp. 042112-1-042112-3, 2006.
- [35] G. Agostinelli, A. Delabie, P. Vitanov, Z. Alexieva, H. F. W. Dekkers, S. DeWolf, and G. Beaucarne, “Very low surface recombination velocities on p-type silicon

- wafers passivated with a dielectric with fixed negative charge," *Sol. Energy Mater. Sol. Cells*, vol. 90, pp. 3438-3443, 2006.
- [36] P. Saint-Cast, J. Benick, D. Kania, L. Weiss, M. Hofmann, J. Rentsch, R. Preu, and S. W. Glunz, "High-efficiency c-Si solar cells passivated with ALD and PECVD aluminum oxide," *IEEE Electron Device Lett.*, vol. 31, no. 7, pp. 695-697, 2010.
- [37] P. Saint-Cast, J. Benick, D. Kania, E. Billot, A. Richter, M. Hermle, M. Hofmann, J. Rentsch, R. Preu, and S. W. Glunz, "High-efficiency p-type PERC solar cells applying PECVD AlO<sub>x</sub> layers," In Proc. of the 25<sup>th</sup> European Photovoltaic Solar Energy Conference, 2010, pp. 1488-1491.
- [38] J. Benick, B. Hoex, G. Dingemans, W.M.M. Kessels, A. Richter, M. Hermle, and S. W. Glunz, "High-efficiency n-type silicon solar cells with front side boron emitter," In Proc. of 24<sup>th</sup> European Photovoltaic Solar Energy Conference, 2009, pp. 863-870.
- [39] A. Richter, M. Horteis, J. Benick, S. Henneck, M. Hermle, S. W. Glunz, "Towards industrially feasible high-efficiency n-type Si solar cells with boron-diffused front side emitter-combining firing stable Al<sub>2</sub>O<sub>3</sub> passivation and fine-line printing," In Proc. of 35<sup>th</sup> IEEE Photovoltaic Specialists Conference, 2010, pp. 003587-003592.
- [40] S.W. Glunz, R. Preu, and D. Biro, "Crystalline silicon solar cells-state-of-the art and future developments," in *Comprehensive Renewable Energy*, A. Sayigh, Ed., vol. 1, Elsevier, 2012, pp. 53-387.
- [41] K. Matsunaga, T. Tanaka, T. Yamamoto, and Y. Ikuhara, "First-principles calculations of intrinsic defects in Al<sub>2</sub>O<sub>3</sub>," *Phys. Rev. B*, vol. 68, pp. 085110-1-085110-9, 2003.
- [42] K. Kimoto, Y. Matsui, T. Nabatame, T. Yasuda, T. Mizoguchi, I. Tanaka, and A. Toriumi, "Coordination and interface analysis of atomic-layer-deposition Al<sub>2</sub>O<sub>3</sub> on Si (001) using energy-loss near-edge structures," *Appl. Phys. Lett.*, vol. 83, pp. 4308-4308, 2003.
- [43] J. Irikawa, S. Miyajima, S. Kida, T. Watahiki, and M. Konagai, "Effects of annealing and atomic hydrogen treatment on aluminum oxide passivation layers for crystalline silicon solar cells," *Jpn. J. Appl. Phys.*, vol. 50, pp. 012301-1-012301-5, 2011.
- [44] B. Hoex, M. Bosman, N. Nandakumar, and W. M. M. Kessels, "C-Si surface passivation by aluminum oxide studied with electron energy loss spectroscopy," in the Proc. of 39<sup>th</sup> IEEE Photovoltaic Specialists Conference, 2013, pp.3333-3336.

- [45] B. Hoex, J. J. H. Gielis, M. C. M. van de Sanden, and W. M. M. Kessels, “On the c-Si surface passivation mechanism by the negative-charge dielectric  $\text{Al}_2\text{O}_3$ ,” *J. Appl. Phys.*, vol. 104, pp. 113703-1-113703-7, 2008.
- [46] W. M. M. Kessels, J. J. H. Gielis, B. Hoex, N. M. Terlinden, G. Dingemans, V. Verlaan, and M. C. M. van de Sanden, “Electric field induced surface passivation of Si by atomic layer deposited  $\text{Al}_2\text{O}_3$  studied by optical second-harmonic generation,” In Proc. of 34<sup>th</sup> IEEE Photovoltaic Specialists Conference, 2009, pp. 000427-000431.
- [47] B. Hoex, J. Schmidt, P. Pohl, M. C. M. van de Sanden, and W. M. M. Kessels, “Silicon surface passivation by atomic layer deposited  $\text{Al}_2\text{O}_3$ ,” *J. Appl. Phys.*, vol. 104, pp. 044903-1-044903-12, 2008.
- [48] G. Dingemans and W. M. M. Kessels, “Recent progress in the development and understanding of Silicon surface passivation by aluminum oxide for photovoltaics,” In Proc. of the 25<sup>th</sup> European Photovoltaic Solar Energy Conference, 2010, pp. 1083-1090.
- [49] E. Langereis, M. Bouman, J. Keijmel, S. B. S. Heil, M. C. M. van de Sanden, and W. M. M. Kessels, “Plasma-assisted ALD of  $\text{Al}_2\text{O}_3$  at low temperatures: reaction mechanism and material properties,” *ECS Trans.*, vol. 16, no. 4, pp. 247-255, 2008.
- [50] H. B. Profijt, S. E. Potts, M. C. M. van de Sanden, and W. M. M. Kessels, “Plasma-assisted atomic layer deposition: basics, opportunities, and challenges,” *J. Vac. Sci. Technol. A*, vol. 29, no. 5, pp. 050801-1-050801-26, 2011.
- [51] G. Dingemans, R. Seguin, P. Engelhart, M. C. M. van de Sanden, and W. M. M. Kessels, “Silicon surface passivation by ultrathin  $\text{Al}_2\text{O}_3$  films synthesized by thermal and plasma assisted atomic layer deposition,” *Phys. Status Solidi – Rapid Res. Lett.*, vol. 4, pp. 10-12, 2010.
- [52] G. Dingemans, P. Engelhart, R. Seguin, M. M. Mandoc, M. C. M. van de Sanden, and W. M. M. Kessels, “Comparison between aluminum oxide surface passivation films deposited with thermal ALD, plasma ALD and PECVD,” In Proc. of 35<sup>th</sup> IEEE Photovoltaic Specialists Conference, 2010, pp. 003118-003121.
- [53] B. Hoex, J. Schmidt, R. Bock, P. P. Altermatt, M. C. M. van de Sanden, and W. M. M. Kessels, “Excellent passivation of highly doped p-type Si surfaces by the negative-charge-dielectric  $\text{Al}_2\text{O}_3$ ,” *Appl. Phys. Lett.*, vol. 91, pp. 112107-1-112107-3, 2007.
- [54] W. Liang, K. J. Weber, D. Suh, S. P. Phang, J. Yu, A. K. McAuley, and B. R. Legg, “Surface passivation of boron-diffused p-type silicon surfaces with (100) and (111)

- orientations by ALD Al<sub>2</sub>O<sub>3</sub> layers," *IEEE J. Photovolt.*, vol. 3, no. 2, pp. 678- 683, 2013.
- [55] B. Hoex, M. C. M. van de Sanden, J. Schmidt, R. Brendel, and W. M. M. Kessels, "Surface passivation of phosphorus-diffused n+-type emitters by plasma-assisted atomic-layer deposited Al<sub>2</sub>O<sub>3</sub>," *Phys. Status Solidi – Rapid Res. Lett.*, vol. 6, no. 1, pp. 4-6, 2012.
- [56] M. Otto, M. Kroll, T. Käsebier, X. Li, B. Gesemann, K. Füchsel, J. Ziegler, A. N. Sprafke, and R. B. Wehrspohn, "Passivation of different black silicon surfaces by ALD deposited Al<sub>2</sub>O<sub>3</sub>," In Proc. of 39<sup>th</sup> IEEE Photovoltaic Specialists Conference, 2013, pp. 1277-1279.
- [57] J. A. Van Delft, D. Garcia-Alonso and W. M. M. Kessels, "Atomic layer deposition for photovoltaics: applications and prospects for solar cell manufacturing," *Semicond. Sci. Technol.*, vol. 27, pp. 074002-1-074002-13, 2012.
- [58] F. Werner, B. Veith, V. Tiba, P. Poodt, F. Roozeboom, R. Brendel, and J. Schmidt, "Very low surface recombination velocities on p- and n-type c-Si by ultrafast spatial atomic layer deposition of aluminum oxide," *Appl. Phys. Lett.*, vol. 97, pp. 162103-1-162103-3, 2010.
- [59] E. Grennman, P. Fischer, D. Pierreux, H. Terhorst, and P. Zagwijn, "Batch ALD: characteristics, comparison with single wafer ALD, and examples," *Surf. Coat. Technol.*, vol. 201, pp. 8899-8907, 2007.
- [60] P. Poodt, V. Tiba, F. Werner, J. Schmidt, A. Vermeer, and F. Roozeboom, "Ultrafast atomic layer deposition of alumina layers for solar cell passivation," *J. Electrochem. Soc.*, vol. 158, no. 9, pp. H937-H940, 2011.
- [61] G. Dingemans, N. M. Terlinden, D. Pierreux, H. B. Profijt, M. C. M. van de Sanden, and W. M. M. Kessels, "Influence of the oxidant on the chemical and field-effect passivation of Si by ALD Al<sub>2</sub>O<sub>3</sub>," *Electrochem. Solid-State Lett.*, vol. 14, no. 1, pp. H1-H4, 2011.
- [62] B. Vermang, A. Rothschild, A. Racz, J. John, J. Poortmans, R. Mertens, P. Poodt, V. Tiba, and F. Roozeboom, "Spatially separated atomic layer deposition of Al<sub>2</sub>O<sub>3</sub>, a new option for high-throughput Si solar cell passivation," *Prog. Photovolt: Res. Appl.*, vol. 19, pp. 733-739, 2011.
- [63] F. Werner, W. Stals, R. Görtzenb, B. Veith, R. Brendel, and J. Schmidt, "High-rate atomic layer deposition of Al<sub>2</sub>O<sub>3</sub> for the surface passivation of Si solar cells," *Energy Procedia*, vol. 8, pp. 301-306, 2011.

- [64] C. H. Lin, H. L. Wang, and M. H. Hon, “Preparation and characterization of aluminium oxide films by plasma enhance chemical vapour deposition,” *Surf. Coat. Technol.*, vol. 90, pp. 102-106, 1997.
- [65] G. Dingemans, M. C. M. van de Sanden, and W. M. M. Kessels, “Plasma-enhance chemical vapor deposition of aluminum oxide using ultrashort precursor injection pulses,” *Plasma Process. Polym.*, vol. 9, no. 8, pp. 761-771, 2012.
- [66] P. Saint-Cast, D. Kania, M. Hofmann, J. Benick, J. Rentsch, and R. Preu, “Very low surface recombination velocity on p-type c-Si by high-rate plasma-deposited aluminum oxide,” *Appl. Phys. Lett.*, vol. 95, pp. 151502-1-151502-3, 2009.
- [67] D. Kania, P. Saint-Cast, M. Hofmann, J. Rentsch, and R. Preu, “High temperature stability of PECVD aluminum oxide layers applied as negatively charges passivation on c-Si surfaces,” In Proc. of the 25<sup>th</sup> European Photovoltaic Solar Energy Conference, 2010, pp. 2291-2296.
- [68] P. Saint-Cast, A. Richter, E. Billot, M. Hofmann, J. Benick, J. Rentsch, R. Preu, and S. W. Glunz, “Very low surface recombination velocity of boron doped emitter passivated with plasma-enhanced chemical-vapor-deposited AlO<sub>x</sub> layers,” *Thin Solid Films*, vol. 522, pp. 336-339, 2012.
- [69] B. Veith, T. Dullweber, M. Siebert, C. Kranz, F. Werner, N.-P. Harder, J. Schmidt, B. F. P. Roos, T. Dippell, and R. Brendel “Comparison of ICP-AlO<sub>x</sub> and ALD-Al<sub>2</sub>O<sub>3</sub> layers for the rear surface passivation of c-Si solar cells,” *Energy Procedia*, vol. 27, pp. 379- 384, 2012.
- [70] G. Dingemans, F. Einsele, W. Beyer, M. C. M. Van de Sanden, and W. M. M. Kessels, “Influence of annealing and Al<sub>2</sub>O<sub>3</sub> properties on the hydrogen-induced passivation of the Si/SiO<sub>2</sub> interface,” *J. Appl. Phys.*, vol. 111, pp. 093713-1-093713-9, 2012.
- [71] F. Werner, B. Veith, D. Zielke, L. Kühnemund, C. Tegenkamp, M. Seibt, R. Brendel, and J. Schmidt, “Electronic and chemical properties of the c-Si/Al<sub>2</sub>O<sub>3</sub> interface,” *J. Appl. Phys.*, vol. 109, pp. 113701-1-113701-6, 2011.
- [72] G. Dingemans, W. Beyer, M. C. M. Van de Sanden, and W. M. M. Kessels, “Hydrogen induced passivation of Si interfaces by Al<sub>2</sub>O<sub>3</sub> films and SiO<sub>2</sub>/Al<sub>2</sub>O<sub>3</sub> stacks,” *Appl. Phys. Lett.*, vol. 97, pp. 152106-1-152106-3, 2010.
- [73] F. Jones and J. Logan, “High rate reactive sputter deposition of aluminum oxide,” *J. Vac. Sci. Technol. A*, vol. 7, pp. 1240-1247, 1989.

- [74] D. M. Mattox, *Handbook of Physical Vapour Deposition (PVD) Processing*, Westwood, NJ: Noyes publications, 1998.
- [75] T. A. Li and A. Cuevas, “Effective surface passivation of crystalline silicon by rf sputtered aluminum oxide,” *Phys. Status Solidi – Rapid Res. Lett.*, vol. 3, no. 5, pp. 160–162, 2009.
- [76] S. Miyajima, J. Irikawa, A. Yamada, and M. Konagai, “High quality aluminum oxide passivation layer for crystalline silicon solar cells deposited by parallel-plate plasma-enhanced chemical vapor deposition,” *Appl. Phys. Exp.*, vol. 3, pp. 012301-1-012301-3, 2010.
- [77] T. A. Li and A. Cuevas, “Role of hydrogen in the surface passivation of crystalline silicon by sputtered aluminum oxide,” *Prog. Photovolt: Res. Appl.*, vol. 19, pp. 320–325, 2011.
- [78] X. Zhang, A. Cuevas, and A. Thomson, “Process control of reactive sputter deposition of AlO<sub>x</sub> and improved surface passivation of crystalline silicon,” *IEEE J. Photovolt.*, vol. 3, no. 1, pp. 183-188, 2013.
- [79] G. Krugel, W. Wolke, F. Wagner, J. Rentsch, and R. Preu, “Sputtered aluminum oxide for rear side passivation of p-type silicon solar cells,” In Proc. of the 27<sup>th</sup> European Photovoltaic Solar Energy Conference, 2012, pp. 1958-1962.
- [80] G. Untila, T. Kost, A. Chebotareva, M. Zaks, A. Sitnikov, and O. Solodukha, “Pyrosol deposited AlO<sub>x</sub> as surface passivation for Si solar cells,” In Proc. of the 25<sup>th</sup> European Photovoltaic Solar Energy Conference, 2010, pp. 2592-2595.
- [81] J. Schmidt, F. Werner, B. Veith, D. Zielke, S. Steingrube, P. P. Altermatt, S. Gatz, T. Dullweber, and R. Brendel “Advances in the surface passivation of silicon solar cells,” *Energy Procedia*, vol. 15, pp. 30-39, 2012.
- [82] G. Dingemans, P. Engelhart, R. Seguin, F. Einsele, B. Hoex, M. C. M. van de Sanden, and W. M. M. Kessels, “Stability of Al<sub>2</sub>O<sub>3</sub> and Al<sub>2</sub>O<sub>3</sub>/a-SiN<sub>x</sub>:H stacks for surface passivation of crystalline silicon,” *J. Appl. Phys.*, vol. 106, pp. 114907-1-114907-4, 2009.
- [83] A. Richter, S. Henneck, J. Benick, M. Hörteis, M. Hermle, and S.W. Glunz, “Firing stable Al<sub>2</sub>O<sub>3</sub>/SiN<sub>x</sub> layer stack passivation for the front side boron emitter of n-type silicon solar cells,” In Proc. of the 25<sup>th</sup> European Photovoltaic Solar Energy Conference, 2010, pp. 1453-1459.

- [84] J. Schmidt, B. Veith, F. Werner, D. Zielke, and R. Brendel, “Silicon surface passivation by ultrathin Al<sub>2</sub>O<sub>3</sub> films and Al<sub>2</sub>O<sub>3</sub>/SiN<sub>x</sub> stacks,” In Proc. of 35<sup>th</sup> IEEE Photovoltaic Specialists Conference, 2010, pp. 000885 – 000890.
- [85] J. Robertson, “High dielectric constant oxides,” *Eur. Phys. J. Appl. Phys.*, vol. 28, pp. 265–291, 2004.
- [86] E. H. Nicollian and J. R. Brews, *MOS (Metal Oxide Semiconductor) Physics and Technology*, New York, USA: Wiley, 1982.
- [87] W. A. Hill and C. C. Coleman, “A single-frequency approximation for interface state density determination,” *Solid-State Electron..*, vol. 23, pp. 987-993, 1980.
- [88] C. Richard Brundle, C. A. Evans Jr., and S. Wilson, *Encyclopedia of Materials Characterization*, Greenwich: Butterworth-Heinemann, 1992.
- [89] M. Yasaka, “X-ray thin-film measurement techniques V.,” *Rigaku J.*, vol. 26, no. 2, pp. 1-9, 2010.
- [90] L.G Parratt, “Surface studies of solids by total reflections of X-rays,” *Phys. Rev.*, vol. 95, no. 2, pp. 359-369, 1954.
- [91] R. F. Egerton, “Electron energy-loss spectroscopy in the TEM,” *Rep. Prog. Phys.*, vol. 72, pp. 016502-1-016502-25, 2009.
- [92] C. W. Brown, “Ultraviolet, visible, and near-infrared spectrophotometers,” *Appl. Spectrosc. Rev.*, vol. 35, no. 3, pp. 151-173, 2007.
- [93] J. Tauc, R. Grigorovici, and A. Vancu, “Optical properties and electronic structure of amorphous germanium,” *Phys. Stat. Sol.*, vol. 15, pp. 627-637, 1966.
- [94] D. Macdonald, R. A. Sinton, and A. Cuevas, “On the use of a bias-light correction for trapping effects in photoconductance-based lifetime measurements of silicon,” *J. Appl. Phys.*, vol. 89, no. 5, pp. 2772-2778, 2001.
- [95] A. G. Aberle, “Surface passivation of crystalline silicon solar cells: A review,” *Prog. Photovolt: Res. Appl.*, vol. 8, pp. 473-487, 2000.
- [96] B. W. Schmidt, B. R. Rogers, C. K. Gren, and T. P. Hanus, “Carbon incorporation in chemical vapor deposited aluminum oxide films,” *Thin Solid Films*, vol. 518, pp. 3658- 3663, 2010.
- [97] F. Wiest, V. Capodieci, O. Blank, M. Gutsche, J. Schulze, I. Eisele, J. Matusche, and U. I. Schmidt, “Conformal aluminum oxide coating of high aspect ratio structures using metal organic chemical vapor deposition,” *Thin Solid Films*, vol. 496, pp. 240-246, 2006.

- [98] J. Schmidt, F. Werner, B. Veith, D. Zielke, R. Bock, R. Brendel, V. Tiba, P. Poodt, F. Roozeboom, A. Li, and A. Cuevas, “Surface passivation of silicon solar cells using industrially relevant Al<sub>2</sub>O<sub>3</sub> deposition techniques,” *Photovoltaic International: the Technology Resource for PV Professionals*, vol. 10, pp. 52–57, 2010.
- [99] P. J. Kelly, P. S. Henderson, R. D. Arnell, G. A. Roche, and D. Carter “Reactive pulsed magnetron sputtering process for alumina films,” *J. Vac. Sci. Technol. A*, vol. 18, no. 6, pp. 2890-2896, 2000.
- [100] L.B. Jonsson, T. Nyberg, I. Katardjiev, and S. Berg, “Frequency response in pulsed DC reactive sputtering processes,” *Thin Solid Films*, vol. 365, pp. 43-48, 2000.
- [101] I. Safi, “Recent aspects concerning DC reactive magnetron sputtering of thin films: a review,” *Surf. Coat. Technol.*, vol. 127, pp. 203-219, 2000.
- [102] Y. Kijima and T. Hanada, “Effect of the pressure of sputtering atmosphere on the physical properties of amorphous aluminum oxide films,” *J. Mater. Sci.*, vol. 35, pp. 2193-2199, 2000.
- [103] B. K. Tay, Z. W. Zhao, C. Q. Sun, “Effects of substrate bias and growth temperature on properties of aluminium oxide thin films by using filtered cathodic vacuum arc,” *Surf. Coat. Technol.*, vol. 198, pp. 94-97, 1999.
- [104] J. Musil, P. Baroch, J. Vlcek, K. H. Nam, and J. G. Han, “Reactive magnetron sputtering of thin films: present status and trends,” *Thin Solid Films*, vol. 475, pp. 208-218, 2005.
- [105] A. J. Moses, “Refractive index of optical materials in infrared region,” Air Force Materials Laboratory, Culver City, California, A.D. 704555, 1970.
- [106] S. P. Wasserman, G. M. Whitesides, I. M. Tidswell, B. M. Ocko, P. S. Pershan, and J. D. Axel, “The structure of self-assembled monolayers of alkylsiloxanes on silicon: a comparison of results from ellipsometry and low-angle X-ray reflectivity,” *J. Am. Chem. Soc.*, vol. 111, pp. 5852-5861, 1989.
- [107] S. Kohli, C. D. Rithner, P. K. Dorhout, A. M. Dummer, and S. Menoni, “Comparison of nanometer-thick films by x-ray reflectivity and spectroscopic ellipsometry,” *Rev. Sci. Instrum.*, vol. 76, pp. 023905-1-023905-5, 2005.
- [108] L. K. Hudson, C. Misra, A. J. Perrotta, K. Wefers, and F. S. Williams, “Aluminum Oxide,” in *Ullmann’s Encyclopaedia of Industrial Chemistry*, Weinheim: Wiley-VCH, 2002, vol. 2, pp. 607-645.

- [109] M. K. Olsson, K. Macák, U. Helmersson, and B. Hjörvarsson, “High rate reactive DC magnetron sputter deposition of Al<sub>2</sub>O<sub>3</sub> films,” *J. Vac. Sci. Technol. A*, vol. 16, pp. 639-643, 1998.
- [110] T. Seino and T. Sato, “Aluminum oxide films deposited in low pressure conditions by reactive pulsed dc magnetron sputtering,” *J. Vac. Sci. Technol. A*, vol. 20, no. 3, pp. 634-637, 2002.
- [111] Y.Y. Chen and C. H. Chien, “Thickness scaling and reliability comparison for the inter-poly high-k dielectrics,” *IEEE Electron Device Lett.*, vol. 28, no. 8, pp. 700-702, 2007.
- [112] Y.Y. Chen, T. H. Li, K. T. Kin, C. H. Chien, and J. C. Lou, “Characterization of inter-poly high-k dielectrics for next generation stacked-gate flash memories,” In Proc. of IEEE conferences Emerging Technologies-Nanoelectronics, 2006, pp. 463-466.
- [113] A. Mishra, H. Kalita, M. Waikar, A. Gour, M. Bhaisare, M. Khare, M. Aslam, and A. Kottantharayil, “Multilayer graphene as charge storage layer in floating gate flash memory,” In Proc. of 4<sup>th</sup> IEEE International Memory Workshop, 2012, pp. 1-4.
- [114] L. E. Black and K. R. McIntosh, “Surface passivation of c-Si by atmospheric pressure chemical vapor deposition of Al<sub>2</sub>O<sub>3</sub>,” *Appl. Phys. Lett.*, vol. 100, pp. 202107-1-202107-5, 2012.
- [115] G. Dingemans, M. C. M. van de Sanden, and W. M. M. Kessels, “Influence of the deposition temperature on the c-Si surface passivation by Al<sub>2</sub>O<sub>3</sub> films synthesized by ALD and PECVD,” *Electrochem. Solid-State Lett.*, vol. 13, pp. H76–H79, 2010.
- [116] J. Benick, A. Richter, T.-T. A. Li, N. E. Grant, K. R. McIntosh, Y. Ren, K. J. Weber, M. Hermle, and S. W. Glunz, “Effect of a post-deposition anneal on Al<sub>2</sub>O<sub>3</sub>/Si interface properties,” In Proc. of 35<sup>th</sup> IEEE Photovoltaic Specialists Conference, 2010, pp. 000891-000896.
- [117] J. Ebser, J. Junge, T. Lüder, S. Seren, B. Terheiden, and G. Hahn, “Al<sub>2</sub>O<sub>3</sub> rear surface passivation for silicon ribbon solar cells,” In Proc. of the 25<sup>th</sup> European Photovoltaic Solar Energy Conference and Exhibition, 2010, pp. 1134-1137.
- [118] J. Schmidt and A. G. Aberle, “Accurate method for the determination of bulk minority-carrier lifetimes of mono- and multicrystalline silicon wafers,” *J. Appl. Phys.*, vol. 81, pp. 6186 -6199, 1997.
- [119] M. J. Kerr, A. Cuevas, and R. A. Sinton, “Generalized analysis of quasi-steady-state and transient decay open circuit voltage measurements,” *J. Appl. Phys.*, vol. 91, pp. 399-404, 2002.

- [120] W. R. Thurber, R. L. Mattis, Y. M. Liu, and J. J. Filiben, “Resistivity-dopant density relationship for boron-doped silicon,” *J. Electrochem. Soc.*, vol. 127, pp. 2291-2294, 1980.
- [121] Y. Jin, K. Saito, M. Shimada, and T. Ono, “Using electron cyclotron resonance sputtering in the deposition of ultrathin Al<sub>2</sub>O<sub>3</sub> gate dielectrics,” *J. Vac. Sci. Technol. B*, vol. 21, no. 3, pp. 942-948, 2003.
- [122] N. M. Terlinden, G. Dingemans M. C. M. van de Sanden, and W. M. M. Kessels, “Role of field-effect on c-Si surface passivation by ultrathin (2–20 nm) atomic layer deposited Al<sub>2</sub>O<sub>3</sub>,” *Appl. Phys. Lett.*, vol. 96, pp. 112101-1-112101-3, 2010.
- [123] M. Hiratani, S. Saito, Y. Shimamoto, and K. Torii, “Effective electron mobility reduced by remote charge scattering in high- $\kappa$  gate stacks,” *Jpn. J. Appl. Phys.*, vol. 41, pp. 4521-4522, 2002.
- [124] G. Dingemans, N. M. Terlinden, M. A. Verheijen, M. C. M. van de Sanden, and W. M. M. Kessels, “Controlling the fixed charge and passivation properties of Si (100)/Al<sub>2</sub>O<sub>3</sub> interfaces using ultrathin SiO<sub>2</sub> interlayers synthesized by atomic layer deposition,” *J. Appl. Phys.*, vol. 110, pp. 093715-1- 093715-6, 2011.
- [125] Angus Rocket, *The Materials Science of Semiconductors*, Berlin, Germani: Springer-Verlag, 2008.
- [126] M. Mbila, “Soil minerals, organisms, and human health: medicinal uses of soils and soils materials” in *Soils and Human Health*, E.C. Brevik and L.C. Burgess, Eds., Boca Raton, FL: CRC Press, 2013, pp. 199-213.
- [127] S. W. Bailey, “Review of cation ordering in micas,” *Clays and Clay Minerals*, vol. 32, no. 2, pp. 81-92, 1984.
- [128] B. Hoex, M. Bosman, N. Nandakumar, and W. M. M. Kessels, “Silicon surface passivation by aluminium oxide studied with electron energy loss spectroscopy,” *Phys. Status Solidi – Rapid Res. Lett.*, vol. 7, no. 11, pp. 937-941, 2013.
- [129] R. W. M. Kwok, *XPS Peak Fitting Program for WIN95/98 XPSPEAK Version 4.1*, 2000. Available: <http://www.phy.cuhk.edu.hk/~surface/XPSPEAK/>
- [130] R.F. Egerton, *Electron Energy-Loss Spectroscopy in the Electron Microscope*, 3<sup>rd</sup> ed., NY: Springer, 2012.
- [131] L. Gu, V. Srot, W. Sigle, C. Koch, P. van Aken, F. Scholz, S. B. Thapa, C. Kirchner, M. Jetter, and M. Rühle, “Band-gap measurements of direct and indirect semiconductors using monochromated electrons,” *Phys. Rev. B*, vol. 75, pp. 195214-1-195214-8, 2007.

- [132] F. El-Diasty, F. A. Abdel Wahab, and M. Abdel-Baki, “Optical band gap studies on lithium aluminum silicate glasses doped with Cr 3+ ions,” *J. Appl. Phys.*, vol. 100, pp. 093511-1-093511-7, 2006.
- [133] K. Kimoto, K. Ishizuka, T. Mizoguchi, I. Tanaka, and Y. Matsui, “The study of Al-L<sub>23</sub> ELNES with resolution- enhancement software and first-principles calculation,” *Jpn. Soc. of Microsc.*, vol. 52, no. 3, pp. 299-303, 2003.
- [134] R. Katamreddy, R. Inman, G. Jursich, A. Soulet, and C. Takoudis, “ALD and characterization of aluminum oxide deposited on Si(100) using tris(diethylamino) aluminum and water vapor,” *J. Electrochem. Soc.*, vol. 153, no. 10, pp. C701-C706, 2006.
- [135] R. Katamreddy, R. Inman, G. Jursich, A. Soulet, A. Nicholls, and C. Takoudis, “Post deposition annealing of aluminum oxide deposited by atomic layer deposition using tris (diethylamino)aluminum and water vapor on Si (100),” *Thin Solid Films*, vol. 515, pp. 6931-6937, 2007.
- [136] T. M. Klein, D. Niu, W. S. Epling, W. Li, D. M. Maher, C. C. Hobbs, R. I. Hegde, I. J. R. Baumvol, and G. N. Parsons, “Evidence of aluminum silicate formation during chemical vapor deposition of amorphous Al<sub>2</sub>O<sub>3</sub> thin films on Si (100),” *Appl. Phys. Lett.*, vol. 75, no. 25, pp. 4001-4003, 1999.
- [137] J.-M. Li, “Shrunk lattice structure and interdiffusion characteristics of 5 nm thick Al<sub>2</sub>O<sub>3</sub> ultrathin films sputtered on silicon,” *Nanotechnol.*, vol. 19, pp. 035604-1-035604-5, 2008.
- [138] P. R. Anderson and W.E. Swartz, “X-ray photoelectron spectroscopy of some aluminosilicates,” *Inorg. Chem.*, vol. 13, no. 9, pp. 2293-2294, 1974.
- [139] F. Zhang, G. Sun, L. Zheng, S. Liu, B. Liu, L. Dong, L. Wang, W. Zhao, X. Liu, G. Yan, L. Tian, and Y. Zeng, “Interfacial study and energy-band alignment of annealed Al<sub>2</sub>O<sub>3</sub> films prepared by atomic layer deposition on 4H-SiC,” *J. Appl. Phys.*, vol. 113, pp. 044112-1-044112-4, 2013.
- [140] C.-F. Sun, H. Zhu, M. Okada, K. Gaskell, Y. Inoue, L. Hu, and Y. H. Wang, “Interfacial Oxygen Stabilizes Composite Silicon Anodes.” *Nano Lett.*, vol. 15, no. 1, pp. 703-708, 2014.
- [141] F.J. Himpsel, F. R. McFeely, A. Taleb-Ibrahimi, and J. A. Yarmoff, “Microscopic structure of the SiO<sub>2</sub>/Si interface,” *Phys. Rev. B*, vol. 38, no. 9, pp. 6084-6096, 1988.
- [142] F. J. Grunthaner and P. J. Grunthaner, “Chemical and electronic structure of the SiO<sub>2</sub>/Si interface,” *Mater. Sci. Rep.*, vol. 1, no. 2, pp. 65-160, 1986.

- [143] O. Benkherouou and J. P. Deville, "Distribution of intermediate oxidation states at the silicon/silicon dioxide obtained by low-energy ion implantation," *J. Vac. Sci. Technol. A*, vol. 6, pp. 3125-3129, 1988.
- [144] J. M. Reyes, B. M. P. Ramos, C. Z. Islas, W. C. Arriaga, P. R. Quintero, and A. T. Jacome, "Chemical and morphological characteristics of ALD Al<sub>2</sub>O<sub>3</sub> thin-film surfaces after immersion in pH buffer solutions," *J. Electrochem. Soc.*, vol. 160, no. 10, pp. B201-B206, 2013.
- [145] P. Vitanov, A. Harizanova, T. Ivanova, T. Dimitrova, "Chemical deposition of Al<sub>2</sub>O<sub>3</sub> thin films on Si substrates," *Thin Solid Films*, vol. 517, pp. 6327-6330, 2009.
- [146] A. Roy Chowdhuri and C.G. Takoudis, "Investigation of the aluminum oxide/Si (100) interface formed by chemical vapor deposition," *Thin Solid Films*, vol. 446, pp. 155-159, 2004.
- [147] P. Tarte, "Infra-red spectra of inorganic aluminates and characteristic vibrational frequencies of AlO<sub>4</sub> tetrahedra and AlO<sub>6</sub> octahedra", *Spectrochimica Acta*, vol. 23A, pp. 2127-2143, 1967.
- [148] C. Morterra and G. Magnacca, "A case study: surface chemistry and surface structure of catalytic aluminas, as studied by vibrational spectroscopy of adsorbed species," *Catalysis Today*, vol. 27, pp. 497-532, 1996.
- [149] E. Langereis, J. Keijmel, M. C. M. van de Sanden, and W. M. M. Kessels, "Surface chemistry of plasma-assisted atomic layer deposition of Al<sub>2</sub>O<sub>3</sub> studied by infrared spectroscopy," *Appl. Phys. Lett.*, vol. 92, pp. 231904-1-231904-3, 2008.
- [150] R.S. Johnson, G. Lucovsky, and I. Baumvol, "Physical and electrical properties of nanocrystalline Al<sub>2</sub>O<sub>3</sub> prepared by remote plasma enhanced chemical vapor deposition," *J. Vac. Sci. Technol. A*, vol. 19, no. 4, pp. 1353-1360, 2001.
- [151] Y-C. Kim, H-H. Park, J. S. Chun, W-J. Lee, "Compositional and structural analysis of aluminum oxide films prepared by plasma-enhance chemical vapor deposition", *Thin Solid Films*, vol. 237, pp. 57-65, 1994.
- [152] J. Park, S. Heo, J.-G.Chung, H. Kim, H. Lee, K. Kim, and G.-S. Park, "Bandgap measurement of thin dielectric films using monochromated STEM-EELS," *Ultramicroscopy*, vol. 109, pp. 1183-1188, 2009.
- [153] M. Stoger-Pollach, H. Franco, P. Schattschneider, S. Lazar, B. Schaffer, W. Grogger, and H.W. Zandbergen, "Cerenkov losses: A limit for bandgap determination and Kramers-Kronig analysis," *Micron*, vol. 37, pp. 396-402, 2006.

- [154] M. Stoger-Pollach and P. Schattschneider, “The influence of relativistic energy losses on bandgap determination using valence EELS,” *Ultramicroscopy*, vol. 107, pp. 1178-1185, 2007.
- [155] M. Stoger-Pollach, A. Laister, and P. Schattschneider, “Treating retardation effects in valence EELS spectra for Kramers-Kronig analysis,” *Ultramicroscopy*, vol. 108, pp. 439-444, 2008.
- [156] K. Dileep and R. Datta, “Phase separation and electronic structure of ZnS<sub>0.3</sub>O<sub>0.7</sub> allow thin film with without (Ag, Li) co-doping,” *J. Alloys and Compounds*, vol. 586, pp. 499-506, 2014.
- [157] K. Dileep, R. Sahu, K. K. Nagaraja, and R. Datta, “Crystallographic phase separation and band gap of ZnO<sub>1-x</sub>S<sub>x</sub> (x=0.1-0.3) alloy thin films grown by pulsed laser deposition,” *J. Cryst. Growth*, vol. 402, pp. 124-129, 2014.
- [158] R. H. French, “Electronic band structure of Al<sub>2</sub>O<sub>3</sub> with comparison to AlON and AlN,” *J. Am. Ceram. Soc.*, vol. 73, no. 3, pp. 477-489, 1990.
- [159] V. Rose and R. Franchy, “The band gap of ultrathin amorphous and well-ordered Al<sub>2</sub>O<sub>3</sub> films on CoAl (100) measured by scanning tunnelling spectroscopy,” *J. Appl. Phys.*, vol. 105, pp. 07C902-1-07C902-3, 2009.
- [160] V. Rose, V. Podgursky, I. Costina, and R. Franchy, “Growth of ultra-thin amorphous Al<sub>2</sub>O<sub>3</sub> films on CoAl (100)”, *Surf. Sci.*, vol. 541, pp. 128-136, 2003.
- [161] R. S. Vemuri, M. H. Engelhard, and C. V. Ramana, “Correlation between surface chemistry, density, and band gap in nanocrystalline WO<sub>3</sub> thin films,” *ACS Appl. Mater. Interfaces*, vol. 4, pp. 1371-1377, 2012.
- [162] R. Reiche, F. Yubero, J. P. Espinos, and A. R. Gonzalez-Elipe, “Structure, microstructure and electronic characterization of the Al<sub>2</sub>O<sub>3</sub>/SiO<sub>2</sub> interface by electron spectroscopies,” *Surf. Sci.*, vol. 457, pp. 199-210, 2000.
- [163] G. D. Wilk, R. M. Wallace, and J. M. Anthony, “High-gate dielectrics: current status and materials properties considerations,” *J. Appl. Phys.*, vol. 89, pp. 5243-5274, 2001.
- [164] R. Hezel and K. Jaeger, “Low-temperature surface passivation for solar cells,” *J. Electrochem. Soc.*, vol. 136, pp. 518-523, 1989.
- [165] W. Liang, K. J. Weber, D. Suh, J. Yu, and J. Bullock, “Humidity degradation and repair of ALD Al<sub>2</sub>O<sub>3</sub> passivated silicon,” In Proc. of 39<sup>th</sup> IEEE Photovoltaic Specialists Conference, 2013, pp. 038-044.
- [166] L. Tous, R. Russell, J. Das, R. Labie, M. Ngamo, J. Horzel, H. Philipsen, J. Snickers, K. Vandermisse, L. van den Brekel, T. Janssens, M. Aleman, D.H. van Dorp, J.

- Poortmans, and R. Mertens “Large area copper plated silicon solar cell exceeding 19.5% efficiency,” *Energy Procedia*, vol. 21, pp. 58–65, 2012.
- [167] A. Richter, J. Benick, M. Hermle, and S. W. Glunz, “Excellent silicon surface passivation with 5 Å thin ALD Al<sub>2</sub>O<sub>3</sub> layers: Influence of different thermal post-deposition treatments,” *Phys. Status Solidi – Rapid Res. Lett.*, vol. 5, no. 5-6, pp. 202–204, 2011.
- [168] Sandeep S. S. K. Warikoo, and A. Kottatharayil, “Optimization of ICP-CVD silicon nitride for Si solar cell passivation,” In Proc. of 38<sup>th</sup> IEEE Photovoltaic Specialists Conference, 2012, pp. 001102-001104.
- [169] S. Duttagupta, F. Lin, K. D. Shetty, M. Wilson, F.-J. Ma, J. Lin, A. G. Aberle, and B. Hoex, “State-of-the-art surface passivation of boron emitters using inline PECVD AlOx/SiNx stacks for industrial high-efficiency silicon wafer solar cells,” In Proc. of 39<sup>th</sup> IEEE Photovoltaic Specialists Conference, 2013, pp. 001036-001039.
- [170] J. Wu, Y. Liu, X. Wang, and G. Xing, “Application of ion implanted emitter in PERC solar cells,” In Proc. of 42<sup>nd</sup> IEEE Photovoltaic Specialists Conference, 2015, pp. 1-6.
- [171] B. Vermang, H. Goverde, V. Simons, I. De Wolf, J. Meersschaut, S. Tanaka, J. John, J. Poortmans, and R. Mertens, “A study of blister formation in ALD Al<sub>2</sub>O<sub>3</sub> grown on silicon,” In Proc. of 38<sup>th</sup> IEEE Photovoltaic Specialists Conference, 2012, pp. 001135 – 001138.
- [172] A. G. Aberle, “Overview on SiN surface passivation of crystalline silicon solar cells,” *Sol. Energy Mater. Sol. Cells*, vol. 65, pp. 239-248, 2001.

## List of Publications

### Journal publications

1. **M. Bhaisare**, A. Misra, and A. Kottanthalayil, “Aluminum oxide deposited by pulsed-DC reactive sputtering for crystalline silicon surface passivation,” *IEEE J. Photovolt.*, vol. 3, no. 3, pp. 930-935, 2013.
2. **M. Bhaisare**, A. Misra, M. Waikar, and A. Kottanthalayil, “High quality Al<sub>2</sub>O<sub>3</sub> dielectric films deposited by pulsed-DC reactive sputtering technique for high-k applications,” *Nanosci. Nanotechnol. Lett.*, vol. 4, no. 6, pp. 645-650, 2012.

### Conference publications

3. K. Midya, **M. Bhaisare**, A. Kottanthalayil, and S. Dhar, “Investigation of nature of UV induced negative charge in Al<sub>2</sub>O<sub>3</sub> film,” In Proc. of 3<sup>rd</sup> IEEE International Conference on Emerging Electronics, 2016, pp. 1-4.
4. **M. Bhaisare**, S. S. Sandeep, and A. Kottanthalayil, “Thermal stability of single layer pulsed-DC reactive sputtered AlO<sub>x</sub> film and stack of ICP-CVD SiN<sub>x</sub> on AlO<sub>x</sub> for p-type c-Si surface passivation,” In Proc. of 2<sup>nd</sup> IEEE International Conference on Emerging Electronics, 2014, pp. 1-4.
5. **M. Bhaisare**, D. Sutar, A. Misra, and A. Kottanthalayil, “Effect of power density on the passivation quality of pulsed-DC reactive sputtered aluminum oxide on p-type crystalline silicon,” In Proc. of 39<sup>th</sup> IEEE Photovoltaic Specialists Conference, 2013, pp. 1207-1211.
6. **M. Bhaisare**, G. Jeevanandam, and A. Kottanthalayil, “Pulsed-DC reactive sputter deposited aluminum oxide for surface passivation of p-type silicon for solar cell applications,” presented at 3<sup>rd</sup> International Conference on Advances in Energy Research, Mumbai, India, 2011.

7. **M. Bhaisare**, A. Misra, M. Waikar, and A. Kottanthalayil, “High quality Al<sub>2</sub>O<sub>3</sub> dielectric films deposited by pulsed-DC reactive sputtering technique for high-k applications,” presented at International Conference on Materials for Advance Technologies 2011, Singapore, 2011.
8. A. Mishra, H. Kalita, M. Waikar, A. Gour, **M. Bhaisare**, M. Khare, M. Aslam, and A. Kottanthalayil, “Multilayer graphene as charge storage layer in floating gate flash memory,” In Proc. of 4<sup>th</sup> IEEE International Memory Workshop, Milano, 2012, pp. 1-4.
9. A. Misra, M. Waikar, A. Gour, **M. Bhaisare**, S. Mane, P. Nyaupane, and A. Kottanthalayil, “SiO<sub>2</sub>/Al<sub>2</sub>O<sub>3</sub> dielectric stack with low power pulsed-DC reactive sputtered high-k Al<sub>2</sub>O<sub>3</sub> as blocking dielectric for NAND flash application,” presented at International Workshop on Physics of Semiconductor Devices 2011, Kanpur, India, 2011.
10. M. A. Khaderbad, R. Pandharipande, A. Gautam, A. Mishra, **M. Bhaisare**, A. Kottanthalayil, Y. Meesala, R. Mangalampalli, and V. R. Rao, “Bottom-up Method for Work Function Tuning in High-k/Metal Gate Stacks in Advanced CMOS Technologies,” In Proc. of 11<sup>th</sup> IEEE International Conference on Nanotechnology, Portland, Oregon, 2011, pp. 269-273.
11. A. Misra, S. Sadana, S. Suresh, **M. Bhaisare**, S. Srinivasan, M. Waikar, A. Gaur, and A. Kottanthalayil, “Effect of different substrate materials on the Pt nanocrystal formation statistics (size, density area coverage and circularity) for flash memory application,” presented at MRS Fall Meeting 2010, Boston, 2010.

## Manuscript under preparation

12. **M. Bhaisare**, S. Kalaivani, K. Dileep, R. Datta, and A. Kottanthalayil, “Study of origin and distribution of fixed oxide charges in pulsed-DC reactive sputtered aluminum oxide using electron energy loss spectroscopy,”